Resonant and High Resolution Photoemission of Rare-earth Cobalt Oxides

A thesis submitted to The University of Manchester for the degree of Doctor of Philosophy in the Faculty of Engineering and Physical Sciences

2010

Hafiz Muhammad Rafique

School of Physics and Astronomy

List of Contents

List of Contents 2

List of Figures 9

List of Tables 23

List of Abbreviations 24

Abstract 28

Declaration 29

Copyright Statement 30

Publication 31

Acknowledgements 32

Dedication 34

Chapter 1 Introduction 35

1.1 Thesis Objectives 35

1.2 Background Concepts 36

1.2.1 Band Structure of Solids 36

1.2.2 Hubbard Model 41

1.2.3 Crystal Structures 43

1.2.3.1 Crystal Structure of Cobaltite Perovskites ABX_3 and 43

$LnBaCo_2O_{5+\delta}$ (Ln = rare earth) - Ln-112

1.2.3.2 Crystal Structure of $LnBaCo_4O_{7+\delta}$ (Ln= Yb, δ =0) -Ln-114 46

1.2.4 Crystal Field Splitting and Spin State Notation for Co in the Octahedral Environment 49

1.2.5 Crystal Field Splitting and Spin State Notation for Co in the Tetrahedral Environment 52

References 55

Chapter 2 Sample Bulk Characterisation Techniques, Crystal Growth and Magnetic Structure 57

2.1 Introduction 57

2.2 X-Ray Diffraction (XRD) 58

2.2.1 Basic concepts about crystals 58

2.2.2 Bragg's Law 62

2.2.3 XRD Technique 63

2.3 Neutron Diffraction 65

2.4 Four-Point Probe for Resistivity Measurement 69

2.5 Crystal Growth 70

2.5.1 Introduction to Crystal Growth of $LnBaCo_2O_{5+\delta}$ 70

2.5.2 Crystal Growth 72

2.5.3 Oxygen Annealing of $DyBaCo_2O_{5+\delta}$ 74

2.6 Magnetic Structure 77

2.6.1 Basic Concepts 77

2.6.1.1 Magnetism 77

2.6.1.2 Types of Magnetic Materials 80

2.6.1.2.1 Diamagnetic 80

2.6.1.2.2 Paramagnetic 80

2.6.1.2.3 Ferromagnetic 81

2.6.1.2.4 Antiferromagnetic 81

2.6.1.2.5 Ferrimagnetic 82

2.6.1.3 Bulk Properties of Magnetic Materials 82

2.6.1.3.1 Magnetisation and Susceptibility 82

2.7 Electronic and Magnetic Behaviour of Rare-earth Cobalt Oxides 86

2.7.1 $LnBaCo_2O_{5+\delta}$ (Ln = rare-earth) - Ln-112 86

2.7.2 Magnetic Structure of $DyBaCo_2O_{5.5}$ 97

2.8 Magnetic and Structural Behaviour of $LnBaCo_4O_{7+\delta}$ (Ln = rare- earth) - Ln-114 103

2.9 Magnetic Characterisation for $LnBaCo_4O_{7+\delta}$ (Ln = Yb, Tb, Lu) - Ln-114 single crystals 106

2.9.1 Super Conducting Quantum Interference Device (SQUID) Magnetometery 106

2.9.2 The SQUID Quantum Design MPMS Facility at the University of Manchester 108

2.9.3 Magnetisation: Results and Discussion 109

2.10 Conclusion 115

References 117

Chapter 3 Photoelectron Spectroscopy: Theoretical Background and Instrumentation 122

3.1 Introduction 122

3.2 Photoemission from Solids 122

	3.2.1		Koopmans' Theory	126
	3.2.2		Surface Sensitivity and Inelastic Electron Mean Free Path	127
	3.2.3		Beer-Lambert Law	128
	3.2.4		Chemical Shifts	130
	3.2.5		Satellite Features	130
	3.2.6		Auger Emission	131
	3.2.7		Spin Orbit Coupling	132
3.3			Ultraviolet Photoemission Spectroscopy	132
	3.3.1		Valence Band Resonant Photoemission	132
	3.3.2		Types of Photoemission Spectra	134
		3.3.2.1	Energy Distribution Curves (EDCs)	134
		3.3.2.2	Constant Initial State Spectra	135
3.4			Synchrotron Radiation	136
	3.4.1		The Daresbury Synchrotron	139
	3.4.2		Daresbury Laboratory Station 3.2	141
		3.4.2.1	The Beamline	141
		3.4.2.2	Flux	143
		3.4.2.3	Resolution	144
		3.4.2.4	End Station	146
	3.4.3		Daresbury Laboratory Station MPW 6.1	146
		3.4.3.1	The Beamline	146
		3.4.3.2	Flux	149
		3.4.3.3	Resolution	150

		3.4.3.4	End Station	151
3.5			Vacuum Conditions	152
	3.5.1		Baking	153
	3.5.2		Vacuum Pumps	153
	3.5.3		Turbomolecular Pump	153
	3.5.4		Ion Pump	154
	3.5.5		Titanium Sublimation Pump (TSP)	155
3.6			Pressure Measurement	156
	3.6.1		Pirani Gauge	156
	3.6.2		Ion Gauge	157
	3.6.3		Quadrupole Mass Spectrometer	157
3.7			Electron Energy Analyser	158
3.8			Electron Detectors (Counters)	162
3.9			Modes of Operation and Analyser Controls	164
3.10			Sample Manipulation	164
		References		165
Chapter 4		**Surface Degradation of Cobaltite Surfaces**		168
4.1			Introduction	168
4.2			Photoemission Measurements; Surface Degradation	168
	4.2.1		Experimental Procedure	168
4.3			Results and Discussion	170
	4.3.1		General Features of the Valence Band Photoemission of the Double Perovskites $LnBaCo_2O_{5+\delta}$ (Ln = Gd, Dy, $Dy_{1-x}Tb_x$) - Ln-112	170

	4.3.2	Temperature Effects on the Valence Band Spectra of $LnBaCo_2O_{5+\delta}$ (Ln = Gd, Dy, $Dy_{1-x}Tb_x$)	172
	4.3.3	General Features of the Valence Band Photoemission of $LnBaCo_4O_{7+\delta}$ (Ln = Yb; δ = 0) - Ln-114	174
	4.3.4	Temperature Effects on the Valence Band Spectra of $YbBaCo_4O_7$	175
4.4		Previous Photoemission Studies of Small Molecule Adsorption and Contamination of Oxide Surfaces	176
4.5		Surface Contamination of Cobaltite Surfaces	181
	4.5.1	Surface Contamination of $LnBaCo_2O_{5+\delta}$ (Ln = Gd, Dy, $Dy_{1-x}Tb_x$)	181
	4.5.2	Surface Contamination of $YbBaCo_4O_7$	184
4.6		Conclusions	186
		References	187
Chapter 5		**High Resolution Photoemission, Results and Discussion on $LnBaCo_2O_{5+\delta}$**	188
5.1		Introduction	188
5.2		Valence Band Spectra of $LnBaCo_2O_{5+\delta}$ (Ln = Gd, Dy, $Dy_{1-x}Tb_x$) as a Function of Temperature	189
	5.2.1	Temperature-dependent Co Spin States in $Dy_{1-x}Tb_xBaCo_2O_{5+\delta}$	193
5.3		The Metal-Insulator Transition in $LnBaCo_2O_{5+\delta}$ (Ln = Gd, Dy, $Dy_{1-x}Tb_x$)	195
5.4		Oxygen Resonance Photoemission	202
	5.4.1	Oxygen Resonance Photoemission in $LnBaCo_2O_{5+\delta}$ (Ln = Gd, $Dy_{1-x}Tb_x$)	203
5.5		Conclusions	207
		References	208

Chapter 6			**Photoelectron Spectroscopy of $LnBaCo_4O_{7+\delta}$ ($\delta = 0$) – Ln-114**	210
6.1			Introduction	210
6.2			Valence Band Photoemission of $YbBaCo_4O_7$	210
6.3			Resonant Photoemission in $YbBaCo_4O_7$	212
	6.3.1		Rare-earth Resonant Photoemission	212
		6.3.1.1	Rare-earth Resonant Photoemission in $YbBaCo_4O_7$	213
	6.3.2		Barium Resonant Photoemission in $YbBaCo_4O_7$	219
	6.3.3		Oxygen Resonant Photoemission in $YbBaCo_4O_7$	220
	6.3.4		Cobalt Resonant Photoemission	222
		6.3.4.1	Cobalt Resonant Photoemission in $YbBaCo_4O_7$	222
6.4			Summary of Resonance Photoemission Results	224
6.5			Comparison of $LnBaCo_2O_{5+\delta}$ and $LnBaCo_4O_{7+\delta}$	226
6.6			Conclusions	228
			References	229
Chapter 7			**Overall Conclusions**	231
7.1			Introduction	231
7.2			$LnBaCo_2O_{5+\delta}$ - Ln-112	231
7.3			$LnBaCo_4O_{7+\delta}$ ($\delta = 0$) - Ln-114	233
7.4			Comparison of $LnBaCo_2O_{5+\delta}$ and $LnBaCo_4O_{7+\delta}$	234
			References	236

[Final word count 51081]

List of Figures

Capter1 **Introduction**

Figure 1.1: *The Fermi surface and the Fermi sphere where v and v_F denote the velocities of electron in velocity space and at the Fermi energy respectively.* 37

Figure 1.2 *Fermi-Dirac distribution at T = 0 K and T > 0 K.* 39

Figure 1.3 (a) *Plot of E vs wave vector k for a free electron* (*b*) *plot of E vs wave vector k for an electron in a monoatomic linear lattice with lattice constant a. The energy gap is associated with the first Bragg reflection at $k = \pm \pi/a$. Other gaps can be found at $k = \pm n\pi/a$ for non-negative integral values of n.* 39

Figure 1.4 *Energy bands of transition metal oxide with empty d-band (left) and partially filled d-band (right).* 40

Figure 1.5 *The overlap of Hubbard sub-bands as the band width W increases relative to the Mott-Hubbard splitting energy U. A represents the electron affinity of neutral atom, I represents the ionisation energy of an electron and E_F shows the Fermi energy.* 42

Figure 1.6 *Idealised crystal structure of $LaCoO_3$.* 43

Figure 1.7 *Single perovskite structure of $LaCoO_3$.* 44

Figure 1.8 *Crystal structure of $LnBaCo_2O_5$.* 45

Figure 1.9 *Crystal structure of $LnBaCo_2O_{5.5}$.* 45

Figure 1.10 *Crystal structure of $LnBaCo_2O_6$.* 45

Figure 1.11 *Crystal structure of $YbBaCo_4O_7$. The Co network of $YbBaCo_4O_7$ consists of Co(1) and Co(2): Co(2) form the Kagomé sheets and Co (1) link these sheets along the c axis. The oxygen ions reside at the corners of the tetrahedra surrounding the cobalt ions. Yb^{3+} and Ba^{2+} ions have twelve and six coordination number with oxygen ions respectively.* 47

Figure 1.12 *A special woven pattern for bamboo baskets - kagomé in Japanese.* 47

Figure 1.13 *Kagomé net of cobalt ions in $YbBaCo_4O_7$.* 47

Figure 1.14 *(a) The hcp stacking of Ba-containing anticuboctahedra (b) four Ba-containing polyhedra showing the tetrahedral space where the rare earth ion resides surrounded by six oxygen atoms (not shown here)(c) four Co-tetrahedra filling the octahedral space in between six Ba.* 48

Figure 1.15 *Crystal structure of $YbBaCo_4O_7$ at 225 K (left) based on joint refinement of neutron and X-ray powder data. Coordination of twelve O atoms to the Ba site is highlighted on the right of the figure.* 48

Figure 1.16 *Crystal field splitting of the energy of an electron in the d - orbitals of the central atom in an octahedral environment.* 49

Figure 1.17 *Different spin states of the Co^{3+} 3d orbitals in an octahedral environment.* 51

Figure 1.18 *A transition metal atom M in a cube surrounded by four ligands L making a tetrahedral environment.* 52

Figure 1.19 *(a) The position of the $3d_{xy}$ orbital of transition metal ion with respect to surrounding ligands (orange coloured) in a tetrahedral environment (b) The position of the $3d_{x^2-y^2}$ orbital in the same environment.* 53

Figure 1.20 *Crystal field splitting of the energy of an electron in the d - orbitals of the central atom in a tetrahedral environment.* 53

Figure 1.21 *Spin states of the Co^{3+} 3d orbitals in a tetrahedral environment.* 54

Chapter 2 **Sample Bulk Characterisation Techniques, Crystal Growth and Magnetic Structure**

Figure 2.1 *A translation vector $\boldsymbol{T} = 2\boldsymbol{a} + 3\boldsymbol{b} + 2\boldsymbol{c}$ representing the position of a point P in the crystal lattice, where **a**, **b** and **c** are the three fundamental vectors along the edges of the unit cell.* 59

Figure 2.2 *The 14 Bravis lattices.* 61

Figure 2.3 *Labelling a plane using Miller indices.* 62

Figure 2.4 *Diagram of the Bragg reflection process.* 63

Figure 2.5	*Schematic diagram of a four-circle diffractometer.*	64
Figure 2.6	*Schematic diagram for neutron diffraction experiment.*	66
Figure 2.7	*Schematic diagram of a four-point probe for the measurement of resistivity of a crystal sample*	69
Figure 2.8	*Schematic layout of the FZ technique for growing single crystals.*	70
Figure 2.9	*Diagram of the two-chamber furnace: 1-Lining with refractory bricks made from porous alumina; 2,3-fixed and removable lids; 4-magnesia crucible; 5-crystal holder; 6- single crystal; 7-resistive heaters; 8-thermocouples; 9-thermal shield between upper and lower chambers; 10-flux melt; 11-support made from porous alumina.*	71
Figure 2.10	*Primary crystallization fields of co-crystallised cobaltite phases in the Co-enriched part of the Dy_2O_3-BaO-CoO quasi-ternary phase diagram, established at the ISSSP, Minsk. ζ_{Co} and ζ_{Ba} denote relative molar ratios of Co and Ba respectively. Numbering I-III and 1-6 represent primary composition ranges and phases respectively.*	73
Figure 2.11	*(a) As-grown single crystal of $DyBaCo_2O_{5+\delta}$ on the surface of the magnesia crystal holder and (b) the same crystal from the back.*	74
Figure 2.12	*Temperature-time diagram of optimal annealing for $DyBaCo_2O_{5+\delta}$ single crystals under flowing oxygen.*	75
Figure 2.13	*Temperature vs time plan followed for the optimal annealing of single crystal $DyBaCo_2O_{5+\delta}$ under flowing oxygen used in this work. This was undertaken in the PSI, Manchester.*	75
Figure 2.14	*A schematic layout of the experimental setup for the optimal annealing of single crystal $DyBaCo_2O_{5+\delta}$ under flowing oxygen in this work.*	76
Figure 2.15	*Magnetic field produced by spinning electron.*	77
Figure 2.16	*Magnetic field produced by a current-carrying loop of wire.*	77
Figure 2.17	*Magnetic field pattern of a bar magnet.*	78
Figure 2.18	*An electron circulating around a nucleus in an atom.*	78
Figure 2.19	*Orientation of dipole moments in (a) paramagnetic materials (b) ferromagnetic materials.*	80

Figure 2.20 *Orientation of dipole moments in (a) antiferromagnetic materials (b) ferrimagnetic materials.* 81

Figure 2.21 *Temperature dependence of the reciprocal magnetic susceptibility showing the Curie law behaviour of paramagnetic materials.* 83

Figure 2.22 *Temperature dependence of the reciprocal magnetic susceptibility showing Curie-Weiss law behaviour of ferromagnetic materials above the Curie temperature in the paramagnetic state.* 84

Figure 2.23 *Antiferromagnetic to paramagnetic transition of antiferromagnetic materials as a function of temperature for $\theta < 0$ where T_N is the Néel temperature.* 85

Figure 2.24 *Temperature dependence of the reciprocal magnetic susceptibility showing Curie-Weiss law behaviour of antiferromagnetic materials.* 85

Figure 2.25 *Temperature dependence of the reciprocal magnetic susceptibility showing the behaviour of ferrimagnetic materials.* 86

Figure 2.26 *Occupation of Co^{3+} spin states in $LaCoO_3$ as a function of temperature determined from measurements of magnetic susceptibility.* 88

Figure 2.27 *Calculated spin state dependence of the Co^{3+} contribution to the valence band density of states of $LaCoO_3$ produced from cluster calculations.* 89

Figure 2.28 *Temperature dependent magnetisation of $GdBaCo_2O_{5+\delta}$. Open and closed marks represent temperature-dependent zero field cooling (ZFC) and field cooling (FC) magnetisations, respectively. The inset shows the magnetisation data for $GdBaCo_2O_{5+\delta}$ ($\delta = 0$) as a function of temperature.* 90

Figure 2.29 *Temperature-dependent resistivity curves of $GdBaCo_2O_{5+\delta}$ measured at 0 T (open circles) and 5 T (solid circles). Solid squares denote MR values. Vertical dots show the magnetic phase boundaries.* 91

Figure 2.30 *(a):Temperature dependence of the resistivity(ρ) for air-synthesised $LnBaCo_2O_{5+\delta}$.The inset shows an enlargement of the transition for Ln = Tb.* 92

Figure 2.30 *(b):Temperature dependent resistivity curves for $GdBaCo_2O_{5+\delta}$ a) air-synthesised, b) argon annealed c) oxygen-annealed; $HoBaCo_2O_{5+\delta}$ d) air-synthesised e) oxygen annealed; $PrBaCo_2O_{5+\delta}$ f) air-synthesised, g) argon annealed.* 92

Figure 2.31 *(a) Cell parameters obtained by high-resolution neutron power diffraction (NPD) data at different temperatures.*
(b) temperature dependence of the mean Co-O distance for tahedra and pyramids. 93

Figure 2.32 *Cell volume of $PrBaCo_2O_{5.5}$ by high-resolution neutron power diffraction and $GdBaCo_2O_{5.5}$ – normalised to that at 10 K.* 93

Figure 2.33 *(a) Valence-band and (b) near E_F XPS spectra of $TbBaCo_2O_{5.5}$ taken at 30, 250, 300, and 380 K.* 95

Figure 2.34 *(a) Valence band and (b) near-E_F XPS spectra of $NdBaCo_2O_{5.5}$ taken at 25, 60, 300, and 380 K. The inset shows an expanded view of the valence band in the vicinity of the Fermi level.* 95

Figure 2.35 *Schematic diagram of the Co 3d band structure suggested by Takubo et al. for (a) metallic state and (b) insulating state of $LnBaCo_2O_{5.5.}$* 96

Figure 2.36 *Temperature dependent in-plane resistivity of $DyBaCo_2O_{5.5.}$* 98

Figure 2.37 *Four unit cells, observed in $LnBaCo_2O_{5+\delta}$ at different oxygen content, degree of oxygen ordering and temperature. Cobalt ions in the pyramidal and octahedral sublattices are shown by the grey and white circles respectively and their positions are labelled by integers 1-16. Oxygen atoms in the apical positions are described by black circles. The other oxygen atoms are in the corners of the coordinating polyhedra. The Ln and Ba atoms are omitted for simplicity.* 99

Figure 2.38 *Temperature-dependent intensity of three neutron Bragg reflections* (1, 1, 2), (0, 0, 1) *and* (1, 1, 1). *These reflections are mainly due to magnetic scattering from a twin-free crystal of $DyBaCo_2O_{5.5}$.* 100

Figure 2.39 *Four models (a)–(d) of magnetic structure in $DyBaCo_2O_{5.50\ (5)}$ at T = 248 K. The green arrows show the spin arrangement and the approximate values at T = 0 corresponding to the columns (a)–(d) in Table 2.4. Displacements of the oxygen atoms from their positions in the Pmmm group are described by the black arrows. Integers 1-8 refer to the column n in Table 2.4.* 101

Figure 2.40 *Magnetic structure of $DyBaCo_2O_{5.50\ (5)}$ at T = 248 K*
(a)G-type (b) approximately G-type. 103

Figure 2.41 (*a*) *Magnetization as a function of temperature for Yb-114 measured on* 105

warming in 1T. ZFC = zero-field cooled; FC = field cooled. Inset: Detail of the temperature region near the structural phase transition. (*b*) *Isothermal magnetization measured at 25 K. The arrow marks Hc, the onset of the irreversible field-induced transition. Inset:* H_c *as a function of T. In each case, the sample was ZFC to the measuring temperature from 150 K then the field was applied.*

Figure 2.42 *Two constant-current-carrying Josephson junctions connected in parallel.* 107

Figure 2.43 *A Quantum Design MPMS XL SQUID magnetometer at the University of Manchester.* 109

Figure 2.44 *MPMS sample probe.* 109

Figure 2.45 *Zero-field-cooled (ZF) and field-cooled (FC) temperature-dependent magnetisation for* $YbBaCo_4O_{7.2}$ *measured in a fixed magnetic field (H) of 600 Oe and parallel to the* (*001*) *plane: (a) the crystal sample was thermally treated in flowing nitrogen at T = 900 °C for about 20 hours after growth* (*c*) *the crystal sample was oxygenated at T = 800 °C for about 20 hours after growth (d). (b) and (d) are expended views of (a) and (c) respectively.* 110

Figure 2.46 *Temperature-dependent magnetisation for* $TbBaCo_4O_{7.2}$ *measured at different values and orientations of the external magnetic field (H): (a) Zero-field-cooled* (*ZFC*) *and field-cooled* (*FC*) *magnetisation curves at H = 600 Oe and parallel to the c-axis,* (*b*) *ZFC and FC magnetisation curves at H = 600 Oe and parallel to the* (*001*) *plane, (c) ZFC and FC magnetisation curves at H = 50 Oe and parallel to the c-axis, (d) ZFC and FC magnetisation curves at H = 50 Oe and parallel to the* (*001*) *plane.* 111

Figure 2.47 *Magnetic hysteresis curves for* $TbBaCo_4O_{7.2}$ *measured at T = 20 K*: *(a) with H || (001),* (b) *with H || c-axis.* 112

Figure 2.48 *Temperature-dependent magnetisation for* $LuBaCo_4O_{7.2}$ *showing possible chiral-glass-like behaviour measured at H = 600 Oe:*
(a) Zero-field-cooled (*ZFC*) *and field-cooled* (*FC*) *magnetisation curves with external field* (*H*) *|| c - axis,* (*b*) *ZFC and FC magnetisation curves with H || (001), (c) ZFC, field-cooled on decreasing temperature* (*FCC*) *and field-cooled on warming* (*FCW*) *magnetisation curves with H || c - axis, (d) ZFC, FCC and FCW magnetisation curves with H || (001).* 113

Figure 2.49 *Isothermal magnetisation M (H) for single crystal* $LuBaCo_4O_{7.2}$ 114

measured at different orientations of the external magnetic field: (a) and (c) reveal hysteresis curves at fields of several hundred Oe and T = 2 K with H || c-axis and H || (001) respectively, (b) and (d) show chiral-glass-like behaviour at T = 20 K with H || c - axis and H || (001) respectively.

Chapter 3 **Photoelectron Spectroscopy: Theoretical Background and Instrumentation**

Figure 3.1 *Geometrical arrangement of photoemission experiment representing the photon source, the sample, the analyser, the detector and the KE spectrum of the emitted photoelectrons.* 123

Figure 3.2 *A schematic diagram of the photoemission process. The energy E of the electrons is plotted along the y-axis and the number of electrons as a function of energy N(E) along the x-axis. The diagram shows how the energy levels in the solid are transferred by absorption of photons into the vacuum where N(E) is measured through the intensity of photoemitted electrons as a function of electron kinetic energy. Here* E_V *denotes the vacuum level and* Φ is *the work function.* 124

Figure 3.3 *An energy level diagram for photoemission from a metallic sample in contact with the spectrometer.* 125

Figure 3.4 *Dependence of the IMFP on the photoelectron kinetic energy for inorganic materials.* 128

Figure 3.5 *Surface sensitivity enhancement by variation of the photoelectron detection angle relative to the surface normal.* 129

Figure 3.6 *Creation of a core hole:* a *1s electron leaves the K shell creating a hole.* 131

Figure 3.7 *Auger emission*: a *transition from a 2p to a 1s state results in emission of an Auger electron from the L shell.* 131

Figure 3.8 *Direct and resonant photoemission*: *(a) transition metal 3d VB and 3p core level before PES; (b) 3d direct PES - an electron from 3d level is ejected; (c) core electron can be excited from the 3p level to VB with a matched energy photon - this transient state decays into a state shown in (d) i.e. a 3d electron is shifted to the 3p level while another 3d electron is emitted.* 134

Figure 3.9 *An illustration of the CIS experiment. The energy interval which defines the KE of electrons accepted from a fixed initial state is scanned* 135

synchronously with the photon energy.

Figure 3.10 *(a) Angular distribution of radiation emitted from an electron moving along a circular path (dashed line) at speeds much less than the speed of light c. (b) Angular distribution distorted by relativistic effects of an electron travelling in the same circular path but at speeds approaching c.* 137

Figure 3.11 *The typical spectral distribution of the radiation emitted by the Synchrotron Radiation Source, Daresbury, UK.* 137

Figure 3.12 *Schematic layout of a synchrotron radiation source.* 138

Figure 3.13 *Daresbury Lab SRS storage ring.* 140

Figure 3.14 *Plan layout of beamline 3 at Daresbury Lab: Mirror details: M_1: cylindrical, SiC, 4:1 demagnification, grazing angle 10°, aperture 7.5 mrad horizontal, 2.5 mrad verti-cal, M_4: cylindrical, SiC, 2:1 demagnification, grazing angle 5°, aperture 10 mrad hori-zontal, 2.5 mrad vertical. M_5: plane, SiC, grazing angle 5°, 5 mrad horizontal and vertical aperture, S: slits; E: experimental chamber; G: diffraction grating.* 142

Figure 3.15 *Five metre McPherson high-resolution normal incidence monochromator.* 143

Figure 3.16 *Flux provided by the McPherson monochromator.* 144

Figure 3.17 *Resolution vs energy of photons for beamline 3.2 at the SRS.* 145

Figure 3.18 *Comparison of the MPW flux output with other insertion devices at the SRS.* 147

Figure 3.19 *Schematic layout of Daresbury SRS beamline MPW 6.1.* 147

Figure 3.20 *Comparison of measured (dashed lines) and calculated (solid lines) flux of beamline MPW6.1.* 150

Figure 3.21 *Comparison of calculated (solid lines) and measured (dots) resolution for the low energy grating on MPW6.1.* 151

Figure 3.22 *Cross section of a turbomolecular pump.* 154

Figure 3.23 *Schematic diagram of a sputter ion pump.* 155

Figure 3.24 *Schematic diagram of a titanium sublimation pump.* 156

Figure 3.25 *Cross section of an ion gauge.* 157

Figure 3.26 *Schematic layout of a quadrupole mass spectrometer.* 158

Figure 3.27 *CLAM-4 analyser.* 159

Figure 3.28 *Schematic diagram of a hemispherical analyser, where S_1 = the entrance slit, S_2 = the exit slit, V_i = inner hemisphere (negative) potential, V_o = the outer hemi-sphere (negative) potential, R_1 = inner hemisphere radius, R_2 = outer hemisphere radius, R_o = radius of average electron path, MCD = multichannel detector assembly and IRL = input retardation lens.* 160

Figure 3.29 *Schematic diagram of multichannel plates.* 163

Chapter 4 **Surface Degradation of Cobaltite Surfaces**

Figure 4.1 *Fermi edge of the copper (Cu) sample holder at 155 K. Two points A and B are marked at 80% and 20% levels of the total height of the Cu Fermi edge plot respectively relative to background level. The best achieved overall resolution (ΔE) on beamline 3.2 was calculated to be 37 meV at 155 K.* 169

Figure 4.2 *Effect of temperature on the high-resolution valence band EDC spectra of $GdBaCo_2O_{5.5}$. Points A-D were later selected for O2s→2p resonance photoemission at room temperature. The spectra are normalised to the incident photon flux.* 171

Figure 4.3 *Effect of temperature on the high-resolution valence band EDC spectra of $Dy_{1-x}Tb_xBaCo_2O_{5+\delta}$. The spectra are normalised to the incident photon flux. Points A-C refer to the points later selected for intensity measurement as a function of temperature.* 172

Figure 4.4 *Effect of temperature on the high-resolution valence band EDC spectra of $DyBaCo_2O_{5.5}$. The spectra are normalised to the incident photon flux.* 173

Figure 4.5 *Valence band EDC spectrum of $YbBaCo_4O_7$ showing general features A, B, C. The spectrum was recorded at room temperature and 21 eV photon energy.* 174

Figure 4.6 *Effect of temperature on the high-resolution valence band EDC spectra of $YbBaCo_4O_7$. Points A-C were later selected for O 2s→2p resonance photoemission at room temperature. The spectra are normalised to the incident photon flux.* 175

Figure 4.7 *Molecular orbital energy level diagram for water.* 177

Figure 4.8 *Photoemission spectra of gas phase water using He I radiation.* 177

Figure 4.9 *(a) Photoelectron spectra of scraped $La_{1.8}Sr_{0.2}CuO_4$ exposed to water. The inset shows the change in the work function, $\Delta\Phi$, versus the logarithm of the dose in L; (b) difference spectrum obtained from clean and water-dosed samples. The dashed curve is an alternative difference spectrum and the dotted curve is the He II photoelectron spectrum obtained from solid NaOH.* 179

Figure 4.10 *(a) Photoemission spectra obtained from scraped $La_{1.8}Sr_{0.2}CuO_4$ exposed to CO_2. The inset shows the change in the work function, $\Delta\Phi$, versus the logarithm of the dose in L; (b) difference spectra are shown by solid curves, the dashed curve is an alternative difference spectrum and the dotted curve is the He II photoelectron spectrum obtained from solid $CaCO_3$.* 180

Figure 4.11 *Difference spectrum (contaminated – clean) generated from 23 eV photoemission spectra of freshly scraped $GdBaCo_2O_{5.5}$ sample at 20 K and the contaminated sample at ca. 320 K.* 182

Figure 4.12 *Difference spectrum (contaminated – clean) generated from 23 eV photoemission spectra of a freshly scraped $Dy_{1-x}Tb_xBaCo_2O_{5+\delta}$ sample at room temperature and the contaminated sample at 144K.* 182

Figure 4.13 *Difference spectrum (contaminated – clean) generated from 23 eV photoemission spectra of a freshly scraped $Dy_{1-x}Tb_xBaCo_2O_{5+\delta}$ sample at room temperature and the contaminated sample at 406 K.* 183

Figure 4.14 *Difference spectrum (contaminated – clean) generated from 23 eV photoemission spectra of a freshly scraped $DyBaCo_2O_{5.5}$ sample at room temperature and the contaminated sample at 140 K.* 184

Figure 4.15 *Difference spectrum (contaminated – clean) generated from 23 eV photoemission spectra of a freshly scraped $DyBaCo_2O_{5.5}$ sample at room temperature and the contaminated sample at 401K.* 184

Figure 4.16 *Difference spectrum generated from spectra of a freshly scraped* 185

$YbBaCo_4O_7$ sample and the contaminated one at 300 K.

Chapter 5 **High Resolution Photoemission, Results and Discussion on $LnBaCo_2O_{5+\delta}$**

Figure 5.1 *Effect of temperature on the high-resolution valence band EDC spectra of $GdBaCo_2O_{5.5}$. Points A-D were later selected for O 2s→2p resonance photoemission at room temperature. The spectra are normalised to the incident photon flux. The VB EDCs do not reveal a smooth trend because the data was not recorded in order of increasing temperature and in one experiment.* 190

Figure 5.2 *Effect of temperature on the high-resolution valence band EDC spectra of $DyBaCo_2O_{5.5}$. The spectra are normalised to the incident photon flux. The VB EDCs do not reveal a smooth trend because the data was not recorded in order of increasing temperature and in one experiment.* 191

Figure 5.3 *Effect of temperature on the high-resolution valence band EDC spectra of $Dy_{1-x}Tb_xBaCo_2O_{5+\delta}$. The spectra are normalised to the incident photon flux. Points A-C refer to the points later selected for intensity measurement as a function of temperature. Later, points A-D were also selected for O 2s→2p resonance photoemission at room temperature. Sample was scraped at 144 K.* 192

Figure 5.4 *Effect of temperature on the density of states related to the features located around 1.25 eV(A), 3.25 eV(B) and 4.95 eV(C) binding energies in the valence band of $Dy_{1-x}Tb_xBaCo_2O_{5+\delta}$. Lines (a) I_A,(b) I_B and(c) I_C are the best fit lines to the Co LS states data points related to features A, B and C respectively in the VB.* 194

Figure 5.5 *Effect of temperature on the high-resolution photoemission of low energy (LE) states of $GdBaCo_2O_{5.5}$. The spectra are normalised to the incident photon flux. The spectra do not reveal a smooth trend because the data was not recorded in order of increasing temperature and in one experiment.* 196

Figure 5.6 *Effect of temperature on the high-resolution photoemission of low energy (LE) states of $Dy_{1-x}Tb_xBaCo_2O_{5+\delta}$. The spectra are normalised to the incident photon flux. Sample was scraped at134K* 196

Figure 5.7 *Effect of temperature on the high-resolution photoemission of the low energy (LE) states of $DyTbBaCo_2O_{5.5}$. The spectra are normalised to the incident photon flux. Sample was scraped at 129 K.* 197

Figure 5.8 *An expansion of the valence band EDCs of $GdBaCo_2O_{5.5}$ in a 400 meV range in the vicinity of E_F exhibiting a gradual and small increase in DOS at E_F between 300 and 400 K. Visible spectrum colours between blue and red have been used to show the increase in temperature from 300 to 400 K* 198

Figure 5.9 *An expansion of the valence band EDCs of $Dy_{1-x}Tb_xBaCo_2O_{5+\delta}$ in 400 meV range in the vicinity of E_F exhibiting the DOS as a function of temperature.* 199

Figure 5.10 *An expansion of the valence band EDCs for a 2nd sample of $Dy_{1-x}Tb_xBaCo_2O_{5+\delta}$ in a 400 meV range in the vicinity of E_F exhibiting a gradual and small increase in DOS at E_F with temperature.* 199

Figure 5.11 *An expansion of the valence band EDC of $DyBaCo_2O_{5.5}$ in a 700 meV range in the vicinity of E_F exhibiting increase in DOS at E_F between 311 and 401 K.* 200

Figure 5.12 *Valence band EDC spectra in the vicinity of E_F from an as-grown sample of $Dy_{1-x}Tb_xBaCo_2O_{5+\delta}$ and a well-oxygenated sample of $DyBaCo_2O_{5.5}$ recorded at 423 K and 401 K respectively. First the spectra were normalised to the incident photon flux and then the intensity of EDC at T = 401 K was reduced by a factor ~ 1.9.* 202

Figure 5.13 *Valence band EDCs recorded from $GdBaCo_2O_{5.5}$, in the vicinity of the O 2s→2p resonance. Spectra are background subtracted using a third order polynomial and normalised to the incident photon flux. The spectra were recorded at room temperature. Points A-D were later selected for CIS measurements.* 204

Figure 5.14 *Valence band EDCs recorded from $Dy_{1-x}Tb_xBaCo_2O_{5+\delta}$ in the vicinity of the O 2s→2p resonance. Points A-D were later selected for CIS measurements. Spectra were recorded at room temperature and are normalised to incident photon flux.* 205

Figure 5.15 *CIS spectra generated from valence band EDCs of $GdBaCo_2O_{5.5}$ in the region of the O 2s→2p resonance at the selected points A, B, C and D in the valence band.* 206

Figure 5.16 *CIS spectra generated from valence band EDCs of $Dy_{1-x}Tb_xBaCo_2O_{5+\delta}$ in the region of the O 2s→2p resonance at the selected points A, B, C and D in the valence band.* 206

Chapter 6 **Photoelectron Spectroscopy of $LnBaCo_4O_{7+\delta}$ (δ = 0) - Ln-114**

Figure 6.1 *Effect of temperature on the high-resolution valence band EDC spectra of $YbBaCo_4O_7$ recorded at 30 eV photon energy. Points A-C were later selected for O 2s→2p resonance at room temperature. The spectra are normalised to the incident photon flux.* 211

Figure 6.2 *Valence band EDC spectra from $YbBaCo_4O_7$ recorded over the photon energy range hυ = 170 to 215 eV passing through the Yb 4d→4f threshold at around 180.5 e. Points A-I refer to the features later selected for CIS measurements. The spectra are normalised to the incident photon flux. The EDCs were recorded at room temperature.* 214

Figure 6.3 *CIS spectra from $YbBaCo_4O_7$ recorded over the photon energy range hυ = 170 to 215 eV passing through the Yb 4d→4f threshold at the selected points A-I in the valence band. The spectra are normalised to the incident photon flux. The spectra were recorded at 300 K.* 215

Figure 6.4 *Valence band EDC spectra from $YbFe_4Sb_{12}$ recorded at 700 eV and 500 eV photon energies and temperature 15 K.* 216

Figure 6.5 *Valence band EDC spectra obtained from clean Yb-doped (lower EDC) and Yb- doped and annealed (upper EDC) CdTe crystal sample surfaces recorded at 150 eV photon energy.* 218

Figure 6.6 *Valence band EDCs from $YbBaCo_4O_7$ recorded at room temperature in the vicinity of the Ba 4d→4f resonance ca.104 eV photon energy. The spectra are normalised to the incident photon flux.* 219

Figure 6.7 *Valence band EDC spectra from $YbBaCo_4O_7$ recorded over the photon energy range hυ = 20.5 to 30 eV passing through the O 2s→2p threshold. Points A-C refer to the features later selected for CIS measurements. The spectra are normalised to the incident photon flux.* 220

Figure 6.8 *CIS spectra generated from the valence band EDC spectra of $YbBaCo_4O_7$ recorded over the photon energy range hυ = 20.5 to 30 eV passing through the O 2s→2p threshold. Points A, B and C correspond to CIS measurements of the selected features in the valence band.* 221

Figure 6.9 *CIS spectra from $YbBaCo_4O_7$ recorded over the photon energy range 55 to 70 eV passing through the Co 3p→3d threshold at the selected points A-E. The binding energy positions of features A-E are shown in Figure 6.6. The CIS spectra were recorded at room temperature and are normalised to the incident photon flux.* 223

Figure 6.10 *An EDC spectrum from $YbBaCo_4O_7$ (recorded at room temperature and photon energy 170 eV) showing atomic character labelled. Points A-I* 225

refer to the features that have been selected for resonance photoemission.

Figure 6.11 *Valence band EDC spectra showing general features A_1, B_1, C_1, D_1 in Gd-112 and A, B, C in Yb-114 cobaltite systems. The spectra are recorded at room temperature and a photon of energy 21 eV. The spectra are normalised to the incident photon flux.* 227

List of Tables

Chapter 2 **Sample Bulk Characterisation Techniques, Crystal Growth and Magnetic Structure**

Table 2.1 *The seven crystal systems and the associated space lattices where P, I, A and F stand for primitive, body centered, centered on a single face and face centered respectively.* 60

Table 2.2 *Occupation of the three spin states in $LaCoO_3$ at 130, 300, 360, 425 and 485 K, calculated from magnetic susceptibility data.* 88

Table 2.3 *Atomic coordinates x/a_1, y/a_2, z/a_3, isotropic temperature factors B, and position occupancies n refined in the framework of the space group Pmma on the basis of the neutron diffraction data collected at T = 308 K from a crystal of $DyBaCo_2O_{5.50(2)}$, with 0.945(4) of the crystal volume being a single twin. The lattice parameters, the oxygen content x, and the refinement quality are: a = 7.745(6) Å, b = 7.778(6) Å, c = 7.490(5) Å; x = 5.50(2); χ^2 = 6.18* [49]. *Atom labelling is as shown in figures 2.38 and 2.40.* 99

Table 2.4 *Four possible models of the Co^{3+} spin ordering in the high-temperature magnetically ordered phase I. There are two lines for every atom, with the first one giving the experimental moment values at T = 248 K and the second (bold numbers)-their approximate values extrapolated to T = 0. The spontaneous moment due to ferrimagnetism at 248 K is given by Σ [Mn (248 K)]/8.* 102

Chapter 3 **Photoelectron Spectroscopy: Theoretical Background and Instrumentation**

Table 3.1 *Record of theoretical and measured resolution, and the settings of entrance and exit slits for beamline 3.2 at the SRS* 145

Table 3.2 *Beamline 6.1 linewidth contributions at various photon energies* 148

List of Abbreviations

AC	Alternating Current
AES	Auger Electron Spectroscopy
AFI	Anti-Ferromagnetic Insulator
AFM	Antiferromagnetic
BM	Bending Magnets
CAE	Constant Analyser Energy
CAMAC	Computer Aided Measurement and Control
CB	Conduction Band
CCD	Charge-coupled device
CFT	Crystal Field Theory
CIS	Constant Initial State
CLAM	Combined Lens Analyser Module
CMR	Colossal Magnetoresistance
CPD	Contact Potential Difference
CRR	Constant Retarted Ratio
DC	Direct Current
DOS	Density of States
EDC	Energy Distribution Curve
E_F	Fermi Energy
ESG	Experimental System Group
EU	European Union

FC	Field Cooling
FM	Ferromagnetic
FWHM	Full Width at the Half Maximum
FZ	Floating Zone
GMR	Giant Magnetoresistance
HEG	High Energy Grating
HiResPES	High Resolution Photoelectron Spectroscopy
HS	High Spin
IMFP	Inelastic Mean Free Path
IRL	Input Retardation Lens
IS	Intermediate Spin
ISSP	Institute of Solid State and Semiconductor Physics
KE	Kinetic Energy
L	Langmuir
LE	Low Energy
LEG	Low Energy Grating
LS	Low Spin
M	Metal
MCD	Multichannel Detector
MCP	Multichannel Plate
MEG	Medium Energy Grating
MI	Metal-Insulator
MoLES	Molecular Electron Spectroscopy

MPW	Multipole Wiggler
MR	Magnetoresistance
NPD	Neutron Powder Diffraction
PES	Photoelectron Spectroscopy
PM	Paramagnet
PSI	Photon Science Institute
QE	Quantum Efficiency
RE	Rare-earth
RF	Radio Frequency
SCD	Single Channel Detector
SCU	Spectrometer Control Unit
SR	Synchrotron Radiation
SRS	Synchrotron Radiation Source
TGA	Thermogravimetric Analysis
TM	Transition Metal
T_{MI}	Metal-Insulator Transition Temperature
TSP	Titanium Sublimation Pump
UHV	Ultra High Vacuum
UPS	Ultraviolet Photoelectron Spectroscopy
UV	Ultra Violet
VB	Valence Band
VUV	Vacuum-vltra Violet
XPS	X-ray Photoelectron Spectroscopy

XRD	X-ray Diffraction
ZFC	Zero Field Cooling

Abstract

The University of Manchester
Faculty of Engineering and Physical Sciences

ABSTRACT OF THESIS submitted by Hafiz Muhammad Rafique for the Degree of Doctor of Philosophy and entitled 'Resonant and High Resolution Photoemission of Rare-earth Cobalt Oxides'

Date of submission: 14th June 2010

$LnBaCo_2O_{5+\delta}$ (Ln-112) where Ln = lanthanide element; $0 \leq \delta \leq 1$ and $LnBaCo_4O_{7+\delta}$ (Ln-114) are highly correlated cobalt oxides. Synchrotron photoemission spectroscopy of $LnBaCo_2O_{5+\delta}$ (Ln = Gd, Dy, $Dy_{1-x}Tb_x$) and $LnBaCo_4O_7$ (Ln = Yb) has been undertaken at the UK Synchrotron Radiation Source (Daresbury Laboratory).
During the photoemission experiments, the samples were observed to be contaminated due to residual gases inside the main vacuum chamber. The surface degradation of the samples is studied using the difference spectra generated from the valence band spectra of freshly scraped and contaminated samples and the nature of contaminated species on these samples is identified in the light of the reviewed literature.
High-resolution photoemission is carried out to study the metal-insulator (MI) transition in double perovskites $LnBaCo_2O_{5+\delta}$ (Ln = Gd, Dy, $Dy_{1-x}Tb_x$ – Ln-112; $0 \leq \delta \leq 1$) as a function of temperature. The high-resolution photoemission results of single crystal samples of $GdBaCo_2O_{5.5}$, $DyBaCo_2O_{5.5}$ and $Dy_{1-x}Tb_xBaCo_2O_{5+\delta}$ show that the temperature-based MI transitions in these compounds occur in the 300-400 K temperature range. A post-growth oxygen annealing treatment for as-grown single crystals of Ln-112 is necessary, achieving oxygen contents close to 5.50, to observe a marked nonmetal-to-metal transition.

Resonant photoemission is used to identify the atomic parentage of the valence band states. A comparison of the electronic structure of $LnBaCo_2O_{5+\delta}$ (Ln = Gd, Dy, $Dy_{1-x}Tb_x$ – Ln-112; $0 \leq \delta \leq 1$) and $LnBaCo_4O_7$ (Ln = Yb – Ln-114) single-crystal surfaces is made using synchrotron photoemission spectroscopy. In both cases, the states close to the Fermi energy are found to be of mixed Co 3d/O 2p character, and the comparison allows identification of states due to low spin Co^{3+} in octahedral environments. The contributions from Ln elements to the valence band are found at higher binding energies.

Decleration

I declare that the work contained herein is my own work and that all supporting work has been noted and fully referenced. No portion of the work referred to in this thesis has been submitted in support of an application for another degree or qualification of this or any other university or institute of learning.

Signed .....

Hafiz Muhammad Rafique

Copyright Statement

The following four notes on copyright and the ownership of intellectual property rights apply to this work:

(i) The author of this thesis (including any appendices and/or schedules to this thesis) owns any copyright in it (the "Copyright") and s/he has given The University of Manchester the right to use such Copyright for any administrative, promotional, educational and/or teaching purposes.

(ii) Copies of this thesis, either in full or in extracts, may be made **only** in accordance with the regulations of the John Rylands University Library of Manchester. Details of these regulations may be obtained from the Librarian. This page must form part of any such copies made.

(iii) The ownership of any patents, designs, trade marks and any and all other intellectual property rights except for the Copyright (the "Intellectual Property Rights") and any reproductions of copyright works, for example graphs and tables ("Reproductions"), which may be described in this thesis, may not be owned by the author and may be owned by third parties. Such Intellectual Property Rights and Reproductions cannot and must not be made available for use without the prior written permission of the owner(s) of the relevant Intellectual Property Rights and/or Reproductions.

(iv) Further information on the conditions under which disclosure, publication and exploitation of this thesis, the Copyright and any Intellectual Property Rights and/or Reproductions described in it may take place is available from the Head of School of Physics and Astronomy (or the Vice-President) and the Dean of the Faculty of Life Sciences, for Faculty of Life Sciences' candidates.

Publication

Large single crystals of $LnBaCo_2O_{5.5}$: Initial nucleation, growth and study

S. N. Barilo, S. V. Shiryaev, G. L. Bychkov, A. S. Shestak, W. R. Flavell, A. G. Thomas, H. M. Rafique, Y. P. Chernenkov, V. P. Plakhty, E. Pomjakushina, K. Conder and P. Allenspach, J. Crystal Growth, **310**,1867 (2008).

Acknowledgements

On completing this project that took four years, I would like to acknowledge a number of people who really helped and supported me one way or the other during my PhD. First, I would express my sincere thanks to my supervisor Prof. Wendy Flavell for her continuous supervision, great support, limitless patience, continual encouragement and valuable guidance. I am proud of being her student.

Great thanks go to Dr Andrew Thomas for his tremendous support, discussions, answering many questions during the whole duration of my studies and accompanying me to Belarus for growing single crystal samples.

Special thanks go to Prof. George King for giving me encouragement, support and guidance, especially in early days of my project. His polite attitude and behaviour is worth remembering.

Sincere thanks also go to Prof. Sergei Barilo, Sergei Shiryaeve, Sergei Ustanovich, Yuri Chernenkov and Bychkov for giving me the opportunity to participate in the crystal growth run in Belarus. I am very thankful for their hospitality during my stay in Minsk.

Sincere thanks also go to the staff at the Synchrotron Radiation Source at Daresbury Laboratory for providing technical assistance. Particularly I am greatful to V Dhanak and A Milan for preparing beamlines 3.2 and MPW6.1.

Heartiest thanks are also due to Gemini, Darren, Samantha Hardman, Chris Chatwin, Stephen Rayner, Paul Kirkhum, Karen Syres, Ben Spencer, Louise, Patrick, David, and Yasir.

Sincere and heartiest thanks go to my family-friends Rashid Jalil and his wife Ibtsam Riaz for their tremendous support and cooperation on every occasion. Life has been so peaceful in Manchester during their company.

Finally I am really indebted to my wife Tayyaba for her consistent and untiring assistance for me and my children. Her great emotional support, encouragement and prayers made a lot of contributions in the completion of this work.

Last but not the least; my special thanks go to the Overseas Research Scholarship (ORS) awarding authorities of the University of Manchester. Without this scholarship, the completion of this PhD project looks impossible.

Dedication

I dedicate this thesis to Rao Family:

My wife, Tayyaba Rafique Rao,
my daughter, Hira Rafique Rao,
and my son Rao Muhammad Haris Rafique Khan

Chapter 1

Introduction

1.1 Thesis Objectives

Transition metal oxides exhibit astonishing electronic properties. They may be insulating, semiconducting, metallic and even superconducting depending upon their doping level. Strong electron correlation leads to fascinating magnetic behaviour, including giant magnetoresistance (GMR), with the electron spin state of the sample changing with magnetic field, sample composition and also with temperature. The GMR effect has already been used practically in the read heads of many hard disk drives. The same strong electron correlation makes the electronic structure of these materials very hard to understand and many of the phenomena observed occur on energy scales that require high resolution experiments.

One of the major techniques used to study such materials is photoemission. This PhD project is concerned with resonant and high-resolution photoemission studies of rare earth cobalt oxides. The aim of the work is to improve our understanding of the forces driving metal-to-non-metal and spin transitions in these materials. The main focus of the current experimental work is to study the metal-insulator (MI) transition, population and origin of electronic energy states near the Fermi level in single crystal samples of double perovskite cobaltites as a function of temperature. This thesis is a record of photoelectron spectroscopy of $LnBaCo_2O_{5+\delta}$ (Ln = Gd, Dy, $Dy_{1-x}Tb_x$) – Ln-112 and $LnBaCo_4O_{7+\delta}$ (Ln = Yb; $\delta = 0$) – Ln-114 undertaken at the Daresbury Laboratory Synchrotron Radiation Source (SRS), UK. The current chapter includes the crystal structure of the compounds under investigation along with some background concepts.

1.2 Background Concepts

1.2.1 Band Structure of Solids

In an isolated atom, the energy levels are discrete in nature but when the atoms come closer, they form bands of allowed energy levels. The energy of the electrons depends upon the associated wave vector *k* which represents its linear momentum in the periodic lattice or reciprocal space. A brief description of band theory is given here. Detailed information about the band structure of solids is available in the literature [1-3].

Many theories exist to describe the band structure of solids and the energy-wave vector relationship in materials. In the simplest case, the free electron theory of metals [4] states that inside the metal, the electrons are continuously in random motion and subject to a weak constant potential *U* which prevents them from leaving the metal. Occasionally the electrons are reflected from the surface, but do not collide with each other. The kinetic energy (K.E.) of the electrons can be found by the equation given below:

$$K.E. = \frac{1}{2}mv^2, \qquad \text{Equation 2.1}$$

where *m* is the rest mass and *v* is the speed of electron. The de Broglie wavelength λ associated with the electron motion can be found by the following equation:

$$\lambda = \frac{h}{mv}, \qquad \text{Equation 2.2}$$

where *h* is Planck's constant. The wave vector *k* along the direction of propagation of electron wave, in the reciprocal lattice, depends upon the wavelength λ, as shown below:

$$k = \frac{2\pi}{\lambda}. \qquad \text{Equation 2.3}$$

Hence the energy E of the free electron can be found by combining equations 2.1 and 2.2 and is given below:

$$E = \frac{h^2 k^2}{8\pi^2 m} = \frac{\hbar^2 k^2}{2m} \quad . \qquad \text{Equation 2.4}$$

For a metal, the volume or area formed by the filled energy states up to the Fermi energy E_F and the corresponding wave vector k_F is known as the Fermi sphere or Fermi surface as shown in Figure 1.1. The Fermi sphere plays an important role in explaining some solid state phenomena such as transport properties because it is not appreciably affected by temperature, so it is considered to be a permanent and independent physical characteristic of the metal [4].

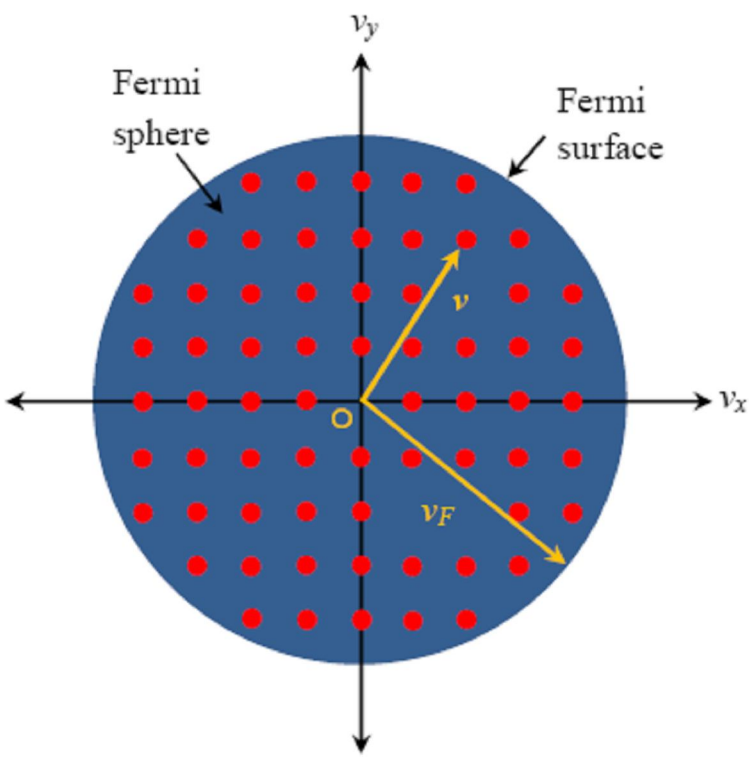

Figure 1.1: *The Fermi surface and the Fermi sphere where v and v_F denote the velocities of electron in velocity space and at the Fermi energy respectively* (*Adapted from* [4]).

The free electrons inside the solid perform random motion with different velocities in different directions when they are in equilibrium. Figure 1.1 shows the velocities of these electrons in velocity space. The points inside the sphere (or inside a circle in two dimensions) represent the end points of the velocity vectors. The maximum velocity of electrons is called Fermi velocity $v_{F,}$ which is the velocity of electrons at the Fermi energy and also represents the radius of the Fermi sphere. All points inside the sphere are occupied. Consequently, the velocity vectors cancel each other pairwise and the net velocity of the electrons comes out be zero at equilibrium. When an electric field is applied, the Fermi sphere is displaced in the direction of the applied field and conduction begins due to the net velocity gain of electrons.

The behaviour of electrons in the energy levels inside the metal is governed by the Fermi-Dirac distribution function [5] which is given below:

$$f(E) = \frac{1}{\exp\left[\frac{E - E_F}{kT}\right] + 1}, \qquad \text{Equation 2.5}$$

where p is the probability of an electron occupying a state of energy E, T is the absolute temperature, k is the Boltzman constant and E_F is the Fermi energy.

At T = 0 K, the electrons only fill the energy states up to the Fermi level but as the temperature of the solid is raised, the probability of occupying the energy levels above the Fermi level increases as shown in Figure 1.2.

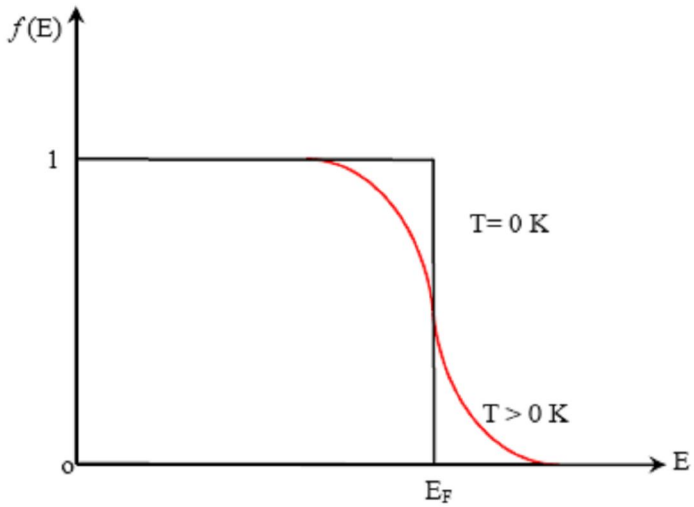

Figure 1.2: *Fermi-Dirac distribution at T = 0 K and T > 0 K* (*Adapted from* [4]).

The free electron theory, with some limitations, successfully explains most of the electronic and thermal properties of metals and some semiconductors. Equation 2.4 shows that all values of *E* and *k* exist for free electrons as shown in Figure 1.3(a). But when an electron is

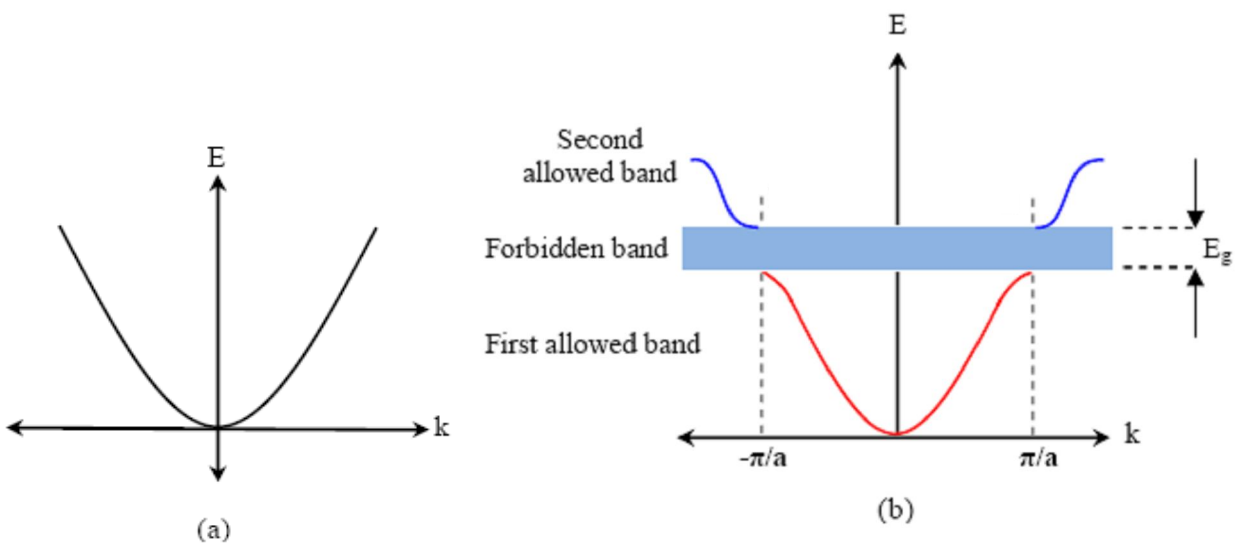

Figure1.3: (a) *Plot of E vs wave vector k for a free electron* (*b*) *plot of E vs wave vector k for an electron in a monoatomic linear lattice with lattice constant a. The energy gap is associated with the first Bragg reflection at k = ± π/a. Other gaps can be found at k = ± nπ/a for non-negative integral values of n* (*Adapted from* [3]).

considered to be passing through a solid bearing a periodic potential developed by the lattice of atomic cores, it can be shown that electron waves with particular values of k cannot propagate through the crystal and they experience Bragg reflections. The waves are then considered to be standing instead of travelling ones for $k = n\pi/a$, where n is a non-zero integer and *'a'* is the lattice spacing. As a result of the periodic potential experienced by free electrons inside the solid, energy gaps can be seen in the E vs k plot at $k = n\pi/a$ as shown in Figure 1.3(b). The energy gaps are produced at those values of k at which free electrons undergo Bragg reflections. The volumes in k space bounded by critical values ($k = \pm n\pi/a$) are known as Brillouin zones. The area bounded by $k = \pm \pi/a$ is called the first Brillouin zone, and similarly the areas bounded by $k = \pm n\pi/a$ for n = 2, 3, 4 etc. are referred to as the second, third, fourth etc. Brillouin zones respectively.

This 'nearly free electron model' of solids is quite successful but it has limitations in some cases. Consider the examples of CoO and $LaCoO_3$. The valence band (VB) is primarily of O 2p character while the conduction band (CB) is of metallic d-band character as shown in Figure 1.4.

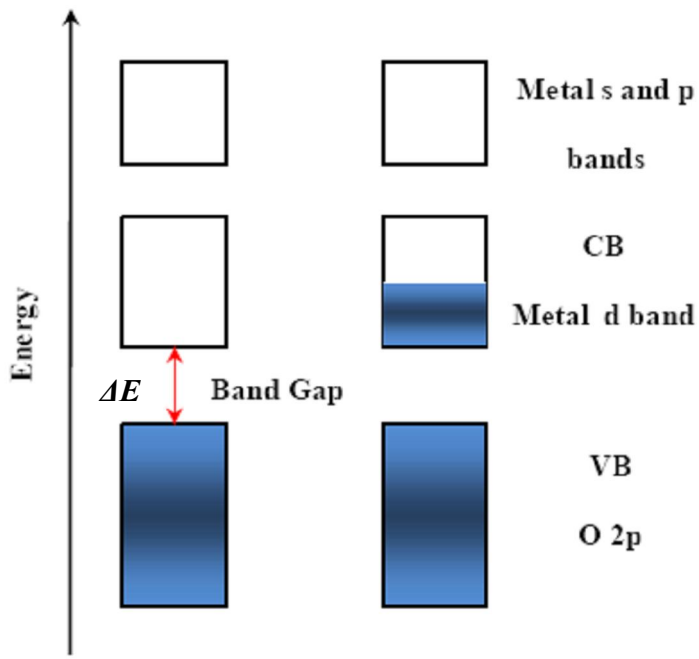

Figure 1.4: *Energy bands of transition metal oxide with empty d-band (left) and partially filled d-band (right)* (*Adapted from* [6]).

According to the band theory of solids, if the metal *d*-band is empty then the compound must be an insulator or semiconductor with a band gap ΔE. But if the *d*-band is partially filled then the compound should be metallic because the electrons are free to move inside the solid. Actually these compounds are insulators and the band theory of solids is unable to explain this discrepancy because it takes into account only the nearly-free electron approach–the effects of repulsion, or correlation, between electrons are ignored, or dealt with implicitly by the periodic potential. The breakdown of band theory in this case must be explained by other models such as the Hubbard Model.

1.2.2 Hubbard Model

The Hubbard Model [7] takes into account the intra-atomic repulsion of electrons that can lead to localisation in the solid. It assumes that the only important repulsion effects are those which occur between the two electrons which reside in the same atom. These intra-atomic effects primarily cause the failure of band theory when the width of the bands is small. The energy required to move an electron from one atomic orbital is the ionisation energy I of that electron. When an electron is placed on an already occupied site, the system receives energy A which is equivalent to the electron affinity of that neutral atom. Hence the energy U required to move an electron is given by:

$$U = I - A, \qquad \text{Equation 2.6}$$

where U is the Mott-Hubbard splitting energy. It may be considered as the repulsion energy between the two electrons orbiting the same atom.

The effect of increasing the band width W, with respect to U, can be observed in Figure 1.5. If $W < U$, then the material will be an insulator because the occupied and unoccupied levels split into two bands with a gap U, which is equivalent to the energy required to excite an electron to another orbital. The resulting sub-bands broaden with the interatomic overlap until they meet when $W = U$. Band theory of solids works well when the band width is greater than the electrostatic repulsion i.e. $W > U$ and the material is metallic. Generally delocalised electrons and hence metallic behaviour are caused by increasing the band width

or decreasing the repulsion energy. In insulating materials this can be done by means of doping.

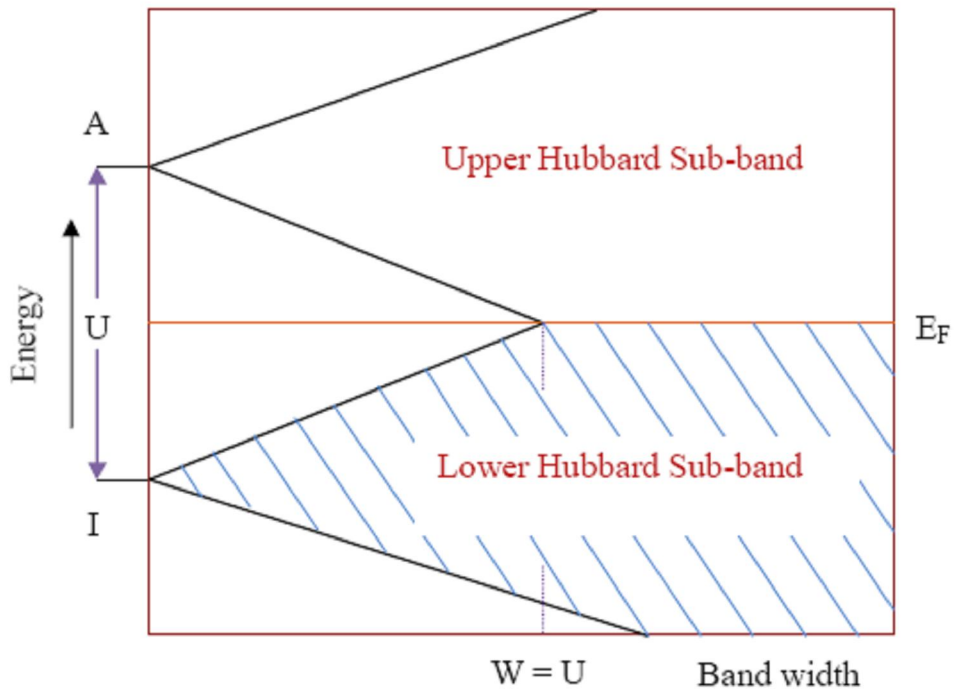

Figure 1.5: *The overlap of Hubbard sub-bands as the band width W increases relative to the Mott-Hubbard splitting energy U. A represents the electron affinity of neutral atom, I represents the ionisation energy of an electron and E_F shows the Fermi energy* (*Adapted from* [8]).

1.2.3 Crystal Structures

1.2.3.1 Crystal Structure of Cobaltite Perovskites ABX_3 and $LnBaCo_2O_{5+\delta}$ (Ln = rare earth) - Ln-112

Perovskites are ceramics (solid materials that combine metallic elements with non metals usually oxygen) and are found abundantly in the Earth's minerals. The general formula for an idealised perovskite is ABX_3 with a cubic unit cell. The elements A and B are metallic cations and the X element is a non-metallic anion, usually oxygen. The cation A, lying at the centre of the cube, is larger in size and dodecahedrally coordinated with the 12 X anion nearest neighbours. These occupy the midpoints of 12 edges while the B cations lie at all 8 corners.

In the simple perovskite $LaCoO_3$, the A cation is lanthanum, the B cation is cobalt and the X anions are oxygen. The idealised crystal structure of $LaCoO_3$ is depicted in Figure 1.6.

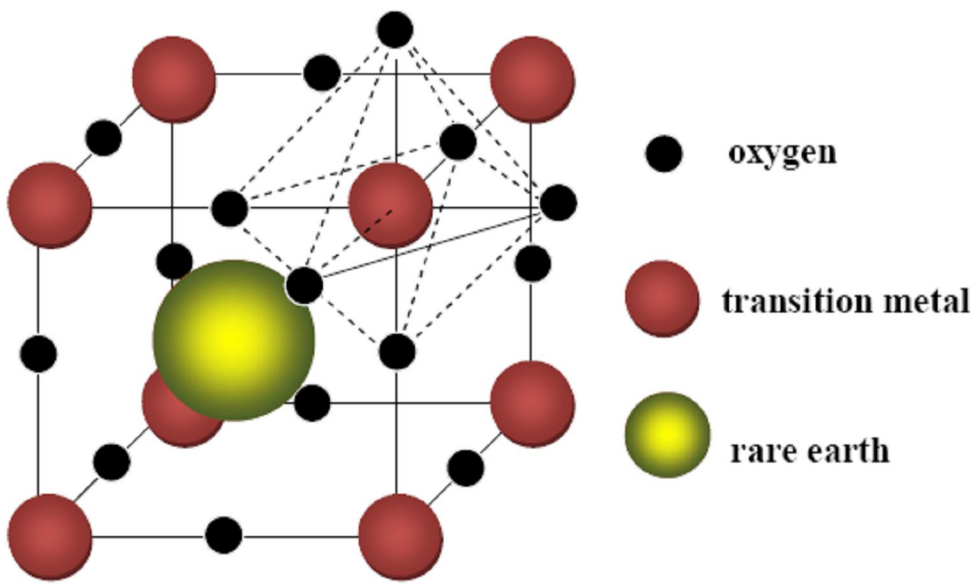

Figure 1.6: *Idealised crystal structure of $LaCoO_3$.*

In fact $LaCoO_3$ has a slightly distorted perovskite structure. The La^{3+} ion is comparatively too small for ideal packing with the Co^{3+} ion. This fact causes the oxygen anions and sometimes the Co cations to move out of position and may be visualised by considering the Co ion as being surrounded by, and bonded to, six oxygen anions in an octahedral arrangement (Figure1.6). The structure can be regarded as a three dimensional network of corner-sharing CoO_6 octahedra (Co-O-Co angles are 180°) with the Co ions in the middle of the octahedra. Eight octahedra form a cube with the La site in its centre. Due to the very small La site, the CoO_6 octahedra tilt and twist as the framework collapses around it lowering the symmetry of the unit cell. Consequently this results in a rhombohedral unit cell as shown in Figure 1.7.

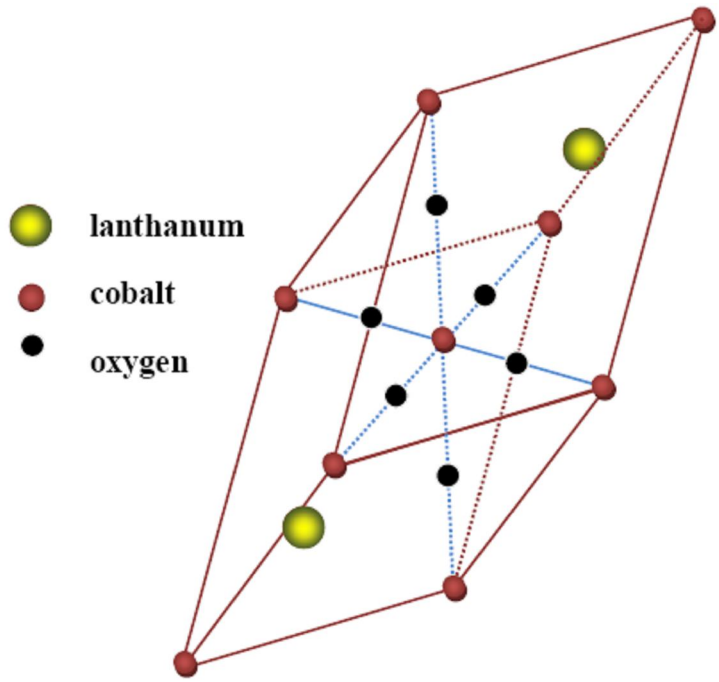

Figure 1.7: *Single perovskite structure of $LaCoO_3$* (*Adapted from* [6]).

The crystal structures of the compounds $DyBaCo_2O_{5+\delta}$, $Dy_{1-x}Tb_xBaCo_2O_{5+\delta}$ and $GdBaCo_2O_{5+\delta}$ are based on the perovskite structure. The crystal structures of $LnBaCo_2O_{5+\delta}$ (Ln = rare earth) with different oxygen contents are shown in Figures 1.8, 1.9 and 1.10. The double perovskites $LnBaCo_2O_{5+\delta}$ ($0 \leq \delta \leq 1$) derive their crystal structure from the 112-type

$LnBaCo_2O_5$

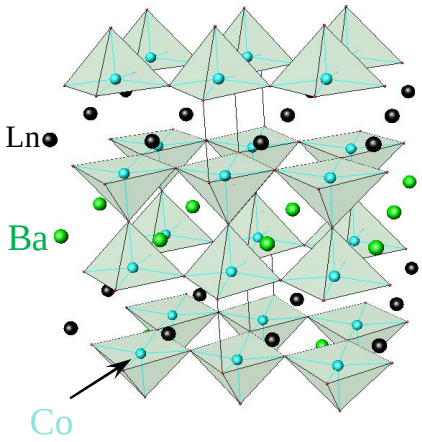

Figure 1.8: *Crystal structure of $LnBaCo_2O_5$ (Taken from* [10]).

$LnBaCo_2O_{5.5}$

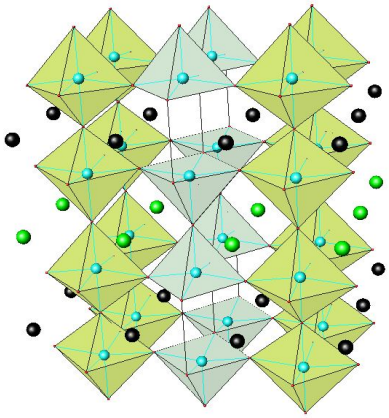

Figure 1.9: *Crystal structure of $LnBaCo_2O_{5.5}$ (Taken from* [10]).

$LnBaCo_2O_6$

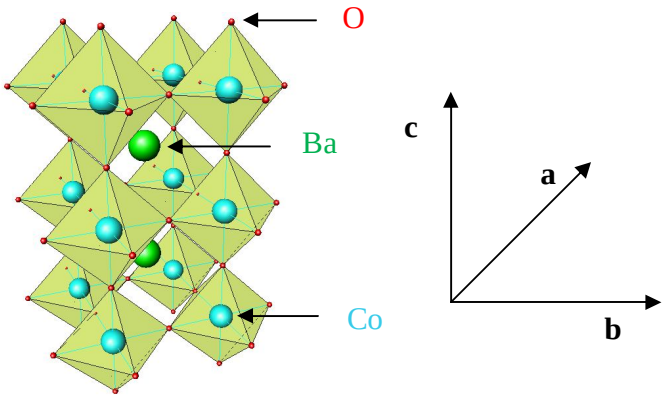

Figure 1.10: *Crystal structure of $LnBaCo_2O_6$ (Taken from* [10]).

structure of $YBaFeCuO_5$ [11]. These compounds are sensitive to oxygen stoichiometry so their magnetic properties and the nominal valence of their cobalt ions change with excess oxygen. Figure 1.8 shows the crystal structure of $LnBaCo_2O_5$ which has double-pyramidal cobalt layers containing the barium cations arranged with lanthanide layers having equal ratios of Co^{3+} and Co^{2+} states. Excess oxygen in these compounds leads to an oxygen vacancy ordering with in the [LnO_δ] layer. The crystal structure of $LnBaCo_2O_{5.5}$ shown in Figure 1.9 exhibits the stacking sequence [CoO_2][BaO][CoO_2][LnO_δ ; $\delta = 0.5$], along the c-axis with both pyramidal (CoO_5) and octahedral (CoO_6) co-ordination environments of cobalt ions. The compound has 100% Co^{3+} states and alternating layers of octahedra (CoO_6) and square pyramids (CoO_5) along the b-axis. In the case of $LnBaCo_2O_6$, the Co^{3+} and Co^{4+} states are equal in ratio and the structure shows consecutive layers of octahedra (CoO_6) along the b-axis as shown in Figure 1.10.

1.2.3.2 Crystal Structure of $LnBaCo_4O_{7+\delta}$ (Ln= Yb, δ =0) -Ln-114

$LnBaCo_4O_{7+\delta}$ (Ln-114) where Ln = Y, Tb, Dy, Ho, Er, Tm, Yb, Lu [12, 13] are a new class of cobalt-based oxides after Ln-112 whose crystal structure is similar to that of hexagonal $LuBaZn_{3.09}Al_{0.91}O_7$ [14] and $BaIn_2Zn_3O_7$ [15]. This layered structure is made up of Kagomé sheets of CoO_4 tetrahedra connected by triangular layers of CoO_4 tetrahedra along the c-axis as shown in Figure 1.11. Kagomé is a Japanese word which is used for a special woven pattern for bamboo baskets as shown in Figure 1.12. The cobalt ions in the Kagomé sheets of CoO_4 also generate a Kagomé net, separately shown in Figure 1.13, in the crystal structure of $LnBaCo_4O_{7+\delta}$ (Ln = Yb). $YbBaCo_4O_7$ is a mixed valence compound which contains Co^{2+} and Co^{3+} ions in a 3:1 ratio and its unit cell contains cobalt ions (Co (1) and Co (2)) at two distinct sites making alternate stacking layers along the c-axis [16]. Also along the same axis, the oxygen is found in a mixture of cubic and hexagonal packing and every eighth atom of oxygen is replaced by a Ba atom which coordinates with 12 surrounding oxygen atoms to form an anticuboctahedron. The Ba-O structure can be described as an *hcp* array of corner sharing BaO_{12}-polyhedra as shown in Figure 1.14(a). In

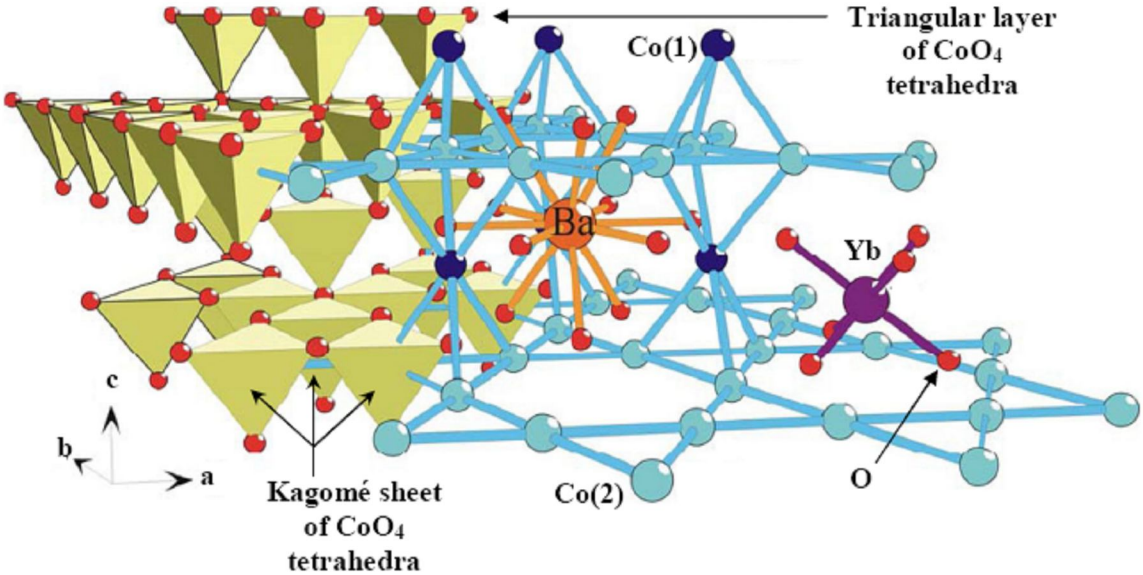

Figure 1.11: *Crystal structure of $YbBaCo_4O_7$ .The Co network of $YbBaCo_4O_7$ consists of Co(1) and Co(2): Co(2) form the Kagomé sheets and Co (1) link these sheets along the c axis. The oxygen ions reside at the corners of the tetrahedra surrounding the cobalt ions. Yb^{3+} and Ba^{2+} ions have twelve and six coordination number with oxygen ions respectively* (*Adapted from* [9]).

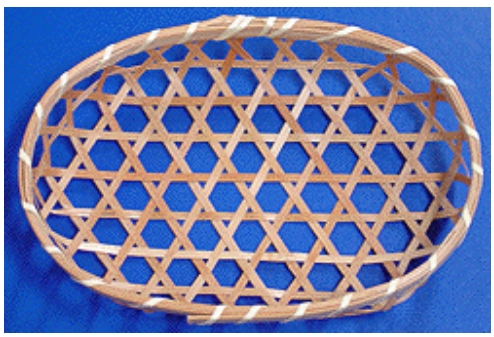

Figure 1.12: *A special woven pattern for bamboo baskets - kagomé in Japanese* [17].

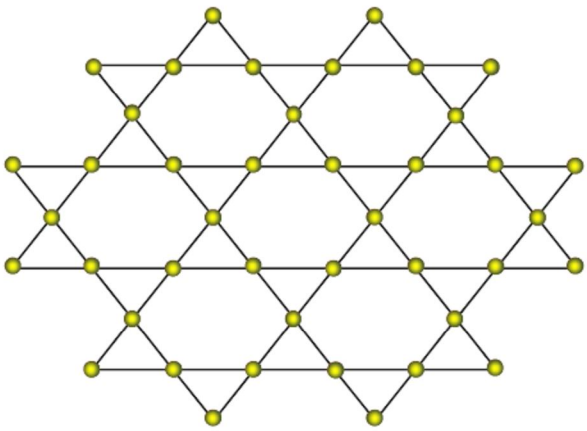

Figure 1.13: *Kagomé net of cobalt ions in $YbBaCo_4O_7$.*

the packing of BaO_{12}-polyhedra, a tetrahedral volume is formed by four Ba-containing anticuboctahedra where the rare earth atom can be found surrounded by six oxygen atoms.

The tetrahedral space formed by these anticuboctahedra (without showing the rare earth atom) is depicted in Figure 1.14(b). Moreover in the BaO_{12} packing, an octahedral space formed by six Ba atoms is filled by four corner-sharing CoO_4 tetrahedra as shown in Figure 1.14(c). The BaO_{12}-polyhedra and the Kagomé sheets of CoO_4 tetrahedra connected by triangular layers of CoO_4 tetrahedra in the crystal structure of $YbBaCo_4O_7$ are collectively shown in Figure 1.15.

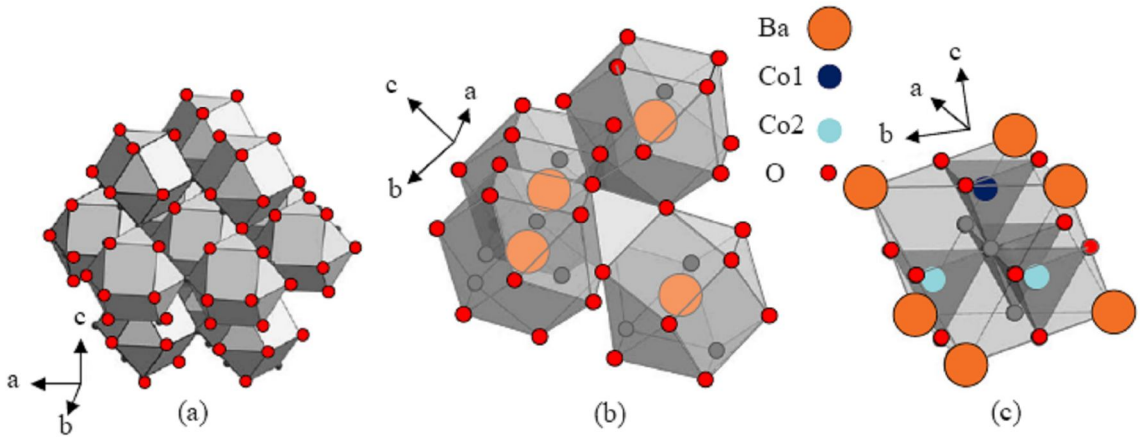

Figure 1.1 4: (*a*) *The hcp stacking of Ba-containing anticuboctahedra* (*b*) *four Ba-containing polyhedra showing the tetrahedral space where the rare earth ion resides surrounded by six oxygen atoms (not shown here) (c) four Co-tetrahedra filling the octahedral space in between six Ba* [13].

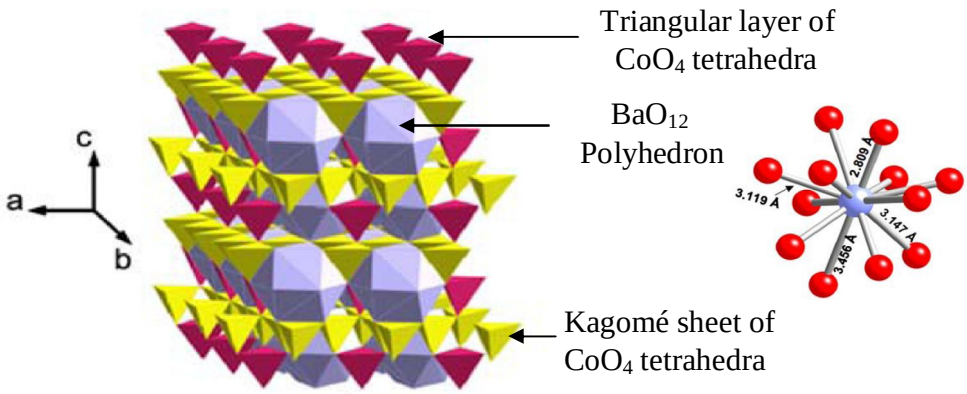

Figure 1.15: *Crystal structure of $YbBaCo_4O_7$ at 225 K (left) based on joint refinement of neutron and X-ray powder data. Coordination of twelve O atoms to the Ba site is highlighted on the right of the figure* (*Taken from* [16]).

1.2.4 Crystal Field Splitting and Spin State Notation for Co in the Octahedral Environment

Crystal Field Theory (CFT) was developed in 1920 to rationalise the electronic structure of compounds that contain transition metals. This theory considers the electronic repulsion between the atomic d orbitals on the central transition metal ion and the surrounding ligands which are approximated to negative point charges. It shows that the orbitals associated with d electrons will increase their energy when the orbital is located in a region of higher negative charge density and lower it when the reverse is true and hence a splitting of energy levels occurs which depends on the orientation of the d orbital in the coordination site. In crystals, a splitting of d band occurs which depends entirely upon the local geometry of the cation. Figure 1.16 shows the crystal field splitting between the higher energy e_g $(d_{z^2}, d_{x^2-y^2})$ and the lower energy t_{2g} (d_{xy}, d_{yz}, d_{xz}) orbitals in an octahedral environment.

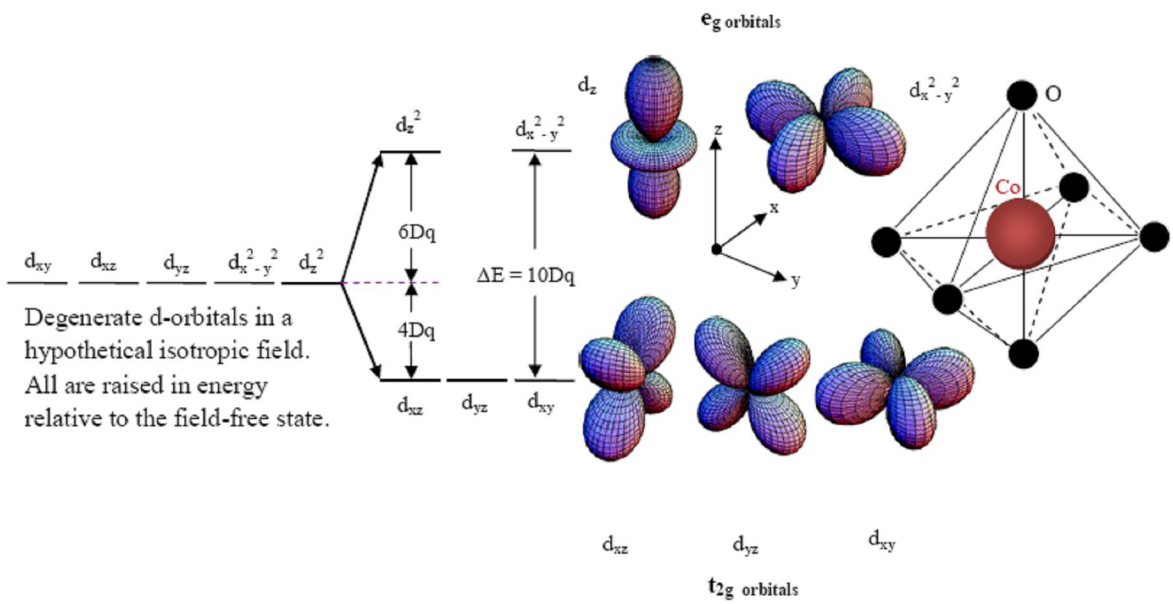

Figure 1.16: *Crystal field splitting of the energy of an electron in the d - orbitals of the central atom in an octahedral environment* (*Adapted from* [20]).

The energy separation between the t_{2g} and the e_g orbitals is termed the crystal field splitting and is denoted by Δ_o. Conventionally the energy separation is called 10 *Dq* and is obtained

directly or may be estimated from spectral measurements of the transition metal compounds in the visible to near-infrared region [18]. Mathematically Δ_o is found by the equation given below:

$$\Delta_o = < r^2 > / R^5 \,, \qquad \text{Equation 2.7}$$

where r is the radius of the d orbital and R the internuclear distance between the metal and the ligand (the ions or atoms surrounding the central atom).

Magnetic properties of transition metal oxides depend upon the crystal field because the orbital splitting allows for spin pairing and formation of high spin and low spin states. Co^{3+} is octahedrally co-coordinated in compounds such as $LaCoO_3$ and $LnBaCo_2O_{5+\delta}$ (δ = 0.5) with an electronic configuration designated as $[Ar]3d^6$. In these compounds, three of the degenerate orbitals are at lower energy than the remaining two orbitals [21] and may be filled according to Hund's rules. Three possible spin states of Co^{3+} in an octahedral environment are shown in Figure 1.17.

In the low spin (LS) state, all the six electrons pair up in the 3d degenerate orbitals and this state is designated as $t_{2g}{}^6 e_g{}^0 \ (S = 0)$. No electron exists in the e_g orbitals. In an alternative arrangement, three of the six electrons enter the lowest energy levels as usual, two of the remaining three electrons pair up with the low-lying orbitals but the sixth electron finds a place in the e_g orbital. This spin state is denoted by $t_{2g}{}^5 e_g{}^1 \ (S = 1)$ and is called the intermediate spin state (IS). The third state is the high spin state (HS) denoted by $t_{2g}{}^4 e_g{}^2 \ (S = 2)$. In the HS state, the first three electrons fill the t_{2g} levels and then the fourth and fifth electrons enter the e_g orbitals without pairing up. The sixth electron pairs up with one of the t_{2g} levels. In the LS state, the compound is non-magnetic because all the spin quantum states are paired. On the other hand, in the HS and the IS states, some electrons are unpaired and this results in magnetic behaviour.

The three spin states of the Co^{3+} ion discussed above appear as a result of a competition between the crystal field splitting (10 Dq), on-site Coulomb correlations, and the intra-atomic exchange energies. The HS and the LS states are associated with small and high

values of 10 *Dq* respectively when compared with the intra-atomic exchange energy. In many cobaltites, the difference of energies between these states is very small and can be overcome by changing temperature and /or altered by the lattice thermal evolution leading to spin state transitions and /or MI transitions. In $LnBaCo_2O_{5.5}$ compounds, the Co^{3+} ions reside in octahedral and pyramidal sites as shown in Figure 1.9. Despite some controversy about the spin state of the Co^{3+} ion , the most common point of view is that , at sufficiently low temperature Co^{3+} adopts the LS state in the octahedral sites and the IS state in the pyramidal sites. The pyramidal sites have the IS state due to smaller crystal field effects compared to those of the octahedral sites, so exchange effects (Hund's rules) win out over electron pairing. However, the Co^{3+} ions are found to be in the HS or the IS states in both the sites above the MI transition [19, 24].

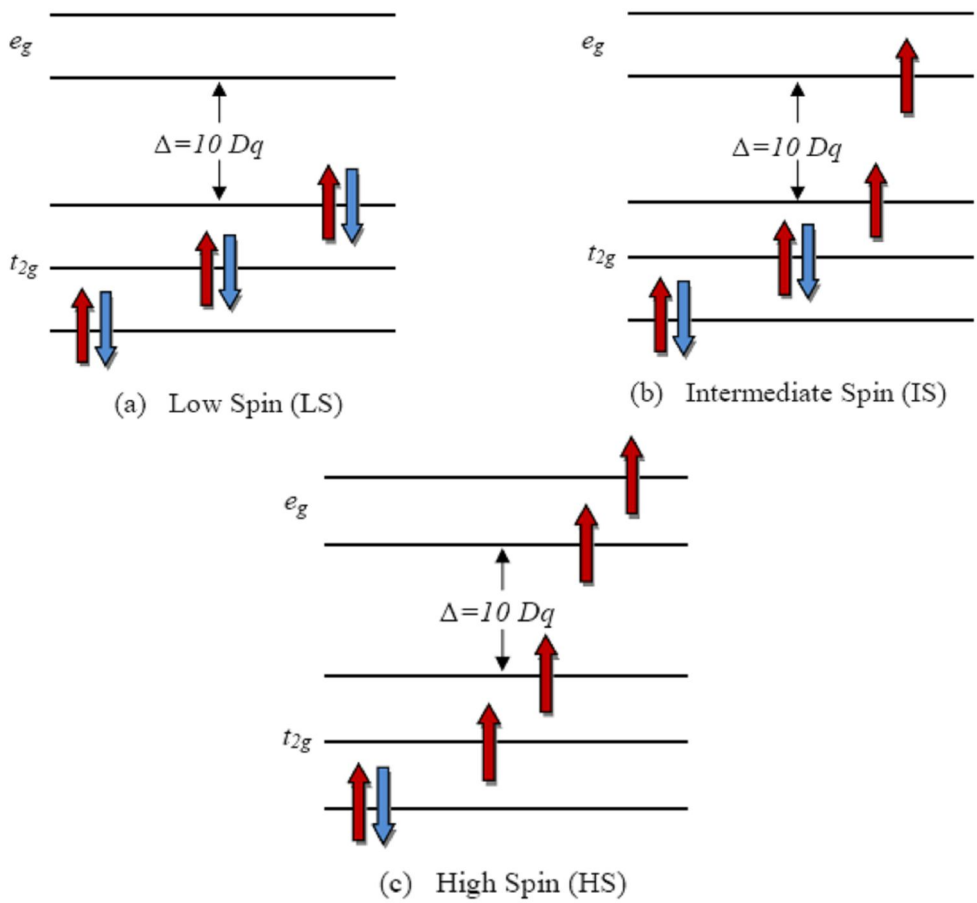

Figure 1.17: *Different spin states of the Co^{3+} 3d orbitals in an octahedral environment.*

1.2.5 Crystal Field Splitting and Spin State Notation for Co in the Tetrahedral Environment

Transition-metal cations are also widely found in tetrahedral environments and the bonding between these transition metal cations and ligands is also explained using crystal field theory. The splitting of the 3d levels in a tetrahedral environment can easily be comprehended if the transition metal atom is supposed to be at the centre of a cube with ligands occupying alternate vertices as shown in Figure 1.18.

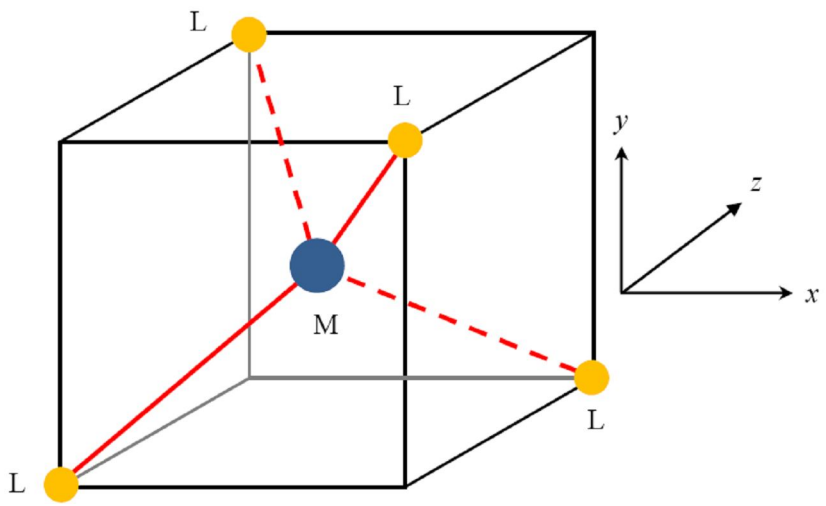

Figure 1.18: *A transition metal atom M in a cube surrounded by four ligands L making a tetrahedral environment* (*Adapted from* [22]).

It is important to note that in the tetrahedral environment, no d orbital points directly at the ligands but some are closer than others. For example, Figure 1.19 (a) shows that an electron in the $3d_{xy}$ orbital is closer to the ligands as compared to an electron in the $3d_{x^2-y^2}$ orbital as depicted in Figure1.19 (b). So, the electrons in the $3d_{xy}$ orbital will experience comparatively more repulsion. Similarly, electrons in the $3d_{xz}$ and the $3d_{yz}$ orbitals will be repelled more than those in the $3d_{z^2}$ orbital. Hence, in the tetrahedral environment, the energy of the $3d_{xy}$, $3d_{xz}$ and the $3d_{yz}$ orbitals is higher than those of the $3d_{x^2-y^2}$ and the $3d_{z^2}$

orbitals. The orbital energy-level diagram for a tetrahedral environment is shown in Figure 1.20.

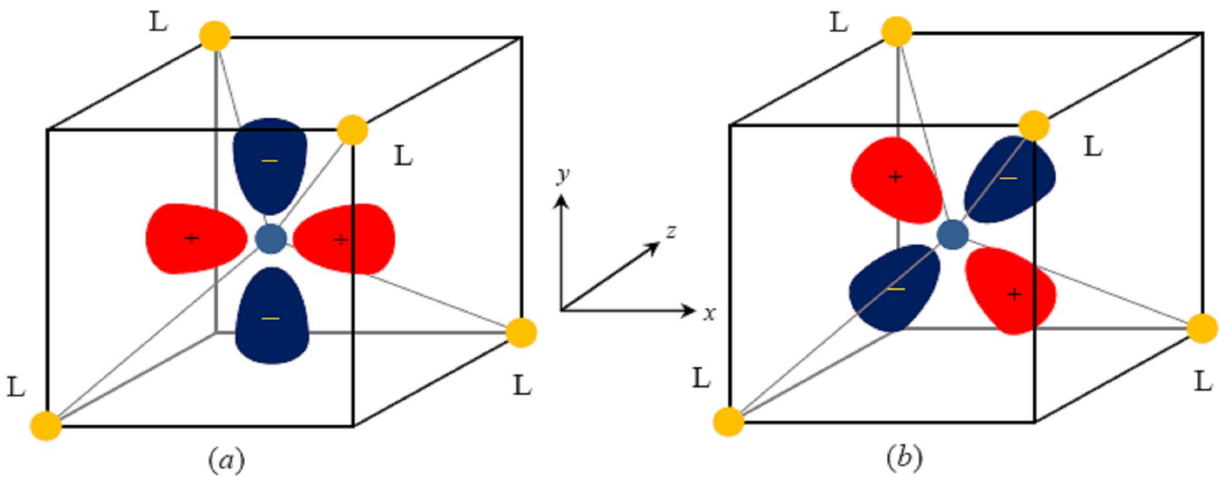

Figure1.19: (a) *The position of the* $3d_{xy}$ *orbital of transition metal ion with respect to surrounding ligands (orange coloured) in a tetrahedral environment* (b) *The position of the* $3d_{x^2-y^2}$ *orbital in the same environment* (*Adapted from* [22]).

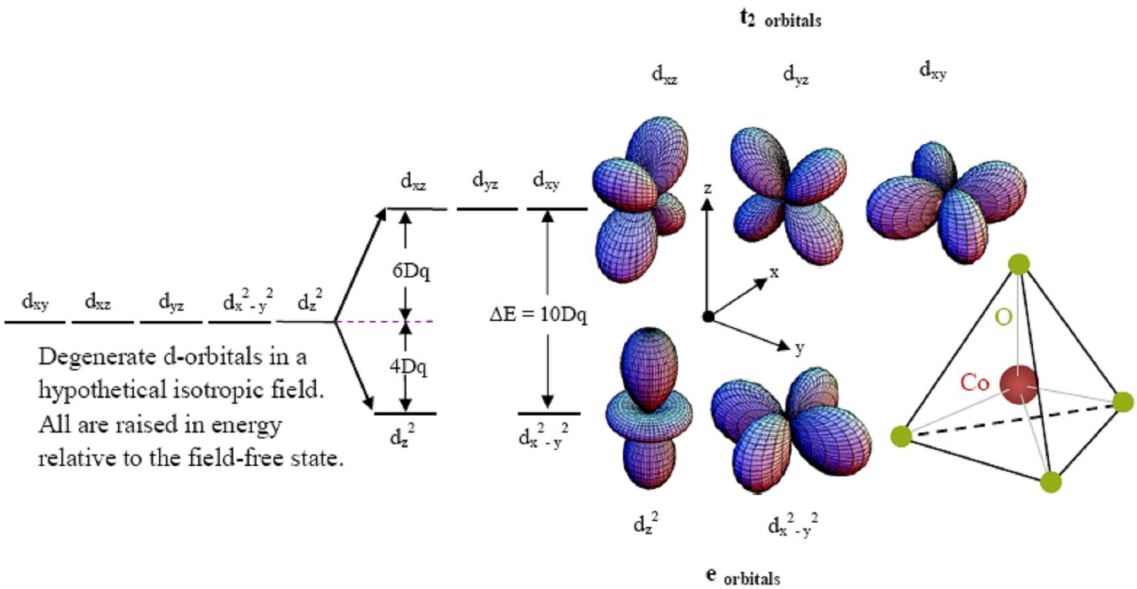

Figure 1.20: *Crystal field splitting of the energy of an electron in the d - orbitals of the central atom in a tetrahedral environment* (*Adapted from* [23]).

The lower energy level group of orbitals ($3d_{x^2-y^2}$ and $3d_{z^2}$) is denoted by *e* and the higher energy level group of orbitals ($3d_{xy}$, $3d_{xz}$ and $3d_{yz}$) is labelled as t_2. The energy difference between the two groups of orbitals is denoted by Δ_t where *t* stands for tetrahedral. As no d orbital directly points at the ligands, the energy difference between *e* and t_2 is smaller than the difference between the t_{2g} and e_g orbitals in the octahedral environment. It can be proved that $\Delta_t \approx 4/9\ \Delta_o$, where Δ_o stands for energy difference in the octahedral environment. As a result, transition metal cations in tetrahedral environments are usually found in the high spin state due to the smaller crystal field splitting [22] as shown in Figure 1.21(b).

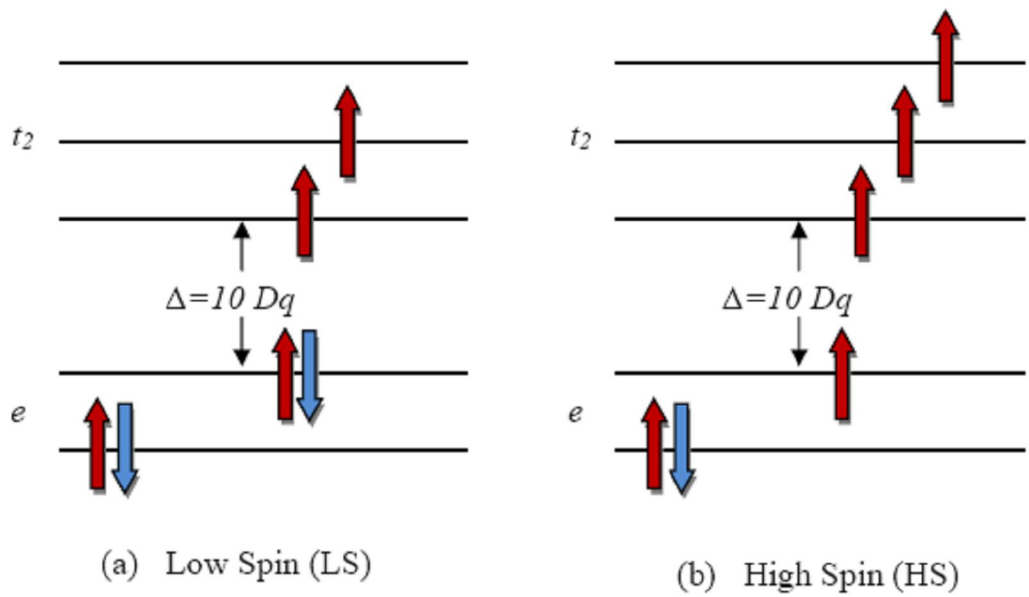

Figure 1.21: *Spin states of the Co^{3+} 3d orbitals in a tetrahedral environment.*

However, a hypothetical LS state of the Co^{3+} ion in the tetrahedral environment is also shown in Figure 1.21(a). As the LS and the HS states both have unpaired electrons in the tetrahedral environment, so they may show magnetic and metallic behaviour.

The magnetic structure of a material is the ordered arrangement of magnetic spins within the crystal lattice of the solid. The consequences of the Co spin state equilibria on the magnetic behaviour of the Ln-112 and Ln-114 compounds and the corresponding characterising techniques are considered further in Chapter 2.

References

[1] J. Bardeen, *Phys. Rev. B*, **79**, 9813 (1950).

[2] L. Cooper, *Phys. Rev. B*, **104**, 1189 (1956).

[3] C. Kittel, *Introduction to Solid State Physics*, J. Wiley and Sons, Inc.7th edition (1996).

[4] M. Ali Omar, *Elementary Solid State Physics*: *Principles and Applications*, Addison-Wesley Publ. (1975).

[5] J. Bardeen, L. Cooper and J. Schrieffer, *Phy. Rev. B*, **108**, 1175 (1957).

[6] J. Hollingworth, PhD Thesis, UMIST (1999).

[7] M. K. Wu, J. R. Ashburn, C. J. Torng, P. H. Hor, R. L. Meng, L. Gao, Z. J. Huang, Y. Q. Wang and C. W. Chu, *Phys. Rev. B*, **58**, 908 (1987).

[8] T. Saitoh, T. Mizokawa, A. Fujimori, M. Abbate, Y. Takeda and M. Takano, *Phys. Rev. B*, **56**, 1290 (1997).

[9] M. Valldor, Y. Sanders and W. Schweika, *Journal of Physics*, **145**, 12076 (2009).

[10] D. Tsoutsou, PhD Thesis, The University of Manchester (2005).

[11] A. Ducouret, J. M. Greneche and B. Raveau, *J. Solid State Chem.*,**114**, 24 (1995).

[12] G. L. Bychkov, S. N. Barilo, S. V. Shiryaev, D. V. Sheptyakov, S. N. Ustinovich, A. Podlesnyak, M. Baran, R. Szymczak and A. Furrer, *J. Cryst. Growth*, **275**, 813 (2005).

[13] M. Valldor and M. Andersson, *Solid State Sci.*, **4**, 923 (2002).

[14] C. Rabbow and H. Muller-Buschbaum, *Z. Naturforsch B*, **51**, 343(1996).

[15] O. Sfreddo and H. Muller-Buschbaum, *Z. Naturforsch B*, **53**, 517(1998).

[16] A. Huq, J. F. Mitchell, H. Zheng, L. C. Chapon, P. G. Radaelli, K. S. Knight and P. W. Stephens, *Journal of Solid State Chemistry*, **179**, 1136(2006).

[17] http://www.fkt.tu-bs.de/images/kagome.gif

[18] R. G. Burns, *Mineralogical Applications of Crystal Field Theory*, Second Edition, Cambridge University Press (1993).

[19] F. Fauth, E. Suard, V. Caignaert and I. Mirebeau, *Phys. Rev. B*, **66**, 184421 (2002).

[20] P. W. Atkins, *Quanta: A Book of Concepts*, Oxford Chemistry Series (1974).

[21] S. Massida, J. Yu and A. Freeman, *Physics C*, **152**, 251 (1988).

[22] R. James and E. Moore, *Metal-Ligand Bonding*, Bath Press, Glasgow (2004).

[23] D. M. P. Mingos, *Essentials of Inorganic Chemistry 2*, Bath Press, Avon (1998).

[24] C. Frontera, J. L. Garcia-Munoz, A. Llobet, and M. A. G. Aranda, *Phys. Rev. B*, **65**, 180405 (2002).

Chapter 2

Sample Bulk Characterisation Techniques, Crystal Growth and Magnetic Structure

2.1 Introduction

For the current PhD project, high quality single crystals of double perovskites $LnBaCo_2O_{5+\delta}$ (Ln = Gd, Dy, $Dy_{1-x}Tb_x$) and $YbBaCo_4O_7$ were grown by Prof. S.N. Barilo and his group at the Institute of Solid State and Semiconductor Physics (ISSSP), Minsk, Belarus using an overstoichiometric flux melt technique. This group is a part of an international collaboration of scientists from the European Union (EU) and former Soviet countries who investigated the properties of the single crystals. The group in the Photon Science Institute (PSI) at the University of Manchester was a part of this collaboration. The author of this thesis participated in crystal growth runs at the ISSSP, Minsk as well as undertaking photoemission measurements.

In the beginning of this chapter, the methods used to characterise the bulk properties of rare-earth cobaltite oxides are described. X-ray diffraction (XRD) determines the lattice parameters of unit cell of the crystal structure and atomic spacing of crystalline solids. Neutron diffraction is a complementary technique to X-ray diffraction as neutrons interact strongly with light elements unlike X-rays. They are used to identify the positions of the light atoms along with the heavy atoms present in the crystal sample and to determine the magnetic structure of the material. In the middle part of the chapter, the crystal growth and oxygen annealing of the $LnBaCo_2O_{5+\delta}$ (Ln = Dy) samples used in this thesis are discussed [1]. In the following sections, some basic background concepts of magnetism are discussed and a brief introduction to various types of magnetic materials is also given. In the later part of the chapter, the electronic and magnetic behaviour of rare earth cobalt oxides is described. The following section include structural and magnetic characterisation results

obtained for $LnBaCo_2O_{5+\delta}$ (Ln = Dy), by other consortia members and contained in our joint paper [1], are presented. Finally, magnetic characterisation measurements undertaken at the University of Manchester with our collaborators, and the results for $LnBaCo_4O_{7+\delta}$ (Ln = Yb, Tb, Lu) single crystals are described.

2.2 X-Ray Diffraction (XRD)

2.2.1 Basic concepts about crystals

Solid materials can be classified as:

a) non-crystalline or amorphous solids;
b) crystalline solids.

In amorphous solids such as glass and some polymers, the atoms are arranged in a random fashion. Nevertheless a short-range order of constituent particles can be observed within the body of the material. On the other hand, crystalline solids show a regular repeating pattern of atoms or ions *i.e.* a long-range order of the particles can be found within the material. The crystalline solids can further be categorised as single crystal and polycrystalline solids. In single crystals, the regular periodic pattern of the atoms continues throughout the whole bulk of the solid without any interruption whereas polycrystalline solids are composed of many grains which are randomly oriented and separated by grain boundaries. Crystal structure determination of the materials is important in the sense that their properties depend much upon the arrangement of the atoms and the strength of the bonds among them [2].

Historically the word *crystal* has been derived from the Greek word κρύσταλλος (*krystallos*) meaning *clear ice* as crystals were initially considered to be a special condensed form of water. In crystallography, a crystal is a larger network in which atoms are periodically arranged in three dimensions. The spatial order of these atoms is known as the crystal structure. An ideal crystal has a perfect order. All real crystals have deviations from the ideal structure because real crystals have defects in them [3]. An ideal crystal is a combination of identical structural units (motifs) superimposed upon an

infinite three dimensional regular, periodic arrangement of geometrical points called a lattice. All the points of the crystal lattice are identical having the same surroundings. A crystal can be characterised through a volume of space, called a unit cell. The unit cell can generate the whole space of the crystal by means of translation along the three spatial axes. The unit cell of a given crystal structure can be specified with six lattice parameters (a, b, c, α, β, γ). The first three *i.e.* a, b, c are the lengths of the three edges of the unit cell while the remaining three are the angles between the edges. The lengths are usually measured in ångström (Å) and the angles in degrees. There is no unique way to choose a unit cell but the volume of the unit cell should be as small as possible and the angles as close as possible to 90° for the sake of convenience. Every lattice point in the crystal has a unique position with respect to an origin. The position of each lattice point in the crystal lattice can be mapped with a translation vector **T** as shown in Figure 2.1. The translation vector is a function of three fundamental vectors **a**, **b**, **c** whose magnitudes are the lengths of the three edges of the unit cell.

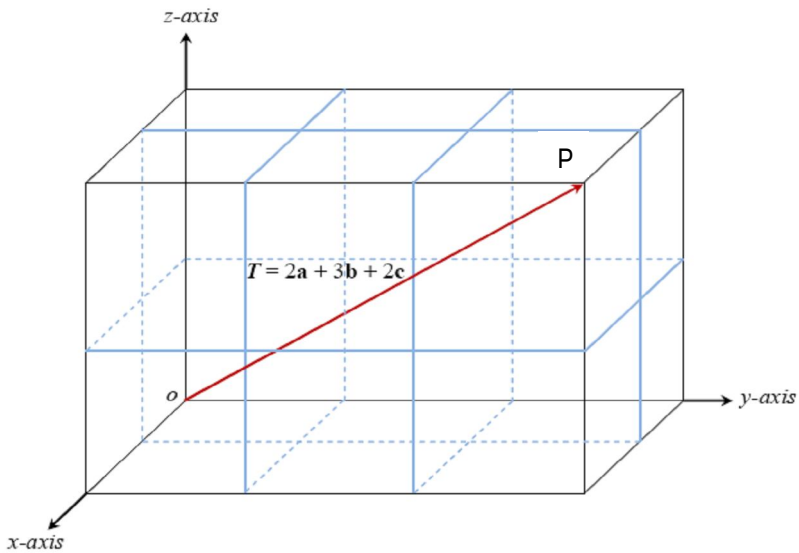

Figure 2.1: *A translation vector **T** = 2**a** + 3**b** +2**c** representing the position of a point P in the crystal lattice, where **a**, **b** and **c** are the three fundamental vectors along the edges of the unit cell.*

The unit cell with the smallest possible volume is called a primitive cell. A primitive cell is not always possible because of symmetry reasons. Keeping in view the symmetry of the

crystal, unit cells can be grouped into one of seven crystal systems as shown in Table 2.1 which describes each crystal system in terms of the six lattice parameters.

In three dimensions, there are four lattice centring types denoted by capital letters as described below:

i) primitive **P**: it contains only one lattice point at each vertex of the unit cell;

ii) body centred **I**: it has lattice points at the corners of the cell and in the body centred position;

iii) face centred **F**: it contains lattice points at the vertices of the unit cell and in the centre of each face of the cell;

iv) centred **A** or **B** or **C**: it contains lattice points at the corners of the cell and at the centre of (100), (010), and (001) faces respectively.

Table 2.1 shows the lattice centring types possible for each crystal system. The 14 distinct lattices are called Bravais lattices and their unit cells are shown in Figure 2.2.

Crystal system	Unit cell parameters	Bravais lattices
Triclinic	$a \neq b \neq c$ $\alpha \neq \beta \neq \gamma \neq 90°$	P
Monoclinic	$a \neq b \neq c$ $\alpha = \gamma = 90°, \beta \neq 90°$	P, A
Orthorhombic	$a \neq b \neq c$ $\alpha = \beta = \gamma = 90°$	P, A, I, F
Tetragonal	$a = b \neq c$ $\alpha = \beta = \gamma = 90°$	P, I
Cubic	$a = b = c$ $\alpha = \beta = \gamma = 90°$	P, I, F
Rhombohedral (Trigonal)	$a = b = c$ $\alpha = \beta = \gamma \neq 90°$	P
Hexagonal	$a = b \neq c$ $\alpha = \beta = 90°, \gamma = 120°$	P

Table 2.1: *The seven crystal systems and the associated space lattices where P, I, A and F stand for primitive, body centered, centered on a single face and face centered respectively* (*Adapted from* [4]).

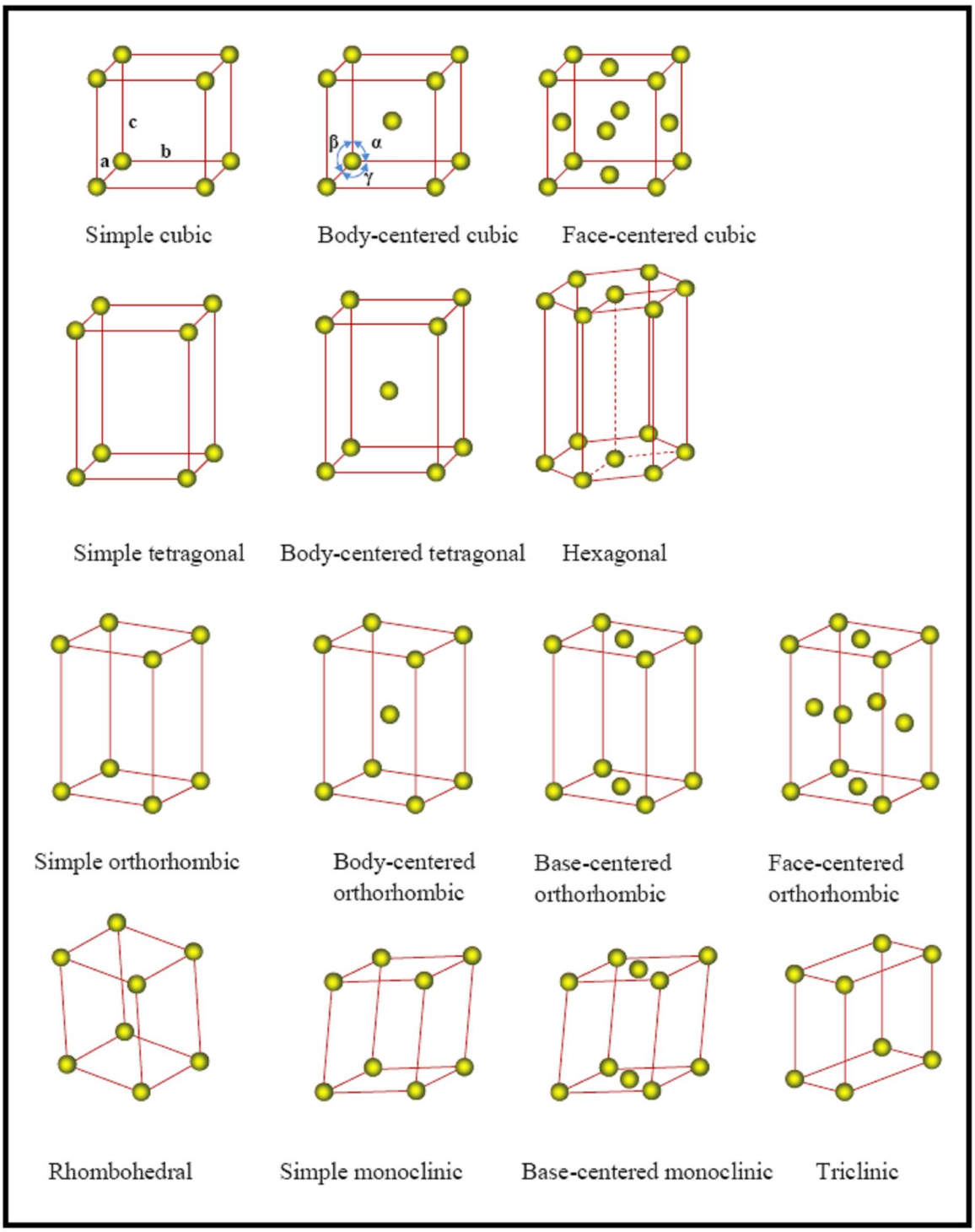

Figure 2.2: *The 14 Bravis lattices* (*Adapted from* [5])

The faces of a crystal can be considered as planes in three dimensional space. These planes are described by a set of three integers h, k and l, known as Miller indices. Miller used this notation to describe the faces of a crystal for the first time in 1939. The Miller indices of a plane of a certain crystal are reciprocals of the fractional intercepts that the plane makes with the three crystallographic axes. For example, if a, b, c are the three axial lengths of a unit cell and (h k l) are the Miller indices of a particular plane, then the plane will have intercepts of (a/h, b/k, c/l) as shown in Figure 2.3.

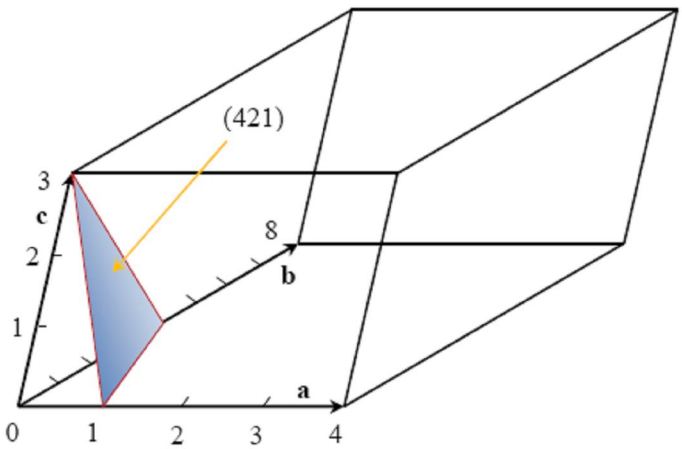

Figure 2.3: *Labelling a plane using Miller indices* (*Adapted from* [6]).

2.2.2 Bragg's Law

To determine the crystal structure of materials, usually X-rays are used. When a beam of X-rays falls on a single crystal, it is elastically scattered by the atomic planes of the material in specific directions. Bragg derived a relationship between the wavelength λ of the impinging radiation and the atomic spacing d_{hkl} between the atomic planes by studying the diffraction of X-rays. The relationship is called Bragg's law. Bragg assumed that each atomic plane behaved as a half-silvered mirror and partially reflected the wave at all angles.

Figure 2.4 shows a wave front IA falling on the atomic planes which is transformed into wave front RB after diffraction from the crystal sample. It is assumed that the incident and the diffracted waves make the same angle θ with the atomic planes of spacing d_{hkl}. For the two rays reflected from C and E to be in phase, their total path difference must be an

integral multiple of the wavelength. Simple trigonometry for the right-angled triangle DCE shows that:

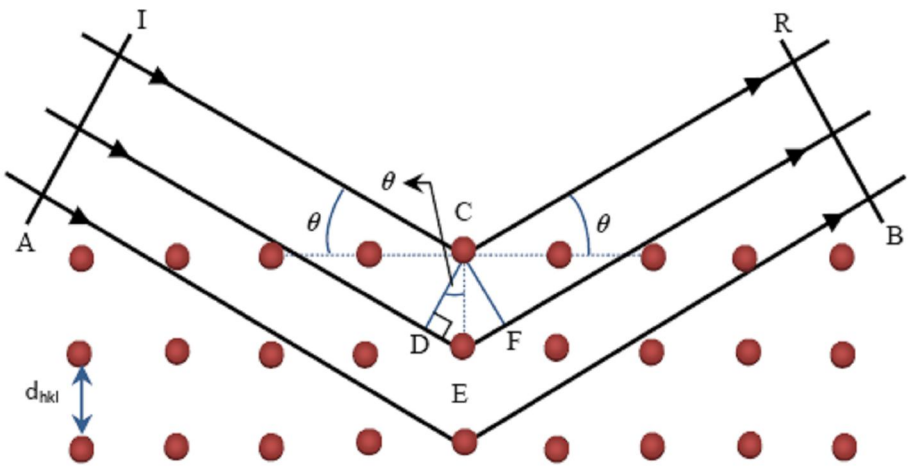

Figure 2.4: *Diagram of the Bragg reflection process* (*Adapted from* [7]).

Path difference = DEF = 2DE = $n\,\lambda$. Equation 2.1

Also, DE = $d_{hkl}\,sin\theta$. Equation 2.2

Combining equations 1 and 2 we have:

$2\,d_{hkl}\,sin\theta = n\,\lambda$ (n = 1, 2, 3….). Equation 2.3

For known values of λ and θ, the atomic spacing for a particular set of planes of a crystal can be determined from equation 2.3.

2.2.3 XRD Technique

Single-crystal X-ray diffraction is an analytical technique which is employed to study the internal structure and atomic spacing of crystalline solids. X-ray diffraction is performed by means of an instrument called X-ray diffractometer. An X-ray diffractometer mainly

comprises three basic parts: an X-ray source, a sample holder and an X-ray detector. The instrument is fitted with a four-circle goniometer (as shown in Figure 2.5) to rotate the sample and the detector in any particular orientation during data collection. Three of the circles of the goniometer are used to provide the desired orientation to the crystal sample through rotation angles χ,Φ and Ω whilst the fourth one is used to give rotation to the detector through an angle 2θ to receive the diffracted beam.

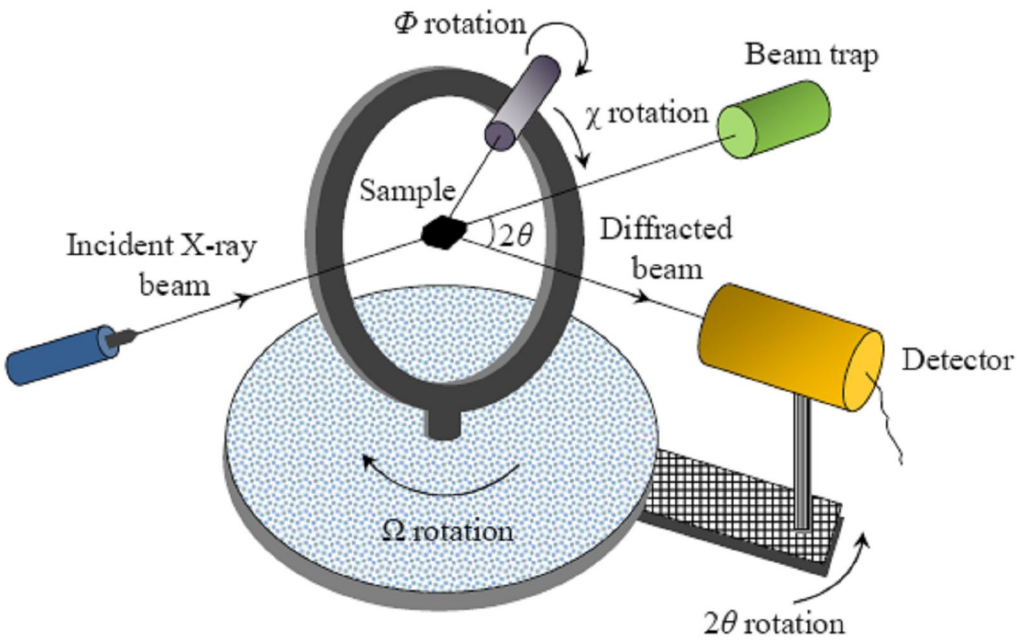

Figure 2.5: *Schematic diagram of a four-circle diffractometer* (*Adapted from* [8]).

In a diffraction experiment, a single-crystal sample is attached to a thin glass fibre using quick-setting epoxy resin and then mounted directly onto the goniometer head. Adjustments of the three circles are made which allow centring of the crystal sample in the X-ray beam. A well-collimated X-ray beam from the lab-based source is directed at the crystal sample. The rotation of the sample to the required direction relative to the incident beam brings crystal lattice planes into the horizontal plane of the detector for diffraction to take place. The detector uses either a charge-coupled device (CCD) or a scintillation counter to convert the diffracted X-ray beam into electrical signals which are processed by

a computer. The transmitted part of the beam is blocked by the beam trap situated opposite to the X-ray source.

2.3 Neutron Diffraction

X-rays scatter from the electron clouds around the atoms of a sample such that the scattering from different parts of the cloud is not always in phase, and as the scattering angle increases, the scattering intensity sharply decreases. On the other hand, neutrons, being neutral particles, interact with the nuclei of the atoms and scatter more strongly over a much shorter distance. Also X-rays are greatly scattered from those atoms which have more electrons; X-ray scattering is proportional to the atomic number Z^2 of the element whilst neutrons scatter from the nuclei of the atoms and their scattering is proportional to $Z^{1/3}$ [4]. Neutron diffraction is thus complementary to X-ray diffraction as neutrons interact strongly with light elements unlike X-rays. So they can be used to find out the positions of the light atoms in the sample in the presence of heavy atoms and for the determination of magnetic structure. It is worth mentioning that any structure which can be identified with X-rays should not be determined with neutrons because of time and cost factors.

Figure 2.6 shows a schematic diagram for a neutron diffraction experiment. In a particular neutron diffraction experiment, fast moving neutrons are obtained from an atomic reactor as a result of a nuclear fission reaction. Because the velocities of these neutrons are very high, they are thermalised with moderators such as graphite to make them suitable for the diffraction experiment. After thermalisation, the neutrons have a typical velocity of about 4000 ms^{-1}. As all quantum particles exhibit wave phenomena, so a wave is associated with these neutrons whose wavelength can be determined by the following de Broglie equation:

$$\lambda = \frac{h}{mv}, \qquad \text{Equation 2.4}$$

where h is Planck's constant, v is the velocity and m is the mass of a neutron (1.67×10^{-27} kg). Equation 2.4 gives to a wavelength of 1 Å for a velocity of about 4000 ms^{-1} and this is compatible with the wavelengths which are usually used in X-ray diffraction experiments. Actually the neutrons coming from the reactor do not have a single wavelength because they move with different velocities which depend on temperature. The relation between temperature and velocity can be found from equation 2.5:

$$\frac{1}{2}mv^2 = \frac{3}{2}kT \quad ; \qquad \text{Equation 2.5}$$

where k is Boltzmann's constant and T is the absolute temperature. By combining equations 2.4 and 2.5, we have:

$$\lambda = \frac{h}{\sqrt{3mkT}}. \qquad \text{Equation 2.6}$$

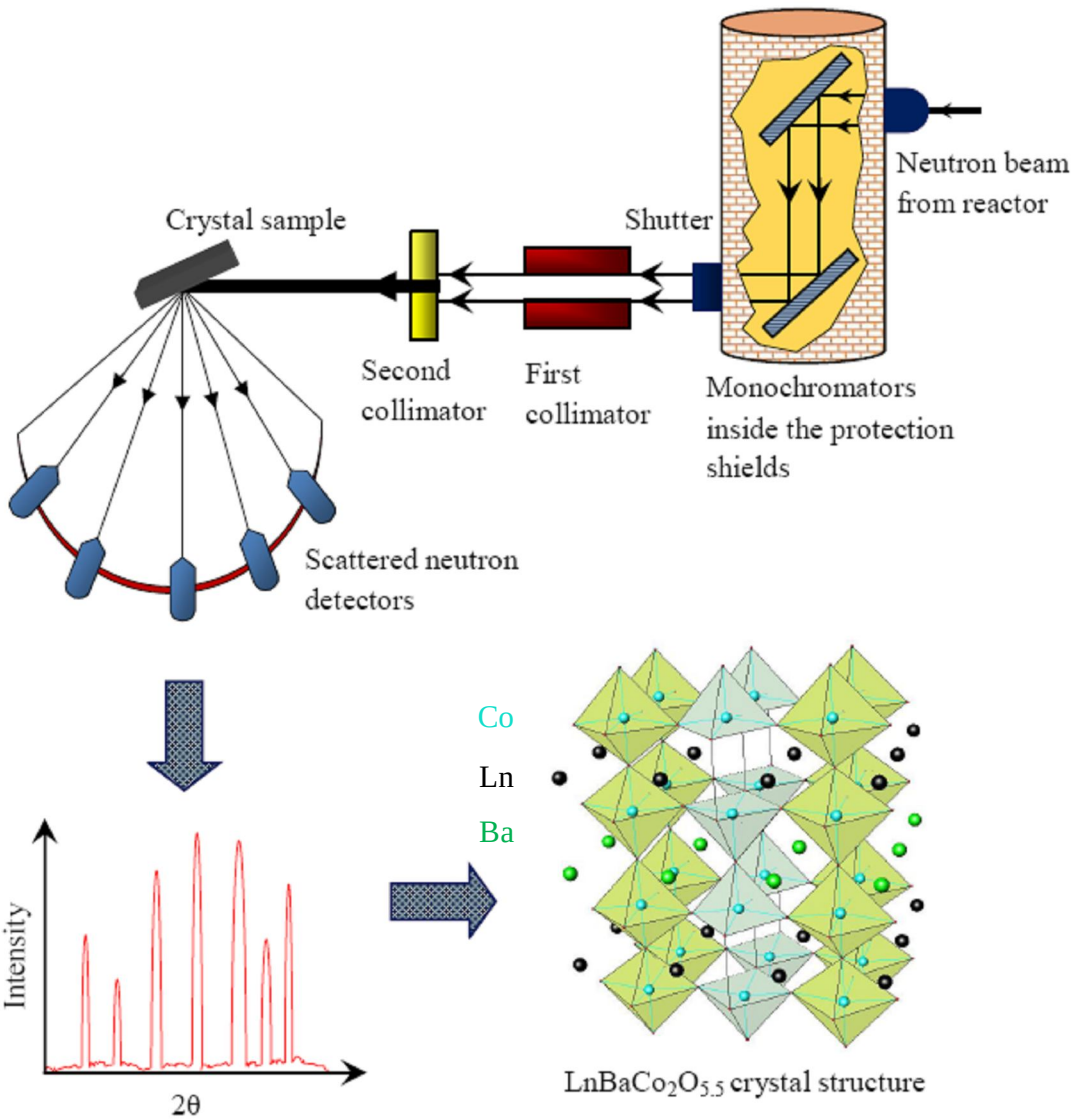

Figure 2.6: *Schematic diagram for neutron diffraction experiment* (*Adapted from* [9]).

Equation 2.6 suggests that a range of wavelengths of neutrons can be obtained for different values of temperature. During the experiment, the temperature of the reactor is adjusted in

such a way that the emitted neutrons have wavelengths in the 1.4-1.7 Å range. To perform a diffraction experiment, a single wavelength is selected by using a double single-crystal monochromator. When the monochromatic beam of neutrons impinges upon the surface of the sample, it is scattered with different intensities at a number of well-defined angles (2θ) satisfying Bragg's law that describes X-ray diffraction.

When a neutron is scattered from the nucleus of an atom, the wave function ψ_{inc} associated with the neutron, incident on a fixed nucleus along the z direction (say), can be represented as :

$$\psi_{inc} = \exp(ikz), \qquad \text{Equation 2.7}$$

where k is the wavevector along the z-axis. The wave function (ψ_{sc}) of the neutron after scattering from the nucleus at a distance r is given by:

$$\psi_{sc} = -\frac{\beta}{r}\exp(ikr). \qquad \text{Equation 2.8}$$

The negative sign in Equation 2.8 is arbitrary and corresponds to a positive value for a repulsive potential and β, called the scattering length, is a constant of proportionality. The scattering length is a measure of the degree of scattering of the radiation and its value depends both on the size of the nucleus and the details of the energy levels of the particular nuclide, but it does not depend upon the scattering angle. When scattering of neutrons from an atom of a nonmagnetic species takes place, the nucleus of the atom does not recoil and scattering amplitude at a distance r from the nucleus is given by β/r.

In general, the scattering length is a complex quantity given by:

$$\beta = b_0 + b_1 + ib_2, \qquad \text{Equation 2.9}$$

where b_0 is the length related to the potential scattering and b_1 and b_2 are the real and imaginary parts of the resonance scattering which occurs with formation of the compound nucleus. The imaginary part of the scattering length signifies absorption of neutrons by the nucleus. Nevertheless, the imaginary term is small for most nuclei and hence the scattering length can be considered as real. No adequate theory of nuclear forces exists so far which can be used to calculate scattering lengths. However, the scattering lengths of most nuclei

have been determined experimentally and are given elsewhere [10]. The complex relationship between atomic number and the scattering length can be used to make distinctions between the neighbouring elements of the periodic table. The scattering lengths can have both negative and positive values. A negative value of the scattering length indicates that the neutrons scattered from the nuclide are 180° out of phase from those that are scattered by the nuclide with positive scattering length [11].

Neutrons have magnetic moment and spin S = 1/2, so these attributes can be utilised to identify the magnetic structure of the sample under investigation. The magnetic scattering length depends both on the scattering angle and the magnetic moment of the atom. By making use of these features, the magnetic moment of the atom and the arrangements of magnetic moments inside the material, in relation to the crystal structure, can be determined. For unpolarised neutrons, the magnetic and crystallographic scattering intensities are additive [11].

The structure obtained as a result of X-ray and neutron diffraction intensities can further be refined by using the Rietveld method. This method can be employed for both crystal and magnetic structure data. The Rietveld method is based on least squares analysis and involves an interpretation of the diffraction peaks and their intensities. The data obtained, as a result of an experiment, consist of many peaks and each peak is assigned a Gaussian shape and then the Gaussian is allowed to fit so that an overall line profile could be calculated. Parameters describing crystal structure, peak width and shape, background, and overall scale are varied so as to obtain the best fit between the calculated pattern and the observed [12]. The validity of the structure obtained is assessed by minimising χ^2 , where χ^2 is defined mathematically by equation 2.10:

$$\chi^2 = \sum_{1}^{n} \frac{1}{\sigma_i^2} (y_{io} - y_{ic})^2 \; ; \qquad \text{Equation 2.10}$$

where y_{io} is observed data profile, y_{ic} is calculated data profile and σ_i^2 is the variance of all observed data profiles y_{io}. In the least squares refinement method, the parameters that can be adjusted are: space group, lattice parameters, atomic positions, atomic thermal parameters and atomic site occupancies.

2.4 Four-Point Probe for Resistivity Measurement

Figure 2.7 shows a schematic diagram of a typical four-point probe. The four-point probe is generally used to measure the resistivity of a single crystal sample. It consists of four thin wire collinear probes usually made of tungsten. To measure the resistivity of a sample under study, these probes are placed at equal distance S on the sample surface. From a constant-current source, a fixed quantity of electric current I is made to flow through the sample using the two outer probes. A voltage drop V is measured between the two inner probes. Hence, the resistivity ρ of the sample can be calculated by using the following formula:

$$\rho = 2\pi \, SV/I, \qquad \text{Equation 2.11}$$

where 2π is the correction factor.

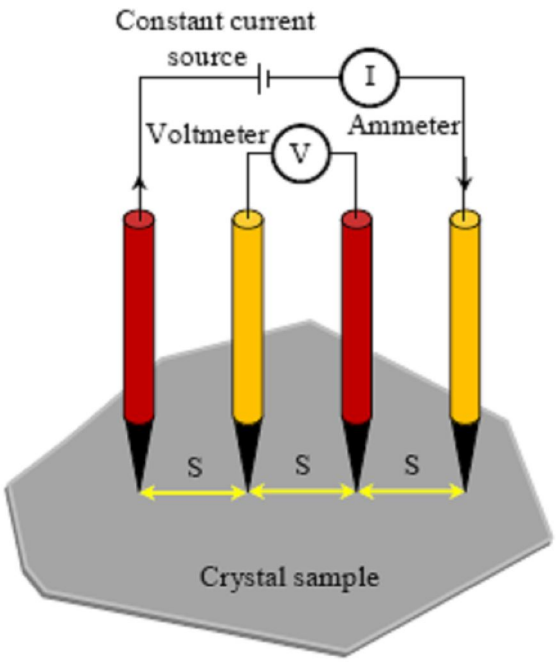

Figure 2.7: *Schematic diagram of a four-point probe for the measurement of resistivity of a crystal sample* (*Adapted from* [13]).

2.5 Crystal Growth

2.5.1 Introduction to Crystal Growth of $LnBaCo_2O_{5+\delta}$

It has been shown that the Ba-doped cobaltites $LnBaCo_2O_{5+\delta}$ (Ln-112; Ln = rare-earth or yttrium, $0 \leq \delta \leq 1$) manifest astonishing properties such as spin, charge and orbital ordering when the oxygen content δ approaches 0.50. Moreover other properties such as a metal-insulator (MI) transition and giant magnetoresistance (GMR) have also been found in this cobalt-based family of compounds [14].

However, growing large single crystals for detailed structural and electronic band structure investigations is a difficult job. There are different methods of growing crystals. The floating zone (FZ) and overstoichiometric flux melt methods are well known [15]. The FZ technique requires no crucible for growing single crystals. In this technique, a melt zone is established between a feed rod and a seed by means of a localised heating source as shown in Figure 2.8. The feed rod is prepared from high purity powders using a rubber tube. The feed rod and the seed are kept in a vertical position by some suitable supports whilst the melt is held in place by surface tension. The floating zone is moved along the rod by giving relative motion to the heating device in such a way that the crystal grows on the seed and melts the feed material above the floating zone at the same time.

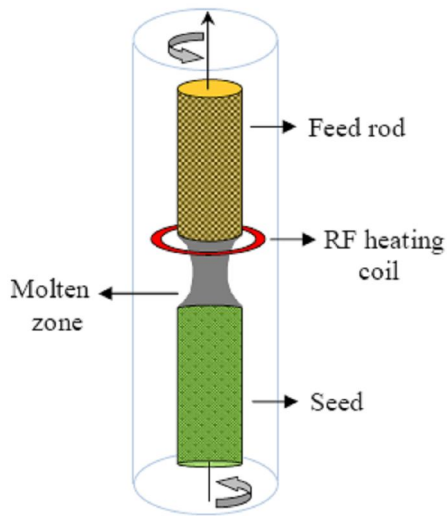

Figure 2.8: *Schematic layout of the FZ technique for growing single crystals* (*Adapted from* [15]).

The overstoichiometric flux melt technique is a high-temperature-solution growth method to grow single crystals of rare-earth cobalt oxides. Figure 2.9 shows a schematic diagram of the overstoichiometric flux melt technique. In this technique, a homogenised mixture of 4N purity of $BaCoO_3$ and Co_3O_4 (used as a solvent) is taken in an appropriate ratio. In addition, a known quantity of powder of the corresponding rare earth oxide is used as a feeder to keep the flux saturated during the crystal growth. First the feeder and then the homogenised mixture are put usually in a 100 cm^3 alumina crucible. The crucible is then placed in a hot furnace. After a calcination of about 12 h at 1000 °C, the temperature of the furnace is increased in 2 h up to ~ 1190 °C in order to achieve a homogeneous melt. At this stage, an alumina rod is slowly dipped by a few millimetres into the flux and rotated slowly. Usually 1/3rd volume of the crucible is occupied by the flux. As a result of successful growth runs, about a week long, several crystals can be separated from the surface of the drawn-out alumina rod.

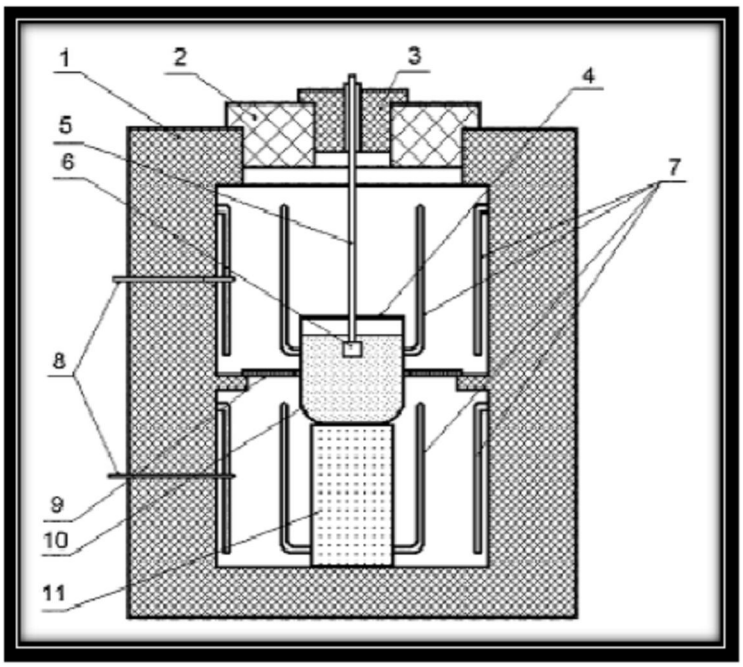

Figure 2.9: *Diagram of the two-chamber furnace: 1-Lining with refractory bricks made from porous alumina; 2,3-fixed and removable lids; 4-magnesia crucible; 5-crystal holder; 6- single crystal; 7-resistive heaters; 8-thermocouples; 9-thermal shield between upper and lower chambers; 10-flux melt; 11-support made from porous alumina* (*Taken from* [1]).

The main advantages of the FZ technique are that no crucible is required, the growth can be carried out at high pressure (up to 10 atm), solid solutions with controlled chemical composition can be prepared, and a steady state can be achieved as compared to crucible techniques. Despite many advantages, this technique also has some disadvantages. It is not suitable for those materials which have high viscosity, high vapour pressure and low surface tension [15].

Crystals grown by the overstoichiometric flux melt technique are usually smaller in size because of the difficulty involved in controlling the spontaneous crystallisation. Though large single crystals of Ln-112 (Ln = Nd, Gd, Tb) have already been grown by the FZ technique, it is quite difficult to compare the merits and demerits of these crystal growing techniques due to the unavailability of complete information regarding crystal growth in the data published on the FZ method .

After a detailed study of phase equilibria in the La-Ba-Co-O system and primary crystallisation fields for Dy-112 as shown in Figure 2.10, a new approach to flux growth involving reduction of the viscosity of the flux melt has been developed to grow large single crystals of $LnBaCo_2O_{5+\delta}$ (Ln = Gd, Dy) at the Institute of Solid State and Semiconductor Physics (ISSSP) Minsk. In this approach, the corundum crucible was replaced by an MgO one to minimise corrosion. The reduction in corrosion of the crucible helped to initiate limited nucleation under a variable/reversible temperature gradient [1].

2.5.2 Crystal Growth

A furnace, based at ISSSP, comprising two vertical chambers each fitted with resistive heaters as shown in Figure 2.9 was used to grow the large single crystals of $LnBaCo_2O_{5+\delta}$ (Ln = Gd, Dy) used in this work, following the newly-developed approach based on controlled growth from a limited number of nuclei. The chambers were separated with porous alumina thermal shields and also separately controlled thermally with RIF-101 (Ukraine) temperature controllers. These temperature controllers had an accuracy of temperature stabilisation of ± 0.1 °C at homogenisation temperatures up to 1250 °C and rates of flux-melt cooling in the range 0.05-10 °C/day.

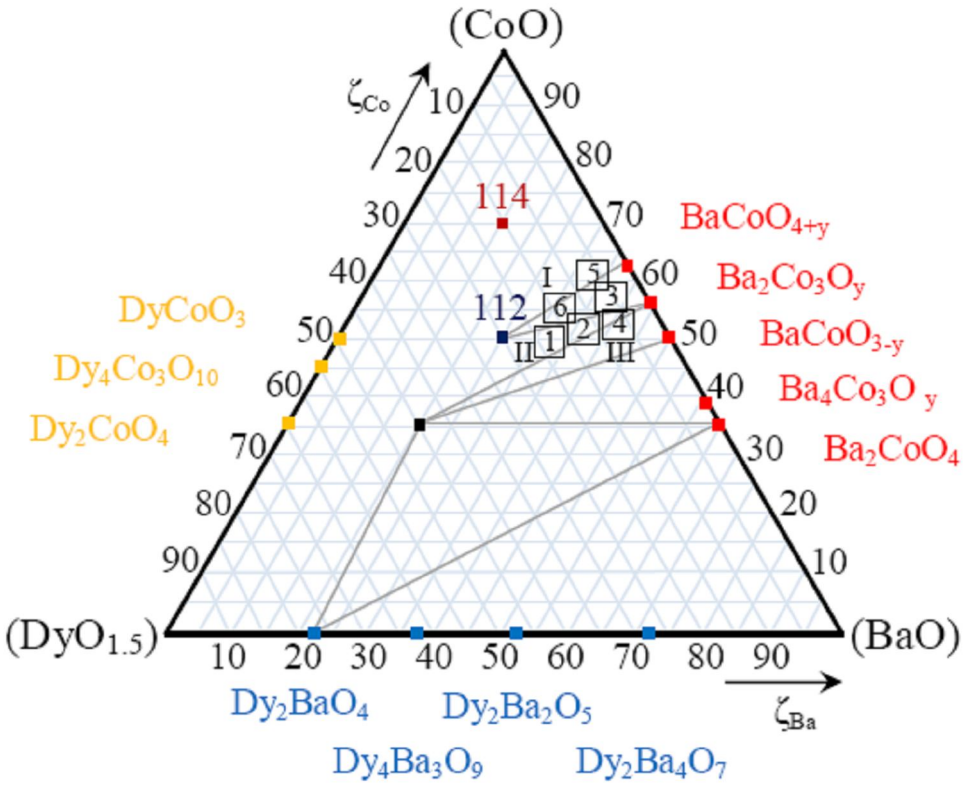

Figure 2.10: *Primary crystallization fields of co-crystallised cobaltite phases in the Co-enriched part of the Dy_2O_3-BaO-CoO quasi-ternary phase diagram, established at the ISSSP, Minsk. ζ_{Co} and ζ_{Ba} denote relative molar ratios of Co and Ba respectively. Numbering I-III and 1-6 represent primary composition ranges and phases respectively* (*Adapted from* [1]).

To obtain large and high quality single crystals of $LnBaCo_2O_{5+\delta}$ (Ln = Gd, Dy), a batch of thoroughly homogenised powdered mixture of $BaCO_3$, Co_3O_4 and corresponding rare-earth oxides in the molar ratio 2:3.35:0.2 was put in 50 cm^3 magnesia crucibles and placed in the furnace. After decomposing barium carbonate at 1000 °C for 12 hours through calcination, the temperature was raised to the melting point of the mixture (~1200 °C) and then kept constant in both chambers of the furnace for 5-10 hours. The flux melt was slowly rotated in a special magnesia crystal holder throughout the growth experiments. The precipitation of small Ln-112 crystals was activated by the initiation of a negative temperature gradient of ~3.5-4 °C/cm inside the furnace for ~20 hours. At the final stage, the sign of the temperature gradient was reversed and about 5-8 nuclei were allowed to grow under a slowly rising temperature gradient. At the end of successful growth experiments which

lasted up to 20 days, high quality rectangular-shaped single crystals of Ln-112 were obtained on the crystal holder and later extracted mechanically. A typical as-grown single crystal of $LnBaCo_2O_{5+\delta}$ (Ln = Dy) with a rectangular shape and dimensions of 20×12×1 mm^3 is depicted in Figure 2.11.

The large, high quality as-grown single crystals of $LnBaCo_2O_{5+\delta}$ (Ln = Gd, Dy) thus obtained were oxygen-annealed to acquire the optimal oxygen content to achieve the MI transition in the compound. Two slightly different oxygen annealing plans for $DyBaCo_2O_{5+\delta}$ are discussed in section 2.5.3. The MI transition of these compounds, discussed later in section 5.3.1, was studied by high-resolution photoemission. The ac and dc susceptibilities of the single crystals were measured in the temperature range 2-300 K, using QUANTUM design systems PPMS-9 and MPMS-7 with external fields up to 9 T and 7 T respectively. The structure determination of the single crystals was carried out using a four-circle X-ray diffractometer at PNPI, Gatchina. The oxygen content and oxygen ordering were confirmed by X-ray diffraction.

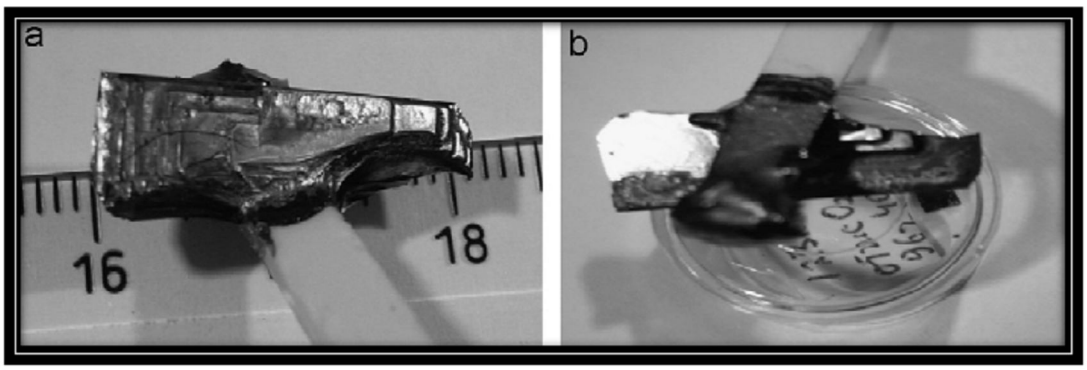

Figure 2.11: (*a*) *As-grown single crystal of* $DyBaCo_2O_{5+\delta}$ *on the surface of the magnesia crystal holder and* (*b*) *the same crystal from the back* (*Taken from* [1]).

2.5.3 Oxygen Annealing of $DyBaCo_2O_{5+\delta}$

It has been reported by Barilo *et al.* [1] that as-grown oxygen-deficient single crystal samples of cobaltites usually require a post growth annealing treatment to achieve an optimal oxygen stoichiometry around δ = 0.5. To get a well-oxygenated single crystal

sample of $DyBaCo_2O_{5+\delta}$, an annealing plan shown in Figure 2.12 has been devised by Barilo *et al*. [1]. A slightly amended annealing plan, because of some limitations of the electric furnace available in Manchester, was applied to a sample of $DyBaCo_2O_{5+\delta}$. This is shown in Figure 2.13.

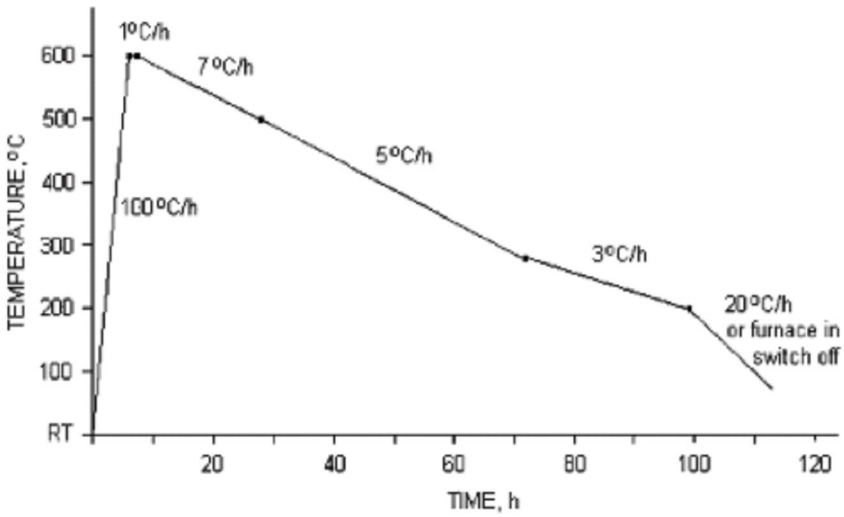

Figure 2.12: *Temperature-time diagram of optimal annealing for $DyBaCo_2O_{5+\delta}$ single crystals under flowing oxygen* (*Taken from* [1]).

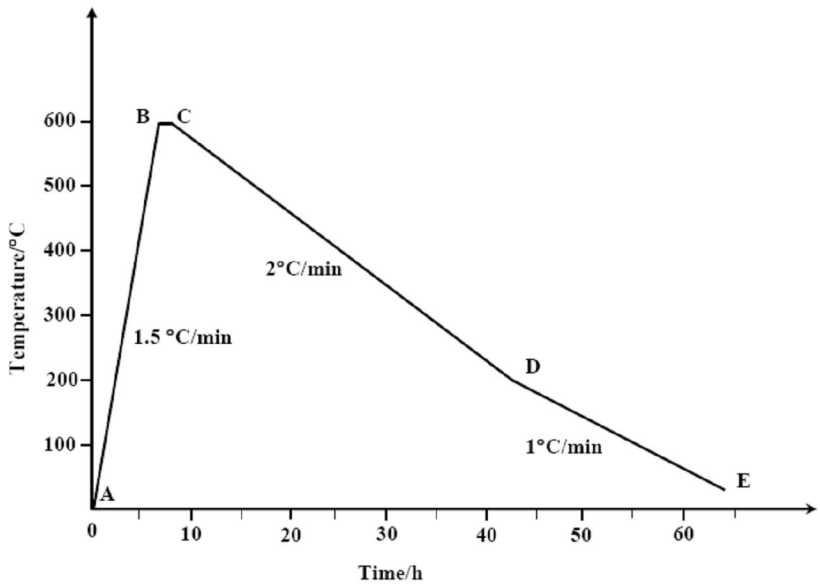

Figure 2.13: *Temperature vs time plan followed for the optimal annealing of single crystal $DyBaCo_2O_{5+\delta}$ under flowing oxygen used in this work. This was undertaken in the PSI, Manchester.*

In the oxygen annealing experiment, a high quality single crystal sample of $DyBaCo_2O_{5+\delta}$ of dimensions 3×3.3×2.1 mm^3 was placed under flowing oxygen in a tube furnace (as shown in Figure 2.14). The sample was then heated by means of a temperature-controlled EUROTHERM-818 furnace up to 600 °C at a ramp rate of 1.5 °C/min as shown by line AB in Figure 2.13. The horizontal line BC shows that this temperature was maintained for 90 minutes and then the sample was cooled down to 200 °C temperature at a ramp rate of 2 °C/min (CD). Finally the sample was further cooled down to room temperature at a ramp rate of 1 °C/min (DE). The well-oxygenated sample, obtained from this experiment, was later used for a high-resolution photoemission experiment at beamline 3.2 of the SRS at Daresbury Laboratory (Chapter 4).

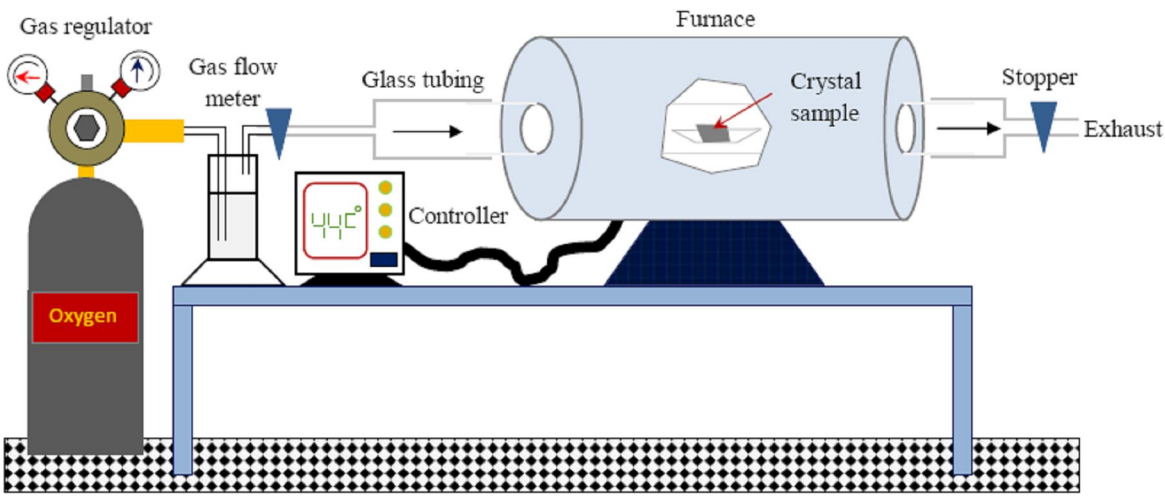

Figure 2.14: *A schematic layout of the experimental setup for the optimal annealing of single crystal $DyBaCo_2O_{5+\delta}$ under flowing oxygen in this work.*

2.6 Magnetic Structure

2.6.1 Basic Concepts

2.6.1.1 Magnetism

Many materials exhibit magnetic behaviour which is intrinsically associated with the electrons inside them. The classical view of magnetism explains that a spinning electron produces a magnetic field as shown in Figure 2.15, and the moment thus produced is called a magnetic moment or magnetic dipole moment denoted by μ.

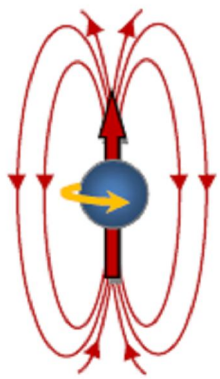

Figure 2.15: *Magnetic field produced by a spinning electron.*

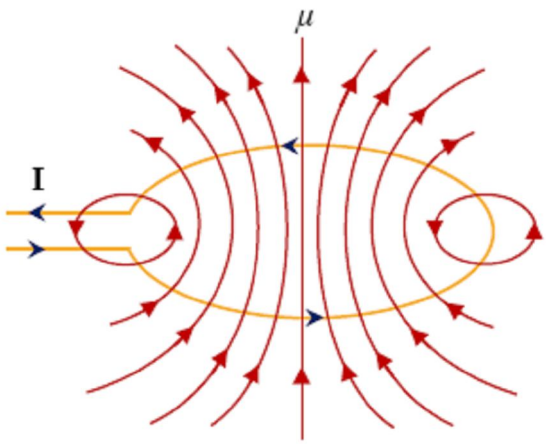

Figure 2.16: *Magnetic field produced by a current-carrying loop of wire.*

From electrodynamics, we know that an electric current I circulating around a loop of wire of area A, as shown in Figure 2.16, also generates a magnetic moment μ given by:

$$\mu = IA. \qquad \text{Equation 2.12}$$

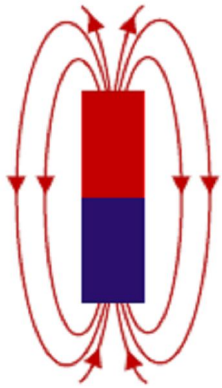

Figure 2.17: *Magnetic field pattern of a bar magnet.*

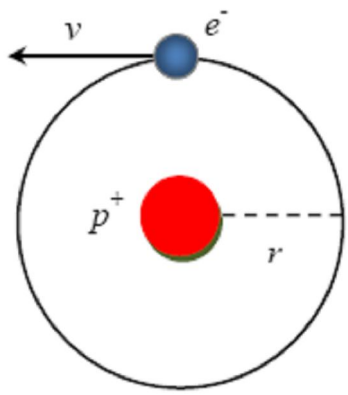

Figure 2.18: *An electron circulating around a nucleus in an atom.*

The magnetic field produced by this current-carrying loop resembles that of a bar magnet as shown in Figure 2.17 and possesses two magnetic poles (N and S). The magnetic moment generated by the angular momentum ($m_e vr$) of a classically orbiting electron, as shown in Figure 2.18, of mass m_e with speed v in its ground state can be derived as:

$$\mu = IA = \pi r^2 \times \frac{-e}{2\pi r / v} = -\frac{e\hbar}{2m_e} = -\mu_B = -9.274\times10^{-24}\ \text{J T}^{-1}, \quad \text{Equation 2.13}$$

where μ_B is called the Bohr magneton.

According to quantum mechanics, the state of an electron in an atom can be represented by four quantum numbers:

principal quantum number; n = 1, 2, 3, 4,……..,

orbital quantum number; l = 0, 1, 2, 3,…….n -1,

magnetic quantum number; m_l = -l,.....,0,.....+l,

and magnetic spin quantum number; m_s = -1/2, +1/2.

The magnitude of the magnetic moment of an isolated electron in terms of orbital quantum number l can be calculated by the following Equation 2.14:

$$\mu_{orbital} = \mu_B \sqrt{l(l+1)}\,. \qquad \text{Equation 2.14}$$

As an unpaired electron possesses spin angular momentum as well, the magnitude of the magnetic moment associated with it is given by:

$$\mu_{spin} = g\mu_B\sqrt{s(s+1)}, \qquad \text{Equation 2.15}$$

where g is known as the free electron g value, numerically equal to 2.0023. s is called the spin quantum number and it has a value equal to 1/2.

A multi-electron atom contains more than one electron, therefore the total contribution of orbital magnetic moment of all the electrons can be determined by using the total orbital angular momentum quantum number L which is the vector sum of the l values for all the valence shell electrons. The total or effective orbital magnetic moment along z-axis (say) is equal to $L\mu_B$. Similarly the total or effective spin magnetic moment of these electrons along the z-axis can be determined using the total spin angular momentum quantum number S which is the vector sum of the spin quantum numbers.

The magnetic moments resulting from the spin and the orbital motion are linked or coupled in isolated atoms or ions to give an overall magnetic dipole moment for the atom. Spin-orbit coupling, also known as Russell-Saunders coupling, is governed by the total angular momentum quantum number J. If the subshell of an atom is less than half-filled, then $J = L-S$ otherwise $J = L + S$. The corresponding effective magnetic moment is given by:

$$\mu_{eff} = g_J\sqrt{J(J+1)}\mu_B, \qquad \text{Equation 2.16}$$

where g_J is called the Landé factor and is given by:

$$\text{Landé factor} = \frac{3}{2} + \frac{S(S+1) - L(L+1)}{2J(J+1)}. \qquad \text{Equation 2.17}$$

For a fully-occupied subshell, $L = 0$ and $S = 0$. Hence, the core electrons of an atom do not have any contribution to the magnetism.

Compounds of 3d transition elements show only spin magnetism because their orbitals are strongly influenced by the ligand field and experience great difficulty in aligning themselves freely in a magnetic field. So, the contribution from the orbital angular

momentum is quenched fully or partially. On the other hand, the 4f electrons in lanthanide ions are shielded by the completely filled 5s and 5p shells and therefore are not influenced by the ligand field. Hence in this case, Russell-Saunders coupling is fully effective.

2.6.1.2 Types of Magnetic Materials

Magnetic materials can be grouped into different categories according to the arrangement of magnetic dipoles in them. These categories are diamagnetic, paramagnetic, ferromagnetic, antiferromagnetic and ferrimagnetic etc.

2.6.1.2.1 Diamagnetic

Diamagnetic materials do not have unpaired electrons and when such materials are placed in an external magnetic field, they are repelled by the field. The reason is that the external magnetic field induces an electric current in the electrons of the material which results in an internal magnetic field which opposes the external magnetic field. Although the internal magnetic field is weak, it is always present.

2.6.1.2.2 Paramagnetic

In paramagnetic materials, there are unpaired electrons in the atoms or molecules that possess permanent magnetic dipole moments. These magnetic moments are isolated and randomly oriented in the absence of any external magnetic field as shown in Figure 2.19(a).

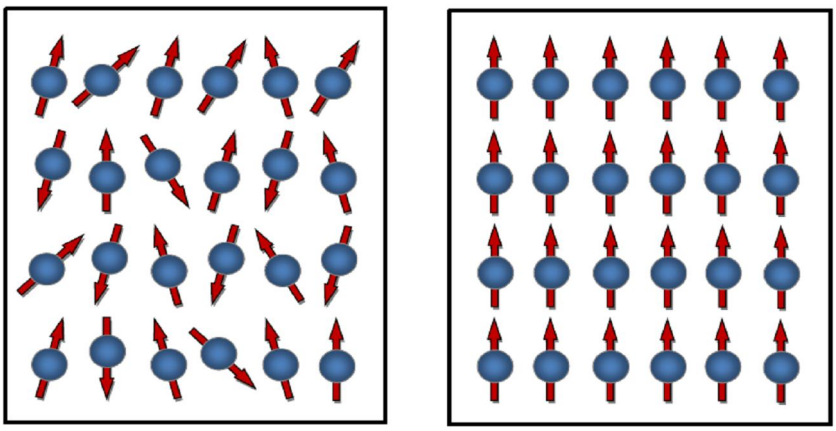

(a) (b)

Figure 2.19: *Orientation of dipole moments in* (*a*) *paramagnetic materials* (*b*) *ferromagnetic materials* (*Adapted from* [5]).

When paramagnetic substances are placed in an external magnetic field, the dipole moments tend to align in the direction of the field and the material is magnetised. A perfect alignment of the dipole moments remains incomplete due to thermal effects and the interaction with neighbouring atoms in the structure. Hence, there is a smaller degree of magnetisation at higher temperature. Unlike diamagnetic materials, paramagnetic materials are attracted by the external magnetic field. Paramagnetic effects are about 10 to 10000 times greater than diamagnetic effects.

2.6.1.2.3 Ferromagnetic

Transition and rare-earth elements have unpaired dipole moments in their d and f orbitals respectively. The parallel alignment of these dipoles over a certain distance in the material as shown in Figure 2.19(b), results in a strong magnetic field. The ferromagnetic effect is about a billion times larger than paramagnetism if a ferromagnetic substance is placed in the same external magnetic field

2.6.1.2.4 Antiferromagnetic

Antiferromagnetic materials are those in which an exchange coupling exists which causes neighbours to align spins in anti-parallel fashion as depicted in Figure 2.20 (a). Therefore, the macroscopic magnetic moment of the crystal sample comes out to be zero.

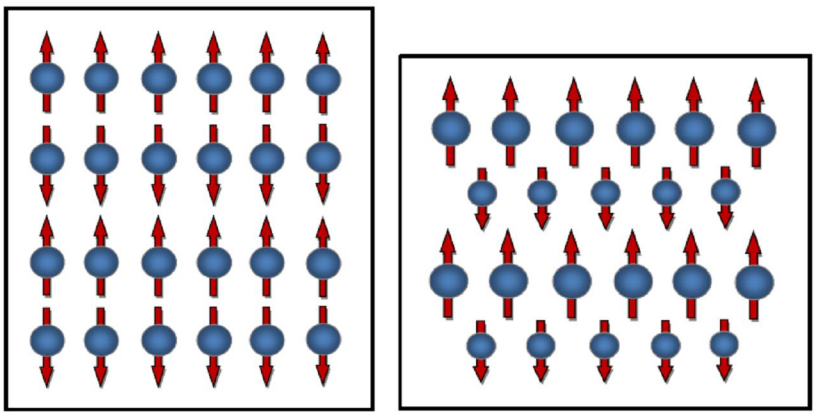

(a) (b)

Figure 2.20: *Orientation of dipole moments in* (*a*) *antiferromagnetic materials* (*b*) *ferrimagnetic materials* (*Adapted from* [5]).

2.6.1.2.5 Ferrimagnetic

In ferrimagnetic materials, the arrangement of spins is similar to that of antiferromagnetic materials but the magnitude of the magnetic moment of upward spins is different from that of downward spins. The orientation of magnetic dipole moments in ferrimagnetic materials is shown in Figure 2.20 (b). Hence, they do not cancel each other and there exists a net magnetic moment of the crystal sample.

2.6.1.3 Bulk Properties of Magnetic Materials

2.6.1.3.1 Magnetisation and Susceptibility

As magnetic materials comprise a large number of magnetic atoms or molecules and when they are placed in a magnetic field *H*, their magnetic dipoles are forced to align parallel to its direction, therefore the total strength of the field in the material is changed and it is characterised by magnetisation *M*. The magnetisation of a material is defined as magnetic moments per unit volume when placed in a magnetic field. For isotropic materials, the relation between *M* and *H* is given by:

$$M = \chi H, \qquad \text{Equation 2.18}$$

where χ is the magnetic susceptibility of the material, which is a measure of the magnetisation induced by a unit applied field. It is a dimensionless quantity.

Magnetic materials are characterised by measuring their magnetisation as a function of applied magnetic field and susceptibility as a function of temperature. For nonisotropic materials, *M* and *H* may not be parallel so the susceptibility of the material varies in different directions.

In paramagnetic materials, the magnetic effects are much stronger in diamagnetic ones. For such materials, the magnetic susceptibility is positive and slightly greater than unity whereas in diamagnetic materials, χ is negative and independent of temperature. The paramagnetic susceptibility depends upon temperature and obeys the Curie law as given by Equation 2.19:

$$\chi = \frac{C}{T}, \qquad \text{Equation 2.19}$$

where T is the absolute temperature and C is the Curie constant, as shown in Figure 2.21.

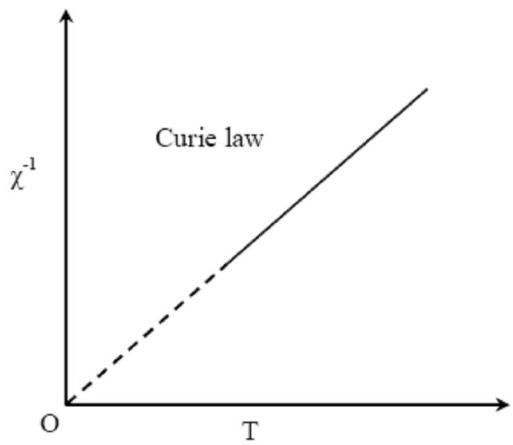

Figure 2.21: *Temperature dependence of the reciprocal magnetic susceptibility showing the Curie law behaviour of paramagnetic materials* (*Adapted from* [5]).

Curie law behaviour indicates that there are isolated ions or atoms in the paramagnetic substances. A variety of magnetic behaviours comes into existence where these magnetic dipoles interact. At low temperature, the interaction increases sufficiently such that the random orientation of the dipoles is restricted and changes slowly only with time. Below a certain temperature T_f called the freezing temperature, the directions of the spins are said to be frozen and the state is called a spin glass. In some other materials below T_f, the interactions are strong enough for local ordering but due to the crystal structure, the localised regions are restricted in size and no long range order comes into existence. This type of arrangement is termed as a cluster glass. An example is Prussian blue, $\{KFe_2(CN)_6\}$, which has a magnetic freezing point of about 25 K [5].

Ferromagnetic materials, above a certain temperature T_C called Curie temperature, become paramagnetic because above T_C, the thermal energy is greater than the magnetic interaction and this spoils the order of the dipoles to cause a transition from ferromagnetic to paramagnetic. Ferromagnetic materials obey the Curie-Weiss law well above the Curie temperature. This is given by:

$$\chi = \frac{C}{T - \theta} \quad . \qquad \text{Equation 2.20}$$

θ is known as Curie-Weiss constant. For a positive value of θ, a graph of Curie-Weiss law behaviour is shown in Figure 2.22. The ferromagnetic to paramagnetic transition is reversible if the temperature is lowered until the dipoles realign parallel to one another and the temperature approaches the Curie temperature [5].

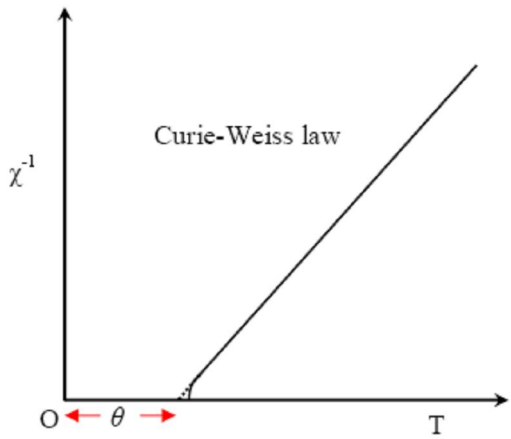

Figure 2.22: *Temperature dependence of the reciprocal magnetic susceptibility showing Curie-Weiss law behaviour of ferromagnetic materials above the Curie temperature in the paramagnetic state* (*Adapted from* [5]).

Antiferromagnetic materials are changed to paramagnetic materials above a temperature T_N called the Néel temperature as shown in Figure 2.23. Antiferromagnetic substances also follow the Curie-Weiss law as given by equation 2.20, but in this case θ is negative which can be seen in Figure 2.24.

Lowering the temperature of the material through the Néel temperature also restores the antiferromagnetic phase. Between ferromagnetic and antiferromagnetic ordering, there exists another type of ordering of dipoles termed a canted antiferromagnetic configuration. It can be considered as an intermediate state between ferromagnetic and antiferromagnetic configurations.

The temperature dependence of ferrimagnetic materials is much more complex because the magnetic ions are sensitive to both temperature and spin interactions. The magnetic behaviour of ferrimagnetic substances can be approximated by equation 2.21:

$$\frac{1}{\chi} = \frac{T}{C} + \frac{1}{\chi_0} + \frac{\xi}{T-\theta} \ , \qquad \text{Equation 2.21}$$

where χ_o, ξ and θ are parameters which depend on the spin interactions and the population of the available cation sites in the crystal sample. A graph of the variation of the inverse susceptibility with temperature for a ferrimagnetic substance is shown in Figure 2.25.

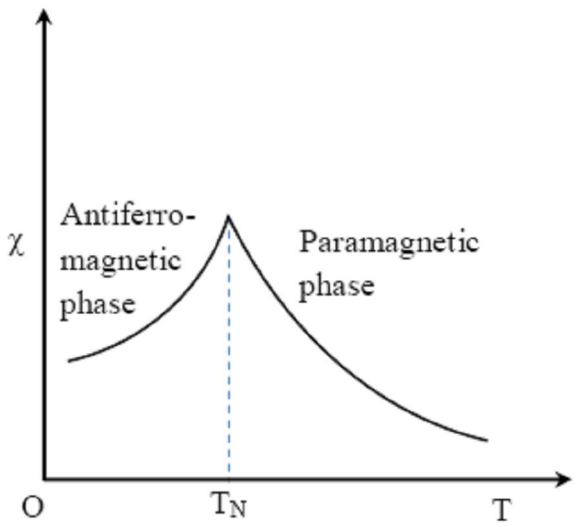

Figure 2.23: *Antiferromagnetic to paramagnetic transition of antiferromagnetic materials as a function of temperature for $\theta < 0$ where T_N is the Néel temperature* (*Adapted from* [16]).

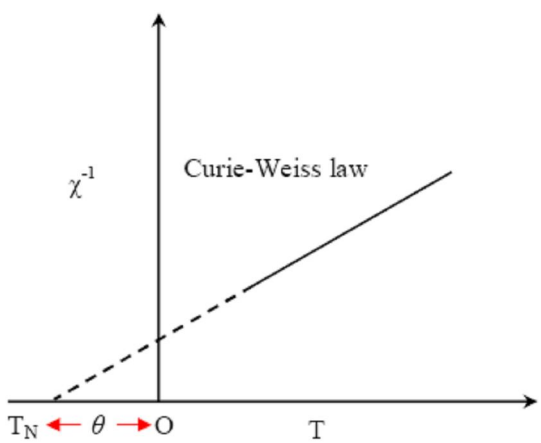

Figure 2.24: *Temperature dependence of the reciprocal magnetic susceptibility showing Curie-Weiss law behaviour of antiferromagnetic materials* (*Adapted from* [5]).

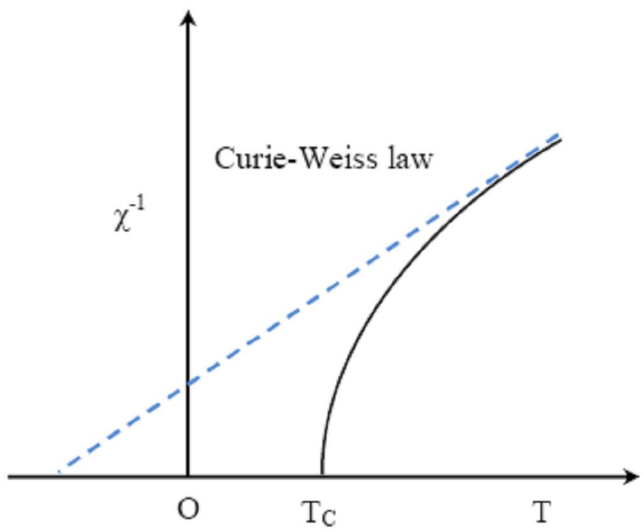

Figure 2.25: *Temperature dependence of the reciprocal magnetic susceptibility showing the behaviour of ferrimagnetic materials* (*Adapted from* [5]).

2.7 Electronic and Magnetic Behaviour of Rare-earth Cobalt Oxides

2.7.1 $LnBaCo_2O_{5+\delta}$ (Ln = rare earth) - Ln-112

Colossal magnetic resistance (MR) materials $Ln_{1-x}A_xM_nO_3$ (where Ln = rare-earth element, A = alkaline earth atom) with the perovskite structure have been studied considerably in recent years because of their special magnetic and electronic properties [17]. The rare-earth simple perovskite $LaCoO_3$ (Co^{3+}, d^6) shows a magnetic transition from the low-spin (LS) to the intermediate-spin (IS) or the high-spin (HS) states when the temperature is raised [18, 19]. In the simple perovskites the Co^{3+} ion, residing in an octahedral environment, presents a challenging system due to the competition between the crystal field splitting and the intra- atomic exchange interaction influenced by strong Co 3d/O 2p hybridisation, affecting the on-site Coulomb repulsions [20].

$LaCoO_3$ shows a temperature-induced transition from a non-magnetic semiconductor to a magnetic state at about 90 K [21, 22]. At this temperature, it has been suggested that a HS state ($t_{2g}^4e_g^2$) exists because the intra-atomic exchange interaction favours aligned spins (Hund's rule). The crystal field splitting (10 Dq) at temperatures below 90 K is large

enough to overcome it so that $LaCoO_3$ is in the LS state ($t_{2g}^6e_g^0$) at low temperatures. Actually the energy difference between these two states is extremely small and the compound has been observed to undergo a gradual low-spin to high-spin transition as the temperature increases. A transition to the IS has also been observed at about 100 K. This state is postulated to be a mixture of $t_{2g}^5e_g^1$ and $t_{2g}^5e_g^2$ $\underline{L}$ states, where $\underline{L}$ represents a ligand hole state. This occurs only when one of the surrounding ligand atoms donates an electron leaving a hole behind. In a purely ionic model, the spin state would be LS or HS depending upon the balance between 10 Dq and the intra-atomic exchange interaction. However, the IS state is considered to be stabilised as compared to the HS state due to strong Co 3d/O 2p hybridisation [20, 23]. These oxides exhibit a general tendency for the transition metals to undergo a ground state ligand to metal electron transfer thus reducing the valency of the metal [23, 24]. In the case of the simple perovskites *e.g.* $LaCoO_3$ and $HoCoO_3$, this corresponds to d^6 to d^7 $\underline{L}$ [20]. The lowering in energy of the IS state through hybridisation explains the LS-IS transition. The intermediate state should be metallic, given the occupancy of its electron orbitals, but actually it is insulating. This has been explained by magnetic orbital ordering leading to the states being pulled back from the Fermi level [20]. At 500 K, a second transition to a metallic state occurs. Korotin *et al.* [20] suggest that this is due to the loss of orbital ordering which allows the bands to cross the Fermi level. They also suggest that the HS state lies above the IS state at such a high energy that it cannot be reached until the temperature exceeds 500 K. Moreover, neutron scattering experiments show a second spin state transition with an anomalous lattice expansion at 500 K. The data obtained from this experiment gave a 3 spin-state model (LS, IS, HS), with *gradual* transitions between the LS and the IS states, and then between the IS and the HS states as a function of temperature as shown in Figure 2.26 [22]. An equilibrium population of all three states occurs at intermediate temperatures that shifts gradually from majority LS to majority HS as the temperature is raised. Calculations, using the self-energy corrected Hartee-Fock approximation, suggest that the IS and the HS states show similar energies both around 1 eV higher than the LS phase [25].

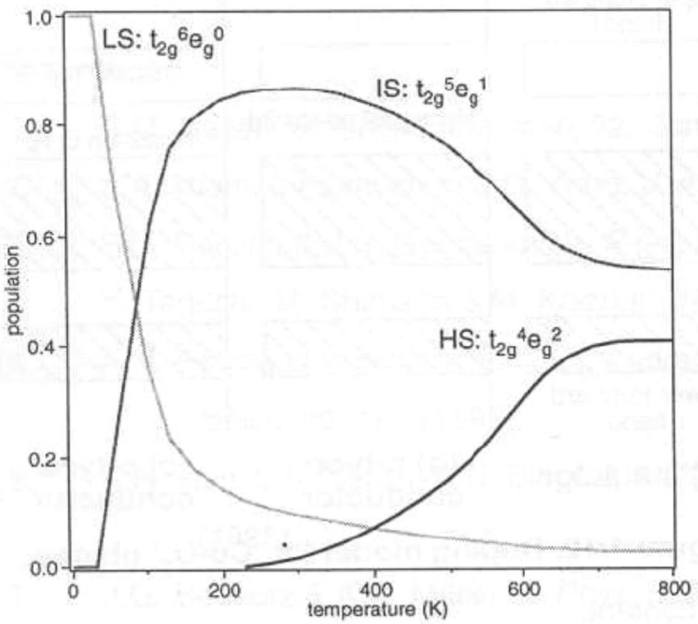

Figure 2.26: *Occupation of Co^{3+} spin states in $LaCoO_3$ as a function of temperature determined from measurements of magnetic susceptibility* (*Taken from* [22]).

Table 2.2 shows the proportions of the LS, the IS and the HS states in $LaCoO_3$ as a function of temperature. It can be seen here that the proportion of the LS state decreases quickly as the temperature is raised between 130 K and 300 K, but thereafter drops very slowly. The dominant contribution at the temperatures shown is from the IS state. The contribution of the HS state is significant only above 400 K [22].

T (K)	LS	IS	HS
130	0.25	0.75	0.00
300	0.10	0.87	0.02
360	0.09	0.86	0.05
425	0.08	0.83	0.09
485	0.07	0.79	0.15

Table 2.2: *Occupation of the three spin states in $LaCoO_3$ at 130, 300, 360, 425 and 485 K, calculated from magnetic susceptibility data* (*Taken from* [22]).

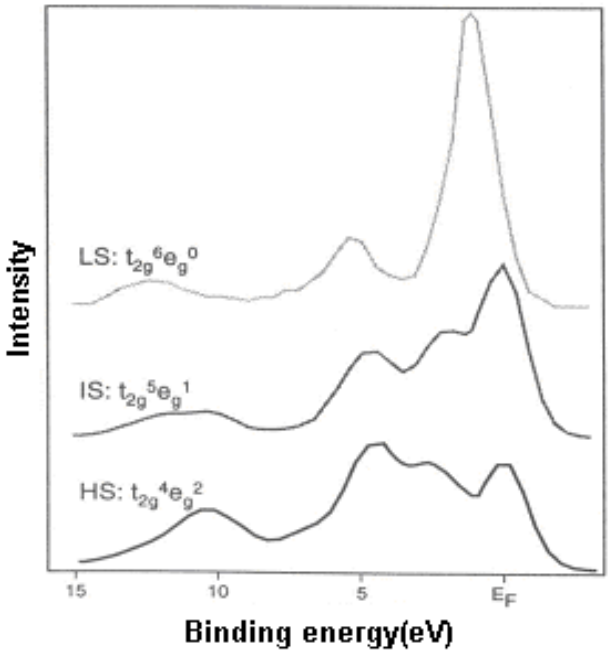

Figure 2.27: *Calculated spin state dependence of the Co^{3+} contribution to the valence band density of states of $LaCoO_3$ produced from cluster calculations* (*Taken from* [23]).

There has been much debate in the literature [26, 27] about the exact nature of the lanthanum cobaltite band picture. The contribution of the valence band density of states (DOS) from cobalt depends upon the spin state [28], as shown by the results of cluster calculations illustrated in Figure 2.27 [23]. Similar spin state transitions caused by orbital ordering at the octahedral CoO_6 sites in the double perovskites $LnBaCo_2O_{5+\delta}$ (where Ln = rare-earth) can also be observed [29]. Kim *et al.* [30] suggest that $GdBaCo_2O_{5+\delta}$ is a paramagnet (PM) above 285 K and shows a FM transition near 285 K. As the temperature decreases, an antiferromagnetic (AFM) phase transition appears at about 220 K. Finally it undergoes a transition to paramagnetic (PM) state below 75 K. Such phase transitions are well matched up with the isothermal magnetisation reversal curves of Kim *et al.* [30], not depicted here. Kim *et al*. [30] extrapolated the magnetic moment of $GdBaCo_2O_{5+\delta}$ in the (ferromagnetic) FM phase from a power law to T = 0 K as shown by the solid line in Figure 2.28. The value of the magnetic moment is 0.8 μ_B which is about 44% of the theoretical value of the Co^{3+} ions with the IS state in the octahedral sites. For this calculation, they

supposed that only the Co^{3+} ion in octahedral environments were responsible for ferromagnetism while the remaining cobalt ions in the square pyramidal sites were PM as shown in the inset of Figure 2.28.

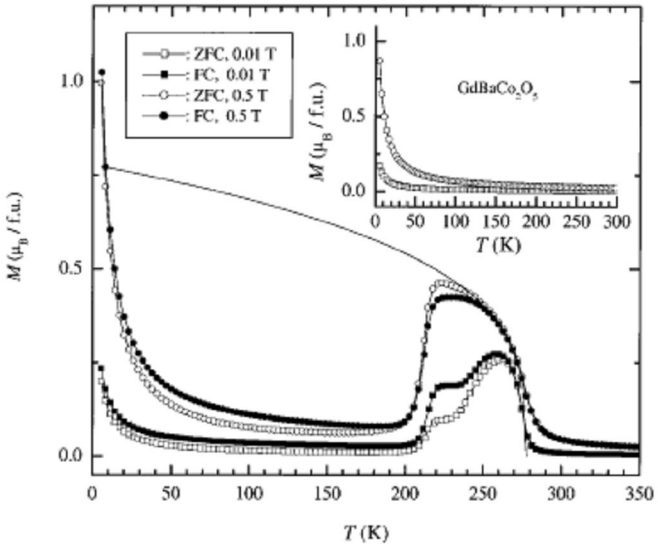

Figure 2.28: *Temperature dependent magnetisation of $GdBaCo_2O_{5+\delta}$.Open and closed marks represent temperature-dependent zero field cooling (ZFC) and field cooling (FC) magnetisations, respectively. The inset shows the magnetisation data for $GdBaCo_2O_{5+\delta}$ ($\delta = 0$) as a function of temperature* (*Taken from* [30]).

Figure 2.29 shows temperature-dependent resistivity curve for $GdBaCo_2O_{5+\delta}$ measured at 0 T (open circles) and at 5 T (solid circles). This resistivity behaviour resembles that of a semiconductor in the entire temperature range except for the narrow range between 160 - 220 K where the resistivity decreases as the temperature increases. Around 220 K, the slope of the zero-resistivity is slightly changed and this gradual change moves towards 160 K under the applied magnetic field of 5 T. This subtle change in resistivity can be associated to the FM to AFM phase transition. The onset of the AFM phase that appears around 220 K is moved to lower temperature (160 K) under an applied magnetic field. Magneto resistance is defined as MR = [ρ(0) - ρ(5 T)]/ρ(0). The measured value of the MR ratio is shown in Figure 2.29 by solid rectangular markers. A maximum MR ratio about 40% has been found to occur around 200 K. This giant magnetoresistance (GMR) effect is attributed to spin dependent scattering [31-34] where the applied magnetic field compels the parallel alignment of the anti-parallel Co^{3+} spins.

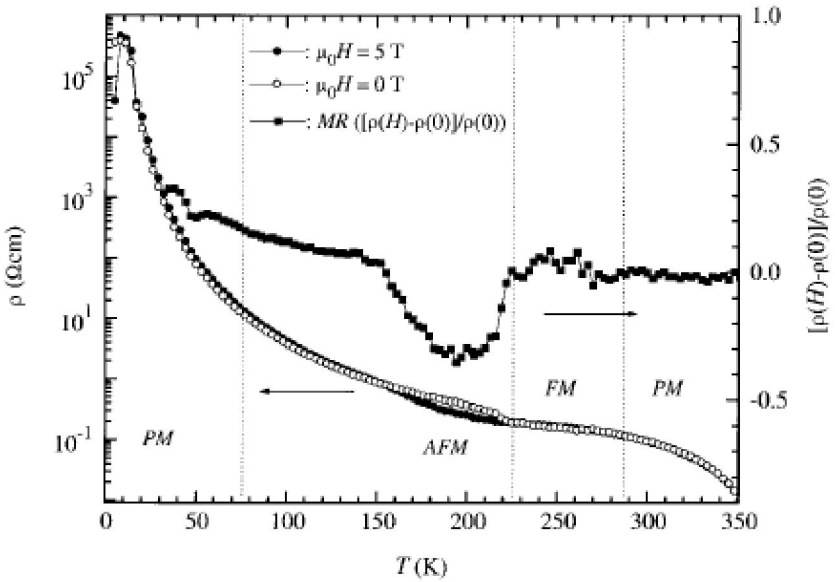

Figure 2.29: *Temperature-dependent resistivity curves of $GdBaCo_2O_{5+\delta}$ measured at 0 T (open circles) and 5 T* (*solid circles*)*. Solid squares denote MR values. Vertical dots show the magnetic phase boundaries* (*Taken from* [30]).

Non-metal-to-metal transitions, in various $LnBaCo_2O_{5+\delta}$ compounds can be seen in the 280-400 K temperature range [29, 35]. The effect of the size of the lanthanide ion and oxygen content on the non-metal-to-metal transition and the corresponding magnetic susceptibility anomaly were studied by Magnan *et al*. [36]. The sharpest transitions can be seen for L*n* = Tb and Dy. This transition is observed at a temperature (T_{MI}) that decreases smoothly with the size of the lanthanide. The resistivity values (10^{-3} -10^{-4} Ω cm) at T = 400 K are characteristic of metallic oxides. It can be notice that at T = 400 K, the resistivity gradually increases from 4×10^{-4} Ω cm (for L*n* = Pr) to 4×10^{-3} Ω cm (for L*n* = Ho). Magnan *et al*. [36] reported that the highest oxygen contents were observed for the largest lanthanides. Therefore it looks like that the metallicity tends to decrease as the oxidation state of cobalt decreases. This indicates that the MI transition not only depends upon the size of the lanthanides but also on the oxygen content in the sample shown in Figure 2.30(b).

The ρ(T) curves clearly show that there is an optimal carrier doping for the appearance of the MI transition. This coincides approximately with the $O_{5.5}$ stoichiometry [36]. In the case of $GdBaCo_2O_{5+\delta}$, the T_{MI} is close to 350 K.

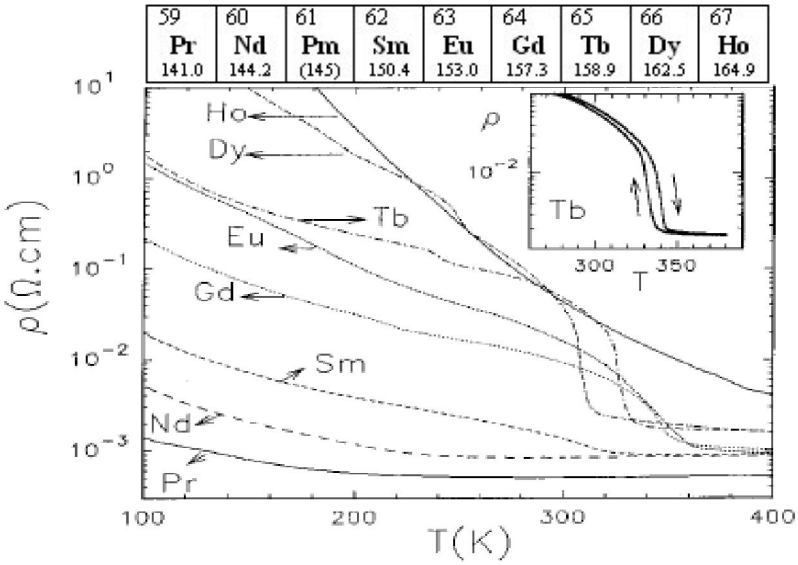

Figure 2.30 (a): *Temperature dependence of the resistivity (ρ) for air-synthesised* $LnBaCo_2O_{5+\delta}$*.The inset shows an enlargement of the transition for Ln =Tb* (*Adapted from* [36]).

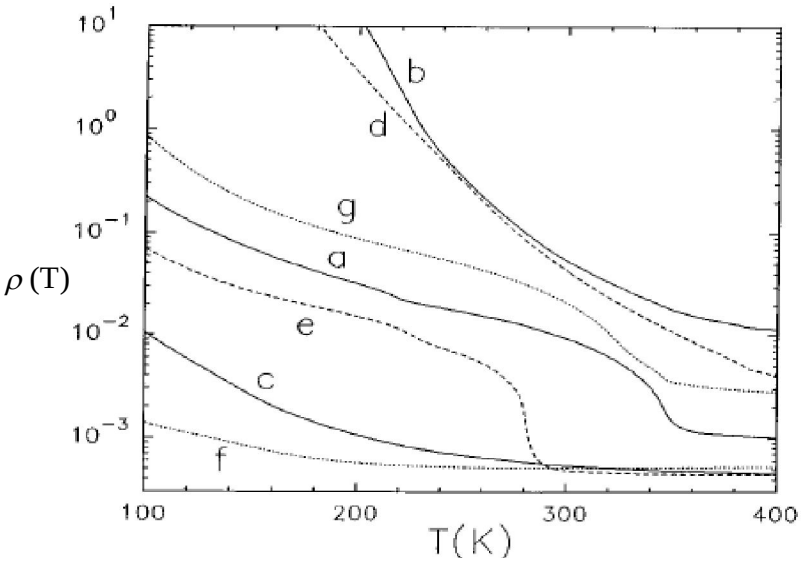

Figure 2.30 (b): *Temperature dependent resistivity curves for* $GdBaCo_2O_{5+\delta}$ *a*) *air-synthesised, b*) *argon annealed c*) *oxygen-annealed*; $HoBaCo_2O_{5+\delta}$ *d*) *air-synthesised, e*) *oxygen annealed*; $PrBaCo_2O_{5+\delta}$ *f) air-synthesised, g*) *argon annealed* [36].

Carlos Frontera *et al.* [37] have recently undertaken a study on $LnBaCo_2O_{5.5}$ (Ln = Pr, Gd) to study structural changes as a function of temperature based on the size of the rare earth atom. Figure 2.31(a) shows lattice parameters of the unit cell and Figure 2.31(b) depicts

Co-O mean distances found for both octahedral and pyramidal sites of $PrBaCo_2O_{5.5}$ as a function of temperature. It can be seen here that the lattice parameter *a* suddenly expands as the temperature decreases. On the contrary, both *b* and *c* shrink on cooling. The variation in the Co-O bond distances with temperature can be seen in Figure 2.31(b). A comparison of the temperature-dependent variation of the volume of the unit cell for both $PrBaCo_2O_{5.5}$ and $GdBaCo_2O_{5.5}$ is shown in Figure 2.32. Above 300 K, the volume of the unit cell for both the compounds changes with temperature in a similar fashion. However, an anomalous expansion in the unit cell has been observed at T_{MI} , coinciding with the changes in the Co-O bond distances. This anomalous cell expansion takes place because of the spin state transition [38]. As a result of this study, Frontera *et al.* suggest that the temperature-dependent anisotropic evolution of cell parameters of $PrBaCo_2O_{5.5}$ is qualitatively equal to that found in $GdBaCo_2O_{5.5}$ [38] and the magnitude of the structural changes with the larger lanthanide, Pr, is also very similar to much smaller rare earths Ln = Gd, Tb and Y [37, 39, 40].

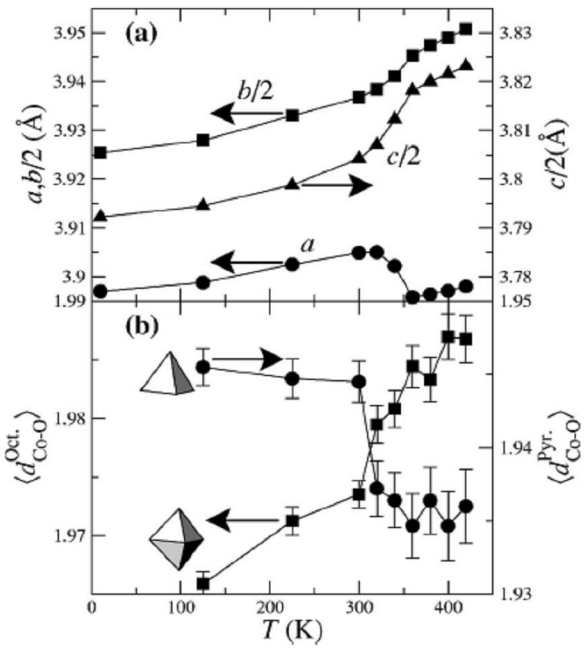

Figure 2.31: (a) *Cell parameters obtained by high resolution neutron power diffraction* (*NPD*) *data at different temperatures*. (b) *temperature dependence of the mean Co-O distance for octahedra and pyramids* (*Taken from* [37]).

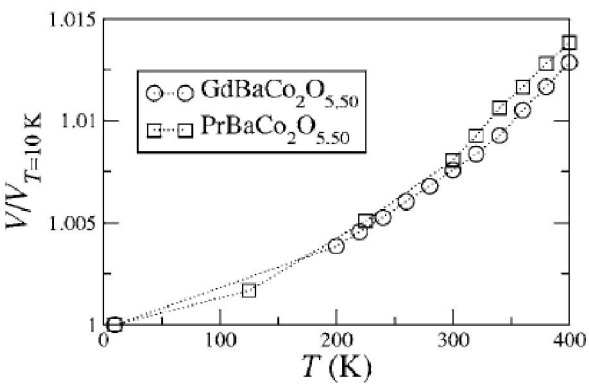

Figure 2.32: *Cell volume of $PrBaCo_2O_{5.5}$ and $GdBaCo_2O_{5.5}$ – normalised to that at 10 K* (*Taken from* [37]).

Results show some consensus of opinion that the spin state in the CoO_5 pyramids does not change with temperature [17, 30, 41-43]. There are also some suggestions about the temperature dependence of the spin states in the octahedral sites but there is no overall consensus. The complex magnetic behaviour may be explained in terms of the spin state transition of the Co^{3+} ion in the octahedral environment from the IS to the LS configuration and the orbital ordering of the e_g electron in the IS state. In contrast, the IS state of Co^{3+} in the CoO_5 square pyramidal site appears not to be involved in the spin state transition process in the temperature range 50-350 K. The reduced symmetry of these pyramidal sites, as compared to CoO_6 octahedra, lifts the degeneracy of the t_{2g} and the e_g orbitals and reduces the crystal field stabilisation, lowering the stability of the LS state as compared to the IS and the HS states. Hence the LS state is not occupied at low temperature. Maignan *et al.* [36] suggested a co-existence of the IS (pyramids) and the LS (octahedra) for $T < T_{MI}$ and HS Co^{3+} at high enough temperatures. However Moritomo *et al*. [44] undertook a study of the structural changes as a function of temperature for $TbBaCo_2O_{5.5}$. They suggested a spin state transition from a full IS state scheme to the HS state in both pyramidal and octahedral environments. In contrast with Kim *et al*. [30] and Moritomo *et al.* [44], Frontera *et al*. [17] attribute the non-metal-to-metal transition around 350 K to sudden LS to HS transition in the octahedral environment. The LSDA+U calculations of Wu [45, 46] show disagreement. Wu suggests that both the AFM/FM and non-metal-to-metal transitions occur through delocalisation of the pdσ holes in the almost HS state of $GdBaCo_2O_{5.5}$ rather than through a sudden Co LS to HS spin flip. As a whole, the calculations imply that the HS state is much more stable in double perovskites such as $GdBaCo_2O_{5+\delta}$ than in simple perovskites *e.g*. $LaCoO_3$ [22].

A recent photoemission study was carried out by K. Takubo *et al*. [47] to study the MI transition in $LnBaCo_2O_{5+\delta}$ (Ln = Tb, Nd; $\delta = 0.5$). Valence band spectra of $TbBaCo_2O_{5.5}$ recorded at 300 K shown in Figure 2.33(a) show a contribution from the Tb 4f states in the 6-10 eV binding energy range. A feature located at 1.5 eV in the valence band is dominated by the Co 3d orbitals hybridised with the O 2p orbitals. Features A and B in the Co 3*d*-O 2*p* hybridised band are consistent with the photoemission studies undertaken by Flavell *et al.* [24] for Ln = Gd, Dy. Takubo *et al*. suggest that the features A and B can be considered as

the contributions of the e_g and the t_{2g} bands respectively. At the Fermi level, a spectral gap at 30, 250 and 300 K (insulating phase) can be observed. This gap has disappeared at 380 K (metallic phase) as shown in Figure 2.33(b). Here a decrease in spectral weight at ~ 1.5 eV (structure B) and increase near E_F (structure A) can be seen in going from 300 to 380 K. Moreover the feature B is slightly moved towards the lower binding energy side. This is indicative of the insulator-to-metal transition and agrees with the previous suggestions of the LS to the HS (or IS) transition [48].

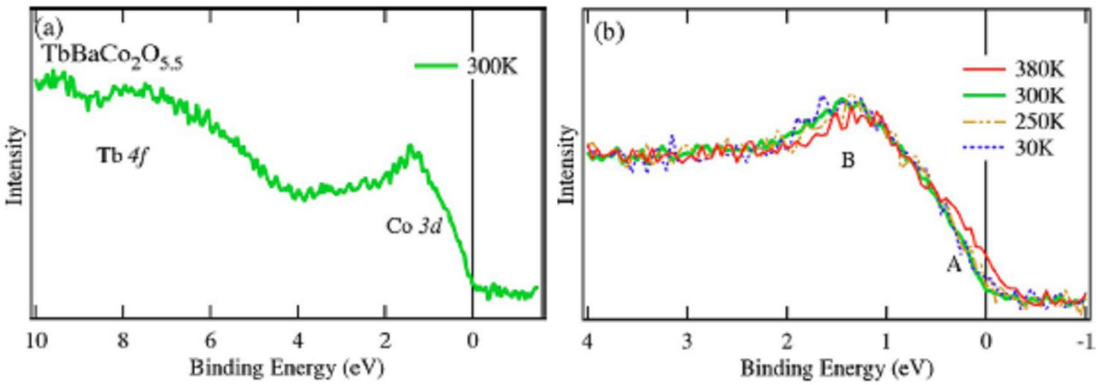

Figure 2.33: (*a*) *Valence-band and* (*b*) *near* E_F *XPS spectra of* $TbBaCo_2O_{5.5}$ *taken at 30, 250, 300, and 380 K* (*Taken from* [47].

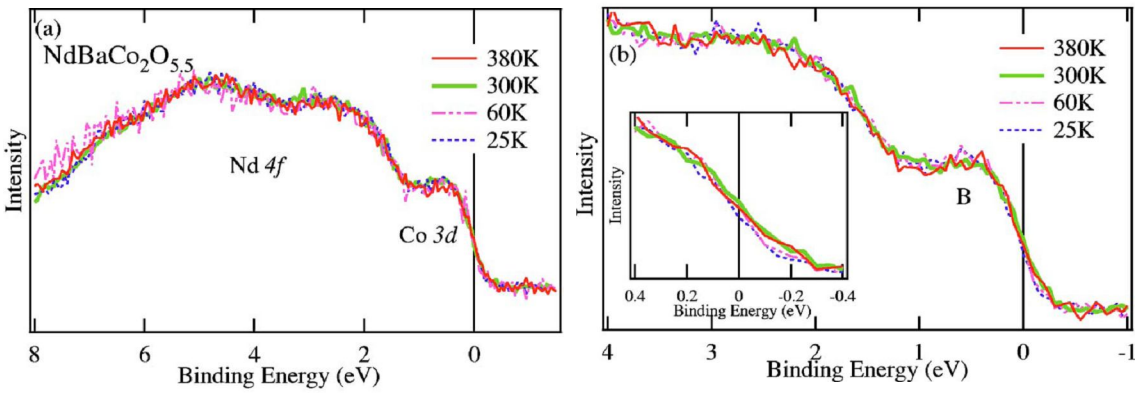

Figure 2.34: *(a) Valence band and (b) near-*E_F *XPS spectra of* $NdBaCo_2O_{5.5}$ *taken at 25, 60, 300, and 380 K. The inset shows an expanded view of the valence band in the vicinity of the Fermi level* (*Taken from* [47]).

Figure 2.34 shows valence band for $NdBaCo_2O_{5.5}$ having contributions from the Nd 4f states distributed in the 2-8 eV binding energy range and from Co 3d states to feature B.

Takubo *et al*. suggest that feature B in the valence band of $NdBaCo_2O_{5.5}$ is mainly derived from the t_{2g} band and comes closer to the Fermi level as compared to that of $TbBaCo_2O_{5.5}$. This shows that the t_{2g} band of $NdBaCo_2O_{5.5}$ is shifted by ~1 eV closer towards the Fermi level than that of $TbBaCo_2O_{5.5}$. Consequently the separation between the t_{2g} and e_g bands is reduced as is schematically shown in Figure 2.35. At the Fermi level, a marked change in the photoemission intensity cannot be seen with the increase of temperature. K. Takubo *et al.* suggest, as a result of this study, that the MI transition behaviour of $LnBaCo_2O_{5.5}$ is associated with the energy separation between the t_{2g} and the e_g bands and the Co 3d electrons are not localised and are distributed to the t_{2g} and the e_g bands even in the insulating phase [47].

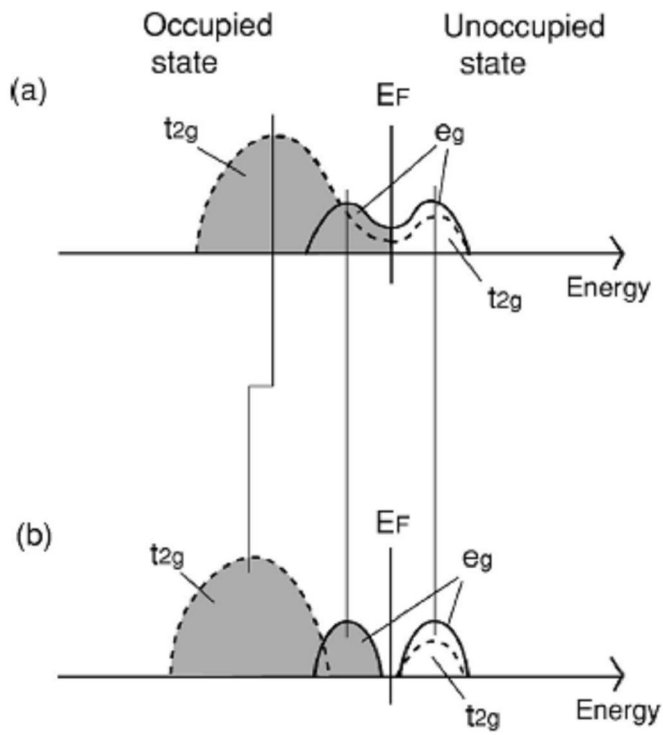

Figure 2.35: *Schematic diagram of the Co 3d band structure suggested by Takubo et al. for (a) metallic state and (b) insulating state of* $LnBaCo_2O_{5.5}$ (*Taken from* [47]).

Only a limited number of different rare-earth 112 compounds have been studied by photoemission [47]. The photoemission study carried out by K. Takubo *et al*. thus provided great motivation for the current project to understand driving force involved in temperature-dependent insulator-to-metal and spin state transitions in double perovskite cobalt oxides.

2.7.2 Magnetic Structure of $DyBaCo_2O_{5.5}$

In this section, we describe results obtained by other members of our research collaboration based at the Institute of Solid State and Semiconductor Physics (ISSSP), Minsk, Belarus and Petersburg Nuclear Physics Institute, Gatchina, Russian Federation and [1, 49], which elucidate the magnetic structure of $DyBaCo_2O_{5.5}$. The magnetic structure of a material is the ordered arrangement of magnetic spins within the crystal lattice of the solid. As $DyBaCo_2O_{5.5}$ shows magnetic behaviour due to unpaired electrons of the Co ions, it must have a particular magnetic structure. To investigate the magnetic structure, crystal structure and the magnetisation density of $DyBaCo_2O_{5.5}$, two diffraction methods were employed. To investigate the magnetic structure of $DyBaCo_2O_{5.5}$, a detwinned crystal sample of $DyBaCo_2O_{5.5}$ was used in neutron diffraction studies. A twin-free crystal sample with dimensions 4×3×0.4 mm^3 was used on 5C1 and 6T2 diffractometers at the ORPHEE reactor of the Laboratoire Leon Brillouin (CEA Saclay, France). However a twinned crystal sample was used for measurements of total oxygen content and resistivity. The oxygen content of the sample was measured by XRD (with Mo Kα radiation of wavelength λ = 0.712 Å) and the resistivity measurements were carried out by the four-probe method. At T ≈ 322 K, a structural transition from the [1]Pmmm to [2]Pmma phase of $DyBaCo_2O_{5.5}$ has already been reported [49] which is in agreement with an anomaly observed in the

---

[1]Pmmm (P2/m 2/m 2/m) space group

The first letter P stands for a primitive lattice and the symmetry elements 2/m, 2/m and 2/m are arranged in the order of crystallographic axes: **a**, **b** and **c** respectively. Each axis has a 2-fold rotation axis parallel to it and a mirror plane perpendicular to it as well.

[2] Pmma ($P2_1/m$ 2/m 2/a) Space Group

The first letter P stands for a primitive lattice, the symmetry element $2_1/m$ indicates 2_1 axis in direction **a** and a reflection plane perpendicular to **a**, 2/m represents 2-fold rotation axis parallel to **b** and a reflection plane perpendicular to **b** and 2/a indicates a 2-fold rotation axis in direction **b** and a glide plane perpendicular to **c** with glide direction **a**.

resistivity (as shown in Figure 2.36), but no anomalies were observed in the X-ray Bragg intensities.

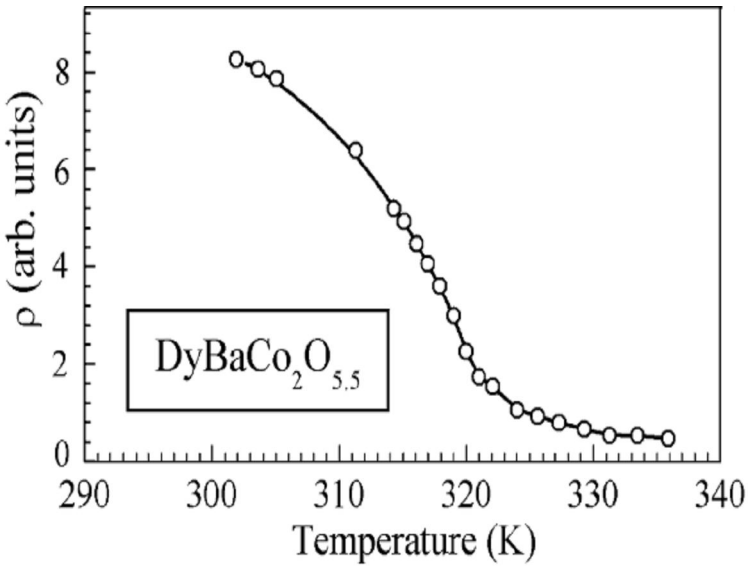

Figure 2.36: *Temperature dependent in-plane resistivity of* $DyBaCo_2O_{5.5}$ (*Taken from* [49]).

For the X-ray intensities of both the superstructure and basic Bragg reflections [49], a big temperature hysteresis of about 100 K (not shown here) was observed [49]. In the paramagnetic phase at T = 308 K, the crystal structure of $DyBaCo_2O_{5.5}$ was refined on the basis of 174 independent reflections. The results of this refined structure are given in Table 2.3.

The structural motif in the crystal structure of $LnBaCo_2O_{5.5}$ is usually given by the oxygen square pyramids and octahedra which coordinate the Co^{3+} ions and alternate along the **b** axis (Figure 2.37). Apical oxygen sites shown by black circles (in Figure 2.37) can be partially occupied. This is indicative of the fact that even at the ideal average oxygen contents of 5.5, some disorder can occur due to redistribution of oxygen among these sites. The total oxygen contents in the sample was found to be 5.50(2) but some oxygen was also found in the O'_1 position, as shown in Figure 2.37, which usually remains vacant in an ideal case.

Atom	Position	x/a	y/b	z/c	B	n
Dy	4*h*	0	0.2688 (2)	0.5	1.5(1)	1
Ba	4*g*	0	0.2475 (6)	0	0.1(1)	1
CoPy1	2*e*	0.25	0	0.254 (2)	2.7(1)	1
CoPy2	2*e*	0.25	0	0.758 (5)	2.7(1)	1
CoOc1	2*f*	0.25	0.5	0.261 (3)	2.7(1)	1
CoOc2	2*f*	0.25	0.5	0.748 (5)	2.7(1)	1
O1	2*e*	0.25	0	0.0066 (4)	1.7(1)	1.00 (2)
O′1	2*e*	0.25	0	0.5	1.7(1)	0.12 (1)
O2	2*f*	0.25	0.5	0.0052 (3)	1.7(1)	0.96 (2)
O3	2*f*	0.25	0.5	0.5014 (2)	1.7(1)	0.91 (2)
O4	4*i*	−0.0013 (1)	0	0.2964 (9)	1.7(1)	1
O5	4*j*	−0.0018 (2)	0.5	0.2627 (9)	1.7(1)	1
O61	4*k*	0.25	0.2420 (5)	0.298 (1)	1.7(1)	1
O62	4*k*	0.25	0.2434 (5)	0.710 (2)	1.7(1)	1

Table 2.3: *Atomic coordinates x/a_1, y/a_2, z/a_3, isotropic temperature factors B, and position occupancies n refined in the framework of the space group Pmma on the basis of the neutron diffraction data collected at T = 308 K from a crystal of $DyBaCo_2O_{5.50(2)}$, with 0.945(4) of the crystal volume being a single twin. The lattice parameters, the oxygen content x, and the refinement quality are: a = 7.745(6) Å, b = 7.778(6) Å, c = 7.490(5) Å; x = 5.50(2); χ^2 = 6.18* [49]. *Atom labelling is as shown in figures 2.37 and 2.39*.

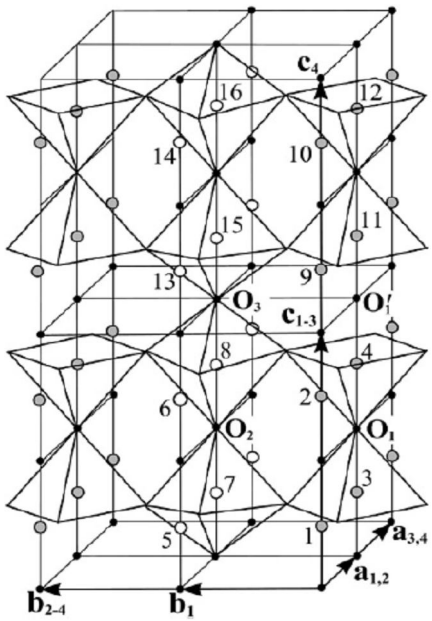

Figure 2.37: *Four unit cells, observed in $LnBaCo_2O_{5+\delta}$ at different oxygen content, degree of oxygen ordering and temperature. Cobalt ions in the pyramidal and octahedral sublattices are shown by the grey and white circles respectively and their positions are labelled by integers 1-16. Oxygen atoms in the apical positions are described by black circles. The other oxygen atoms are in the corners of the coordinating polyhedra. The Ln and Ba atoms are omitted for simplicity* [49].

As a result of neutron diffraction experiments, three magnetically-ordered phases of $DyBaCo_2O_{5.5}$ in three temperature ranges, 235 K < T < T_N (phase-I), 212 K < T < 235 K (phase-II) and T < 212 K (phase-III) where T_N = 280 K, were discovered [49] as shown in Figure 2.38. The figure shows the temperature-dependent intensity of three magnetic reflections (1, 1, 2), (1, 1, 1) and (0, 0, 1). These reflections characterise best of all the evolution of the magnetic order in $LnBaCo_2O_{5.5}$ (Ln = Dy, Tb, Gd) [49].

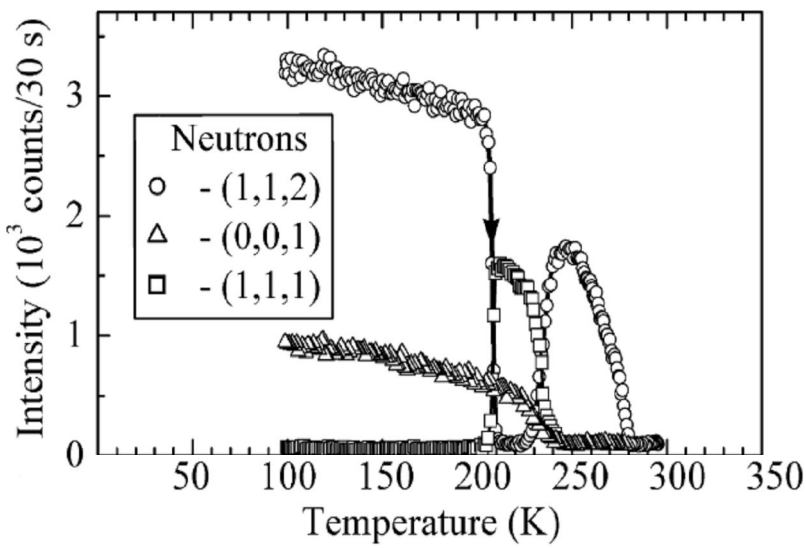

Figure 2.38: *Temperature-dependent intensity of three neutron Bragg reflections* (1, 1, 2), (0, 0, 1) *and* (1, 1, 1). *These reflections are mainly due to magnetic scattering from a twin-free crystal of* $DyBaCo_2O_{5.5}$ [49].

In Phase-I, the reflection (1, 1, 2) reveals an antiferromagnetic order in $DyBaCo_2O_{5.5.}$ The intensity of reflection (1, 1, 2) abruptly drops off to zero at 235 K. The other two reflections are invisible in this phase. For phase-II, the reflections (0, 0, 1) and (1, 1, 1) appear simultaneously and their intensity increases with decreasing temperature whilst the reflection (1, 1, 2) remains absent. In this phase, unusual magnetic properties have been observed probably due to the coexistence of two phases with different crystal and magnetic structures [50, 51]. In the last phase, the reflection (1, 1, 1) is absent and the other two reflections (1, 1, 2) and (0, 1, 1) show considerable intensity values. This phase has been ascribed to a complicated spin-state ordered antiferromagnetic structure [49].

Only the first magnetically ordered phase (the high-temperature ferrimagnetic phase) in the 235 K< T < T_N temperature range) was studied in detail and is presented here. On the basis of the data obtained from neutron diffraction studies and other related previous reports [52, 53] on $DyBaCo_2O_{5.5}$, four models of magnetic structure for $DyBaCo_2O_{5.5}$ (shown in Figure 2.40 (a-d)) have been suggested [1]. For these models, the positions of cobalt ions (Co^{3+}) in the pyramidal and octahedral sites within the four unit cells of $DyBaCo_2O_{5.5}$ are shown in Figure 2.39. The four models are in agreement with the data given in Table 2.4 because the value of the least-square residuals $\chi^2 \leq 1.6$ for all four models.

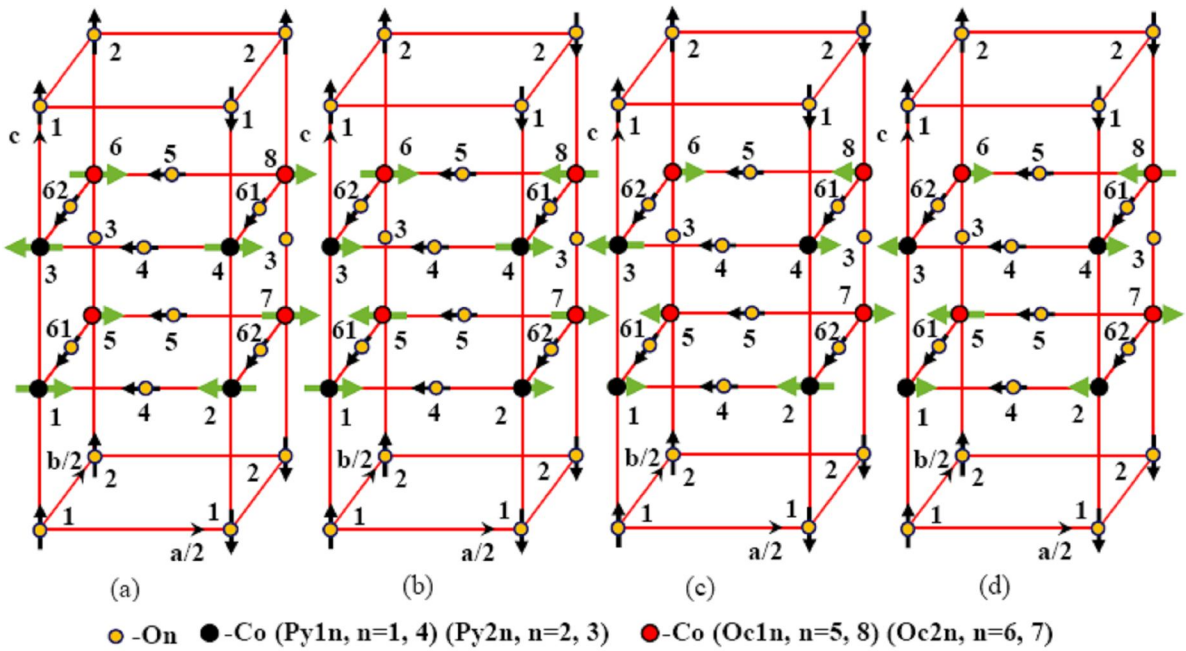

Figure 2.39: *Four models (a)–(d) of magnetic structure in $DyBaCo_2O_{5.50\,(5)}$ at T = 248 K. The green arrows show the spin arrangement and the approximate values at T = 0 corresponding to the columns (a)–(d) in Table 2.4. Displacements of the oxygen atoms from their positions in the Pmmm group are described by the black arrows. Integers 1-8 refer to the column n in Table 2.4* (*Adapted from* [1]).

n	x, y, z	M_n (μ_B)			
		(a)	(b)	(c)	(d)
1	$\frac{1}{4}$ 0 z_{Py1}	1.51(2)	1.33(1)	0.67(2)	0.48(1)
		2.63	**2.31**	**1.17**	**0.84**
2	$\frac{1}{4}$ 0 z_{Py2}	−1.41(3)	0.26(1)	−2.27(1)	−0.57(2)
		−2.45	**0.45**	**−3.94**	**−0.99**
3	$\frac{3}{4}$ 0 $-z_{Py2}$	−1.41(3)	0.26(1)	−2.27(1)	−0.57(2)
		−2.45	**0.45**	**−3.94**	**−0.99**
4	$\frac{3}{4}$ 0 $-z_{Py1}$	1.51(2)	1.33(1)	0.67(2)	0.48(1)
		2.63	**2.31**	**1.17**	**0.84**
5	$\frac{1}{4}$ $\frac{1}{2}$ z_{Oc1}	0.26(1)	−1.44(3)	−0.57(1)	−2.30(1)
		0.45	**−2.51**	**−0.99**	**−3.99**
6	$\frac{1}{4}$ $\frac{1}{2}$ z_{Oc2}	1.33(2)	1.50(2)	0.49(2)	0.66(1)
		2.31	**2.61**	**0.85**	**1.15**
7	$\frac{3}{4}$ $\frac{1}{2}$ $-z_{Oc2}$	1.33(1)	1.50(2)	0.49(2)	0.66(1)
		2.31	**2.61**	**0.85**	**1.15**
8	$\frac{3}{4}$ $\frac{1}{2}$ $-z_{Oc1}$	0.26(1)	−1.44(3)	−0.57(1)	−2.30(1)
		0.45	**−2.51**	**−0.99**	**−3.99**
$\sum[M_n(248\ \mathrm{K})]/8$		0.42	0.41	−0.42	−0.43
χ^2		1.54	1.62	1.59	1.50

Table 2.4: *Four possible models of the Co^{3+} spin ordering in the high-temperature magnetically ordered phase I. There are two lines for every atom, with the first one giving the experimental moment values at T = 248 K and the second (bold numbers)-their approximate values extrapolated to T = 0 following Taskin et al.* [54]. *The spontaneous moment due to ferrimagnetism at 248 K is given by Σ [Mn (248 K)]/8* (*Taken from* [1]).

Models (c) and (d) describe a G-type magnetic structure (in which each magnetic ion is antiferromagnetically coupled to its six nearest neighbours), as shown in Figure 2.40, and comprise a combination of the low spin (LS, S = 0) and the high spin (HS, S = 1) states whereas (a) and (b) have a combination of the LS (S = 0) and the intermediate spin (IS, S = 1) states, probably with a contribution arising from hybridization with the O 2p level, and is approximately G-type. The G-type and approximately G-type magnetic structures are shown in Figure 2.40.

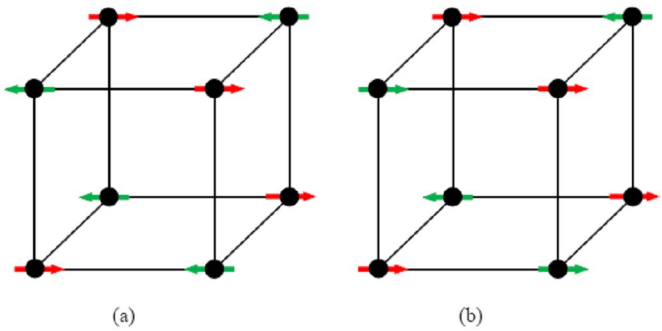

Figure 2.40: *Magnetic structure of $DyBaCo_2O_{5.50\,(5)}$ at T = 248 K* (*a*) G-type (*b*) approximately G-type [1].

Additional experiments on spin-density mapping and full polarization analysis of the data are required to make a choice between the above described four models for the high-temperature magnetically-ordered phase of Dy-112.

2.8 Magnetic and Structural Behaviour of $LnBaCo_4O_{7+\delta}$ (Ln = rare- earth) - Ln-114

Transition metal oxides form a number of geometrically frustrated spin systems in compounds such as pyrochlores, oxide spinels, jarosites etc. A geometrically frustrated spin system is disordered at all temperatures and acquires no Curie point [54-56]. Geometric frustration basically arises from interactions of spins that favour their anti-alignment and involve fully connected units comprising three or more spins that cannot be mutually anti-aligned [57]. The kagomé net is considered to be one of the commonest structural motifs linked with geometric frustration in such compounds [55, 58-63]. Specific examples of compounds containing Kagomé nets are $SrCr_{9x}Ga_{12-9x}O_{19}$ [64-66], $CaBaCo_4O_7$ [63] and $YbBaCo_2O_7$ [67]. $SrCr_{9x}Ga_{12-9x}O_{19}$ contains Kagomé sheets of Cr^{3+} with a triangular layer of Cr^{3+} sandwiched between the sheets and connecting them to form Cr^{3+} tetrahedra whereas in $CaBaCo_4O_7$ and $YbBaCo_4O_7$, the Kagomé sheet is made up of cobalt ions in a similar fashion.

$LnBaCo_4O_7$ (Ln-114) where Ln = Y, Tb, Dy, Ho, Er, Tm, Yb, Lu was initially reported by Valldor *et al*. [68] and Bychkov *et al.* [69]. Valldor *et al.* [68] and Tsipis *et al.* [70] in their

neutron diffraction and magnetic studies revealed that Ln-114 (Ln = Y) is not geometrically frustrated but rather antiferromagnetically ordered with a ferromagnetic component. However, Tsipis *et al.* [70] proposed a spin-glass state at low temperature for Y-114.

Thermogravimetric analysis (TGA) analysis of as-grown samples of Yb-114 shows that the samples are oxygen hyperstoichiometric [67, 71] *i.e.* they exhibit high oxygen diffusion and take up additional oxygen in interstitial positions. The excess oxygen content in the as-prepared samples of Yb-114 is in agreement with the reports given by Tsipis *et al.* [70]. The excess oxygen from the samples can be removed by thermal treatment in a nitrogen atmosphere [70, 72].

Figure 2.41 (a) shows temperature-dependent DC magnetisation measurements for Yb-114, undertaken by A. Huq *et al.* [67], with zero-field cooling (ZFC) and field cooling (FC) in 1 T. Two special features at T = 80 K and 175 K are of particular interest. The former corresponds a transition into a long-range ordered antiferromagnetic state because the ZFC data are dominated by a paramagnetic response from the Yb^{3+} ions (J = 7/2). The anomaly at T = 175 K is not associated with a magnetic transition but belongs to a structural transition and the inset of Figure 2.41 (a) reveals that this feature shows hysteresis. The anomaly at T = 175 K was also seen in the electrical transport measurements (not shown here) where the resistivity of the sample rises by an order of magnitude across the transition with thermal hysteresis. The FC curve differs markedly from that for ZFC because at 80 K, the magnetisation shows an abrupt change.

Isothermal magnetization measurements at T = 25 K, shown in Figure 2.41 (b), provide an additional insight on the high-field state. At T = 25 K, M (H) is linear and reversible for H_c < 2.5 T which is considered to be a characteristic of the AFM state. A change in slope occurs when the value of the field is increased beyond H_c (25 K) = 2.5 T. This transition is irreversible because it reduces the field in the sample after exceeding H_c and the compound enters a field-induced state which persists through additional magnetic field cycling. The heating of the sample well above 80 K followed by ZFC turns it back to the AFM state. The inset of Figure 2.41 (b) shows that H_c strongly depends upon temperature, changing from 7.5 T at 2 K to 0.05 T at 75 K.

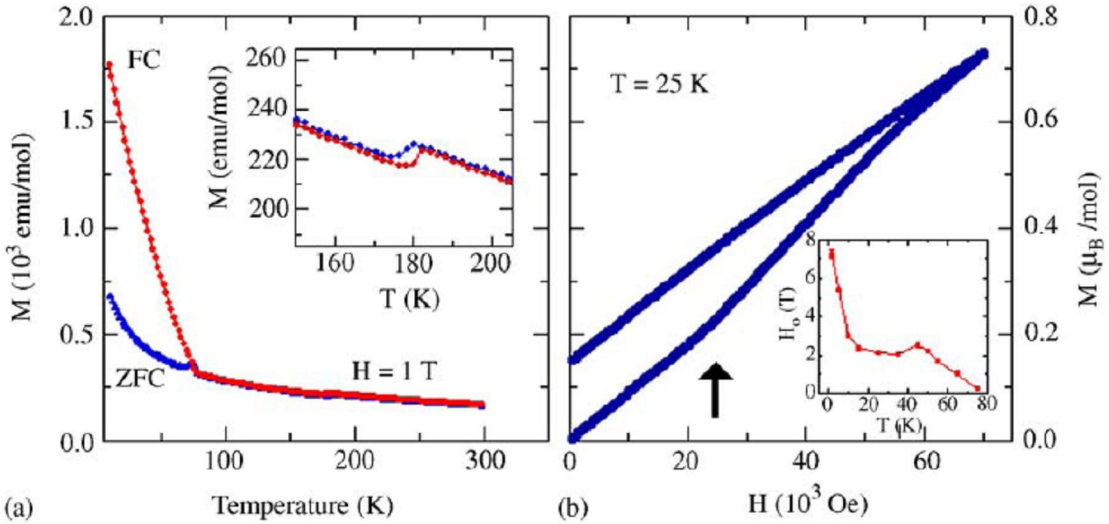

Figure 2.41: (*a*) *Magnetization as a function of temperature for Yb-114 measured on warming in 1T. ZFC = zero-field cooled; FC = field cooled. Inset: Detail of the temperature region near the structural phase transition.* (*b*) *Isothermal magnetization measured at 25 K. The arrow marks Hc, the onset of the irreversible field-induced transition. Inset:* H_c *as function of T. In each case, the sample was ZFC to the measuring temperature from 150 K then the field was applied* [67].

Data related to Ba-O bond distances in $YbBaCo_4O_7$ [67] indicate that there are only three Ba-O contacts less than 3 Å (2.809 Å) and rest of the nine contacts are (three of each) 3.119, 3.147 and 3.456 Å, which cannot realistically be classified as Ba-O bonds. A mean Ba-O distance ($d_{Ba\text{-}O}$) of 3.13 Å convincingly suggests that the O environment does not satisfy the bonding requirements of the large Ba^{2+} ion [67]. A similar behaviour of Ba^{2+} has been observed recently for $CaBaCo_4O_7$ [63]. Yb-114 is geometrically frustrated at room temperature and it undergoes a structural phase transition at 175 K from trigonal to orthorhombic. This is thought to be driven by the drastically underbonded Ba^{2+} ion seeking to satisfy its bond valence requirements [67]. No photoemission studies have been reported on $LnBaCo_4O_{7+\delta}$. This is carried out for the first time in the current project and discussed later in Chapter 6.

2.9 Magnetic Characterisation for $LnBaCo_4O_{7+\delta}$ (Ln = Yb, Tb, Lu) - Ln-114 single crystals

2.9.1 Super Conducting Quantum Interference Device (SQUID) Magnetometery

When two constant-current-carrying Josephson junctions (thin insulating layers sandwiched between superconducting layers), shown in Figure 2.42, are connected in parallel, there is a quantum interference between the electron wave functions. This gives rise to an oscillatory variation in the voltage across the terminals with magnetic flux linking the circuit. This phenomenon is the working principle for a SQUID (Superconducting Quantum Interference Device) as a high-resolution flux counting device for the characterisation of magnetic materials. When a sample is moved through the superconducting coils, an electric current is induced in the detection coils. The detection coils and the SQUID input coils make a closed superconducting loop. Therefore, any change produced is detected and is proportional to the change in magnetic flux. SQUID magnetometers are highly sensitive devices and can be used to measure changes in flux down to a micro flux quantum of 10^{-21} Wb. The flux associated with a Josephson junction is quantised by:

$$\Phi_0 = \frac{h}{2e} \cong 2.07 \times 10^{-15} tesla.m^2, \qquad \text{Equation 2.22}$$

where h is Planck's constant, e is charge on electron and the quantity Φ_0 is termed the flux quantum.

The nominal resolution of the SQUID is 1 f T.

Pure niobium or lead alloy with 10 % gold or iridium is used as the superconducting material for SQUIDs. To maintain superconductivity, liquid helium is used. The entire device is operated within a few degrees of absolute zero.

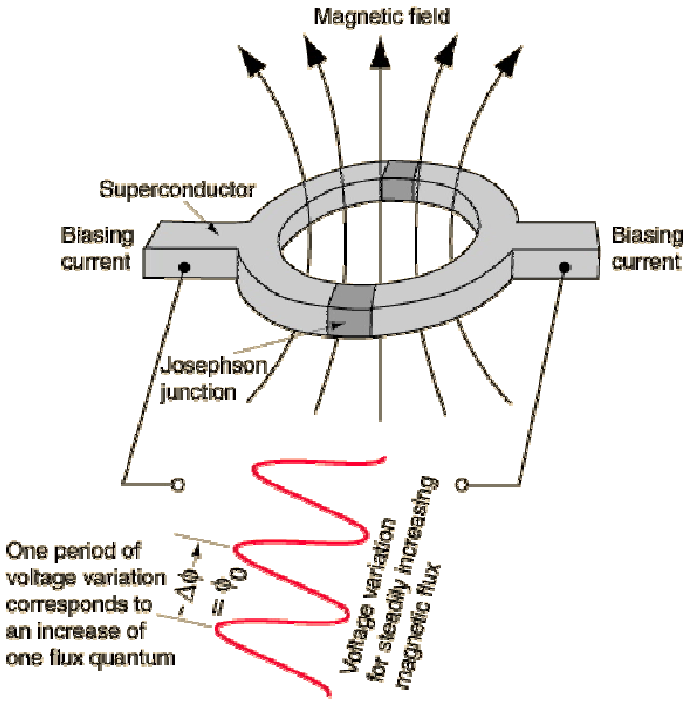

Figure 2.42: *Two constant-current-carrying Josephson junctions connected in parallel* (*Taken from* [73]).

A SQUID Magnetic Property Measurement System (MPMS) is used to measure the magnetic properties of materials as a function of magnetic field and temperature. The MPMS can measure AC and DC magnetisations, susceptibilities and magnetoresistance for both powder and single crystal samples. Using a SQUID magnetometer, one can also measure the Hall Effect as a function of magnetic field and temperature. Due to the high sensitivity of the instrument, measurements on small samples (a few mg) are possible.

The magnetic properties are derived from zero-field-cooled (ZFC) and field-cooled (FC) magnetisations as a function of temperature. The temperature-dependent ZFC-FC curves provide information about the intrinsic energy barrier distribution in the magnetic materials. The suitability of a magnetic material for a particular application is mainly investigated from its magnetic hysteresis analysis.

2.9.2 The SQUID Quantum Design MPMS Facility at the University of Manchester

Magnetic characterisation for $LnBaCo_4O_{7+\delta}$ (Ln = Yb, Tb, Lu) single crystals, grown by the overstoichiometric flux melt technique, was performed in the 1.8 – 300 K temperature range under magnetic fields of up to 6 T using a Quantum Design MPMS XL magnetometer (Figure 2.43.) at the University of Manchester. Temperature-dependent DC magnetisation and magnetic hysteresis curves were recorded for as-grown single crystal samples of $TbBaCo_4O_{7.2}$ and $LuBaCo_4O_{7.2}$. However for $YbBaCo_4O_7$ crystal samples (which were thermally treated in flowing nitrogen and oxygen at T = 900 °C and T = 800 °C respectively for about 20 hours after their growth), only temperature-dependent DC magnetisation measurements were undertaken.

The MPMS XL system is equipped with a SQUID which is based on superconducting loops containing Josephson junctions. The main components of a typical SQUID magnetometer are: a superconducting magnet, a pick-up or superconducting detection coil, a SQUID and a superconducting magnetic shield. The magnetic signal produced by the movement of the sample is detected through the superconducting pick-up coil which is joined to the SQUID device and positioned away from the sample in a liquid helium bath. This device functions as a magnetic-flux-to-voltage converter. When the sample moves up and down, it generates an alternating magnetic flux in the pick-up coil which corresponds to an alternating output voltage in the SQUID device. This voltage is then amplified and measured by the magnetometer electronics. The output signal is proportional to the magnetic moment of the sample which is ultimately magnetised by a magnetic field generated by the superconducting magnet. To load a sample in the device, it is first placed into a gelatin capsule (which gives a weak diamagnetic signal). The capsule is filled with cotton to avoid any slip of the sample during the measurement. The capsule is then placed in a plastic straw and attached to the MPMS sample probe (Figure 2.44) using sticking tape. One must make sure that the straw is properly attached to avoid any movement during the measurement.

Figure 2.43: *A Quantum Design MPMS XL SQUID magnetometer at the University of Manchester* (*Taken from* [74]).

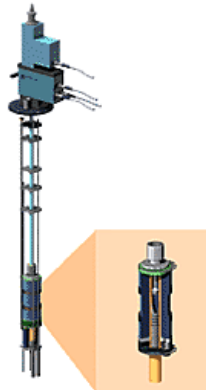

Figure 2.44: *MPMS sample probe* (*Taken from* [74]).

2.9.3 Magnetisation: Results and Discussion

Figure 2.45 shows ZFC and FC temperature-dependent magnetisation curves for two differently treated single crystal samples of $YbBaCo_4O_{7+\delta}$ measured in a fixed magnetic field (H) of 600 Oe and parallel to the (001) plane. Figure 4 (a) and (c) depict magnetisation curves for samples annealed after growth for about 20 h in flowing nitrogen at T = 900 °C and in flowing oxygen at T = 800 °C respectively. Expanded views of panels (a) and (c) are displayed in panels (b) and (d) respectively. The magnetisation increases as the temperature decreases. One can see a pronounced peak in the ZFC curves at the transition to the AF state at 25 K. This is particularly marked in the case of the nitrogen-treated sample, which shows the decrease in magnetisation towards 0 K expected for an antiferromagnet. The magnitude of the magnetisation at the AF transition point is increased by nitrogen-annealing. This is indicative of the fact that oxygen stoichiometry controls the structural, the magnetic and the electronic properties of cobaltites and variation in the oxygen content (reduced by nitrogen treatment) of the sample affects these properties [1]. A neutron diffraction study on a powder sample of $YbBaCo_4O_7$ revealed a structural phase transition at 175 K from trigonal to monoclinic on cooling [67]. No change in the magnetisation is found at this temperature. However, one can suppose that the inflection points (T_s), in the 260-280 K temperature range, may correspond to this structural phase transition. These magnetisation results differ significantly from those reported by Huq *et al.* [67] on powder

samples of $YbBaCo_4O_7$. The transition to the AF state is much more pronounced and the low temperature ZFC and FC dependences do not show a sharp increase in magnetisation (except perhaps in Figure 2.45(c)).We also did not observe a spin-flip transition at 25 K. Nevertheless, a confirmation of long range magnetic ordering of cobalt spins at lower temperatures in these samples, even in off- stoichiometric $YbBaCo_4O_{7+\delta}$ single crystal samples, can be made.

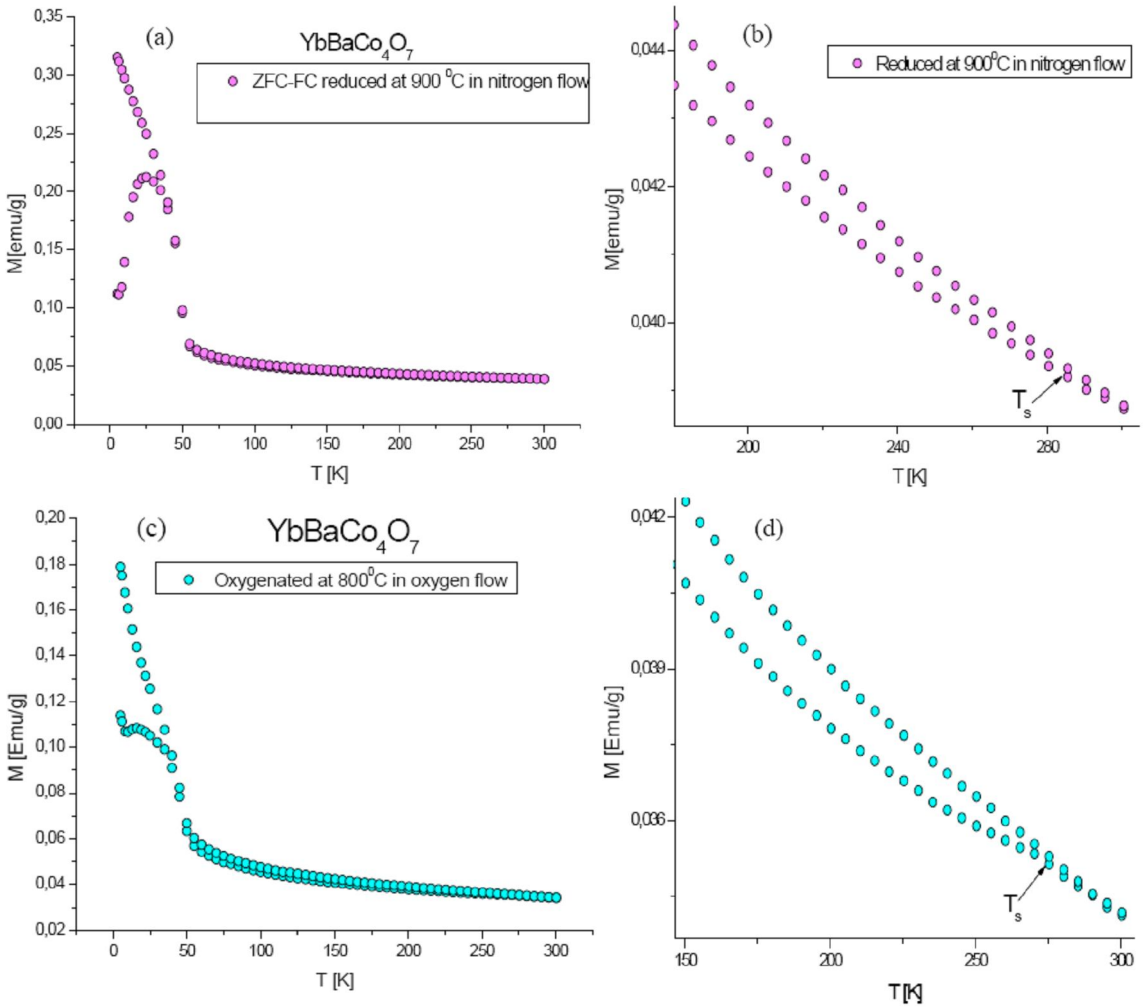

Figure 2.45: *Zero-field-cooled (ZF) and field-cooled (FC) temperature-dependent magnetisation for $YbBaCo_4O_{7.2}$ measured in a fixed magnetic field (H) of 600 Oe and parallel to the (001) plane:* (*a*) *the crystal sample was thermally treated in flowing nitrogen at T = 900 ℃ for about 20 hours after growth* (*c*) *the crystal sample was oxygenated at T = 800 ℃ for about 20 hours after growth (d). (b) and (d) are expended views of (a) and (c) respectively.*

Figure 2.46 displays zero-field-cooled (ZFC) and field-cooled (FC) magnetisation curves as a function of temperature for an as-grown $TbBaCo_4O_{7+\delta}$ (δ = 0.2) single crystal sample measured under external fields of 600 Oe and 50 Oe parallel and perpendicular to the c-axis. The oxygen content of the sample was measured by iodometric titration technique. The magnetisation curves recorded at 600 Oe reveal comparatively larger magnetisation at low temperatures. A pronounced peak in the ZFC curves at the transition to the AF state can be seen at 25 K. One can notice that the magnetisation is slightly larger for H || (001).

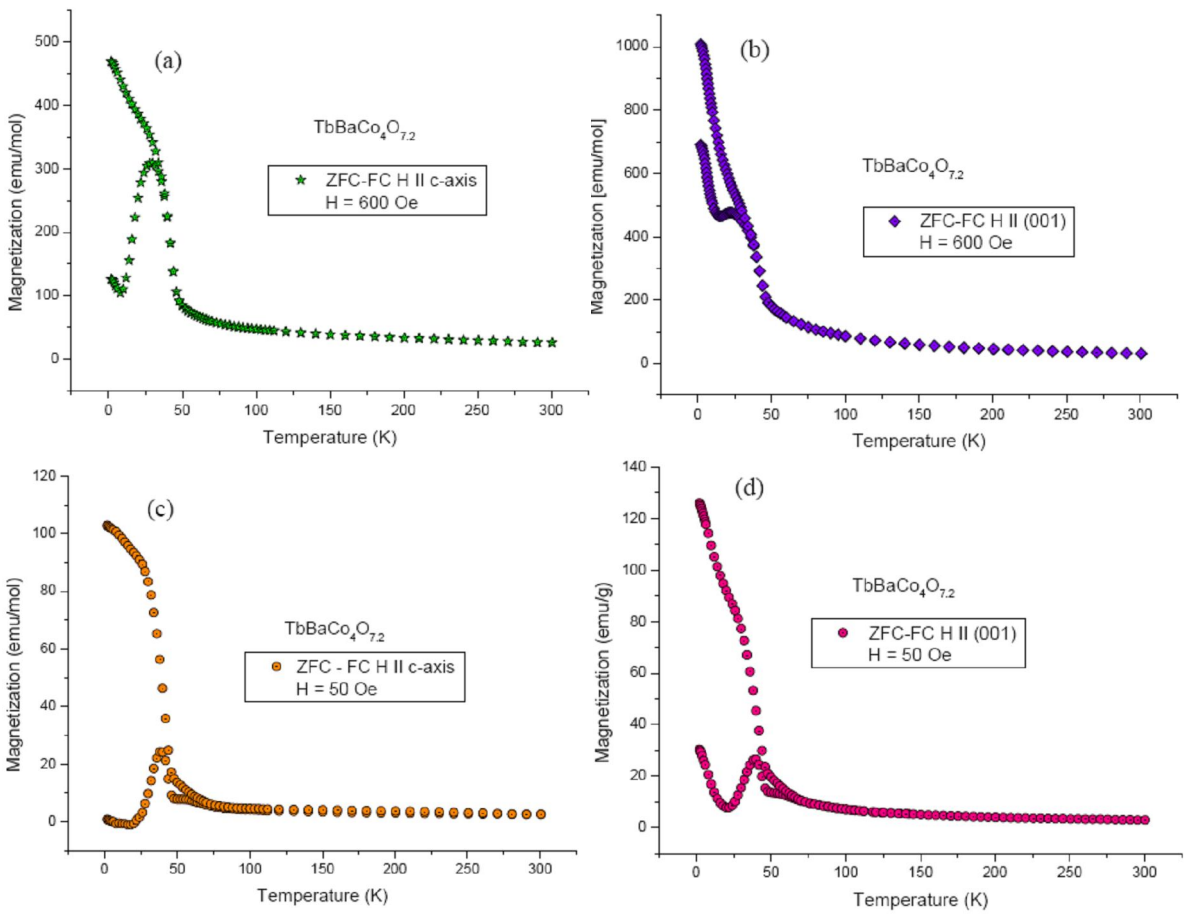

Figure 2.46: *Temperature-dependent magnetisation for $TbBaCo_4O_{7.2}$ measured at different values and orientations of the external magnetic field (H): (a) Zero-field-cooled (ZFC) and field-cooled (FC) magnetisation curves at H = 600 Oe and parallel to the c-axis, (b) ZFC and FC magnetisation curves at H = 600 Oe and parallel to the (001) plane, (c) ZFC and FC magnetisation curves at H = 50 Oe and parallel to the c-axis, (d)) ZFC and FC magnetisation curves at H = 50 Oe and parallel to the (001) plane.*

Figure 2.47 shows magnetic hysteresis curves for the same $TbBaCo_4O_{7+\delta}$ single crystal sample recorded at T = 20 K parallel and perpendicular to the c-axis. Figure 2.47 shows spontaneous magnetisation with coercive field strength H_c. Magnetic hysteresis data are consistent with the magnetisation results and undoubtedly reveal the presence of stable AF ordering in $TbBaCo_4O_{7+\delta}$ under applied fields $H < H_c$ and a weak ferromagnetic component at fields higher than H_c.

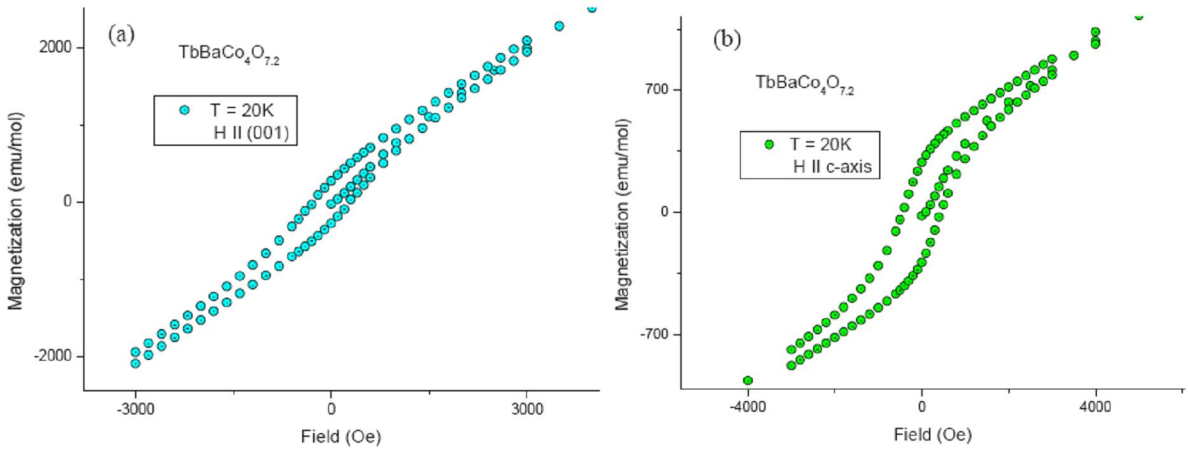

Figure 2.47: *Magnetic hysteresis curves for $TbBaCo_4O_{7.2}$ measured at T = 20 K*: (a) *with H || (001)*, (b) *with H || c-axis*.

Figure 2.48 ((a), (b)) shows temperature-dependent zero-field-cooled (ZFC) and field-cooled (FC) magnetisation curves for an as-grown $LuBaCo_4O_{7+\delta}$ (δ = 0.2) single crystal sample recorded under a fixed external field (H) of 600 Oe parallel and perpendicular to the c-axis. Magnetisation measurements, under the same orientation and magnitude of the magnetic field, were also made on warming and cooling the sample. The results are displayed in the corresponding panels (c) and (d) of Figure 2.48.

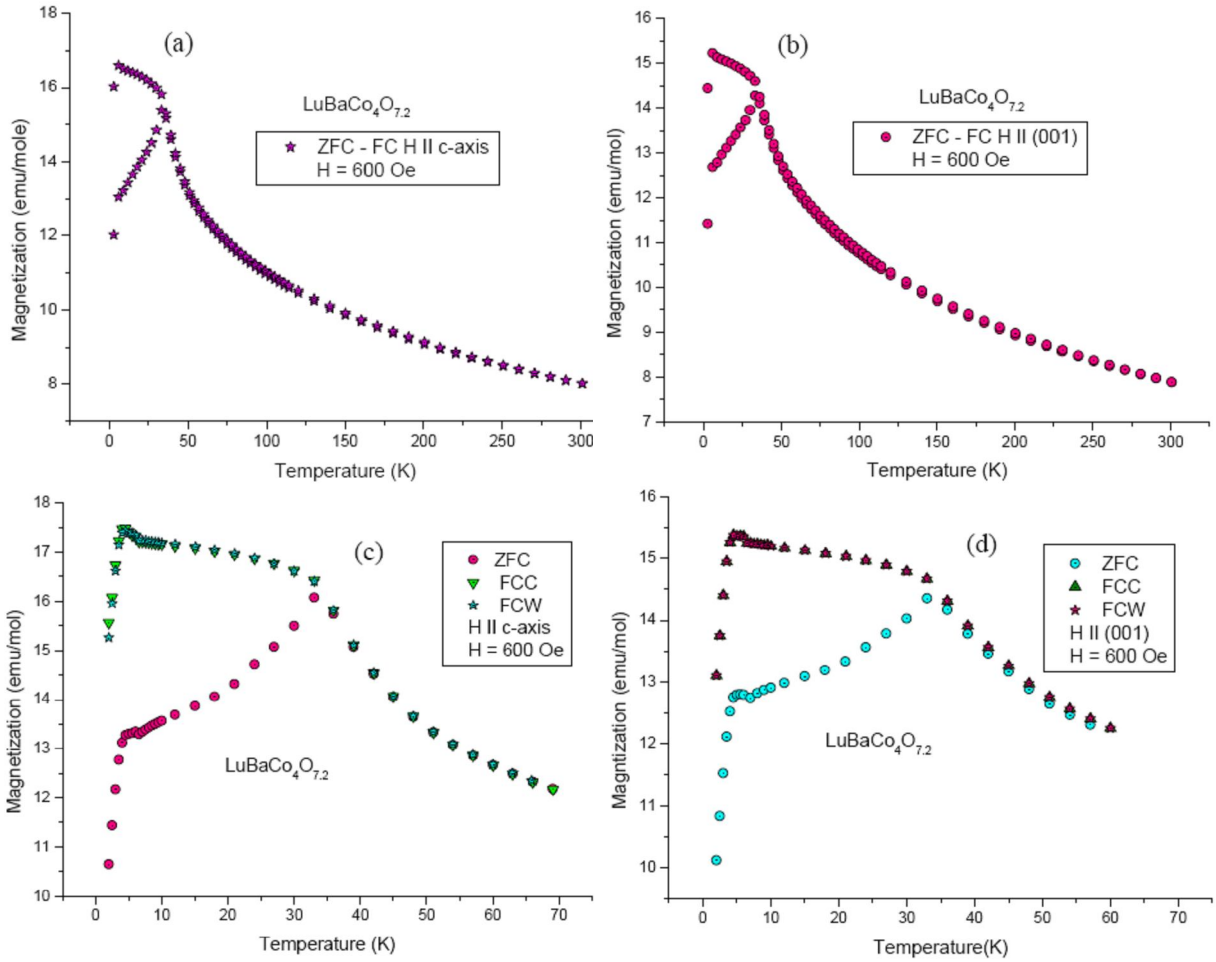

Figure 2.48: *Temperature-dependent magnetisation for $LuBaCo_4O_{7.2}$ showing possible chiral-glass-like behaviour measured at H = 600 Oe:* (*a*) *Zero-field-cooled* (*ZFC*) *and field-cooled* (*FC*) *magnetisation curves with external field* (*H*) || *c - axis,* (*b*) *ZFC and FC magnetisation curves with H* || (*001*), (*c*) *ZFC, field-cooled on decreasing temperature* (*FCC*) *and field-cooled on warming* (*FCW*) *magnetisation curves with H* || *c - axis, (d) ZFC, FCC and FCW magnetisation curves with H* || (*001*).

One can see a pronounced peak in the ZFC curves at the transition to the AF state at 34 K. In the low temperature regime, T < 70 K, the magnetisation shows a particular type of behaviour which may be indicative of a long range antiferromagnetic ordering in $LuBaCo_4O_{7.2}$. This is termed the chiral-glass magnetic behaviour and has been observed in many geometrically frustrated systems [75-79]. A chiral-glass-like behaviour takes place when the spin reflection symmetry is broken without disturbing spin-rotation symmetry. Previous magnetisation measurements on powder samples and single crystals of

$LnBaCo_4O_{7+\delta}$ (Ln = Y, Dy, Ho, Lu, Yb) clearly show spin-glass- like behaviour [60, 80, 81]. However, the crystal structure of this material indicates a 2D critical dimensionality which should not allow a spin-glass state [80]. Therefore, this family of compounds presents a good candidate for a chiral-glass state with ordered local chirality as predicted theoretically by Kawamura [80]. Figure 2.49 displays magnetic hysteresis measurements for the same $LuBaCo_4O_{7.2}$ single crystal sample recorded at temperatures of 2 K and 20 K under an external magnetic field parallel and perpendicular to the c-axis.

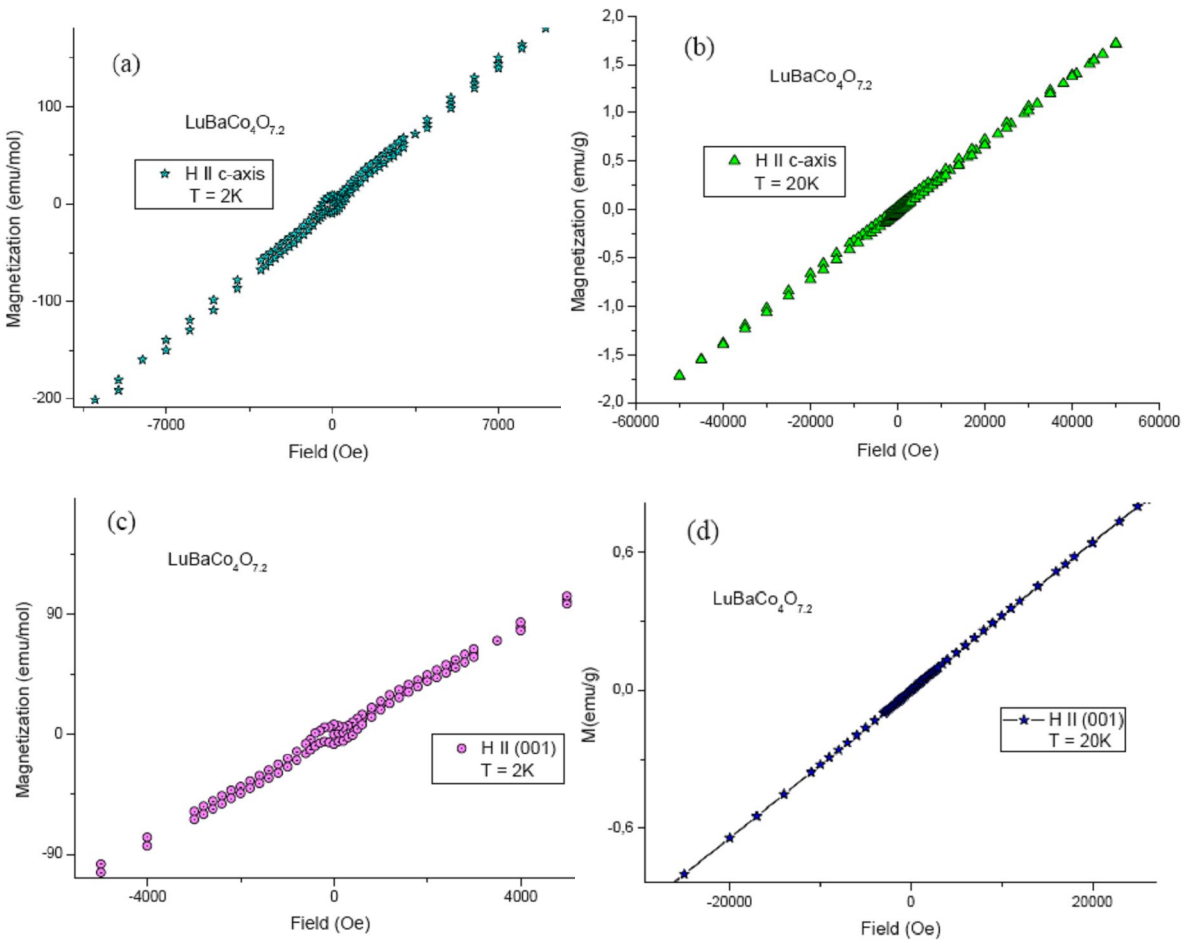

Figure 2.49: *Isothermal magnetisation M (H) for single crystal $LuBaCo_4O_{7.2}$ measured at different orientations of the external magnetic field: (a) and (c) reveal hysteresis curves at fields of several hundred Oe and T = 2 K with H || c-axis and H || (001) respectively, (b) and (d) show chiral-glass-like behaviour at T = 20 K with H || c - axis and H || (001) respectively.*

The shapes of both hysteresis loops look unusual which may indicate the chiral-glass-like behaviour of the material at low temperatures.

There is still a poor understanding of these findings. Polarised neutron diffraction and AC magnetic susceptibility experiments, at different frequencies, are scheduled by our collaborators in future. These experiments are designed to confirm the chiral-glass-like state, determine the correlation lengths and chirality parameters of short range magnetic ordering at different temperatures, and study the possible AF ordering at 5 K in the $LnBaCo_4O_{7+\delta}$ geometrically frustrated magnetic system.

2.10 Conclusions

High quality single crystal samples of $GdBaCo_2O_{5.5}$ and $DyBaCo_2O_{5+\delta}$ were prepared in Minsk by a newly-developed approach. Large single crystals for detailed structural and electronic band structure investigations are required. After detailed study of the phase equilibria in the La-Ba-Co-O system and primary crystallisation fields for Dy-112, a new approach to flux growth involving reduction of viscosity of the flux melt has been developed to grow large single crystals of $LnBaCo_2O_{5+\delta}$ (Ln = Gd, Dy) at the Institute of Solid State and Semiconductor Physics (ISSSP) Minsk in which the corundum crucible was replaced by an MgO crucible to minimise corrosion. The reduction in corrosion of the crucible helped to initiate a limited nucleation under a variable/reversible temperature gradient [77]. A post-growth treatment for $LnBaCo_2O_{5+\delta}$ samples, by controlling oxygen stoichiometry close to $\delta = 0.50$ through oxygen annealing, is necessary to study a marked MI transition in the compounds as discussed in detail later in Chapter 5.

It can be concluded from the neutron diffraction data obtained on the single crystal sample of $DyBaCo_2O_{5.5}$ for the high temperature range of the ferrimagnetic phase, the highest magnetic moment arises from a combination of the low spin (LS, $S = 0$) and the high spin (HS, $S = 2$) states. This is the case for the cobalt ions $n = 2, 3$ in model (c) and $n = 5, 8$ in model (d).

On the basis of the data obtained on $DyBaCo_2O_{5.5}$, four models can be proposed which describe equally well the magnetic structure for the high-temperature magnetically ordered phase of Dy-112. Two of them describe a G-type magnetic structure showing a combination of the low LS and HS states, and the other two represent a combination of the

LS and IS states, and are approximately G-type. Additional experiments on spin-density mapping and full polarization analysis of the data are required to choose between these four models.

Magnetic characterisation results, for $LnBaCo_4O_{7+\delta}$ (Ln = Yb, Tb, Lu) single crystals, confirm long- range magnetic ordering of cobalt spins at lower temperatures in nitrogen-annealed, oxygen-annealed and even in off- stoichiometric $YbBaCo_4O_{7+\delta}$ single crystal samples. We did not observe a spin-flip transition at 25 K. These magnetisation results are significantly different from those reported by Huq *et al.* [67] on powder samples of $YbBaCo_4O_7$ and show much more marked AF transition. Our magnetic hysteresis data recorded at T = 20 K reveal the presence of stable AF ordering in $TbBaCo_4O_{7+\delta}$ under applied fields $H < H_c$ and a weak ferromagnetic component at fields higher than H_c. The magnetic hysteresis data on $LuBaCo_4O_{7.2}$ indicate the possible chiral-glass-like behaviour of the material at low temperatures. There is still a poor understanding of these findings. Further studies are required to improve understanding about these findings.

References

[1] S. N. Barilo, S. V. Shiryaev, G. L. Bychkov, A. S. Shestak, W. R. Flavell, A. G. Thomas, H. M. Rafique, Y. P. Chernenkov, V. P. Plakhty, E. Pomjakushina, K. Conder and P. Allenspach, *J.Crystal Growth* , **310**,1867 (2008).

[2] L. S. Dent Glasser, *Crystallography and its Applications*, Van Nostrand Reinhold Company Limited (1977).

[3] M. M. Woolfson, *An introduction to X-Ray Crystallography*, Cambridge University Press (1970).

[4] M. F. C. Ladd, R. A. Palmer, *Structure Determination by X-ray Crystallography*, Plenum Press (1994).

[5] R. J. D. Tilley, *Understanding Solids*: *The Science of Materials*, John Wiley and Sons, Ltd. (2004).

[6] C. C .Wilson, *Single Crystal Neutron Diffraction from Molecular Materials*, World Scientific Publishing Co. Pte. Ltd.(2000).

[7] J. C. Anderson, K.D. Leaver, *Material Science*, Butler and Tanner Ltd (1969).

[8] http://serc.carleton.edu/research_education/geochemsheets/techniques/SXD.html

[9] http://inac.cea.fr/Images/astImg/173_1.jpg

[10] V. F. Sears, *Methods of Experimental Physics*, vol. 23, eds. K. Sköld and D. L. Price, Part A, Academic Press, London (1986).

[11] G. M. Kalvius and Robert S. Tebble, *Experimental Magnetism*,Volume1, John Wiley & Sons (1979).

[12] E. H. Kisi and C. J. Howard, *Applications of Neutron Power Diffraction*, Oxford Science Publication, Oxford (2008).

[13] W. R. Runyan and T. J. Shaffner, *Semiconductor Measurements and Instrumentation*, 2nd edition, The McGraw-Hills Companies, Inc. (1975).

[14] Z. X. Zhou, S. McCall, C. S. Alexander, J. E. Crow, P. Schlottmann , S. N. Barilo, S. V. Shiryaev, G. L. Bychkov and R. P. Guertin , *Phys. Rev. B* ,**70**, 24425 (2004).

[15] K. Byrappa, H. Klapper, T. Ohachi and R. Fornari, *Crystal Growth of Technologically Important Electronic Materials*, Allied Publishers PVT. Limited (2003).

[16] A. F. Orchard, *Magnetochemistry*, Oxford University Press (2003).

[17] W. E. Pickett and D. J. Singh, *Phys. Rev. B*, **53**, 1146 (1996).

[18] H. L. Hu, H. C. Sohn and K. M. Krishnan, *Phys.Rev.Lett*,**79**, 3230 (1997).

[19] J. Zaanen, G. A. Sawatzky and J. W. Allen, *Phys. Rev. Lett.*, **55**,418 (1985).

[20] M. A. Korotin, S. Y. Ezhore, I. V. Soloyere, V. I. Anismore, D. I. Khomski and G.A. Sawatzky, *Phys. Rev. B*, **54**, 5309 (1996).

[21] S. Yamaguschi, H. Taniguchi, H. Takagi and T. Arima, *J. Phys. Soc. Jpn*. **64,** 1885 (1995).

[22] K. Asai, A. Toneda, O. Yokokura, J. M. Tranquada, G. Shirane and K. Kohn, *J. Phys. Soc. Jpn.*, **67**, 290 (1998).

[23] T. Saitoh, T. Mizokawa, A. Fujimori, M. Abbate, Y. Takeda and M. Takano, *Phys. Rev. B*, **56**,1290 (1997).

[24] W. R. Flavell, A. G. Thomas, D. Tsoutsou, A. K. Mallick, M. North, E. A. Seddon, C. Cacho, A. E. R. Malins, S. Patel, R. L. Stockbauer, R. L. Kurtz, P. T. Sprunger, S. N. Barilo, S. V. Shiryaev and G. L. Bychkov, *Phys. Rev. B*, **70**, 224427 (2004).

[25] M. Takahashi and J .I. Igarashi, *Phys. Rev*, **55**, 13557(1997).

[26] I. Soloyev, N. Hamada and K. Terakura, *Phys. Rev. B*, **53**, 7158 (1996).

[27] T. Mizokawa and A. Fujimori, *Phys. Rev. B*, **54**, 5368 (1996).

[28] H. Takahashi, F. Munakata and M. Yamanaka, *Phys. Rev. B*, **53**, 3731 (1996).

[29] L. Siurakshina, B. Paulus and V. Yushankhai, *Eur. Phys. J. B.*, **63**, 445 (2008).

[30] W. S. Kim, E.O. Chi, H.S. Choi, N.H. Hur, S.J. Oh, H.C. Ri, *Solid State Commun*.,**116**, 609 (2000).

[31] M. N. Baibich, J. M. Broto, A. Fert, F. Nguyen van Dau, F. Petroff, P. Eitenne, G. Creuzet, A. Friedrich and J. Chazelas, *Phys. Rev. Lett.*, **61**, 2472 (1988).

[32] P. Gruenberg, R. Schreiber, Y. Pang, M.B. Brodsky and H. Sowers, *Phys. Rev. Lett.*, **57**, 2442 (1986).

[33] A. K. Kundu, B. Raveau1, V. Caignaert, E. Rautama and V. Pralong, *J. Phys.: Condens. Matter*, **21**, 56007 (2009).

[34] V. Sikolenko, V. Efimov, E. Efimova, A. Sazonov, C. Ritter, A. Kuzmin and I. Troyanchuk, *J. Phys.: Condens. Matter*, **21**, 436002 (2009).

[35] A. Bharathi, P. Yasodha, N. Gayathri, A. T. Satya, R. Nagendran, N. Thirumurugan, C. S. Sundar and Y. Hariharan, *Phys. Rev. B*, **77**, 85113 (2008).

[36] A. Maignan, C. Martin, D. Pelloquin, N. Nguyen, and B. Raveau, *J. of Solid State Chem.*,**142**, 247 (1999).
[37] C. Frontera, J. L. García-Muñoz and A. E. Carrillo, *Phys. Rev. B*,**74**, 054406 (2006).
[38] C. Frontera, J. L. García-Muñoz, A. Llobet, and M. A. G. Aranda, *Phys. Rev. B*, **65**,180405 (2002).
[39] M. Respaud, C. Frontera, J. L. Garcia-Munoz, Miguel Angel G. Aranda, B. Raquet, J. M. Broto, H. Rakoto, M. Goiran, A. Llobet, and J. Rodríguez-Carvajal, *Phys. Rev. B*, **64**, 214401 (2001).
[40] H. Kusuya, A. Machida, Y. Moritomo, K. Kato, E. Nishibori, M. Takata, M. Sakata, and A. Nakamura, *J. Phys. Soc. Jpn.*, **70**, 3577 (2001).
[41] M. G. Fernández, V. Scagnoli, U. Staub, A. M. Mulders, M. Janousch, Y. Bodenthin, D. Meister, B. D. Patterson, A. Mirone, Y. Tanaka, T. Nakamura, S. Grenier, Y. Huang and K. Conder, *Phys. Rev. B*, **78**, 54424 (2008).
[42] J. E. Jorgensen and L. Keller, *Phys. Rev. B*, **77**, 24427 (2008).
[43] I. O. Troyanchuk, D. V. Karpinsky and F Yokaichiya, *JETP Letters*, **87**, 541 (2008).
[44] Y. Moritomo, T. Akimoto, M. Takeo, A. Machida, E. Nishibori, M. Takata, M. Sakata, K. Ohoyama and A. Nakamura, *Phys. Rev. B*, **61**, 13325 (2000).
[45] H. Wu, *Phys . Rev. B*, **64**, 092413 (2001).
[46] H. Wu, *Phys. Rev. B*, **62**, R11953 (2000).
[47] K. Takubo, J.Y. Son, T. Mizokawa, M. Soda, and M. Sato, *Phys. Rev. B*, **73**, 075102 (2006).
[48] H. Kusuya, A. Machida, Y. Moritomo, K. Kato, E. Nishibori, M. Takata, M. Sakata, and A. Nakamura, *J. Phys. Soc. Jpn.*,**70**, 3577 (2001).
[49] Yu. P. Chernenkov, V. P. Plakhty, A. G. Gukasov, S. N. Barilo, S. V. Shiryaev, G. L. Bychkov. Hinkov, V. I. Fedorov, V. A. Chekanov, *Phys. Lett. A*, **365**,166 (2007).
[50] H. D. Zhou, J.B. Goodenough, *J. Solid State Chem.*, **177**, 3339 (2004).
[51] M. Baran, V. I. Gatalskaya, R. Szymczas, S. V. Shiryaev, S. N. Barilo, K. Piotrowski, G. L. Bychkov and H. Szymczak, *J. Phys. Condens. Matter*, **17**, 5613 (2005).
[52] D. D. Khalyavin, *Phys. Rev. B*, **72**,134408 (2005).
[53] A. A. Taskin, A.N. Lavrov, Y. Ando, *Phys. Rev. B*, **71**, 134414 (2005).
[54] H. D. Diep, *Frustrated Spin Systems*, World Scientific Publishing Co. Pte. Ltd. (2004).

[55] M. Valldor, Y. Sanders and W. Schweika, *Journal of Physics: Conference Series*, **145**, 12076 (2009).

[56] B. Raveau, V. Caignaert, V. Pralong and A. Maignan, *Z. Anorg. Allg. Chem.*, **635**, 1869 (2009).

[57] B. Nachtergaele, J. P. Solovej and J. Yngvason, *Condensed Matter Physics and Exactly Soluble Models: Selecta of Elliott H. Lieb*, Springer (2004).

[58] R. Ballou, B. Canals, M. Elhajal, C. Lacroix and A. S. Wills, *Phys. Stat. Sol.*, **236**, 240 (2003).

[59] A. Harrison, *J. Phys. Condens. Matter*, **16**, 553 (2004).

[60] M. Valldor, N. Hollmann, J. Hemberger and J. A. Mydosh, *Phys. Rev. B*, **78**, 24408 (2008).

[61] E. A. Juarez-Arellano, A. Friedrich, D. J. Wilson, L. Wiehl, W. Morgenroth and B. Winkler, *Phys. Rev. B*, **79**, 64109 (2009).

[62] D. D. Khalyavin, L. C. Chapon, and P. G. Radaelli, *Phys. Rev. B*, **80**, 144107 (2009).

[63] V. Caignaert, V. Pralong, V. Hardy, C. Ritter and B. Raveau, *Phys. Rev. B*, **81**,94417 (2010).

[64] J. Greedan, *J. Mater. Chem.*, **11**, 37 (2001).

[65] C. Broholm, G. Aeppli, S.H. Lee, W. Bao, J.F. DiTusa, *J. Appl. Phys.* **79**, 5023 (1996).

[66] P. Schiffer, A.P. Ramirez, K.N. Franklin and S.W. Cheong, *Phys. Rev. Lett.*,**77**, 2085 (1996).

[67] A. Huq, J. F. Mitchell, H. Zheng, L. C. Chapon, P. G. Radaelli, K. S. Knight and P.W. Stephens, *Journal of Solid State Chemistry*, **179**, 1136 (2006).

[68] M. Valldor and M. Andersson, *Solid State Sci.*, **4**, 923 (2002).

[69] G. L. Bychkov, S. N. Barilo, S. V. Shiryaev, D. V. Sheptyakov, S. N. Ustinovich, A. Podlesnyak, M. Baran, R. Szymczak and A. Furrer, *J. Cryst. Growth*, **275**, 813 (2005).

[70] E. V. Tsipis, D. D. Khalyavin, S.V. Shiryaev, K. S. Redkina and P. Nunez, *Mater. Chem. Phys.*, **92**, 33 (2005).

[71] H. Hao, J. Cui, C. Chen , L. Pan, J. Hu and Xing Hu, *Solid State Ionics*, **177**,631 (2006).

[72] A. I. Rykova, Y. Uedab, M. Isobeb, N. Nakayamac, Yu. T. Pavlyukhind, S. A. Petrovd, A. N. Shmakova, V.N. Kriventsova, A. N. Vasiliev, unpublished work.

[73] http://hyperphysics.phy-astr.gsu.edu/hbase/hframe.html.

[74] http://www.qdusa.com/products/mpms.html.

[75] F. Matsubara, T. Shirakura and S. Endoh, *Phys. Rev. B*, **64**, 92412 (2001).

[76] T. Nakamura and S. Endoh, *J. Phys. Soc. Jpn*., **64**, 2113 (2002).

[77] F. Matsubara, T. Shirakura, S. Endoh and S. Takahashi, *J. Phys. A*, **36**, 10 881 (2003).

[78] L. W. Lee and A. P. Young, *Phys. Rev. Lett.*, **90**, 227203 (2003).

[79] L. Berthier and A. P. Young, *Phys. Rev. B*, **69**, 184423 (2004).

[80] H. Kawamura, *Phys. Rev. Lett.*, **68**, 3785 (1992).

[81] W. Schweika, M. Valldor and P. Lemmens, *Phys. Rev. Lett.*, **98**, 67201 (2007).

Chapter 3

Photoelectron Spectroscopy: Theoretical Background and Instrumentation

3.1 Introduction

Photoelectron spectroscopy (PES), also known as photoemission spectroscopy is extensively used in probing the electronic structure of different materials. The principle of the technique is based on Koopmans' theorem and the photoelectric effect. The photoelectric effect is a phenomenon in which photoelectrons are ejected from matter when it is exposed to electromagnetic radiation such as X-rays or visible light [1]. This effect was first discovered by Hertz [2] in 1887 but it could not be described by classical physics [3]. Later, Einstein successfully explained it in 1905 [4]. He suggested that light was composed of discrete quanta (photons) instead of continuous waves and the energy of each photon was equal to frequency multiplied by a constant (Planck's constant). A photon above a threshold frequency was able to pull an electron from the matter when it was exposed to light as described in the following section.

3.2 Photoemission from Solids

In solids, electrons possess different energy states. Photoemission is employed to find out the energy distribution of these electron states. It is a direct method which gives an indication of the band structure in solids. In the current research work, photoemission techniques have primarily been used to study the electronic structure of clean transition metal oxide surfaces. Figure 3.1 represents the geometrical arrangement whilst Figure 3.2 illustrates the fundamental principle of the photoemission process. When photons fall on the sample, they transfer their energy to the electrons inside to make a transition from a filled initial state to an empty final state.

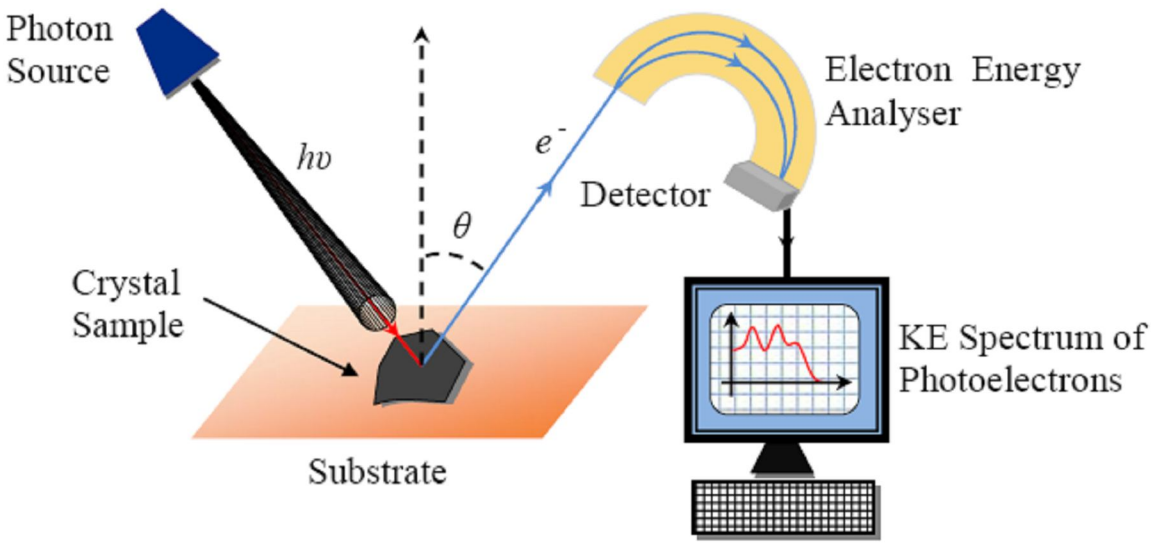

Figure 3.1: *Geometrical arrangement of photoemission experiment representing the photon source, the sample, the analyser, the detector and the KE spectrum of the emitted photoelectrons.*

The kinetic energy (E_K) of the photoelectrons is given by the Einstein equation [5],

$$E_K = h\nu - E_B - \Phi_S, \qquad \text{Equation 3.1}$$

where $h\nu$ is the photon energy, E_B is the binding energy of the electrons relative to the Fermi level and Φ_s (the work function of the sample) is the difference between the vacuum and the Fermi energy levels.

The work function of a material is defined as the minimum amount of energy required to remove an electron from the topmost occupied level into vacuum. Experimentally, only the work function of the spectrometer is required to estimate the binding energies of the photo-

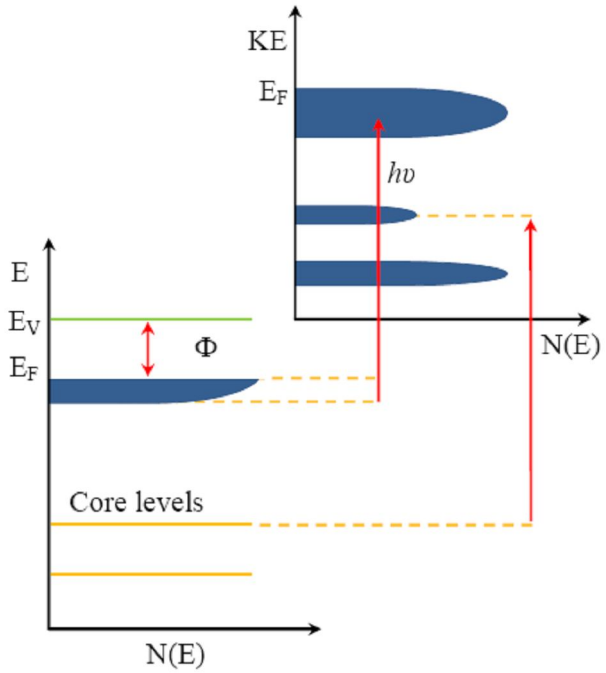

Figure 3.2: *A schematic diagram of the photoemission process. The energy E of the electrons is plotted along the y-axis and the number of electrons as a function of energy N(E) along the x-axis. The diagram shows how the energy levels in the solid are transferred by absorption of photons into the vacuum where N(E) is measured through the intensity of photoemitted electrons as a function of electron kinetic energy. Here* E_V *denotes the vacuum level and Φ* is *the work function* [6].

electrons. The spectrometer work function can be calculated by referring to an already known level such as Au $f_{7/2}$ [7]. The work function of the spectrometer depends upon the materials it is made from and is considered to be fixed under normal conditions (room temperature, room pressure and earthed). The energies involved in the detection of emitted photoelectrons are shown in Figure 3.3. When the analyser and the sample are earthed together, then there is a contact potential difference (CPD) between the work function of the analyser and that of the sample. This causes a modification in the kinetic energy of the electron on entering the analyser (*i.e.* $E_K \neq E'_K$). Now the binding energy of the original electron state can be found from Equation 3.2 which is a modified form of Equation 3.1 and is given below:

$$E'_K = h\nu - E_B - \Phi a, \qquad \text{Equation 3.2}$$

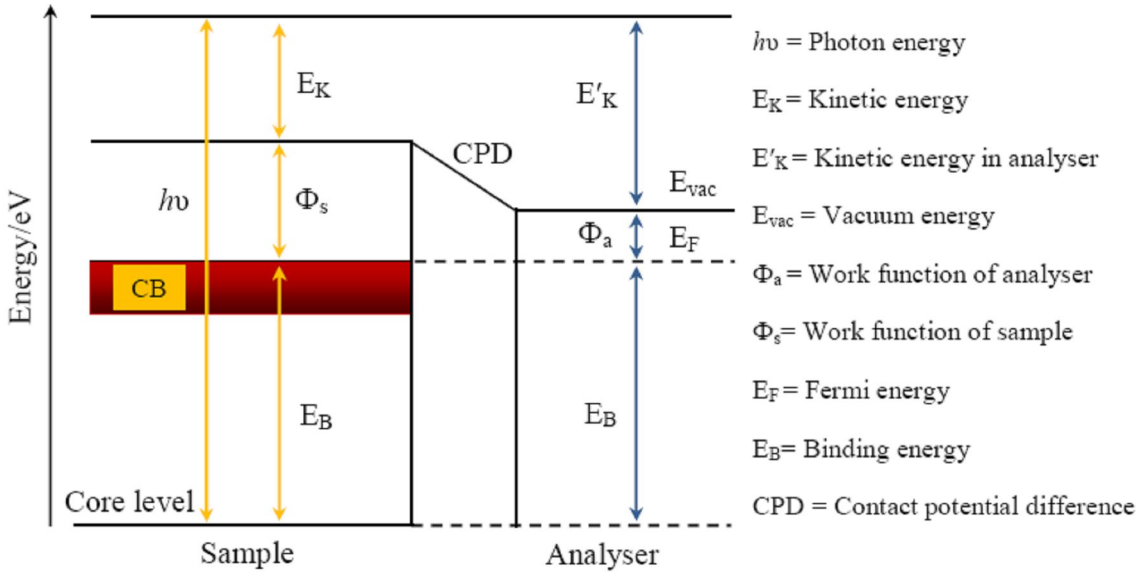

Figure 3.3: *An energy level diagram for photoemission from a metallic sample in contact with the spectrometer* (*Adapted from* [8]).

where E'_K is the energy of the electron in the analyser and Φa is the work function of the analyser being used. Photoelectrons which have enough energy to overcome the work function of the material are detected and observed in the photoemission spectrum. The inelastically scattered electrons give up their energy within the sample and appear on a rising background (secondary electron tail), increasing to lower E'_K (higher E_B), in a photoemission spectrum. The well-defined peaks on the photoemission spectrum can be divided into two main categories: valence or core level photoemission and X-ray excited Auger emission.

Photoemission techniques have two main forms, X-ray photoelectron spectroscopy (XPS) and ultraviolet photoelectron spectroscopy (UPS). The XPS and UPS techniques can be distinguished from each other on the basis of energy of the incident photons. UPS involves low energy photons from a helium (He) discharge lamp, ranging from 21.2 eV (He I) to 40.8 eV (He II) or, up to 200 eV from a synchrotron source. In XPS, the incident energy ranges from 200 eV to 1500 eV [9, 10] whereas a lab-based source provides fixed energies (1253.6 eV and 1486.6 eV). However the rigid boundary between these two techniques

(XPS and UPS) has been made indistinguishable by the use of modern synchrotron sources that provide tunable radiation spanning a much wider energy range (5-5000+ eV).

As electrons inside the atom reside in different energy levels, the innermost energy levels are called core levels and the shallow energy levels can be termed valence energy levels. The valence energy level electrons are loosely bound as compared to those of core levels, because the core orbitals of an atom are highly contracted towards the positively-charged nucleus. These highly contracted orbitals do not significantly overlap with other atoms in the molecule or a solid. Valence electrons are involved in chemical bonding so their orbitals overlap with each other. For the core levels, chemical bonding has little influence on these orbitals. In XPS, the core level orbitals appear as sharp lines in the spectra of molecules and solids unlike the broad bands of valence orbitals [11].

With the exception of hydrogen and helium, XPS can identify all of the elements within 2 to 25 monolayers or 1-10 nm of the sample surface depending upon the orientation of the sample [12]. The filled density of states function has an organised pattern that the photoemission spectrum replicates [13]. Though XPS can provide information about the valence electrons, the low energy photons of the UV technique can probe the valence level electrons with better resolution because of the much lower energy spread of the exciting line [11] and longer lifetime of the hole state created in valence level photoemission.

3.2.1 Koopmans' Theory

In the photoemission process, when an electron comes out of the metal surface it leaves a hole behind it. The hole represents the deficiency of an electron or an excess of positive charge. This hole may affect the energy levels of the remaining electrons and hence whether the kinetic energy of the photoelectrons recorded by the analyser is a true reflection of the binding energy.

Koopmans' theory assumes that when the electron leaves its atomic site creating a hole, the remaining electrons remain frozen at their original energies [14]. Hence the binding energy of the recorded electrons is a true reflection and is equivalent to the binding energy in the unionised system. Koopmans' theory has some flaws in it, because the hole created after the electron leaves its position changes the Coulombic attraction between the nucleus and the remaining electrons, and may change the final state energies on the timescale of the

photoemission. The final state hole may also be filled by electron transfer from elsewhere in the solid on the timescale of electron emission, again leading to a breakdown of Koopmans' theory.

3.2.2 Surface Sensitivity and Inelastic Electron Mean Free Path

One of the most salient features of photoelectron spectroscopy is its surface sensitivity. This comes from the fact that the emitted electrons in solids may travel only a short distance without significant loss of energy due to inelastic processes such as plasmon excitations (quantised collective oscillations of the valence or conduction electrons of solid), electron-hole pair formation (excitation of a valence electron to a conduction band caused by the ejected electron) and electron-phonon interactions (where the emitted ejected electron causes the excitation of the quantised vibrations of the solid lattice) [17]. The ejected electrons from a solid have energies $10\text{-}10^3$ eV [15]. The average distance that an electron travels between successive inelastic collisions with a given energy can be described by a parameter λ which is known as the inelastic mean free path (IMFP) and is almost independent of material. Only the electrons emitted within a distance of the order of $\sim 3\lambda$ have a chance of escaping into the vacuum. Therefore, 3λ is also called the escape depth. The emitted photoelectrons that lose energy in the sample do not show any contribution to the characteristic primary photoemission peaks but appear in the so-called 'secondary electron' background. The actual relationship between the kinetic energy of the electrons and the IMFP depends on the electronic structure of the sample under investigation but the general characteristics are similar for all elements.

For inorganic materials, Seah and Dench [16] compiled the universal curve of IMFP as shown in Figure 3.4. It is clear from the figure that the minimum value of IMFP occurs for electron kinetic energies in the 10-100 eV range. As the kinetic energy of electrons increases, the corresponding value of λ also increases, but not considerably. It can be inferred that at 1000 eV, the value of IMFP in metals is probably less than about 20 Å which is of the order of about 10 atomic monolayers. In the lower energy region, the probability of inelastic scattering decreases because the electrons do not have enough

energy to cause plasmon excitation and hence the distance between the inelastic collisions increases.

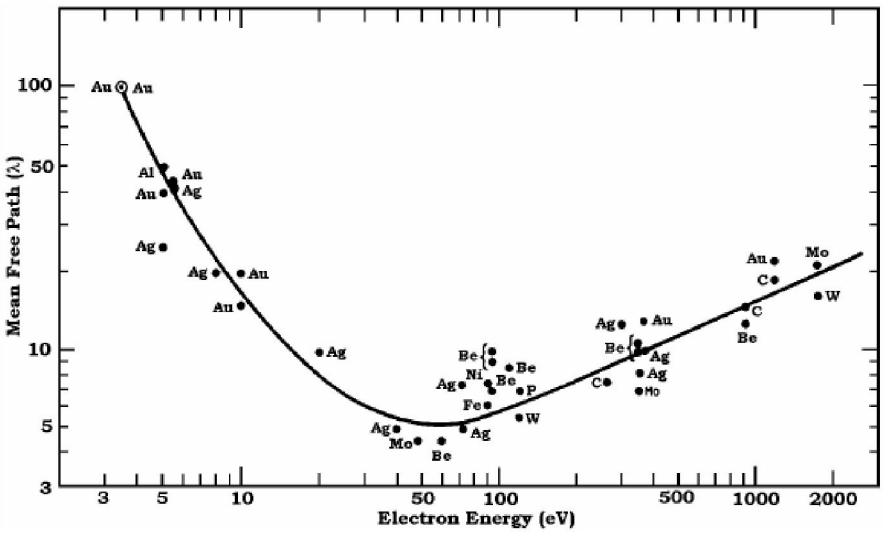

Figure 3.4: *Dependence of the IMFP on the photoelectron kinetic energy for inorganic materials* [12].

3.2.3 Beer-Lambert Law

When a photon or an electron wave enters some material of interest, its initial intensity I_o is attenuated due to absorption in the medium. The Beer law explains this effect. The amount of attenuation I in the material can be found by using the following mathematical equation for Beer's law:

$$I = I_o e^{-\alpha d} \quad , \qquad \text{Equation 3.3}$$

where α is the absorption coefficient and d is the distance travelled in the medium. Photons are neutral particles and interact weakly with the charge distribution of the atoms of the material; they can travel deeply into the sample to eject both valence and core level electrons to the vacuum level if they have enough energy. If the photon does not have sufficient energy, then it will simply pass through without any effect.

The flux of electrons leaving the sample is exponentially attenuated in exactly the same way, but the interaction of electrons within the solid is much larger than photons (as they

are charged). So the escape depth for electrons is very small (compared with the penetration depth for photons). The contribution of ejected electrons from the bulk sample depends upon the mean free path which is a function of *K.E.* and the angle at which the electrons are emitted. The Beer-Lambert law (Equation 3.4) gives the relationship between the mean free path and the flux of the emitted electrons:

$$I(x) = I_o(x)\exp\left[-\frac{x}{\lambda\cos\theta}\right], \qquad \text{Equation 3.4}$$

where $I(x)$ is the emitted electron intensity from a distance x into the sample. This depends upon the initial electron intensity $I_o(x)$ created at depth x. θ is the exit angle measured from the normal to the surface.

Equation 3.4 together with the universal curve can be used to evaluate the depth below the surface at which photoelectrons originate in angle-resolved measurements. In normal emission ($\theta = 0$), 95% of the electrons detected either in UPS or XPS originate from a depth which is equivalent to 3 inelastic mean free paths of the surface (the sampling depth). Figure 3.5 shows the surface sensitivity enhancement as a function of θ. At larger values of θ ($0^o \leq \theta < 90^o$), the effective sampling depth decreases and hence only those electrons can escape and be detected that originate very close to the surface.

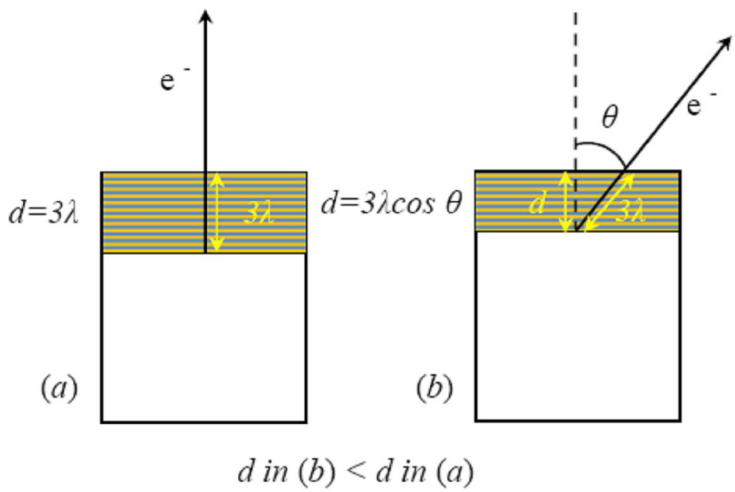

Figure 3.5: *Surface sensitivity enhancement by variation of the photoelectron detection angle relative to the surface normal.*

3.2.4 Chemical Shifts

In solids, the atoms are bonded with different species. The precise binding energy of the core levels of the atoms depends upon the type of these species i.e. the binding energy of the core levels is significantly affected by the chemical environment of an atom or a molecule. The energy required to eject an electron from a particular core level is known as its binding energy [17]. It depends upon the attractive potential on the electron due to the nucleus and the repulsive Coulomb interaction of the other electrons present inside the atom. Any change in the chemical environment may result a charge transfer between the atoms making them partially positively (or negatively) charged. Consequently, this charge transference leads to a shift in core levels to higher (or lower) binding energies associated with increased (or decreased) Coulomb interaction between the core electrons and the nucleus [17, 18]. Hence atoms with higher formal oxidation state usually generate XPS peaks at higher binding energy as compared to the same atoms with lower oxidation state. The oxidation states of the surface features can be identified by using XPS and this feature is termed the 'chemical shift' [19].

3.2.5 Satellite Features

In photoemission experiments, photoelectrons undergo inelastic collisions within their mean free path and lose energy, causing phenomena such as interband plasmon and phonon scattering etc. These interactions bring additional shake-up and shake-off satellite contours or peaks in the XPS spectra. A shake-up satellite arises from a situation where an outgoing photoelectron loses energy by exciting another electron from a lower energy level to a higher energy level, for example across the bandgap of a semiconductor. It is not ejected from the excited atom [11, 20]. The shake-up satellites always appear in the spectra at higher binding energies (i.e. lower kinetic energy) than the main peak. They may have a wide range of possible energies and may be hidden within any background signal present. If the valence electrons are completely ionised to unbound continuum states and there is no discrete interaction with the excited core level electrons, then 'shake-off' satellites occur in the broad inelastic secondary electron region of the spectrum. Shake-off satellites always have lower kinetic energies than the main photoemission peak to which they relate.

3.2.6 Auger Emission

In photoemission experiments, the XPS spectrum also contains contributions from an alternative process called Auger emission. Figures 3.6 and 3.7 explain the principle of Auger emission.

Figure 3.6 represents a 1s electron that leaves the K shell leaving a hole behind after absorbing a photon. Another 2p electron from the L shell fills this hole and causes a release of some energy either as X-ray fluorescence or further emission of another electron (an Auger electron) as shown in Figure 3.7.

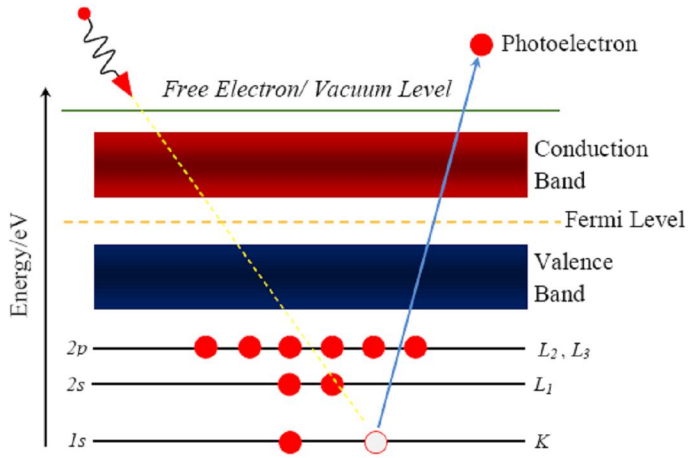

Figure 3.6: *Creation of a core hole:* a *1s electron leaves the K shell creating a hole.*

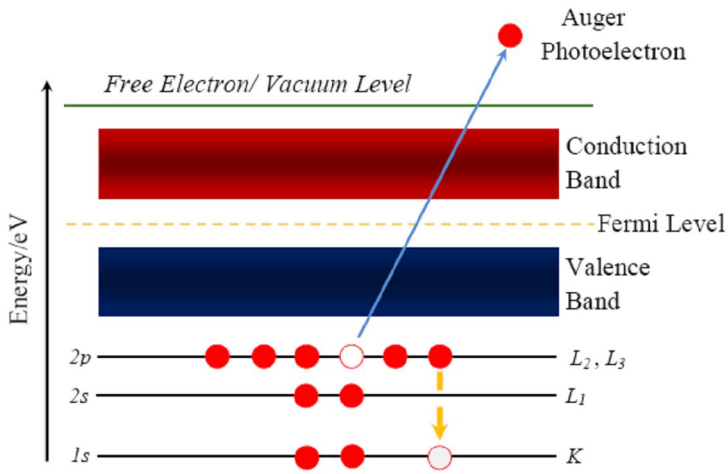

Figure 3.7: *Auger emission*: a *transition from a 2p to a 1s state results in emission of an Auger electron from the L shell.*

This particular Auger emission is denoted by 'KLL'. The energies involved in this process are given by Equation 3.5 below:

$$E_{Auger} = BE - E_{L2} - E_{L3}, \qquad \text{Equation 3.5}$$

where *BE* is the binding energy of the 1s electron and E_{L2}, E_{L3} are the energies of the 2p level electrons. The *2l+1* degeneracy in these energy levels must be taken into consideration because of the spin up and spin down states of electrons. Hence the E_{L3} level may have a slightly lower value than E_{L2} in binding energy [8].

3.2.7 Spin Orbit Coupling

An electron possesses both orbital angular momentum and spin angular momentum that are defined by the quantum numbers *l* and *s* respectively. The interaction between these angular momenta is known as spin-orbit interaction. Spin-orbit coupling effects in the final states can cause splitting of photoemission peaks and are treated by either *j-j* or *L-S* coupling.

For heavy elements (Z >75), the spin-orbit coupling is strong and is described by *j-j* coupling. For such elements, the total angular momentum (j) of an electron is obtained from the vectorial sum of the individual spin angular and orbital angular momenta to give $l+s$ or $l-s$. The total angular momentum (J) of whole atom is then calculated by adding all the j quantum numbers *i.e.* $J = \Sigma j$. However, for low atomic number elements (Z < 20), the spin-orbital interactions are weak and are governed by *L-S* (or Russell-Saunders) coupling. In this case, the total angular momentum (J) for the whole atom is calculated separately by summing the orbital angular momenta (Σl) and spin angular momenta (Σs) for all the electrons, and adding these to give $J = \Sigma\, l + \Sigma\, s$.

3.3 Ultraviolet Photoemission Spectroscopy

3.3.1 Valence Band Resonant Photoemission

Resonant photoemission is a significant technique that is widely being used to study the electronic properties of transition metal oxides. Basically resonance is an outcome of interference between two decay channels in the photoemission process. The concept of

resonance can be comprehended by considering the case of a 3p→3d transition. In the form of an equation, the direct photoemission process for a 3d electron can be represented as:

$$3p^6 3d^n + h\nu \rightarrow 3p^6 3d^{n-1} + e^- , \qquad \text{Equation 3.6}$$

where $3p^6 3d^n$ is the general initial state configuration and hν is the energy of the photon that ionises the neutral atom imparting kinetic energy *E* to the outgoing electron e^- [27]. Using a tunable photon source, hν can be adjusted to match an internal excitation in the atom. If the incoming photon has energy just greater than the 3p→3d transition then the atom is promoted to an excited state followed by a Super-Coster Krönig [SCK] decay process. This can be expressed as :

$$3p^6 3d^n + h\nu \rightarrow \{3p^5 3d^{n+1}\}^*, \qquad \text{Equation 3.7}$$

where the asterisk (*) represents a transient excited state that comprises an extra electron in the 3d shell and a hole in the 3p shell of the atom. Eventually the transient excited state decays away via SCK by the loss of two electrons to give the same final state as the normal process [22]. This step can be represented as:

$$\{3p^5 3d^{n+1}\}^* \rightarrow 3p^6 3d^{n-1} + e^-. \qquad \text{Equation 3.8}$$

Photoemission near the 3p-3d threshold of the transition metal can give additional information about the electronic structure regarding the contribution of states from particular elements/orbitals. Figure 3.8 gives a pictorial view of the two main processes involved in resonant photoemission: when the energy of the photon becomes equal to the energy required to excite an electron from 3p level to the unoccupied 3d level, the photoemission increases extraordinarily, and the transient excited state decays into a final state like the normal 3d photoemission. So, resonant photoemission can be regarded as the interference of the processes ((c) + (d)) and (b) as shown in Figure 3.8. Changes in intensity (usually enhancement) of the photoemission at a particular binding energy when the photon

energy is tuned to a resonance of a particular element imply that the DOS at that binding energy contains contributions from that element.

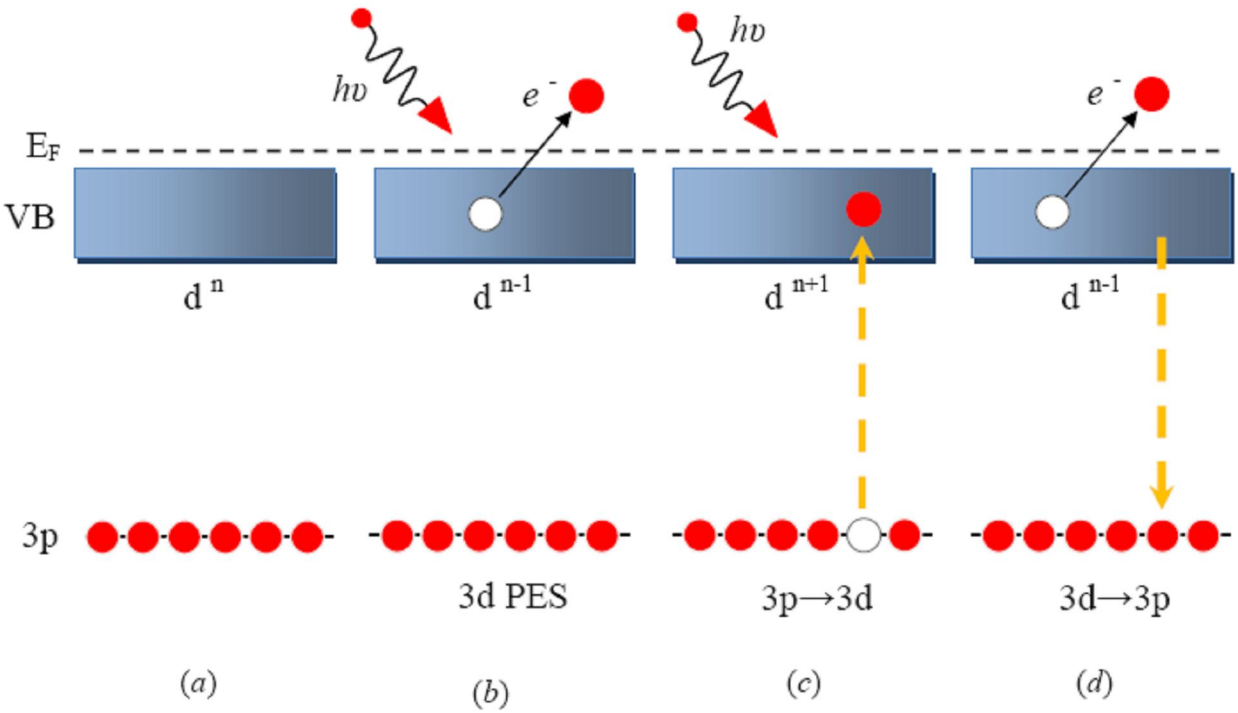

Figure 3.8: *Direct and resonant photoemission*: (*a*) *transition metal 3d VB and 3p core level before PES;* (*b*) 3d *direct PES - an electron from 3d level is ejected;* (*c*) *core electron can be excited from the* 3p *level to VB with a matched energy photon - this transient state decays into a state shown in* (*d*) *i.e. a* 3d *electron is shifted to the* 3p *level while another* 3d *electron is emitted* (*Adapted from* [23]).

3.3.2 Types of Photoemission Spectra

3.3.2.1 Energy Distribution Curves (EDCs)

Energy distribution curves or EDCs are used widely in surface science. This mode of experimentation is used both for lab-based and synchrotron radiation sources. An energy distribution curve (EDC) is obtained by recording the number of photoelectrons emitted per unit time plotted against the kinetic energy of the photoelectrons, keeping the photon flux constant. EDCs are considered to be the sums of the primary distribution of electrons and the background of secondary electrons.

3.3.2.2 Constant Initial State Spectra

Constant Initial State (CIS) mode is a relatively more complex mode for data acquisition in photoemission. This sort of mode is possible only using a tunable radiation source such as a synchrotron radiation source. CIS spectra render information about the final density of states above the vacuum level. Experimentally, CIS spectra are obtained by varying both the energy of the incident photons and the kinetic energy of the photoelectrons such that the energy difference (KE - $h\upsilon$) between them remains constant as illustrated in Figure 3.9 and given in Equation 3.9:

$$E_i = KE_1 - h\,\upsilon_1 = KE_2 - h\,\upsilon_2; \qquad \text{Equation 3.9}$$

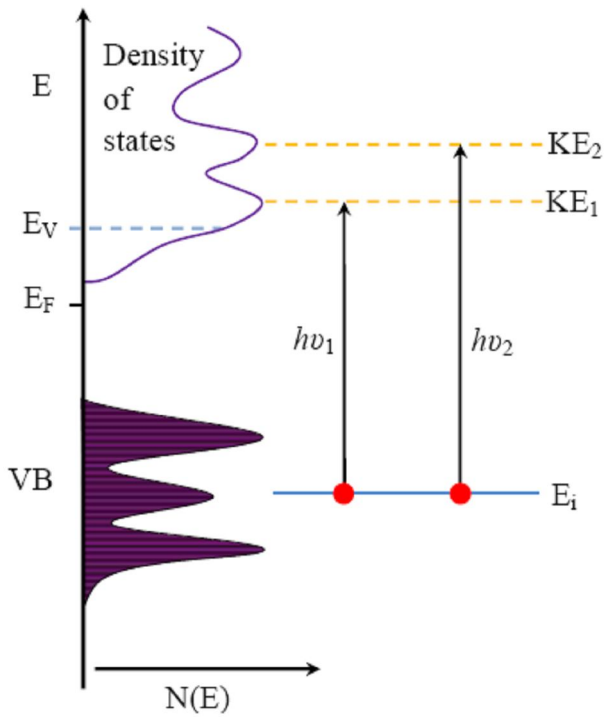

Figure 3.9: *An illustration of the CIS experiment. The energy interval which defines the KE of electrons accepted from a fixed initial state is scanned synchronously with the photon energy* (*Adapted from* [15])

where E_i is the initial state energy. By fixing E_i equal to the binding energy of a particular EDC feature, it is possible to observe changes in intensity of the feature as a function of

photon energy. This represents a resonance process and enables the determination of the atomic character of the density of states function [24]. CIS spectra can also be generated by measuring the peak heights at a given binding energy directly from conventional background-subtracted energy distribution curves and plotting them against the incident photon flux.

3.4 Synchrotron Radiation

A synchrotron facility is an excellent source that provides tunable radiation with high flux to probe materials and biological systems. For different research applications, different types of radiation (X-rays, UV, infrared etc.) are used.

Synchrotron radiation (SR) is a term which is used for the electromagnetic radiation emitted from circulating charged particles such as electrons or positrons with relativistic velocity. When the charged particles orbit at a speed *v*, much less than that of light, the emitted radiation has a large range of angular distribution with characteristic frequencies [26]. However, when the speed of charged particles approaches the speed of light *c*, the angular distribution is distorted by relativistic effects and the radiation emission concentrates around a tangential direction to the orbit [26] as shown in Figure 3.10. The theory of synchrotron radiation is based on classical electrodynamics and is comprehensively discussed in the works of Jackson [28], Hofmann [29] and Winick [30].

Synchrotron radiation has properties such as high intensity, natural collimation in the plane normal to the orbit, high polarization, small-source-spot size, stability and broad spectral distribution etc. These superior features of SR over a lab based X-ray source facilitate many experiments.

Figure 3.11 represents the range of wavelengths emitted by a typical bending magnet at the Synchrotron Radiation Source (SRS, UK) corresponding to photon flux in the energy range of a few meV to 10^5 eV. Hence, synchrotron radiation has a suitable energy range to explore the properties of low energy valence electrons and those of low lying core electrons having relatively higher binding energy. To perform an experiment, a monochromatic source is needed which can be provided by using a monochromator. A variety of different wavelengths from SR, within a given range, can be selected by the monochromator throughout the course of an experiment according to the requirement.

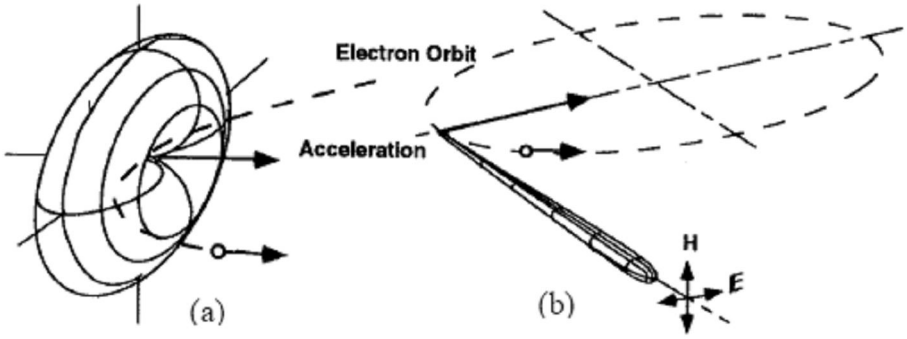

Figure 3.10: (a) *Angular distribution of radiation emitted from an electron moving along a circular path (dashed line) at speeds much less than the speed of light c.* (b) *Angular distribution distorted by relativistic effects of an electron travelling in the same circular path but at speeds approaching c* [27].

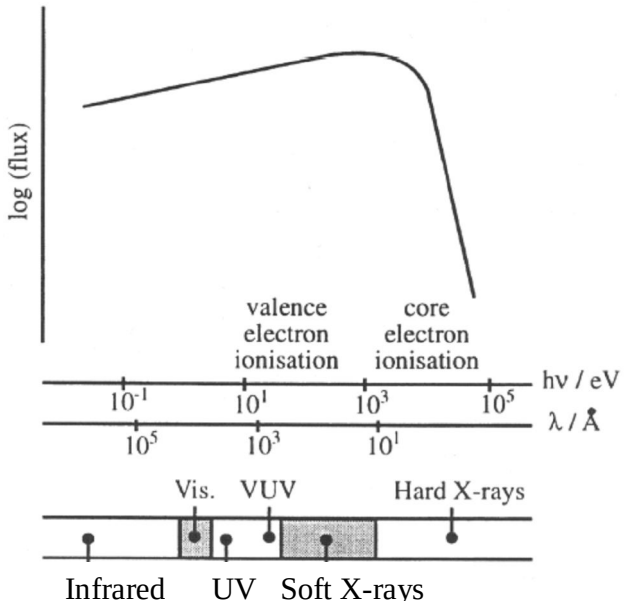

Figure 3.11: *The typical spectral distribution of the radiation emitted by the Synchrotron Radiation Source, Daresbury, UK* (*Taken from* [31]).

Figure 3.12 shows a schematic layout of a synchrotron radiation source. The main part of the synchrotron is its electron storage ring which is kept under a pressure lower than 10^{-13} atmospheres [25]. Electrons are injected into the main storage ring using a device called injector (a synchrotron or a linear accelerator). Here electrons circulate for many hours and also lose energy through emission of synchrotron radiation and during collisions with the residual gas atoms. Focusing magnets are used to keep the circulating electrons in stable

orbits along the ring. Besides the focusing magnets, other devices called undulators, wigglers and bending magnets are also used along the main ring. The main ring has some straight and curved sections. On the straight sections, the undulators and the wigglers are inserted.

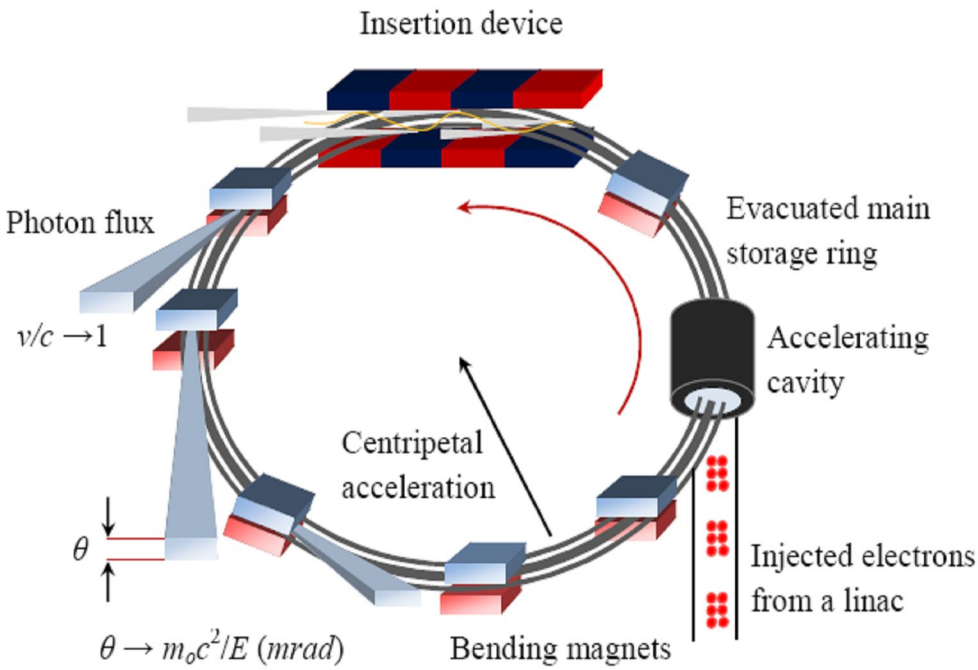

Figure 3.12: *Schematic layout of a synchrotron radiation source.*

The circulating electrons emit electromagnetic radiation and emit synchrotron radiation when they are given centripetal acceleration using bending magnets. The power (P) radiated by a circulating electron with charge e and mass m in the storage ring is given by the Larmor formula [30] as shown by Equation 3.10 below:

$$P = \frac{2}{3}\frac{e^2 c}{\rho^2}\beta^4\left(\frac{E}{mc^2}\right)^4, \qquad \text{Equation 3.10}$$

where ρ is the radius of curvature, E is the energy, v is the speed of the electron , c is the speed of light and $\beta = v/c$.

The energy lost per turn ΔE by one electron can be calculated by using Equation 4.2 below:

$$\Delta E = \frac{4\pi}{3}\frac{e^2}{\rho}\beta^3\left(\frac{E}{mc^2}\right)^4 . \qquad \text{Equation 3.11}$$

Equations 3.10 and 3.11 show that P and ΔE are inversely proportional to m^4 which implies that a heavier circulating charged particle than an electron (such as a proton) produces negligible synchrotron radiation power. In practical units, the energy and power lost per turn by a highly relativistic electron is given by Equations 3.12 and 3.13 below:

$$\Delta E\,(\text{keV}) = 88.47E^4/\rho\ , \qquad \text{Equation 3.12}$$

$$P\ (\text{kW}) = 88.47E^4 I/\rho = 2.654BE^3 I\,, \qquad \text{Equation 3.13}$$

where E is in GeV, ρ is in metres, B is in kilogauss and I is in amperes.

3.4.1 The Daresbury Synchrotron

The Synchrotron Radiation Source (SRS)* at Daresbury in Cheshire has many workstations, each of which has different purpose-built beamlines. Some provide low energy X-rays and others use high intensity UV. The SRS comprises a linear accelerator, a small booster synchrotron and a main storage ring. Figure 3.13 depicts the main storage ring at the centre which is considered to be the heart of operation because it provides synchrotron radiation.

Firstly, the electrons are accelerated in the linear accelerator where they acquire energy of 12 MeV. Secondly, bunches of electrons are injected into the booster synchrotron which accelerates them up to an energy of 600 MeV. Finally, the electrons are directed into the main storage ring where they are accelerated by a high intensity radio frequency (RF) cavity system to a kinetic energy of 2 GeV. Here, high power electromagnets called

---

* The SRS closed to user operations in August 2008.

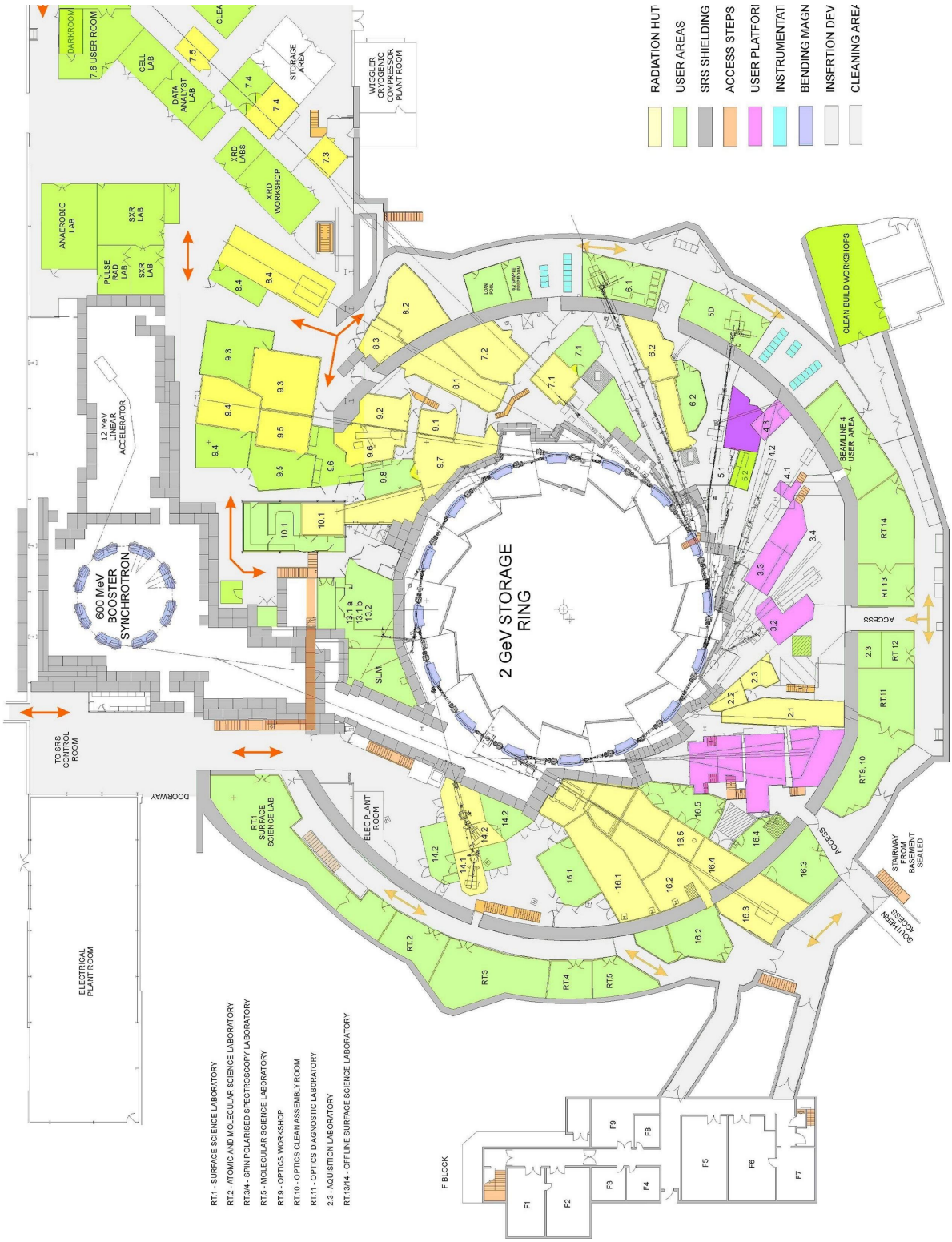

Figure 3.13: *Daresbury Lab SRS storage ring* (*Taken from* [31]).

bending magnets (BM) are used to keep them in stable orbits inside the storage ring. Normally the electron bunches constitute a high current beam of 150-250 mA. Despite the vacuum (10^{-10} mbar) inside the main storage ring, the electrons collide with the residual gas atoms, lose energy and are removed from the electron bunches that make up the beam. So, daily refill of the beam is needed. To collect electromagnetic radiation from the electrons, dipole bending magnets are used that provide them centripetal acceleration. Hence, the electrons emit radiation along tangents to the storage ring at each magnet that constitutes the beamlines. At the end of each beamline, there are end stations equipped with different types of instruments to meet the requirements of the system under investigation. The beamlines are enhanced by undulators and wigglers that use high strength alternating magnetic fields to oscillate electrons in the horizontal plane. The difference between undulators and wigglers is the frequency that they generate to oscillate the electrons. The wigglers are provided with a high magnetic field strength *B*. It causes larger transverse undulations of the electrons compared to undulators. The energy emitted by the electrons is restored by devices called 'radio frequency (RF) cavities'. Synchrotron radiation detected in the plane of the ring is linearly polarised and elliptically polarised when received out of plane.

3.4.2 Daresbury Laboratory Station 3.2

3.4.2.1 The Beamline

Beamline 3.2 is a source of vacuum ultra violet (VUV) radiation which is equipped with a five metre-long McPherson high resolution normal incidence monochromator. The two gratings of the monochromator provide radiation in the range 5-35 eV (2500-350 Å) with a best resolution of 2 meV (0.05 Å) [34]. Primarily the beam is used for gas-phase atomic and molecular experiments but also provides a facility for molecular electron spectroscopy (MoLES) and high resolution photoelectron spectroscopy (HiResPES). Port 3 receives a horizontal fan of 28 mrad from the main storage ring, and further distributes it among four beamlines (3.1, 3.2, 3.3 and 3.4) according to the requirements and specifications of the equipment installed there. A 5×5 mrad share of the total photon flux is given to the pre-focusing mirrors of station 3.2. Figure 3.14 below shows the optical layout of the four

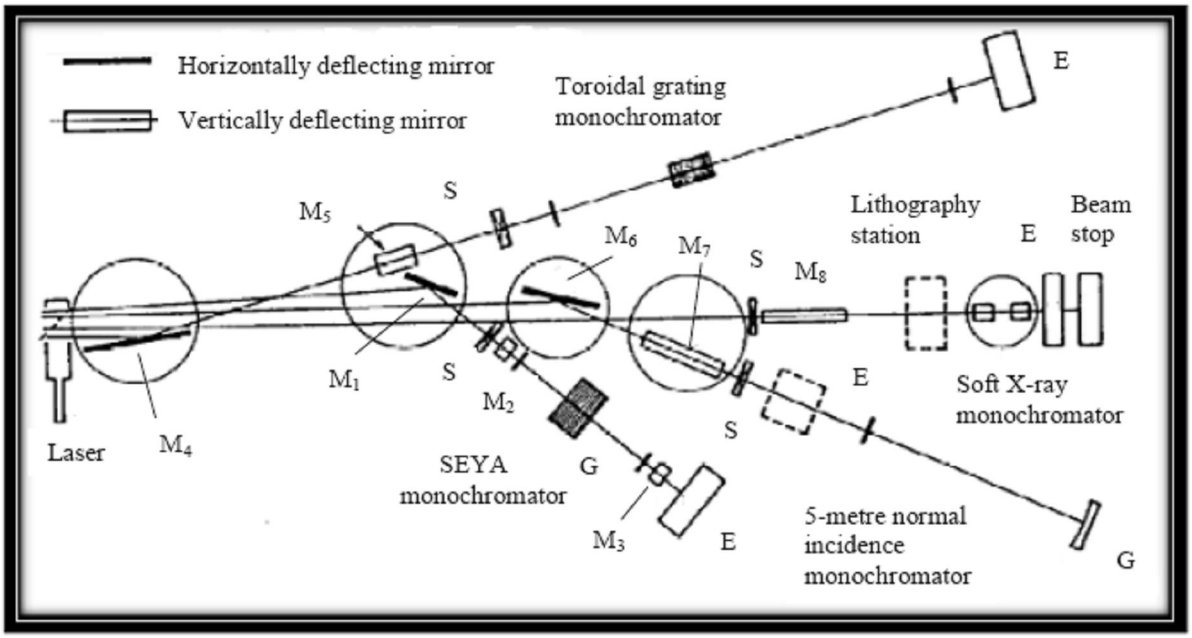

Figure 3.14: *Plan layout of beamline 3 at Daresbury Lab: Mirror details:M_1:cylindrical, SiC,4:1 demagnification, grazing angle 10°, aperture 7.5 mrad horizontal,2.5 mrad vertical, M_4:cylindrical, SiC, 2:1 demagnification, grazing angle 5°, aperture 10 mrad horizontal,2.5 mrad vertical. M_5: plane, SiC, grazing angle 5°, 5 mrad horizontal and vertical aperture, S:slits;E:experimental chamber; G:diffraction grating* (*Taken from* [33]).

stations that receive radiation flux from the main storage ring through port 3. Mirrors M_1, M_2, M_3, M_4, M_5, and M_6 are used to deflect synchrotron light towards the respective monochromators. M_6 and M_7 serve this purpose for beamline 3.2. Before starting an experiment at this beamline, it is very important to obtain the maximum flux by the proper adjustment of these mirrors. The first pre-mirror M_6 is a plane mirror, adjusted vertically on a moveable platform that deflects the radiation in a horizontal plane. The second pre-mirror is a vertically deflecting ellipsoid. A micrometer is provided to adjust M_6 while M_7 is set by a large rotary drive, a 3:1 demagnifying mirror (both horizontally and vertically) that focuses the light onto the monochromator. The optical layout of beamline 3.2 and the five metre McPherson high resolution normal incidence monochromator is shown in Figure 3.15. The monochromator has two diffraction gratings, called the Low Energy Grating (LEG) and the High Energy Grating (HEG).

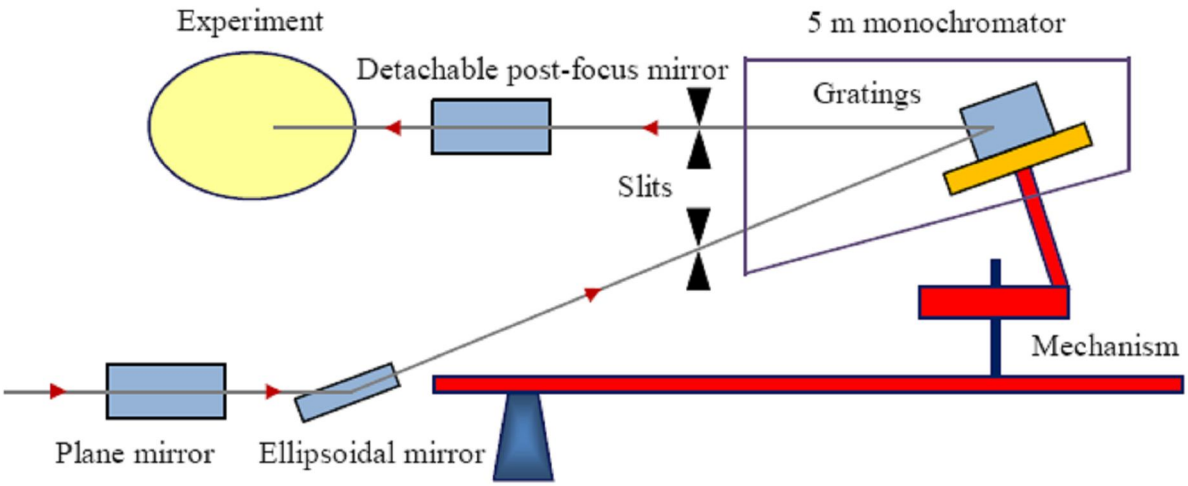

Figure 3.15: *Five metre McPherson high resolution normal incidence monochromator* (*Adapted from* [33]).

The two gratings are placed on the end of a moveable tilt arm whose motion is controlled with a stepper motor around a cam by a lead screw**.** The cam mechanism keeps the flux in focus all the time by means of translational and rotational motions of the gratings. A calibrated cyclometer at the bottom reads the wavelength of the light selected. After the exit slit, a 2:1 demagnifying ellipsoidal mirror deflects the beam onto the work station platform.

3.4.2.2 Flux

The two interchangeable gratings of the McPherson monochromator provide a peak flux of 1.4×10^{12} photons/s at a current of 200 mA in the main storage ring at the Daresbury Synchrotron. This flux was measured at approximately 23 eV photon energy. The flux response of both LEG and HEG gratings was measured in July 2003 and is shown in Figure 3.16. The flux output of the LEG and HEG has now been improved significantly after the installation of two new pre-mirrors.

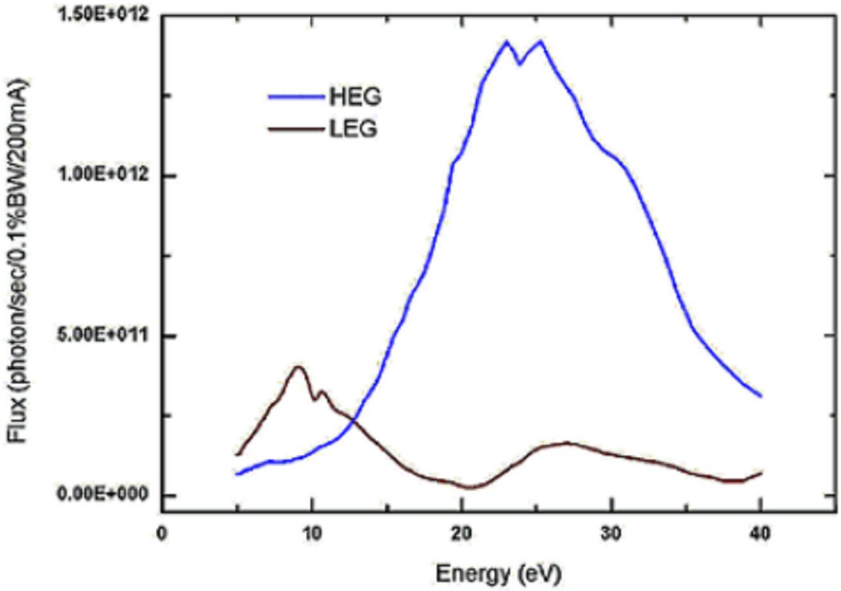

Figure 3.16: *Flux provided by the McPherson monochromator* (*Taken from* [34]).

3.4.2.3 Resolution

The exit and entrance slits have been provided with micrometers that can be used to change the photon energy resolution of the beam. Contracting the micrometer by 1 mm opens the slit by 0.25 mm. Table 3.1 gives a record of theoretical and measured resolution in ångstrom and the settings of both slits. The dependence of the resolution ΔE on the energy of the photons is shown in Figure 3.17.

Entrance slit (mm)	Exit slit (mm)	Theoretical resolution (Å)	Measured resolution (Å)
9.99	12.45	1	1.0
11.27	13.75	0.5	0.5
11.54	13.97	0.4	0.41
11.80	14.24	0.3	0.33
11.92	14.38	0.25	0.28
12.04	14.51	0.2	0.22
12.17	14.62	0.15	0.18
12.29	14.73	0.1	0.13
12.43	14.85	0.08	0.08
12.56	14.93	0.05	_

Table 3.1: *Record of theoretical and measured resolution, and the settings of entrance and exit slits for beamline 3.2 at the SRS* (*Adapted from* [34]).

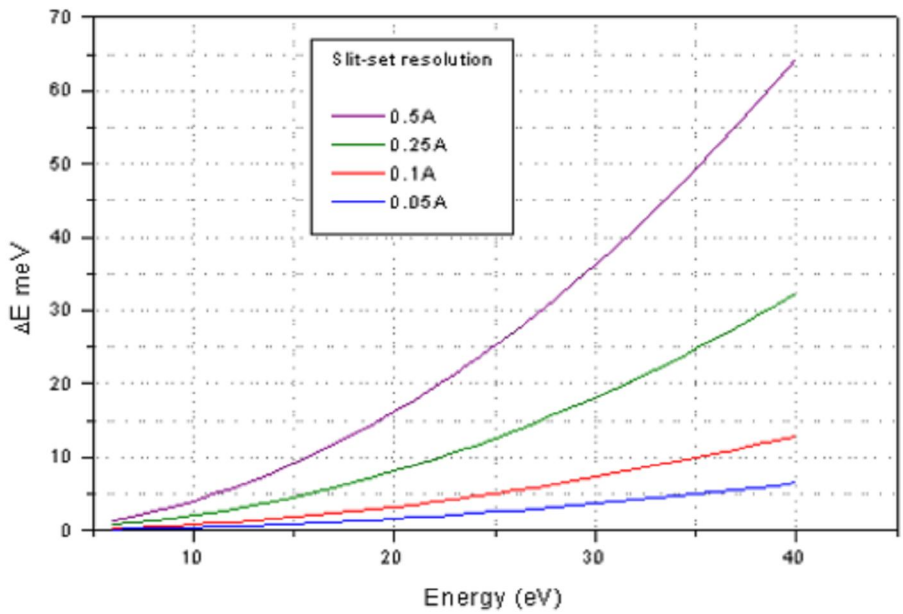

Figure 3.17: *Resolution vs energy of photons for beamline 3.2 at the SRS* (*Taken from* [34]).

3.4.2.4 End Station

HiRMES (High Resolution Multichannel Electron Spectroscopy) is the name given to the end station that was used for the experiments undertaken on beamline 3.2. This end station was developed by Dr David Teehan of the Experimental System Group (ESG) of SRD at Daresbury. HiRMES consists of an ultra high vacuum (UHV) system with re-optimised pumping, a liquid helium cryogenic sample manipulator and a Combined Lens Analyser Module (CLAM-4) spherical sector analyser [35]. After the developments made on HiRMES and post-focusing optics in 2005, the beamline now provides a much improved beam spot. The improvements made on beamline 3.2 have made possible new photoemission studies of solid surfaces and nanostructures using the synchrotron radiation source. The HiRMES UHV chamber is made from mu-metal (77% Ni, 15% Fe, plus Cu and Mo) which screens the interior from weak magnetic fields (i.e. the earth's magnetic field). The chamber is fitted with an RGA mass spectrometer and a sample scraping assembly. The manipulator can be turned through 360° around a vertical axis along with translational motions on x, y, z axes to align the beam spot on the sample under investigation. The sample can also be cooled using liquid helium.

3.4.3 Daresbury Laboratory Station MPW 6.1

3.4.3.1 The Beamline

Part of the current work was carried out on the XUV 6.1 beamline at the SRS. The beamline, called PHOENIX, was established in 1998 to exploit the output from a multipole wiggler (MPW) for surface science, nanotechnology and atomic/molecular experiments.

The MPW is an insertion device of length 1 m fitted with 9 full poles and 2 half poles that generate a magnetic field of period 0.2 m. The photon flux output from it ranges from 40 to 320 eV and can be adjusted according to the requirements of the experiment. It produces a peak axial magnetic field of 2 T at the operating gap of 20 mm. Figure 3.18 shows a graph of photon flux versus photon energy for the MPW and it can be seen here that its output flux is about 10 times greater than that of a bending magnet.

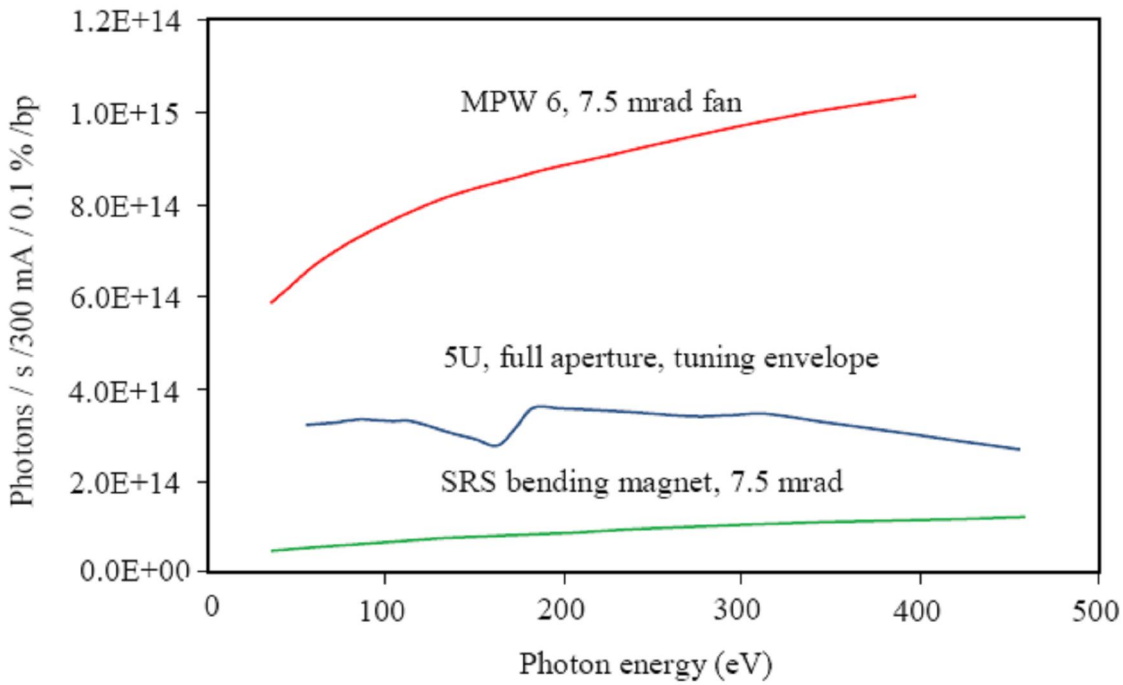

Figure 3.18: *Comparison of the MPW flux output with other insertion devices at the SRS* (*Taken from* [36]).

Figure 3.19 depicts a schematic layout of the beamline optics. After the MPW, there are two pre-focusing mirrors M_1 and M_2. M_1 is used for horizontal focusing while M_2 is used for vertical focusing of the beam onto the entrance slit of the spherical grating monochromator. Both the mirrors are gold-coated with the polished side of silicon as a substrate. These mirrors are water-cooled as extreme power loading is involved. After every refill of the beam, the angle of these mirrors must be readjusted to optimise the output flux.

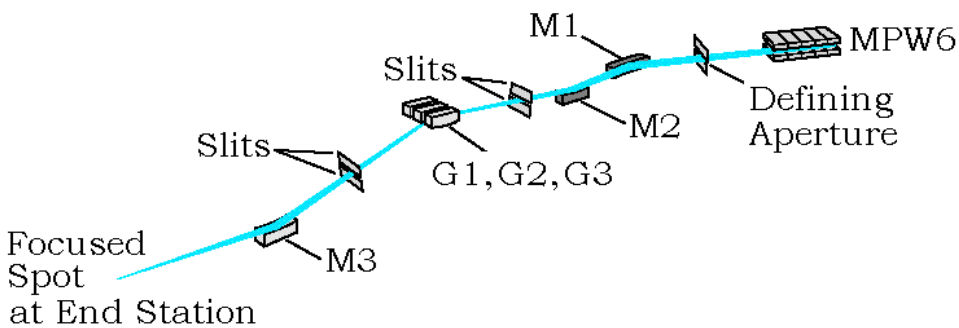

Figure 3.19: *Schematic layout of Daresbury SRS beamline MPW 6.1* (*Taken from* [36]).

Prior to the monochromator, there is an entrance slit which receives white light and after the monochromator there is an exit slit which provides monochromatic light. There are three gold-coated and fused silica gratings inside the grating housing. The first grating, with line density of 300 lines/mm, is called the low-energy grating (LEG) and provides photon energy in the 40-80 eV range. The second one is the medium-energy grating (MEG), with 600 lines/mm, and covers the 80-160 eV photon energy range. The third grating is called the high-energy grating (HEG), with line density of 1200 lines/mm, and gives energy output of 160-320 eV. The monochromatic light that emerges from the exit slit of the monochromator, with a spot size less than 1 mm^2, is refocused using the toroidal mirror M_3 whose adjustment is not under user control. To acquire optimum resolution of the monochromator, the widths of both the entrance and the exit slits can be adjusted by computer-controlled stepper motors. Table 3.2 shows the measured resolution of LEG, MEG and HEG at photon energies of 60 eV, 144 eV and 264 eV respectively. Beamline 6.1 has also been provided with three pairs of baffles B_1, B_2 and B_3 in addition to the energy resolution defining slits. These baffles are situated prior to the entrance slit, prior to the grating and prior to the toroidal mirror respectively and can be brought in to block the path of the beam. Careful modification in the baffle settings can improve resolution and reduce scattered light but at the expense of intensity of the beam.

Slit width μm	Resolution/eV (60 eV)	Resolution/eV (144 eV)	Resolution/eV (264 eV)
20	0.010	0.037	0.054
50	0.022	0.068	0.109
100	0.043	0.127	0.210
200	0.085	0.249	0.415

Table 3.2: *Beamline 6.1 linewidth contributions at various photon energies* (*Adapted from* [36]).

As the monochromator contributes to the flux throughput from higher order at any particular wavelength, thin metal foils can be placed in the path of light to absorb this higher order radiation. The available foils are 1014 Å aluminium, 2949 Å boron and 2704 Å carbon. The aluminium filter has a peak transmission of about 82 % and is suitable when working in the 40-72 eV photon energy range. The boron filter works well in the 70-180 eV photon energy range with a peak transmission of about 80 %. The third filter *i.e*. the carbon one also has a peak transmission of about 80 % and is used when dealing with photon energies between 100 eV and 280 eV. A manual control console allows grating change, baffle control and in-line filter change from within the hutch. For normalisation purposes, a drain current from an aluminium mesh is used for flux measurements on the end station. The beamline appears to become more and more unstable with time due to warming of the optics during use and causes a drift in the position of mirror M_2. Consequently the flux of the beam drops and needs re-optimisation of the tilt on mirror M_2. After every refill of the beam at the SRS, the zero order position needs resetting to correct for any movements. This is done by scanning the wavelength and re-determining the value at which the maximum flux occurs.

3.4.3.2 Flux

To measure the output of the spherical grating monochromator as a function of photon energy, the resolution was set to 50 meV by adjustment of both the entrance and the exit slits. The photo-current from a Si diode was recorded for different values of photon energy. Figure 3.20 [37] depicts the graph of photon flux versus photon energy for beamline 6.1 for each grating. Dashed lines represent the data recorded, whereas solid lines indicate predicted values. A severe dip at 270 eV due to contamination by carbon can also be seen.

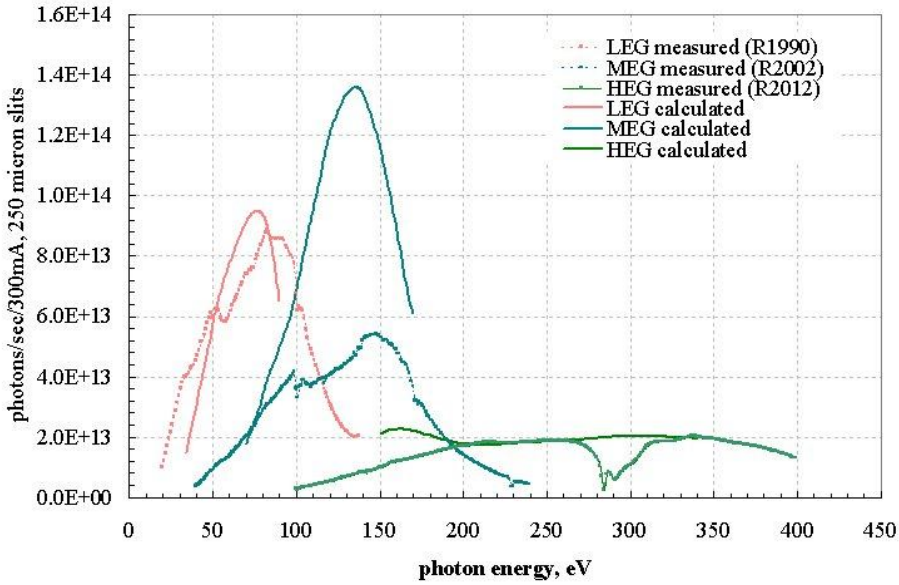

Figure 3.20: *Comparison of measured* (*dashed lines*) *and calculated* (*solid lines*) *flux of beamline MPW6.1* (*Taken from* [37]).

However the flux of the beam has greatly been improved through a recent *in situ* ozone treatment. The improved results especially for the LEG and the HEG are in good agreement with the calculated values. The peak outputs from LEG, MEG and the HEG were recorded at around 80 eV, 144 eV and 264 eV respectively.

3.4.3.3 Resolution

The beamline resolution was measured on the LEG by recording the widths of neon and helium absorption lines. A comparison between the measured and the predicted values is shown in Figure 3.21. A reasonable agreement with the calculated values for neon absorption can be seen of 11 meV (at 46 eV photon energy with 10 µm slits) and 20 meV (at 64 eV photon energy with 10 µm slits).

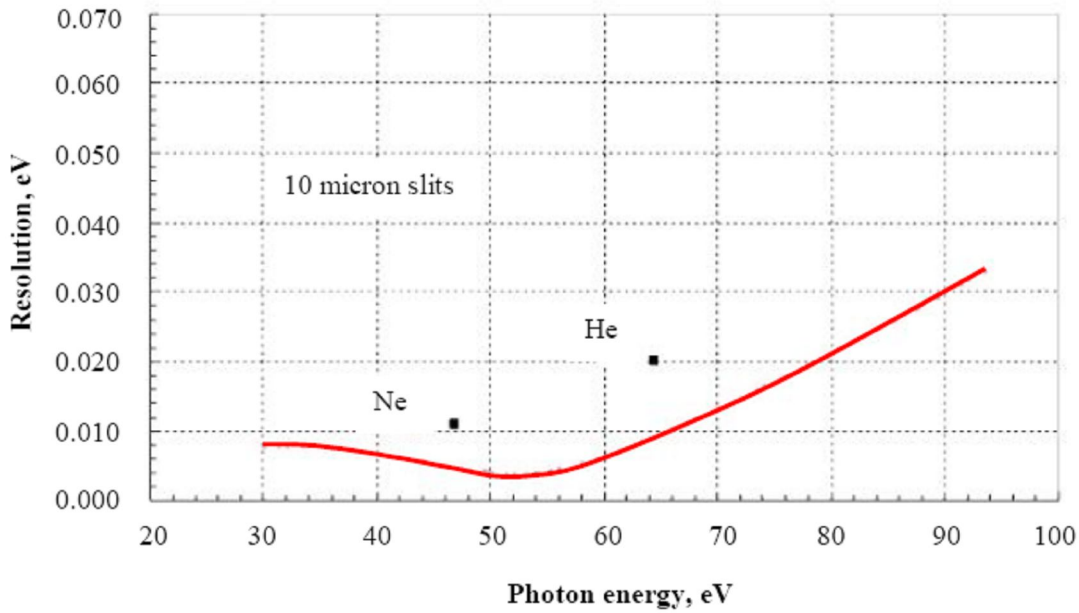

Figure 3.21: *Comparison of calculated* (*solid lines*) *and measured* (*dots*) *resolution for the low energy grating on MPW6.1* (*Taken from* [32]).

3.4.3.4 End Station

The end station used for the experiments on beamline MPW 6.1 was on ARUPS 10 system supplied by VG Microtech Ltd. The station comprises a large two-level ultra-high vacuum chamber with an internal diameter of 457 mm. It is made of 5 mm thick mu-metal which prevents magnetic fields from penetration and can withstand vacuum pressures greater than 10^{-10} mbar. The chamber is cylindrical and provided with numerous ports of various sizes where observation windows, excitation sources, sample manipulators, sample scraping assembly, pumps and electrical connections can be attached. The chamber is mounted on a custom designed portable frame which provides supports to the chamber pumping system. The combination of vacuum pumps used with the end station consists of a Varian ion pump, a water cooled Pfeiffer 520 turbo pump that is backed by an Alcatel Drytel rotary pump, and a titanium sublimation pump. Using this combination of vacuum pumps, a vacuum pressure of 1×10^{-10} mbar is usually achieved inside the chamber after 'bake out'. Equipment for analyser control and data collection is mounted in a separate control rack.

3.5 Vacuum Conditions

The key element to surface science experiments is an ultra-high vacuum (UHV). Generally, the term vacuum means a position of space which contains a gaseous pressure significantly less than 1 bar. For photoemission experiments, UHV is achieved for two main reasons; first, the photoelectrons emitted from the sample under investigation should collide with as few residual gas molecules as possible. In this way, they will not be lost or scattered on their way to the analyser. This requires a high vacuum of the order of 10^{-6} mbar. Second, a clean surface of the sample is required to receive true signal from it as long as the experiment is carried out. The level or quality of vacuum acquired is judged by the amount of residual matter present inside the main vacuum chamber.

A perfect vacuum with gaseous pressure equal to zero is a hypothetical concept so residual gas molecules are always present inside the main chamber. Hence contamination on the surface of the sample builds up over a period of time. From kinetic theory of gases, the arrival rate R of molecules striking the surface is given by [38]:

$$R = \frac{dN}{dt} = \frac{P}{\sqrt{2\pi mkT}} = \frac{3.51\times10^{22}P}{\sqrt{MT}} \text{ molecules cm}^{-2}\text{ s}^{-1}, \qquad \text{Equation 3.14}$$

where P is the pressure in torr, m is the molecular mass in kg, M is the molecular weight and T is the absolute temperature.

The arrival rate of molecules of a particular species of residual gases such as nitrogen (M = 28) to a particular surface, at room temperature (293 K) and a pressure of 1 torr, is 3.88×10^{20} molecules $cm^{-2}s^{-1}$. This shows that for an ideal condition where the sticking coefficient of residual gases is 1, a clean sample placed in a vacuum chamber at a pressure of 1 torr will be contaminated with one monolayer (a complete single atomic layer contains ~10^{15} atoms cm^{-2}) in approximately 3×10^{-6} seconds. To maintain a slow rate of contamination on the sample surface, during a photoemission experiment which usually lasts for several hours, a vacuum of the order of 10^{-10} torr is generally maintained.

3.5.1 Baking

In order to acquire vacua in a short time, a bakeout of the whole vacuum system is performed. In a typical bakeout, first the heat-sensitive parts of the chamber are covered with aluminium foil and then the whole chamber is wrapped by some heat resistant covering. The whole system is heated to around 180° C and this heating process lasts for about 12 hours. The heating removes impurities adsorbed on the walls of the vacuum system and the vapour pressure of the chamber increases temporarily. When the impurities are desorbed and pumped out, then the heating process is switched off and the system is cooled down to room temperature to reduce the rate of adsorption. In this way the gas load on the pumps is reduced and a lower pressure is maintained.

3.5.2 Vacuum Pumps

Vacuum pumps are used to produce, improve and/or maintain a vacuum by removing gas molecules from a sealed volume where the sample under investigation is placed. The vacuum pumps can be divided into two categories: entrapment and gas transfer or momentum transfer pumps based on the techniques employed in them. The gas transfer pumps are further divided into positive displacement and kinetic pumps. In positive displacement pumps, repeated volumes of residual gas are exhausted into the atmosphere. On the other hand in kinetic pumps to generate vacuum, a momentum is given to the gases to take them away from the vacuum chamber. In entrapment pumps, a sorption or condensation technique is used and the pumps capture residual gases in a solid or absorbed state on their internal surfaces [39, 40].

Ultra high vacuum can be produced by using several combinations of vacuum pumps depending upon the requirement of the experiment. The pumps used in this work are briefly described here.

3.5.3 Turbomolecular Pump

The turbomolecular pump shown in Figure 3.22 is a momentum transfer pump. It consists of a rotor fitted with a series of specially designed slotted discs or blades. The blades on the rotor rotate between the corresponding stators (having gas transfer holes in them) driven by of a water-cooled electric motor. The speed of the motor can be controlled within a range of

20,000-50,000 rpm. As the blades rotate with the rotor, they have impact with the molecules of the gas coming from the inlet and their mechanical energy is used up in giving momentum to the gas molecules. The molecules are directed to the exhaust port while passing through the holes of the stator and finally drawn off by the backing pump.

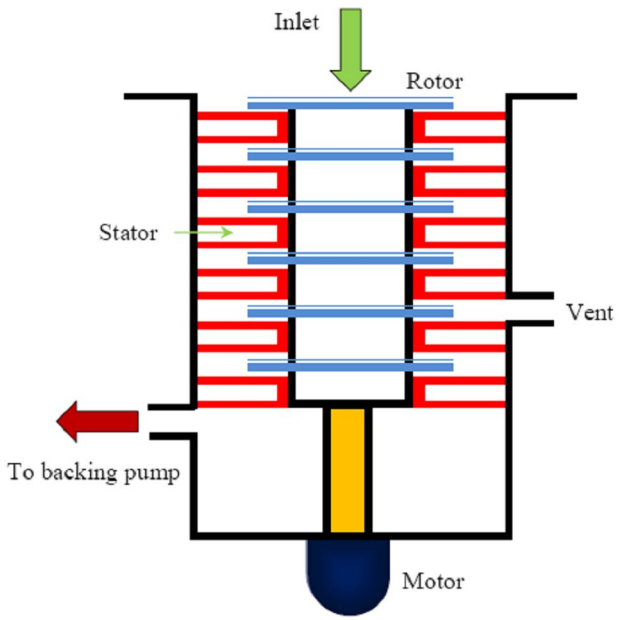

Figure 3.22: *Cross section of a turbomolecular pump* (*Adopted from* [39]).

3.5.4 Ion Pump

In an ion pump, gases are retained by sorption or condensation on the internal surfaces instead of directly passing to the backing pump. This pump belongs to the category of entrapment pumps. Sputter ion pumps do not require cooling but need a pre pressure of at most 10^{-4} mbar in the main vacuum chamber. Figure 3.23 shows a cross section of a sputter ion pump which consists of a pair of cathodes made of titanium and a stainless steel cylindrical anode along with an applied transverse magnetic field. A high electric potential applied between the pair of cathodes and the anode ionises the gas molecules. The highly energetic positive ions are attracted towards the titanium cathodes and cause sputtering of titanium on the surfaces of the pump. The pumping of the gas takes place by two mechanisms: a chemical reaction between the active gas molecules and fresh titanium, and burial of the original ions in the bulk titanium plate. These pumps operate in the pressure range of 10^{-8}-10^{-10} mbar.

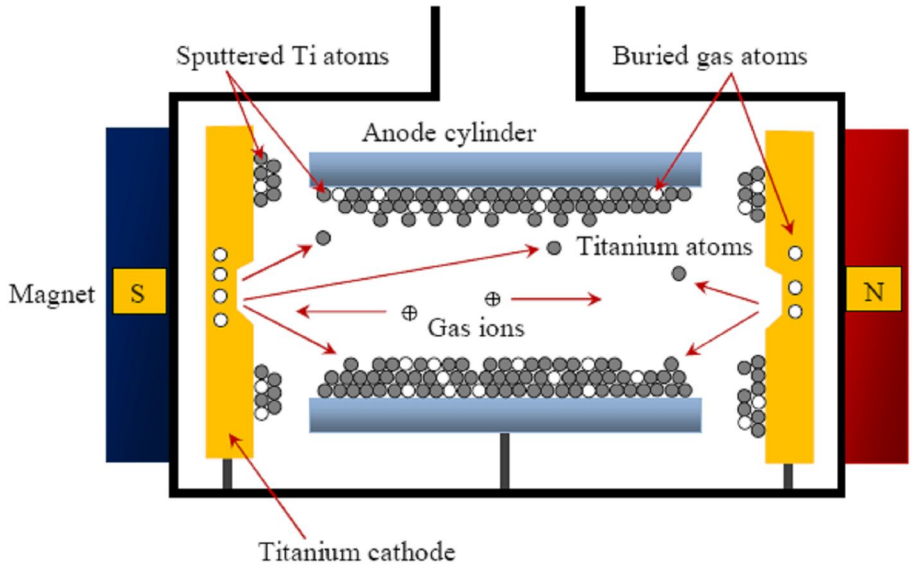

Figure 3.23: *Schematic diagram of a sputter ion pump* (*Adapted from* [15]).

3.5.5 Titanium Sublimation Pump (TSP)

A titanium sublimation pump is a kind of auxiliary pump. A typical TSP shown in Figure 3.24 comprises a chamber fitted with a titanium/molybdenum alloy filament. When the filament is heated by passing an electric current through it, titanium vapours are produced which condense on the liquid nitrogen-cooled surrounding surfaces. Later, these vapours react chemically with the active gases present in the vacuum chamber to form stable compounds such as titanium oxides. As the vaporisation process continues, further layers of active titanium are deposited. The pumping speed of the TSP depends on the surface area and temperature of the titanium layer. A TSP is particularly useful when operated in short bursts to lower the pressure from 10^{-8} to 10^{-10} mbar.

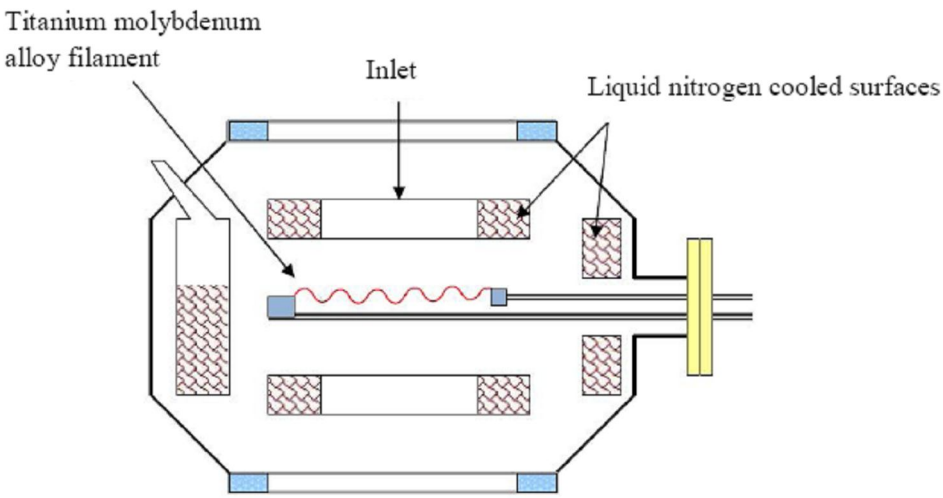

Figure 3.24: *Schematic diagram of a titanium sublimation pump* (*Adapted from* [39]).

3.6 Pressure Measurement

For a photoemission experiment, the measurement of total pressure in a vacuum system is important. To produce a vacuum in a surface science experiment, an extreme large range of pressures is involved (from atmospheric down to 10^{-12} mbar or less). Therefore it is not possible to measure the whole range with a single pressure-measuring instrument. A pirani gauge measures the pressure in the $0.5\text{-}1\times10^{-3}$ mbar range while an ion gauge covers a range of $10^{-3}\text{-}10^{-11}$ mbar. These are described in sections 3.6.1 and 3.6.2.

3.6.1 Pirani Gauge

An electric circuit called a wheatstone bridge is used in a pirani gauge which is suspended in a tube connected to the system whose pressure is to be measured. The sensing element is a hot filament (in one arm of the wheatstone bridge) whose temperature and hence resistance changes with gas pressure. When the molecules of the gas collide with the hot filament, they take away heat from it. If the pressure of the gas decreases, then the number of collisions between the molecules and the filament also decrease proportionally and subsequently the temperature of the filament increases.

3.6.2 Ion Gauge

Ion gauges are the most sensitive instruments to measure pressure. The working principle of an ion gauge is based on the measurement of the ions produced when a gas is bombarded with electrons. Fewer ions will be produced at lower density of the gas. Figure 3.25 shows the cross section of a conventional ion gauge which consists of a thermionic filament F, a cylindrical open mesh grid G and an ion collector C. The collector is earthed and the grid is at a relatively higher positive potential than that of the filament. Electrons are produced by thermionic emission from F and accelerated towards the grid. The majority of the electrons passes through the mesh and ionise the gas molecules on their way to the collector. The positive ions thus produced are attracted towards the collector to produce ion current which is proportional to the gas pressure.

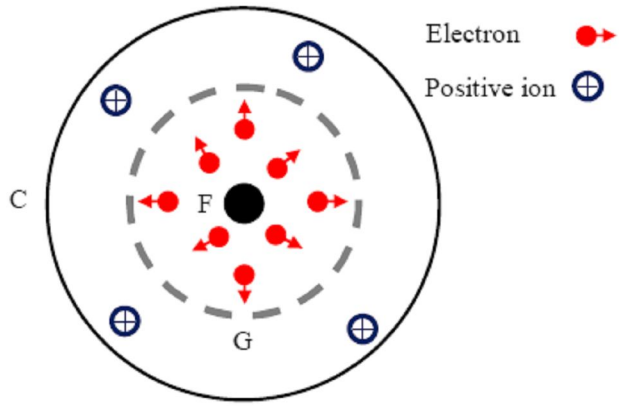

Figure 3.25: *Cross section of an ion gauge* (*Adapted from* [39]).

3.6.3 Quadrupole Mass Spectrometer

To measure partial pressures and to monitor the composition of any gases in the vacuum chamber, a device such as quadrupole mass spectrometer is used. Quadrupole mass spectrometers are the most widespread systems in vacuum technology and can measure masses in 1-100 a.m.u. range. A quadrupole mass spectrometer (Figure 3.26) comprises three main parts: an ioniser, a quadrupole mass filter and an ion detector.

In the ioniser, the gas molecules are ionised by bombarding them with accelerated electrons just as in the ion gauge. The positive ions are accelerated toward the quadrupole mass filter.

The quadrupole comprises four parallel metal bars which set up an electric quadrupole field as a result of a superposition of DC and radio frequency AC voltages. The filter lets pass through only those ions which have mass/charge ratio for a given ratio of voltages. Finally these ions are detected by the ion detector containing an electron multiplier. The multiplier can amplify the signal by a factor of 10^4-10^6. Partial pressures with a lower limit of about 10^{-14} mbar can be measured with such a spectrometer.

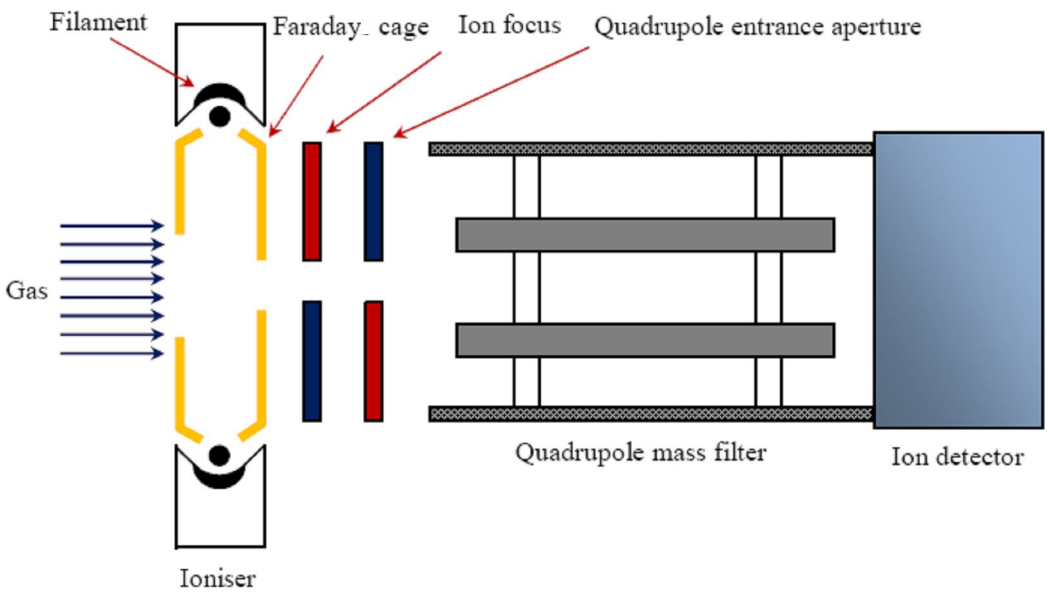

Figure 3.26: *Schematic layout of a quadrupole mass spectrometer* (*Adapted from* [43]).

An RS232C cable is used to transfer data from the detector to a computer. Software installed on the computer displays spectra of the residual gas pressure as a function of a.m.u., the residual gas pressure as a function of time, a bar graph of recordings and a large range of other display modes.

3.7 Electron Energy Analyser

The analyser used for the experiments on both beamlines was a VG Microtech CLAM-4 analyser connected with a 20-way multichannel detector based upon a twin michrochannel assembly. The analyser has four slits of sizes 5.0, 1.5, 0.5, 0.15 mm [45]. The CLAM-4 shown in Figure 3.27 is a mu-metal shielded hemispherical type of electron/ion analyser.

The hemispherical electron analyser has a mean radius of 150 mm, port size FC100 and 300 mm port length.

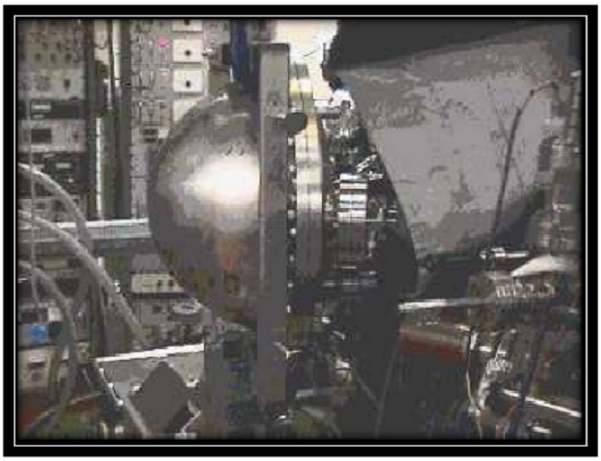

Figure 3.27: *CLAM-4 analyser* (*Taken from* [44]).

The analyser has three main components: the electrostatic lens, the hemispherical analyser and the detector (channeltron, channel plates). The lens focuses the photoelectrons emitted from the sample on to the hemispherical analyser entrance slit while the analyser analyses the electrons. The working principle of the analyser is shown in Figure 3.28.

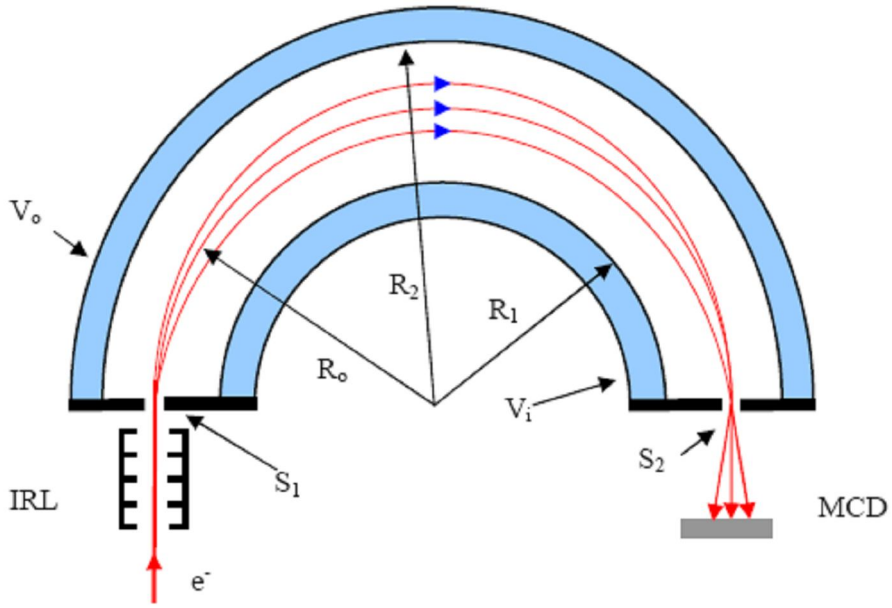

Figure 3.28: *Schematic diagram of a hemispherical analyser, where S_1 =* the entrance slit, *S_2 =* the exit slit, *V_i = inner hemisphere* (*negative*) *potential, V_o = the outer hemisphere* (*negative*) *potential, R_1 = inner hemisphere radius, R_2 = outer hemisphere radius, R_o = radius of average electron path,* MCD = *multichannel detector assembly and* IRL = *input retardation lens* (*Adapted from* [6]).

The electrons are retarded by the input retardation lens (IRL) prior to entering the analyser. A hemispherical analyser mainly consists of two concentric hemispheres. It works by deflecting and focusing the electrons that enter into it using the electric field produced between the inner and the outer hemispheres. V_o and V_i are the values of the negative potentials at the outer and the inner hemispheres respectively. The entrance slit S_1 is held at the electrical midpoint of V_o and *Vi*. The values of V_o and V_i are adjusted in such a way that the electrons make their way in the space between the two hemispheres towards the multichannel detector (MCD). Higher energy electrons have larger radii of curvature than those of lower energy. By scanning the potential S_1, successive groups of electrons are brought into a condition where they can pass through the analyser, to the detector, without striking one or other of the hemispheres.

The potential difference between the two hemispheres multiplied by the electron charge is known as the pass energy, E_p, of the analyser. During high resolution photoemission

experiments carried out at beamline 3.2, a pass energy of 5-10 eV was used for the EDC scans. The pass energy E_p is related to the inner and the outer radii R_1 and R_2 respectively, by the following equations:

$$V_x = V_0\left[3 - \frac{2R_0}{R_x}\right], \qquad \text{Equation 3.15}$$

where x = 1 or 2(for inner or outer hemispheres),

$$\Delta V = (V_2 - V_1) = V_0\left[\frac{R_2}{R_1} - \frac{R_1}{R_2}\right], \qquad \text{Equation 3.16}$$

$$E_p = eV_0 = e(V_2 - V_1)\left[\frac{R_1 R_2}{R_2^2 - R_1^2}\right]. \qquad \text{Equation 3.17}$$

where,

R_0 = *Electron central path radius,* V_1 = *Inner hemisphere potential,*

R_1 = *Inner hemisphere radius,* R_2 = *Outer hemisphere radius,*

V_2 = *Outer hemisphere potential,* e = *Electron charge,*

V_0 = *Potential at electron path,* E_p = *Pass energy.*

The energy resolution depends upon the pass energy of the analyser. By lowering the pass energy, the potential difference between the hemispheres decreases and this reduces the energy spread of the electrons allowed to traverse the analyser for a particular setting of the retard voltage on slit S_1. Hence, consequently the energy resolution improves. Equations 3.18 and 3.19 [6] given below define the factors influencing instrumental resolution:

$$R_a = \Delta E, \qquad \text{Equation 3.18}$$

$$R_r = \frac{\Delta E}{E_p} = \frac{\Delta E}{e(V_2 - V_1)}\left[\frac{R_2^2 - R_1^2}{R_1 R_2}\right], \qquad \text{Equation 3.19}$$

$$R_T = \sqrt{R_r^2 + R_B^2}\ . \qquad \text{Equation 3.20}$$

where,

R_a = *Absolute analyser resolution,* R_T = *Total instrumental resolution,*

R_r = *Relative analyser resolution,* ΔE = *Energy spread* (FWHM),

R_B = *Beamline resolution* (*dependant on slits, analyser focus, etc.*).

The absolute resolution R_a of the analyser depends upon the energy spread ΔE which is also a function of input slit, exit slit and the input lens (or retarding lens). The electric field of the input lens controls the kinetic energy of the electrons and collimates their path as well giving maximum accuracy to the hemisphere by retarding the electrons. The strength and configuration of the fields inside the hemisphere and the lens ultimately determine the final resolution and the value of the kinetic energy of electrons. The kinetic energy of the electrons is given by equation 3.20 [6],

$$E_k = E_p + V_r + \Phi_a. \qquad \text{Equation 3.20}$$

where,

E_K = *Kinetic energy of detected electron,* V_r = *Retarding potential*
E_p = *Pass energy* Φ_a = *Analyser work function.*

3.8 Electron Detectors (Counters)

In order to construct an energy distribution curve from the analysed photoelectrons, at a given kinetic energy within the desired kinetic energy range, it is necessary to count them. In electron spectroscopy, the magnitude of the current produced by the photoelectrons is usually too small to be detected directly with a reasonable signal-to-noise ratio (which requires an electron current of at least 10^{-15} A [46]). Therefore, it is necessary that the electrons must be multiplied to be able to count them. Multichannel detectors (MCDs) which have multiple readout channels serve this purpose and are much better than single channel detector (SCD) systems such as resistive anode detectors.

In the current photoemission work, photoelectrons were detected by micro-channel plates (MCPs) which had comparatively high gain. The characteristics and the performance of the MCPs can be found elsewhere [21, 47]. A multichannel plate (MCP) comprises an annular array made of thousands of tiny glass capillaries fused together that act as independent

electron multipliers. To accelerate electrons from one side of the capillary to the other, usually a potential difference of 2.2 kV is applied across the MCPs. When the electrons, as a result of this potential difference, are accelerated deep down the capillaries, they have many collisions with the walls and produce many secondary electrons. These electrons strike further against the walls to develop an avalanche of secondary electrons which emerges from the other side of the capillaries and hits an anode to generate a detector signal.

To achieve a high gain, the performance of the MCPs can be improved by stacking them on top of one another with opposite tilt direction as shown in Figure 3.29. Gains of between 10^6 and 10^7 are readily obtainable with the MCPs. There are two parameters: aspect ratio (channel length/diameter) and quantum efficiency (QE) value which govern the performance of the MCPs. The gain of the MCPs is proportional to the aspect ratio and the QE value depends upon the probability that the incoming electron liberates at least one

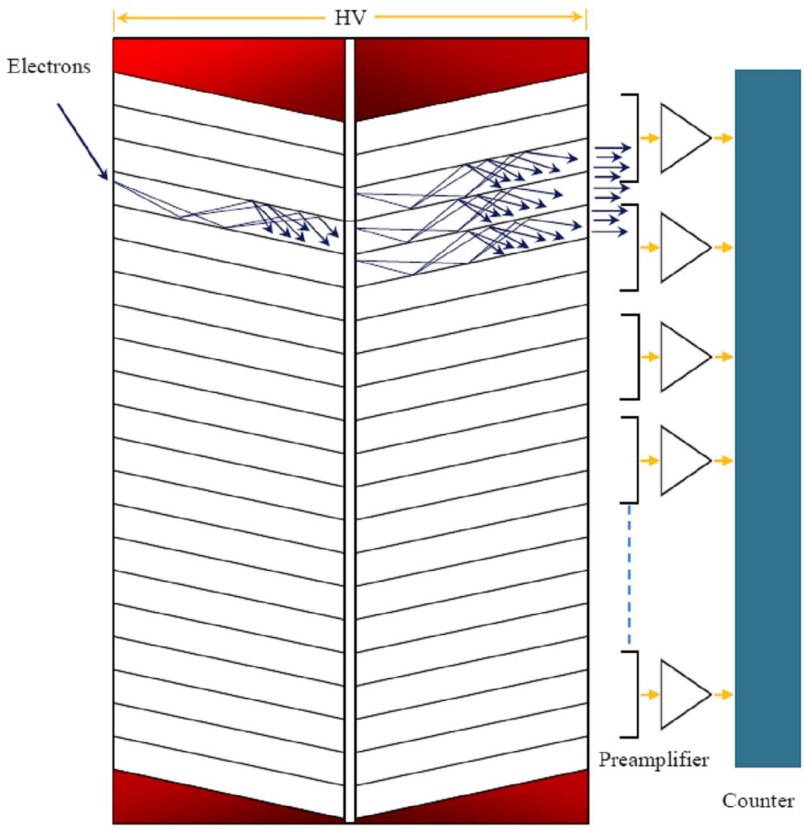

Figure 3.29: *Schematic diagram of multichannel plates* (*Adapted from* [5]).

electron from the MCP surface and finds its way into a capillary to initiating an avalanche. The QE value for a particle such as an electron, with a few hundred eV KE, is about 50 % or higher.

3.9 Modes of Operation and Analyser Controls

The CLAM-4 analyser can be operated in two modes, Constant Analyser Energy (CAE) mode and Constant Retard Ratio (CRR) mode. The CAE mode is generally preferred when the peaks tend to be of high K.E (e.g. XPS) while the CRR mode is used in AES where peaks are broad and generally lower in K.E.

The CLAM-4 analyser does not have any manual control. All the functions of the analyser, including the MCP, are controlled electrically through the signals from the lens supply, the spectrometer control unit (SCU), the rate meter, multiplier supply unit and the digital panel meter. A (CAMAC) crate converts the analogue voltage signal from the transducers into a signal from the various measuring devices simultaneously [45].

3.10 Sample Manipulation

The cobaltite samples used for photoemission experiments were mounted on a metallic sample holder using a silver-loaded epoxy-resin. The sample plate itself was mounted on a liquid helium manipulator. One narrow-bore stainless steel tube took liquid helium from the end of the transfer tube to a copper block onto which sample stages were bolted; another stainless steel tube was connected via the transfer siphon to a pump which drew helium through by pumping away the boil-off gas. The entire range of temperature (20-406 K) was accurately controlled by a good combination of helium gas flow and the heaters provided.

References

[1] R. A. Serway, R. J. Beichner, John W. Jewett, *Physics for Scientists and Engineers*, Saunders College Pub. (1990).

[2] H. Hertz, Wiedemannsche, *Ann. Phys*, **31**, 982 (1887).

[3] T. Barr, *Modern ESCA*, CRC Press, Boca Raton (1994).

[4] A. Einstein, *Ann. Phys*, **17**,132 (1905).

[5] http://www.amptek.com/a111aray.gif

[6] D. Tsoutsou, PhD Thesis, The University of Manchester (2005).

[7] E. Bellin-Ferre, *J.Physics.Conds. Matter*,**13**, 7885 (2001).

[8] P. Kirkham, PhD Thesis, The University of Manchester (2009).

[9] J. Purton, Daresbury Lab station 5u.1, http://www.srs.ac.uk/srs/stations/station 5u.1.htm.(2001)

[10] S. Patel, Daresbury Laboratory, Multipole Wiggler Station MPW 6.1"PHOENIX", http://www.srs.ac.uk/srs/stations/station 6.1 (2006).

[11] P. A. Cox, *The Electronic Structure and Chemistry of Solids*, Oxford University Press, Oxford (1987).

[12] D. Briggs and M. P. Seah, *Practical Surface Analysis-Auger and X-ray Photoelectron Spectroscopy*, Vol.1, Wiley, New York (1990).

[13] A. Goldman, J. Tejeda, N. J. Shevchik and M. Cardona, *Phys. Rev. B*, **10**, 4388 (1974).

[14] J. Stohr, NEXAFS *Spectroscopy, 2nd edition ,Vol*. **25**, Springer, pg 400 (1996).

[15] J. Hollingworth, PhD Thesis,UMIST (1999).

[16] M. P. Seah and W. A. Dench, *Surf. Int. Anal*.,**1**, 2 (1979).

[17] G. Attard and C. Burnes in *Surfaces*, Spectroscopic *Techniques for Probing Solid Surfaces*, Oxford University Press, Oxford (1998).

[18] A. J. Roberts, PhD Thesis, UMIST (1995).

[19] K. Siegbahn, C. N. Nordling, A. Fahlman, R. Nordbery, K. Hamrin, K. Hedman, G. Johansson, T. Bergmark, S.E. Karlsson, I. Lidgren, B. Lindberg in *ESCA:Atomic,*

molecular and Solid State Structure Studied by means of Electron Spectroscopy, Almqvist and Wiksells,Uppsala (1967).

[20] R. J. Nauman http://matsci.uah.edu/ (2006).

[21] G. W. Fraser, E. Mathieson, K. D. Evans, D. H. Lumb and B. Steer *Nucl. Instrum. Methods*, **180**, 225 (1981).

[22] A. G. Thomas, W.R.Flavell, A. R. Kumarasinghe, A. K. Mallick, D.Tsoutsou, and G. C. Smith. *Phys. Rev., B*, **67**,035110 (2003).

[23] http://sls.web.psi.ch/view.php/beamlines/sis/research/PRES_Falub.pdf

[24] G. D. Marr, PhD Thesis, UMIST (2001).

[25] G. Margaritondo, *Elements of Synchrotron Light*, Oxford University Press (2002).

[26] W. R. Flavell, Lecture Notes, UMIST (2002).

[27] W. R. Flavell, Advanced Experimental Techniques Course Notes, p.82 (2003).

[28] J. D. Jackson, *Classical Electrodynamics*, Wiley New York (1975).

[29] A. Hofmann, *Phys. Reports*, **64**, 253 (1980).

[30] H. Winick and S. Doniach, *Synchrotron Radiation Research*, Plenum Press, New York and London (1980).

[31] A. R. Kumarasinghe, PhD Thesis, UMIST, Manchester, 304 (2004).

[32] http://srs.dl.ac.uk/XUV-VUV/science/mpw6.1/training/sld023.htm

[33] http://srs.dl.ac.uk/XUV-VUV/science/MANUALS/32/32man2.html.

[34] http://srs.dl.ac.uk

[35] http://www.srs.ac.uk/srs/news_archive05.html

[36] http://srs.dl.ac.uk/XUV-VUV/science/mpw6.1

[37] http://srs.dl.ac.uk/XUV-VUV/science/mpw6.1/training/sld021.htm

[38] D. P. Woodruff, T.A.Delchar, *Modern Techniques of Surface Science*, Cambridge University Press, 2nd Edition (1994).

[39] A. Chambers, R.K.Fitch and B.S.Halliday, *Basic Vacuum Technology*, IOP Publishing Bristol and Philadelphia 2nd Edition, (1998).

[40] J. F. O. Handon, *A User's Guide to Vacuum Technology*, John Wiley and Sons, Inc., (1980).

[41] N. Harris, *Modern Vacuum Practice*, Mc Graw-Hill Publisher (1989).

[42] R. Benedict, *Fundamentals of temperature, pressure and flow measurement*, 3rd edition, John Wiley & Sons (1984).

[43] A. K.Mallick, PhD Thesis, The University of Manchester (2005).

[44] http://srs.dl.ac.uk/ssl/equipment/CLAM4/clam4.gif

[45] Personal Communication, Andrew Malins, Daresbury Laboratory (2007).

[46] K. Birkenshaw, *J. Mass Spectrom*., **33**, 64 (1998).

[47] J. L. Wiza, *Nucl. Instrum. Methods*,**162**, 589 (1979).

Chapter 4

Surface Degradation of Cobaltite Surfaces

4.1 Introduction

This thesis presents and discusses temperature-dependent photoelectron spectroscopy results for $GdBaCo_2O_{5.5}$, $DyBaCo_2O_{5.5}$, $Dy_{1-x}Tb_xBaCo_2O_{5+\delta}$ and $YbBaCo_4O_7$. During the photoemission experiments, the samples were observed to be contaminated due to the residual gases inside the main vacuum chamber. The surface degradation of the samples was checked by the difference spectra generated from the valence band spectra of freshly scraped and contaminated samples. To investigate the nature of the contaminants on the surfaces of the samples, literature related to surface degradation of different metal oxide surfaces by H_2O and CO_2 was reviewed. In the light of the reviewed literature, the nature of contaminated species on these samples was identified. The experimental results concerning stability of the surfaces is important because the surface degradation information is needed in order to differentiate between changes caused by contamination effects and those which occur due to spin state transitions.

4.2 Photoemission Measurements; Surface Degradation

4.2.1 Experimental Procedure

High quality, single crystal samples of $LnBaCo_2O_{5+\delta}$ (Ln = Gd, Dy, $Dy_{1-x}Tb_x$ – Ln-112) and $YbBaCo_4O_7$ (Ln-114) of typical dimension $3\times3.5\times2$ mm^3 were grown at Institute of Solid State and Semiconductor Physics (ISSSP) Minsk, Belarus, using the overstoichiometric flux melt technique thoroughly discussed in Section 2.5. High resolution photoemission of the crystals was performed at beamline 3.2 of the Synchrotron Radiation Source (SRS) Daresbury Laboratory, UK. The crystal samples were mounted, using a silver-loaded epoxy resin, on a copper plate attached to a liquid helium manipulator.

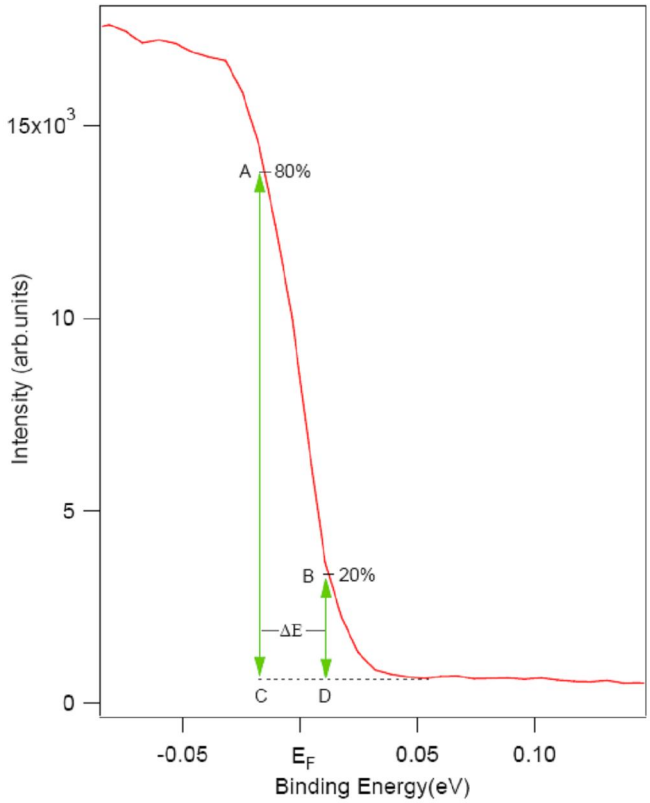

Figure 4.1: *Fermi edge of the copper* (*Cu*) *sample holder at 155 K. Two points A and B are marked at 80% and 20% levels of the total height of the Cu Fermi edge plot respectively relative to background level. The best achieved overall resolution* (ΔE) *on beamline 3.2 was calculated to be 37 meV at 155 K.*

The main experimental chamber was baked out at 180° C for about 30 hours. The vacuum system provided at the beamline comprised a backing pump, a water cooled turbo pump and a titanium sublimation pump (TSP). An ultra high vacuum (UHV) of 1.25×10^{-10} mbar was achieved and maintained by means of this vacuum system. To analyse the energy of the emitted photoelectrons from the samples, a CLAM-4 electron energy analyser was used. A total (monochromator + analyser + natural width of the atomic level) resolution of 37 meV for valence band energy distribution curves (EDCs), estimated from the recorded copper Fermi edge as shown in Figure 4.1, was achieved in the experiment at 155 K. The samples inside the vacuum chamber were prepared for photoemission by successive scrapes with a clean diamond file. The surface cleanliness of the samples were monitored during the experiment until no further changes on scraping were observed using features of the

valence band spectra of $LnBaCo_2O_{5+\delta}$ (Ln = Gd, Dy, $Dy_{1-x}Tb_x$) located around 9.1 eV and 5.1 eV binding energy that were shown later to be associated to surface contamination [1]. After every scrape, the position of the synchrotron radiation beam on the samples was checked using the visible part of the zeroth-order diffraction light from the monochromator. The valence band EDCs were recorded at 30 eV photon energy as a function of temperature in different temperature ranges. All the collected spectra were normalised to the photon flux which was measured independently using a tungsten mesh placed just prior to the point where light enters the experimental chamber. For these samples, the spectra for the valence band (VB), the low energy (LE) states and the Fermi edge (E_F) were recorded in the 0-13 eV, 0-4 eV and 0-1 eV binding energy ranges at pass energies 5 eV, 2.5 eV and 1 eV respectively. Finally, the whole set of photoemission data obtained from the experiments was analysed by using Igor Pro (Version 4.01) software to create data sets and graphs.

4.3 Results and Discussion

4.3.1 General Features of the Valence Band Photoemission of the Double Perovskites $LnBaCo_2O_{5+\delta}$ (Ln = Gd, Dy, $Dy_{1-x}Tb_x$) - Ln-112

Valence band EDCs recorded, as a function of temperature, from single crystal samples of $GdBaCo_2O_{5.5}$, $Dy_{1-x}Tb_xBaCo_2O_{5+\delta}$ and $DyBaCo_2O_{5.5}$, are shown in Figures 4.2, 4.3 and 4.4 respectively. Features labelled by the letters A, B, C and D in the valence band spectra of the double perovskite cobaltites ($LnBaCo_2O_{5.5}$, Ln = Gd , Dy , $Dy_{1-x}Tb_x$) appear at around 1 eV, 3 eV, 5 eV and 9 eV binding energies respectively. The peaks A-C have contributions from Co 3d states [2, 3]. The 4f states, which vary in energy depending on the rare earth element, can be anticipated to be somewhere in the range of C-D and their positions can be determined by resonant photoemission [2, 4]. In general, the density of states (DOS) in the vicinity of the Fermi edge of the valence band of $LnBaCo_2O_{5+\delta}$ (Ln = Gd, Dy, $Dy_{1-x}Tb_x$) is of Co 3d /O 2p character but some rare-earth 4f character near the Fermi energy has also been reported on doping Tb in $DyBaCo_2O_{5+\delta}$ [4].

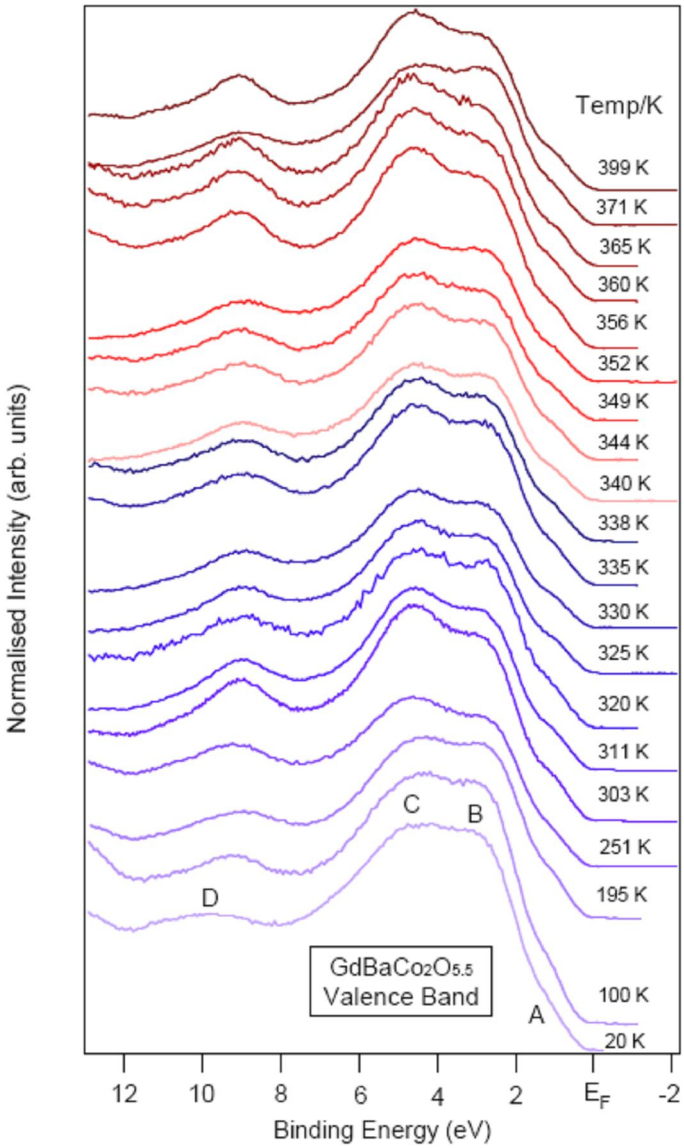

Figure 4.2: *Effect of temperature on the high-resolution valence band EDC spectra of $GdBaCo_2O_{5.5}$. Points A-D were later selected for O 2s→2p resonance photoemission at room temperature* (*Chapter 5*)*. The spectra are normalised to the incident photon flux.*

4.3.2 Temperature Effects on the Valence Band Spectra of $LnBaCo_2O_{5+\delta}$ (Ln = Gd, Dy, $Dy_{1-x}Tb_x$)

Figures 4.2, 4.3 and 4.4 present valence band EDCs of $GdBaCo_2O_{5.5}$, $Dy_{1-x}Tb_xBaCo_2O_{5+\delta}$ and $DyBaCo_2O_{5.5}$ respectively recorded at different temperatures within the range 20-406 K

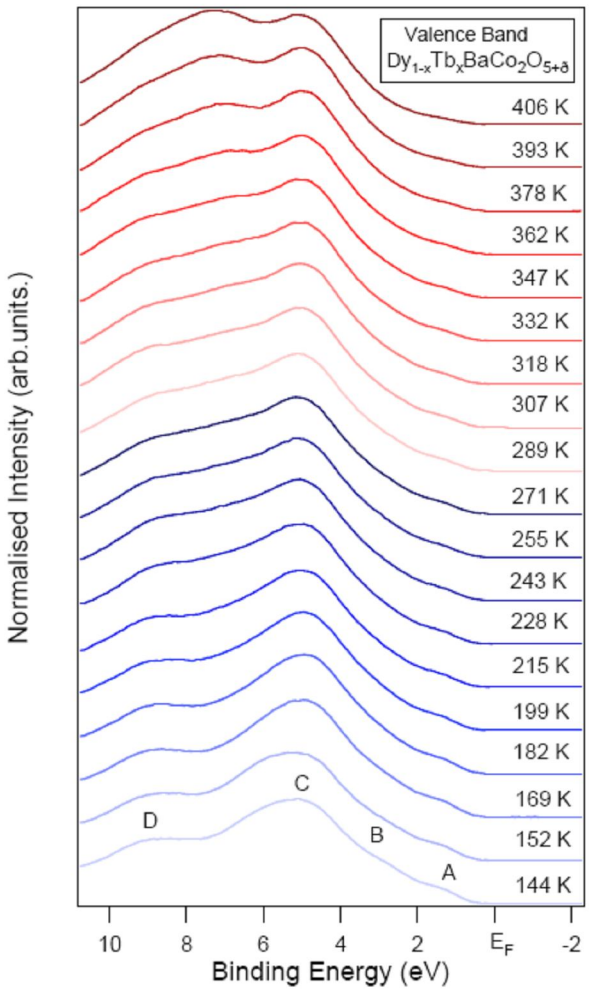

Figure 4.3: *Effect of temperature on the high-resolution valence band EDC spectra of $Dy_{1-x}Tb_xBaCo_2O_{5+\delta}$. The spectra are normalised to the incident photon flux. Points A-C refer to the points later selected for intensity measurement as a function of temperature* (*Chapter 5*).

The spectra have been normalised to the incident flux. The feature at approximately 2 eV binding energy, associated predominantly with Co^{3+} LS states, decreases in intensity slowly

and gradually as the temperature increases. This subtle reduction in intensity as a function of temperature points out the depopulation of the Co LS states which consequently causes the non-metal-to-metal transition in the material. The depopulation of the Co LS states as a function of temperature for $Dy_{1-x}Tb_xBaCo_2O_{5+\delta}$ and the MI transition of all these compounds are discussed later in Sections 5.2.1 and 5.3 respectively.

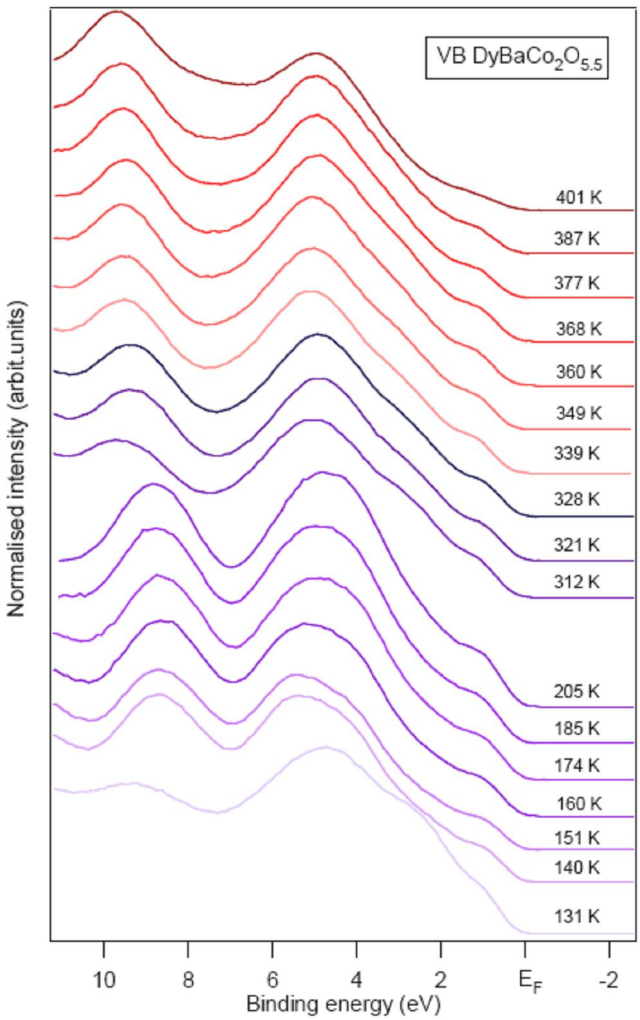

Figure 4.4: *Effect of temperature on the high-resolution valence band EDC spectra of $DyBaCo_2O_{5.5}$. The spectra are normalised to the incident photon flux.*

Here, we are more concerned with the features towards the higher binding energy side in the valence band, which may indicate contamination of the samples because their intensity slightly increases as the temperature increases. The degradation of the sample surface and

the nature of the contaminants for $LnBaCo_2O_{5+\delta}$ and $YbBaCo_4O_7$ are examined by taking difference spectra (contaminated – clean) and are discussed in Sections 4.5.1 and 4.5.2 respectively.

4.3.3 General Features of the Valence Band Photoemission of $LnBaCo_4O_{7+\delta}$ (Ln = Yb;δ = 0) - Ln-114

Figure 4.5 shows a valence band energy distribution curve (EDC) for a single crystal sample of $YbBaCo_4O_7$ showing general features labelled by the letters A, B, C located at 1.4 eV, 5.6 eV and 9.6 eV binding energies respectively in the valence band . The EDC was recorded at room temperature and 21 eV photon energy and later normalised to the incident photon flux. The photoemission on $YbBaCo_4O_7$ has been performed for the first time and the contribution of energy states to peaks A-C in the valence band from the elements present in the compound is thoroughly discussed later in Section 6.3 through resonant photoemission undertaken at room temperature.

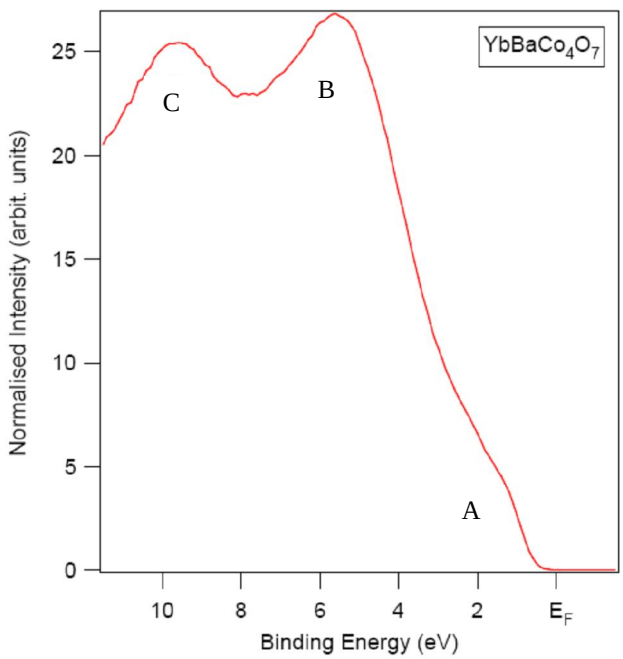

Figure 4.5: *Valence band EDC spectrum of $YbBaCo_4O_7$ showing general features A, B, C. The spectrum was recorded at room temperature and 21 eV photon energy.*

4.3.4 Temperature Effects on the Valence Band Spectra of $YbBaCo_4O_7$

The valence band EDCs for $YbBaCo_4O_7$ shown in Figures 4.6 were recorded within the temperature range 120-300 K. The features A-C were later selected for O 2s→2p resonance photoemission at room temperature. The results of the resonance experiment are discussed later in Section 6.3.3. The spectra are normalised to the incident flux.

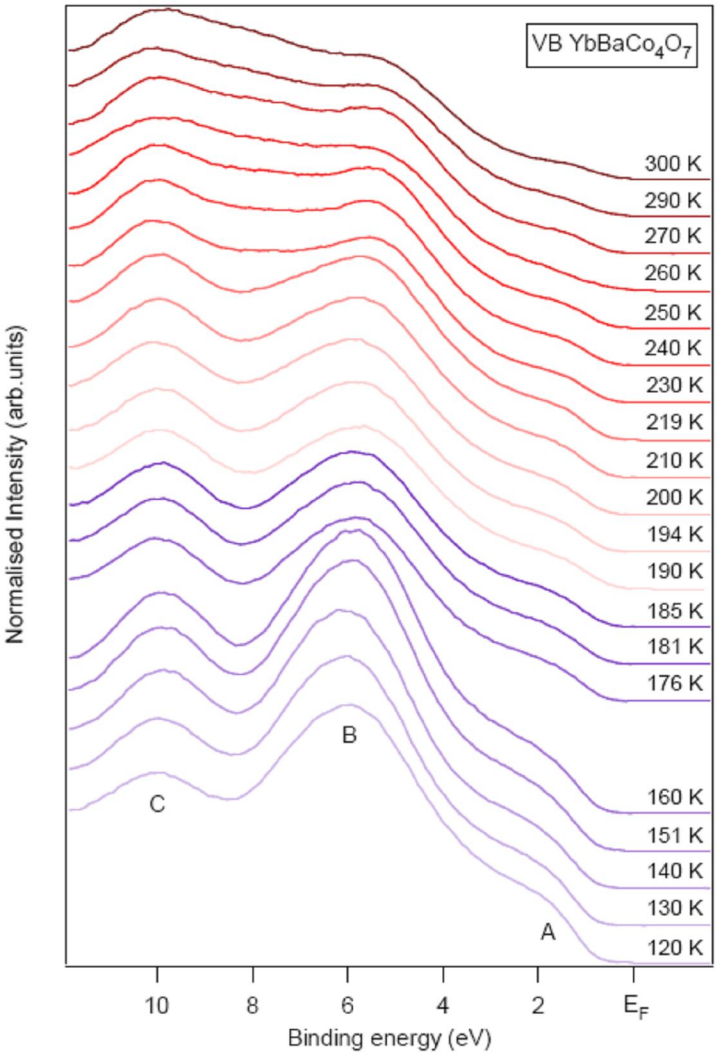

Figure 4.6: *Effect of temperature on the high-resolution valence band EDC spectra of $YbBaCo_4O_7$. Points A-C were later selected for O 2s→2p resonance photoemission at room temperature (Chapter 6). The spectra are normalised to the incident photon flux.*

The feature located around 1.4 eV binding energy in the valence band does not show any significant change with the increase of temperature. On the other hand, the features towards the higher binding energy side of the valence band may indicate contamination of the samples because their intensity considerably changes as the temperature increases. The contamination of the sample surface and the nature of contaminated species are identified by difference spectra (contaminated - clean) and are discussed later in Section 4.5. Moreover, in 230-300 K temperature range, slight dispersion of feature B towards lower binding energy can be observed. The reason for the dispersion is not clear.

4.4 Previous Photoemission Studies of Small Molecule Adsorption and Contamination of Oxide Surfaces

Transition metal and non-transition metal oxide single crystals show different behaviour towards adsorbates [5]. The transition metal oxides (other than d^0 oxides) exhibit greater reactivity towards H_2O and other adsorbate molecules.

Three possible cases arise when water adsorbs on a surface:

(a) physisorption of molecular water;

(b) chemisorption of molecular water (stronger interaction between the substrate and water);

(c) chemisorption of molecular water followed by dissociation.

In physisorption, the interaction between the adsorbate and the substrate is very weak whereas it is much stronger in chemisorption due to a partial charge transfer between the two. Chemisorption has been observed on reactive single crystal surfaces [6].

The water molecular orbitals $1b_2$, $3a_1$ and $1b_1$ have binding energies less than 20 eV. The relative positions of these orbitals can be seen in the molecular orbital energy level diagram for water shown in Figure 4.7.

These orbitals give a three-peaked structure for gaseous H_2O molecules in valence band photoemission spectroscopy (as shown in Figure 4.8) [7]. The separation between these peaks plays a key role in identifying any change occurring in bonding from the molecular to the adsorbed state. The binding energy difference between the peaks can be used to make

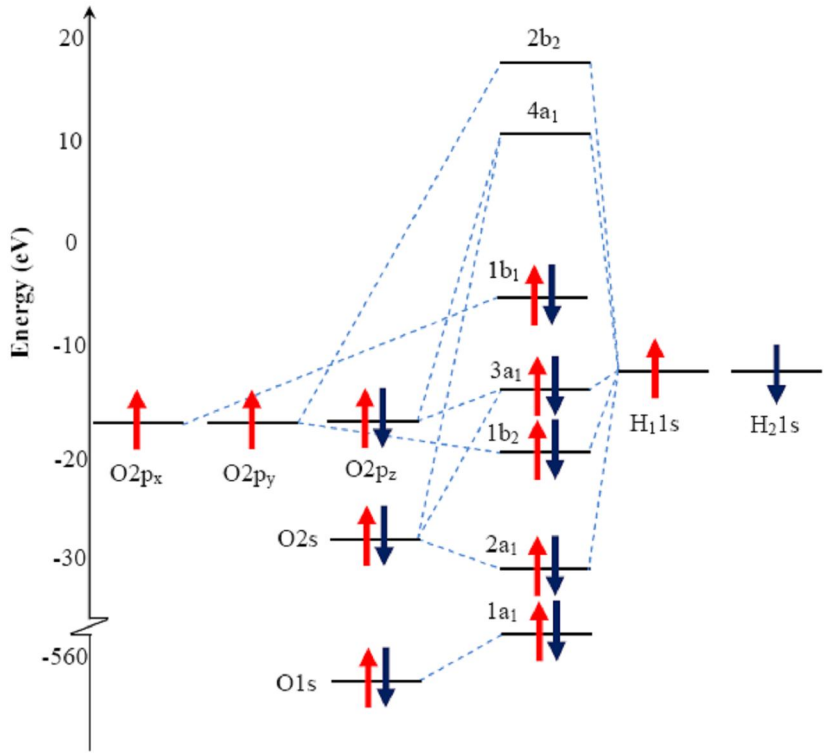

Figure 4.7: *Molecular orbital energy level diagram for water* (*Adapted from* [6]).

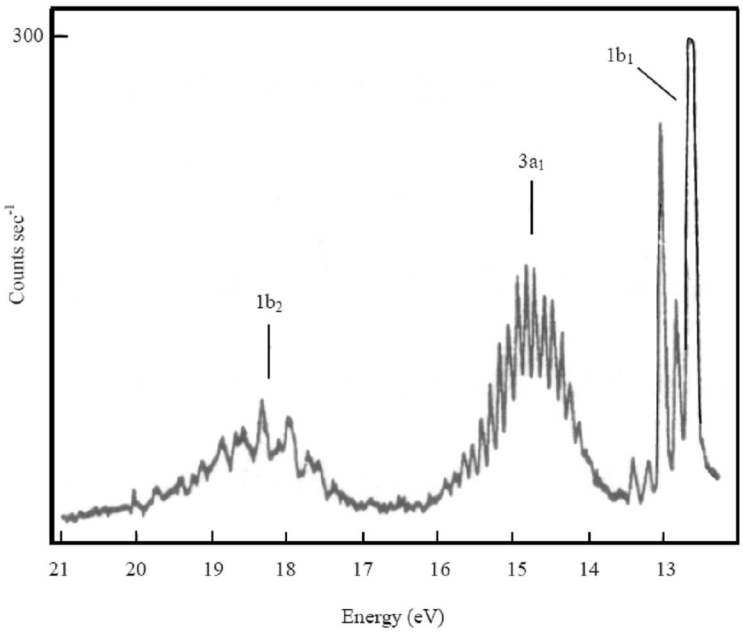

Figure 4.8: *Photoemission spectra of gas phase water using He I radiation* (*Taken from* [11]).

a distinction between chemisorption and physisorption. The binding energies of these levels and their differences in gaseous water are:

$$1b_1 = 13.9 \text{ eV}, 3a_1 = 15.9 \text{ eV and } 1b_2 = 19.5 \text{ eV [6]},$$
$$\Delta (1b_2 - 3a_1) = 3.6 \text{ eV}, \Delta (3a_1 - 1b_1) = 2.0 \text{ eV [6]}.$$

In physisorption, the interaction with the substrate is negligibly small and does not have any effect on the binding energies of these orbitals. The binding energy difference between the peaks for the adsorbed molecule remains the same as gaseous water. On the other hand in chemisorption, a charge transfer from the $3a_1$ orbital to the sample surface shifts the binding energy of the orbital to a higher value. The size of the binding energy shift shows the relative strength of the chemisorption bond [8]. In $SrTiO_3$ (001), binding energy shifts of the $3a_1$ orbital of up to 1.3 eV have been observed [9]. There is another possibility that water adsorbs on the surface of the sample in the form of ice. In this scenario, the three peaked structure can still be observed in the photoemission spectrum with the $3a_1$ orbital peak considerably broadened and reduced in intensity [9]. A binding energy shift of the $1b_1$ orbital in the case of ice has been observed. Flavell *et al.* [8] reported that, for $Bi_2Sr_2CaCu_2O_8$ (001), a binding energy shift of the $1b_1$ orbital was 6.1 eV to lower energy relative to the ionisation potentials for gaseous water. This can be compared with the shift observed in polycrystalline $YBa_2Cu_3O_7$ [13], and is slightly larger than the shift observed for $Na_{0.7}WO_3$ (100) [14]. However, semiconducting oxides such as $SrTiO_3$ (001) [9, 10] and SnO_2 (110) [15] reveal a rather smaller shift. The binding energies of adsorbate features may be used as a measure of the relative polarisation-relaxation shift (due to the stabilisation of the final state with respect to the initial gas-phase water) [12].

In chemisorption followed by dissociation, formation of OH^- on the surface of the sample takes place. This molecule has a considerably different binding energy pattern from that of molecular H_2O in UPS so that a distinction between the two can easily be made. The photoemission spectrum for OH^- gives only two peaks attributed to 1π and 3σ orbitals. For example in the case of NaOH, the binding energy difference of these orbitals is around 4 eV. These orbitals (1π and 3σ) have binding energy in the ranges 5-7 eV and 9-11 eV respectively.

Kurtz *et al.* [10] in an adsorption study of water on the layered perovskite $La_{2-x}Sr_xCuO_4$ found that water adsorption was dissociative and there was also a drop in the workfunction of the surface on water exposure at 1 Langmuir (L). As a result of water exposure, two additional peaks situated at 5.2 eV and 8.8 eV binding energies in the spectrum were observed. The binding energy difference of 3.6 eV between these two peaks was in good agreement with the peak separation of 3 σ and 1π levels of OH^- adsorbed on the oxide surfaces. The difference spectrum produced for 100 L dose shown in Figure 4.9(b) gave a peak separation of 4.1 eV (9.0 eV- 4.9 eV) which was also in good agreement with the peak separation observed in the photoemission of solid NaOH. In case of NaOH, the 3σ orbitals have a binding energy of around 9 eV while the 1π orbital is observed at around 5 eV binding energy.

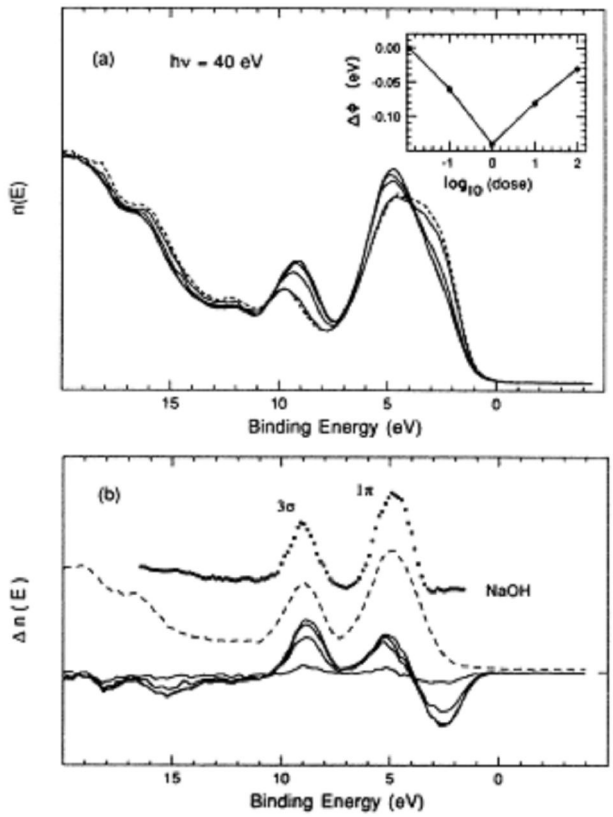

Figure 4.9: (a) *Photoelectron spectra of scraped $La_{1.8}Sr_{0.2}CuO_4$ exposed to water. The inset shows the change in the work function, $\Delta\Phi$, versus the logarithm of the dose in L; (b) difference spectrum obtained from clean and water-dosed samples. The dashed curve is an alternative difference spectrum and the dotted curve is the He II photoelectron spectrum obtained from solid NaOH* [10].

Kurtz *et al.* [10] also exposed the surface of $La_{1.8}Sr_{0.2}CuO_4$ to CO_2. Their study of 100 L CO_2 dosing revealed that the peaks located at 4.9 eV, 9.3 eV and 11.5 eV could be associated respectively with the $1\pi_g$, the unresolved overlap of $1\pi_u$ and 3 σ_u and the 4 σ_g molecular orbitals of CO_2 as shown in Figure 4.10(b). The binding energy difference of 4.2 eV between the two large peaks was in good agreement with the CO_3^{2-} spectrum obtained from $CaCO_3$.

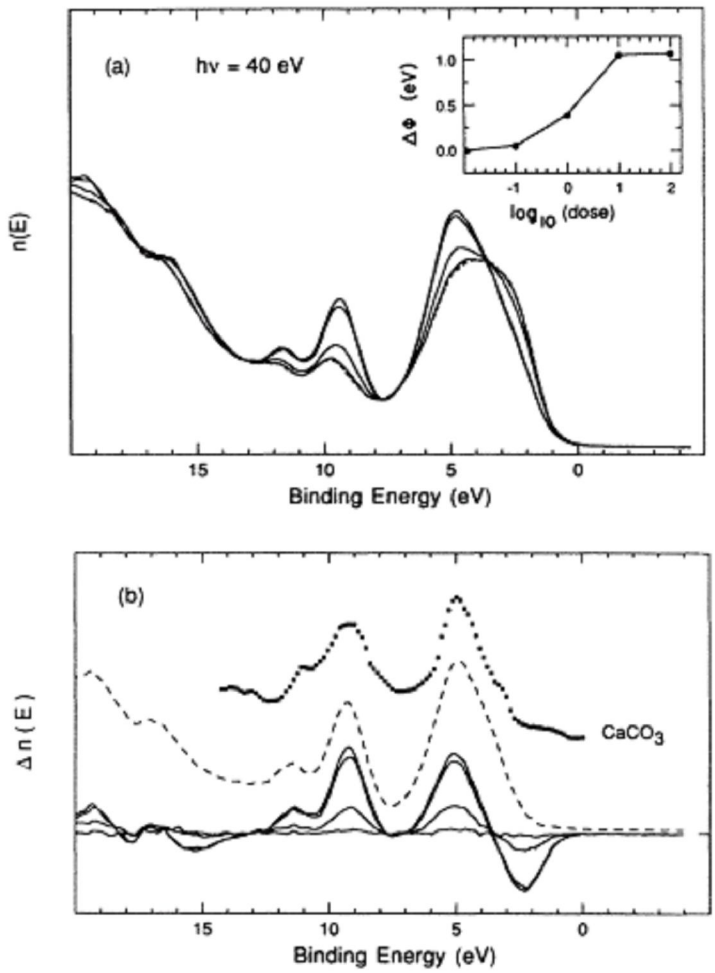

Figure 4.10: *(a) Photoemission spectra obtained from scraped $La_{1.8}Sr_{0.2}CuO_4$ exposed to CO_2. The inset shows the change in the work function, $\Delta\Phi$, versus the logarithm of the dose in L; (b) difference spectra are shown by solid curves, the dashed curve is an alternative difference spectrum and the dotted curve is the He II photoelectron spectrum obtained from solid $CaCO_3$* [10].

4.5 Surface Contamination of Cobaltite Surfaces

4.5.1 Surface Contamination of $LnBaCo_2O_{5+\delta}$ (Ln = Gd, Dy, $Dy_{1-x}Tb_x$)

The surface stability of the double perovskites cobaltites has been studied in previous work and it was found that water adsorbed on the sample over a 1-2 hour period after cleaning. The surface degradation of the samples depends upon the quality of scraping, temperature and the length of time in the UHV [4].

Usually in photoemission experiments, the nature of the contaminants on the surface is identified by difference spectra generated by subtracting the spectrum of the clean surface from that of the contaminated one. Figure 4.11 shows the difference spectrum generated from the spectra of freshly scraped $GdBaCo_2O_{5.5}$ at 20 K and the contaminated one at *ca*. 320 K. The difference spectrum reveals a three peaked structure of molecular water. The peaks situated at 2.7 eV, 4.6 eV and 8.7 eV are assigned to the $1b_1$, $3a_1$ and $1b_2$ molecular orbitals respectively. The peak separation Δ ($1b_2$ - $3a_1$) and Δ ($3a_1$ - $1b_1$) are 1.9 eV and 4.1 eV respectively and suggest a mixture of water and OH^- (mostly OH^-), because the intensity of $1b_1$ is too small, on the surface of $GdBaCo_2O_{5.5}$ sample. This result is in good agreement with the water adsorption study previously carried out on perovskites such as $La_{1-x}Sr_xCoO_3$ [6, 16] and $La_{1.8}Sr_{0.2}CuO_4$ [10].

The difference spectrum shown in Figure 4.12 has been generated from spectra of a freshly scraped $Dy_{1-x}Tb_xBaCo_2O_{5+\delta}$ sample at room temperature and the contaminated sample at 144 K. Two peaks labelled by letters A and B are situated around 6 eV and 8.6 eV respectively with a binding energy difference of 2.6 eV. A shoulder to peak A can also be observed around 5 eV. Figure 4.13 depicts the difference spectrum for the same sample using the contaminated spectrum at 406 K. At higher temperature, the peak difference between peaks A and B has been reduced by 0.3 eV compared to that obtained at lower temperature. The binding energy peak difference of A and B for both difference spectra of $Dy_{1-x}Tb_xBaCo_2O_{5+\delta}$ does not match well with any of the peak differences previously discussed spectra related to H_2O and CO_2 adsorbed on oxide surfaces. So, particularly in

this case, the nature of the contaminants on the surface of $Dy_{1-x}Tb_xBaCo_2O_{5+\delta}$ is difficult to identify.

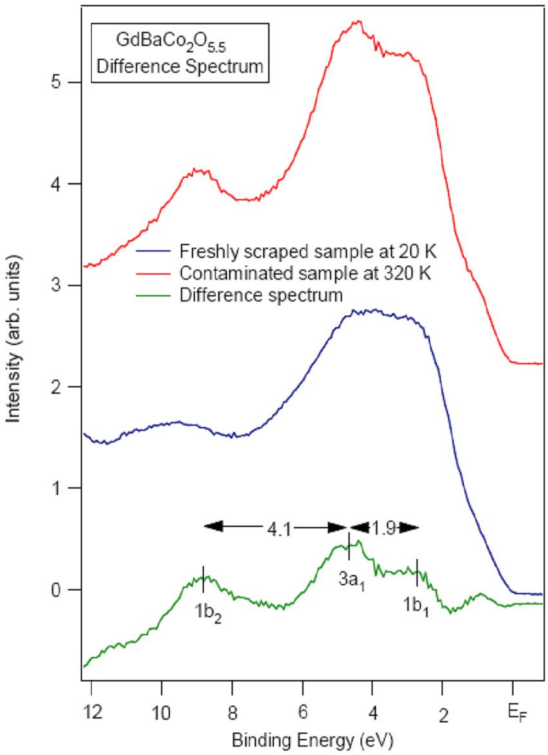

Figure 4.11: *Difference spectrum (contaminated – clean) generated from 23 eV photoemission spectra of freshly scraped $GdBaCo_2O_{5.5}$ sample at 20 K and the contaminated sample at ca. 320 K.*

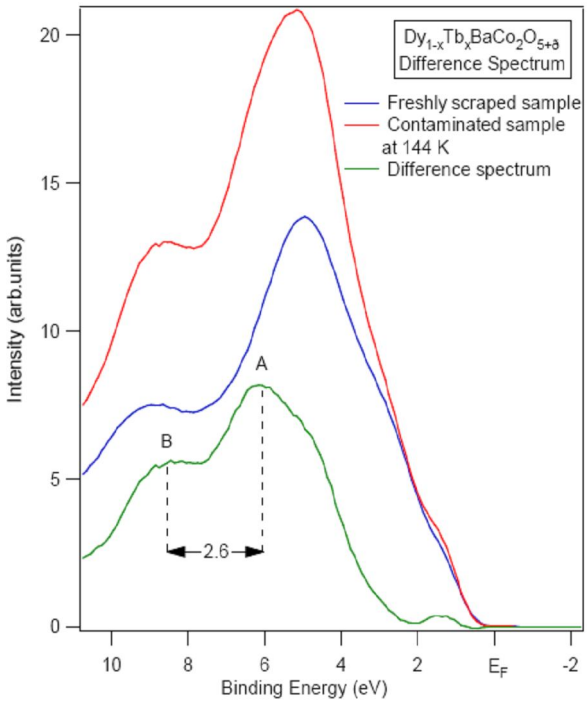

Figure 4.12: *Difference spectrum (contaminated – clean) generated from 23 eV photoemission spectra of a freshly scraped $Dy_{1-x}Tb_xBaCo_2O_{5+\delta}$ sample at room temperature and the contaminated sample at 144 K.*

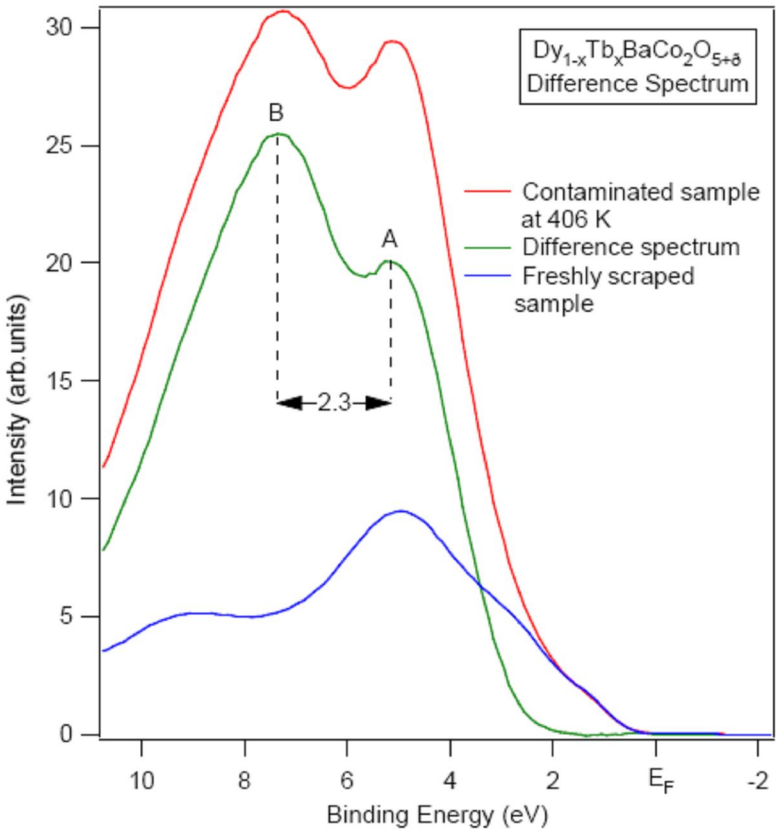

Figure 4.13: *Difference spectrum* (*contaminated – clean*) *generated from 23 eV photoemission spectra of a freshly scraped* $Dy_{1-x}Tb_xBaCo_2O_{5+\delta}$ *sample at room temperature and the contaminated sample at 406 K.*

Figure 4.14 shows the difference spectrum produced from spectra of a freshly scraped $DyBaCo_2O_{5.5}$ sample at room temperature and the contaminated sample at 140 K. The peaks labelled by the letters A, B are situated at 5.8 eV and 8.9 eV binding energy with a difference of 3.1 eV. These two peaks can be assigned to hydroxide (OH^-) orbitals 1π and 3σ respectively. The difference spectrum shown in Figure 4.15 for the same sample at temperature 401 K reveals a three-peaked structure. The peaks labelled by the letters A, B and C are situated at 5.3 eV, 8 eV and 10 eV binding respectively. It is difficult to notice the middle peak B due to its small size as compared to those of A and B peaks. The binding energy differences Δ (B - A) and Δ (C - B) are 2.7 eV and 2 eV respectively. Although the difference spectrum shows three peaks structure, it is difficult to associate these peaks with the molecular orbitals of water or those of CO_2. The binding energy difference between the peaks of the difference spectrum is not in good agreement with any of the peak differences

previously discussed spectra related to H_2O and CO_2 adsorbed on oxide surfaces. Hence, it can be concluded that the nature of the contaminants on the surface of $DyBaCo_2O_{5.5}$ sample at 401 K is difficult to determine. However, it seems to be the case that the contaminant species at low temperature are not identical to those seen at 401 K.

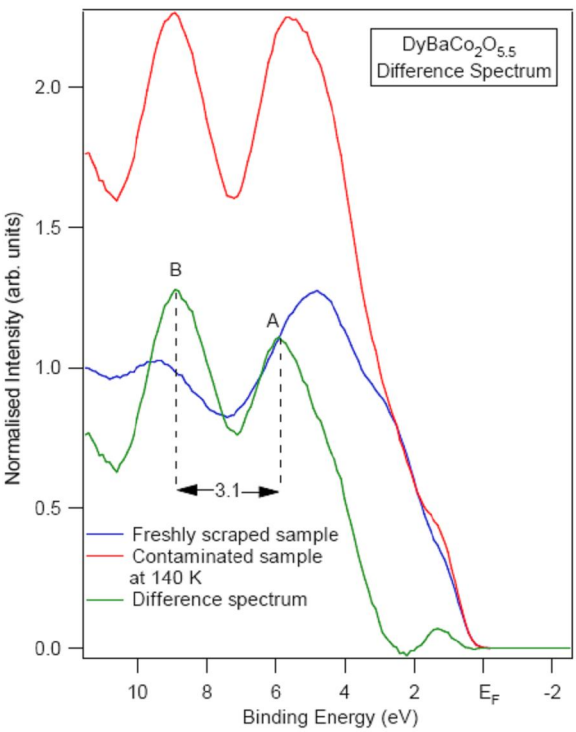

Figure 4.14: *Difference spectrum (contaminated – clean) generated from 23 eV photoemission spectra of a freshly scraped $DyBaCo_2O_{5.5}$ sample at room temperature and the contaminated sample at 140 K.*

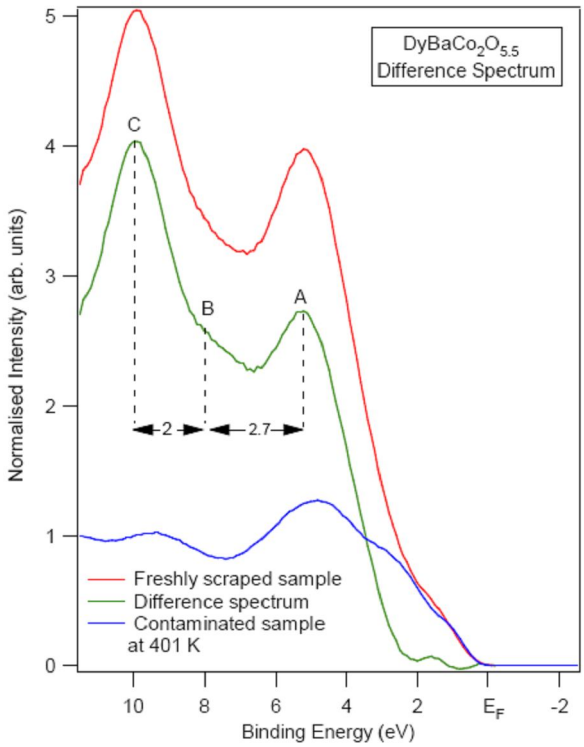

Figure 4.15: *Difference spectrum (contaminated – clean) generated from 23 eV photoemission spectra of a freshly scraped $DyBaCo_2O_{5.5}$ sample at room temperature and the contaminated sample at 401K.*

4.5.2 Surface Contamination of $YbBaCo_4O_7$

The difference spectrum shown in Figure 4.16 has been produced from spectra of a freshly scraped $YbBaCo_4O_7$ sample and that of a contaminated one at 300 K. Two peaks labelled by letters A and B are situated around 5.25 eV and 9.85 eV respectively with a binding

energy difference of 4.6 eV. The peaks at 5.25 eV and 9.85 eV binding energies can be attributed to the OH^- orbitals 1π and 3σ respectively. This peak difference is in agreement with the water-dosed study previously carried out on $LaCo_{0.8}Cu_{0.2}O_3$ at 5.5 L [11, 17]. Hence it can be concluded that the surface degradation of $YbBaCo_4O_7$ may be due to the presence of surface OH^-.

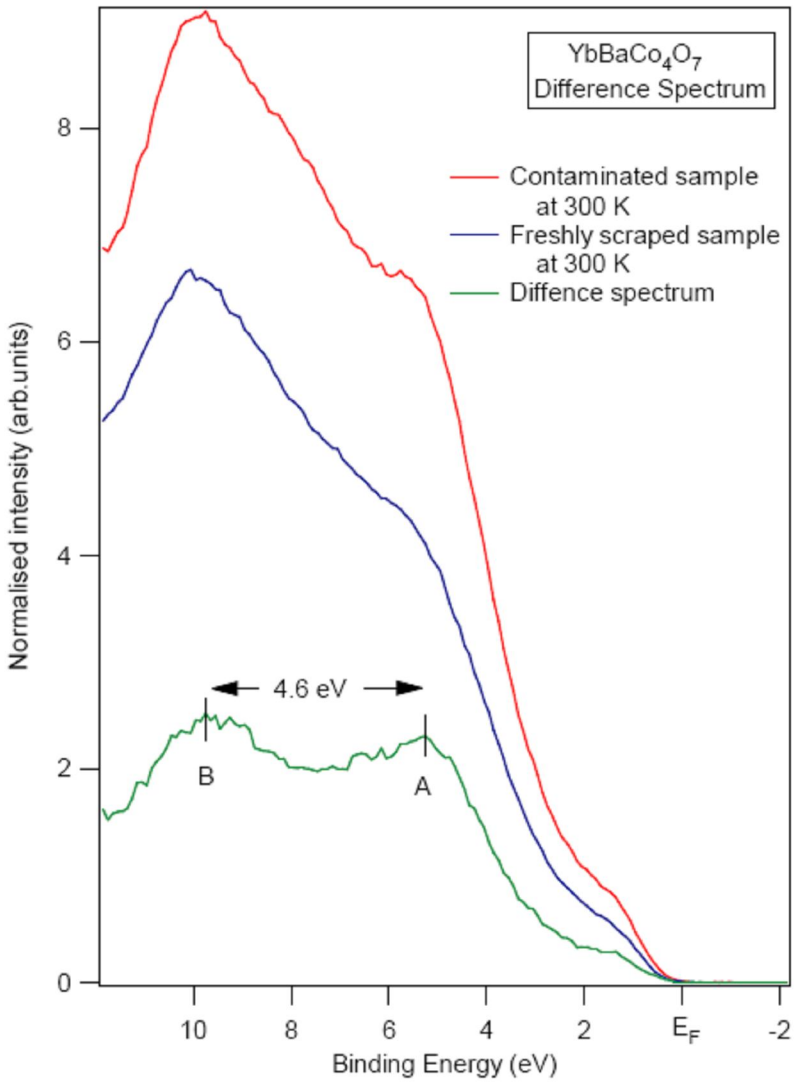

Figure 4.16: *Difference spectrum generated from spectra of a freshly scraped $YbBaCo_4O_7$ sample and the contaminated one at 300 K.*

4.6 Conclusions

From the above results and discussions, one can conclude that the surfaces of single crystals of transition metal oxides are highly reactive and undergo degradation in UHV due to adsorption of residual gases. Difference spectra generated from the freshly scraped and the contaminated surfaces reveal the spectral signature of the contamination. Some physisorption of water and dissociation to OH^- on the surfaces of $GdBaCo_2O_{5.5}$ and $DyBaCo_2O_{5.5}$ samples have been identified. Though the sample of $Dy_{1-x}Tb_xBaCo_2O_{5+\delta}$ showed contamination, the nature of the contaminants from its difference spectra could not be identified. In surface degradation of $YbBaCo_4O_7$, the formation of OH^- is likely. These general observations are consistent with the water adsorption studies previous carried out on transition metal oxides [6, 10, 16, 17]. Signatures of surface degradation are typically observed in the valence band spectra at 9.1 eV and 5.1 eV. It is important that these signals are monitored during experiments, and the samples rescraped at intervals in order to maintain surface cleanliness.

References

[1] J. A. Clarke, *J. Synchrotron Rad*., **5**, 434 (1998).

[2] W. R. Flavell, A. G. Thomas, D. Tsoutsou, A. K. Mallick, M. North, E. A. Seddon, C. Cacho, A. E. R. Malins, S. Patel, R. L. Stockbauer, R. L. Kurtz, P. T. Sprunger, S. N. Barilo, S. V. Shiryaev, and G. L. Bychkov, *Phys. Rev. B* ,**70**, 224427 (2004)

[3] C. Frontera, J.L. Garcia-Munoz, A. Llobet, M.A.G. Aranda, *Phys. Rev. B,* **65,** 180405 (2002).

[4] D. Tsoutsou, PhD Thesis, The University of Manchester (2005).

[5] V. E. Henrich, P.A. Cox, *Applied Surf Sci*,**72**, 277 (1993).

[6] S. Warren, PhD Thesis, UMIST (1997).

[7] K. Siegbahn, *J. Electron Spectrosc. Relat. Phenom.*, **5**, 1(1974).

[8] W. R. Flavell, J. H. Laverty, D. S. L. Law, R. Lindsay, C. A. Muryn, C. F. J. Flipse, G. N. Raiker, P. L. Wincott and G. Thornton, *Phys. Rev. B*,**41**,11623(1990).

[9] P. A. Thiel, T. E. Madley, *Surf Sci Reports*, **7**, 211(1987).

[10] R. L. Kurtz, R. Stockbauer, T. E. Madey, D. Mueller, A. Shih and L. Toth, *Phys. Rev. B*, **37**,7936 (1988).

[11] J. Hollingworth, PhD Thesis, UMIST (1999).

[12] A. J. Yencha, H. Kubota, T. Fukuyama, T. Kondow and K. Kuchitsu, *J. Electron Spectrosc Relat Phenom*, **23**, 431 (1981).

[13] S. L. Qui, M. W. Ruckman, N. B. Brooks, P. D. Johnson, J. Chen, C. L. Lin and M. Strongin, *Phys. Rev*. B, **37**, 3747 (1988) .

[14] D. G. Aitken, P. A. Cox, R. G. Egdell, M. D. Hill and I. Sach, *Vacuum*, **33**, 753 (1983).

[15] W. R. Flavell, Pt. II thesis, University of Oxford (1983).

[16] S. C. Grice, W. R. Flavell, A. G. Thomas, S. Warren, P. G. D. Marr, D. E. Jewitt, N. Khan, P. M. Dunwoody and S. A. Jones, *Int. J. Mol. Sci.*, **2**, 197(2001).

[17] J. Hollingworth, W. R. Flavell, A. G. Thomas, S. C. Grice, C. E. J. Mitchell, P. M. Dunwoody, S. Warren, S. J. Squire, P. G. D. Marr, S. W. Downes and F. E. Hancock, *J. Electron Spectrosc. Relat. Phenom*., **103**, 765 (1999).

Chapter 5

High Resolution Photoemission, Results and Discussion on $LnBaCo_2O_{5+\delta}$

5.1 Introduction

The current chapter discusses high resolution photoemission measurements for $LnBaCo_2O_{5+\delta}$ (Ln = Gd, Dy, $Dy_{1-x}Tb_x$). These include depopulation of the Co^{3+} LS states in $Dy_{1-x}Tb_xBaCo_2O_{5+\delta}$ and studies of the insulator to metal (MI) transition in $GdBaCo_2O_{5.5}$, $Dy_{1-x}Tb_xBaCo_2O_{5+\delta}$ and $DyBaCo_2O_{5.5}$ as a function of temperature. The Co^{3+} ions can exist in low-spin states (LS, $t_{2g}^6 e_g^0$, $S = 0$), intermediate-spin states (IS, $t_{2g}^6 e_g^1$, $S = 1$) and high-spin states (HS, $t_{2g}^2 e_g^2$, $S = 2$) in $LnBaCo_2O_{5.5}$ (Ln = rare earth) as a result of competition between the intra-atomic exchange and the crystal field [1]. Very small energy differences of about 30–100 meV are involved between these states and all the three states can co-exist over a wide range of temperature, so the LS evolves to the IS and then to the HS as the temperature increases [2, 3]. Furthermore, the oxygen content of $LnBaCo_2O_{5+\delta}$ can be changed by means of thermal treatment in a suitable atmosphere [4-6]. The oxygen content controls the average valence state of the cobalt ions (+3 for $\delta = 0.5$) and their coordination environment. The geometry of the coordination environment (either pyramidal CoO_5 or octahedral CoO_6) greatly influences the spin state of the cobalt ions. The following sections include oxygen resonant photoemission results for $LnBaCo_2O_{5+\delta}$ (Ln = Gd, $Dy_{1-x}Tb_x$). CIS spectra generated from the corresponding valence band EDCs of $Dy_{1-x}Tb_xBaCo_2O_{5+\delta}$ and $GdBaCo_2O_{5.5}$ are also discussed.

5.2 Valence Band Spectra of $LnBaCo_2O_{5+\delta}$ (Ln = Gd, Dy, $Dy_{1-x}Tb_x$) as a Function of Temperature

The valence band EDCs of $GdBaCo_2O_{5.5}$, $DyBaCo_2O_{5.5}$ and $Dy_{1-x}Tb_xBaCo_2O_{5+\delta}$ as a function of temperature are shown in Figures 5.1, 5.2 and 5.3 respectively. The spectra were recorded within the temperature range of 20-406 K and normalised to the incident photon flux. The features towards the higher binding energy side in the valence band have been discussed earlier in Section 4.5 but here we are mainly concerned with the features towards the lower binding energy side in the vicinity of the Fermi level. Features located within 1-3.5 eV binding energy range, have been previously linked primarily with Co^{3+} LS states [7]. A gradual reduction of these features with increase of temperature indicates depopulation of the Co LS states which ultimately gives rise to a non-metal-to-metal transition in the material [8, 9].

From Figures 5.1 and 5.2, it is difficult to observe an obvious reduction in intensity as a function of temperature for the features linked with Co^{3+} LS states for $GdBaCo_2O_{5.5}$, $DyBaCo_2O_{5.5}$. However in case of $Dy_{1-x}Tb_xBaCo_2O_{5+\delta}$, a decrease in intensity with temperature for these features is apparent in Figure 5.3. Figures 5.1 and 5.2 do not reveal a smooth trend in the data unlike that of Figure 5.3 because the data was not recorded in order of increasing temperature for figures 5.1 and 5.2. The studies related to surface contamination of $LnBaCo_2O_{5+\delta}$ (Ln = Gd, Dy, $Dy_{1-x}Tb_x$), discussed in Section 4.5.1, revealed that the contamination species at low temperatures were not identical to those seen at higher temperatures and that contamination occurs as a function of time after scraping. The temperature dependent depopulation of the Co LS states for $Dy_{1-x}Tb_xBaCo_2O_{5+\delta}$ and the MI transitions in $LnBaCo_2O_{5+\delta}$ (Ln = Gd, Dy, $Dy_{1-x}Tb_x$) are discussed later in Sections 5.2.1 and 5.3 respectively.

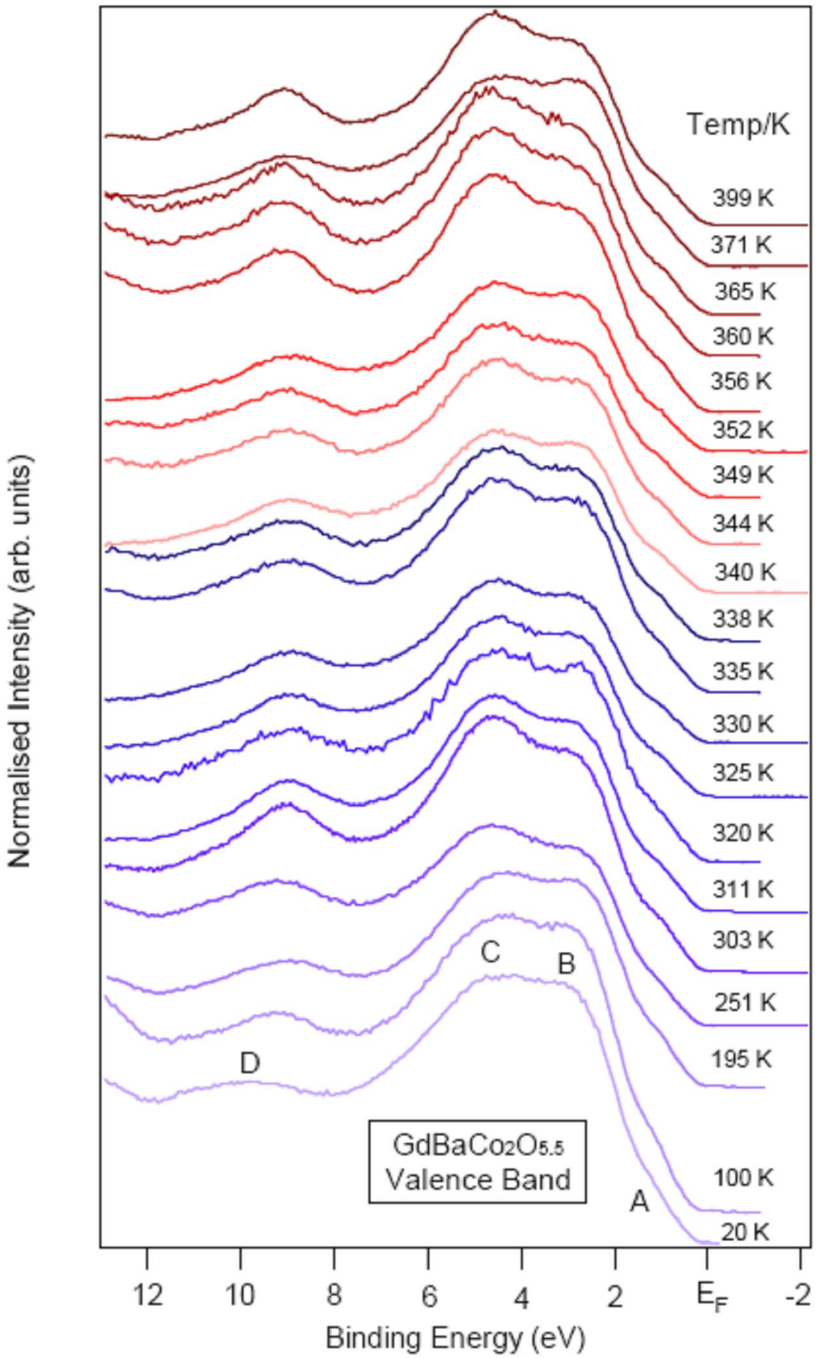

Figure 5.1: *Effect of temperature on the high-resolution valence band EDC spectra of $GdBaCo_2O_{5.5}$. Points A-D were later selected for O 2s→2p resonance photoemission at room temperature. The spectra are normalised to the incident photon flux. The VB EDCs do not reveal a smooth trend because the data was not recorded in order of increasing temperature and in one experiment.*

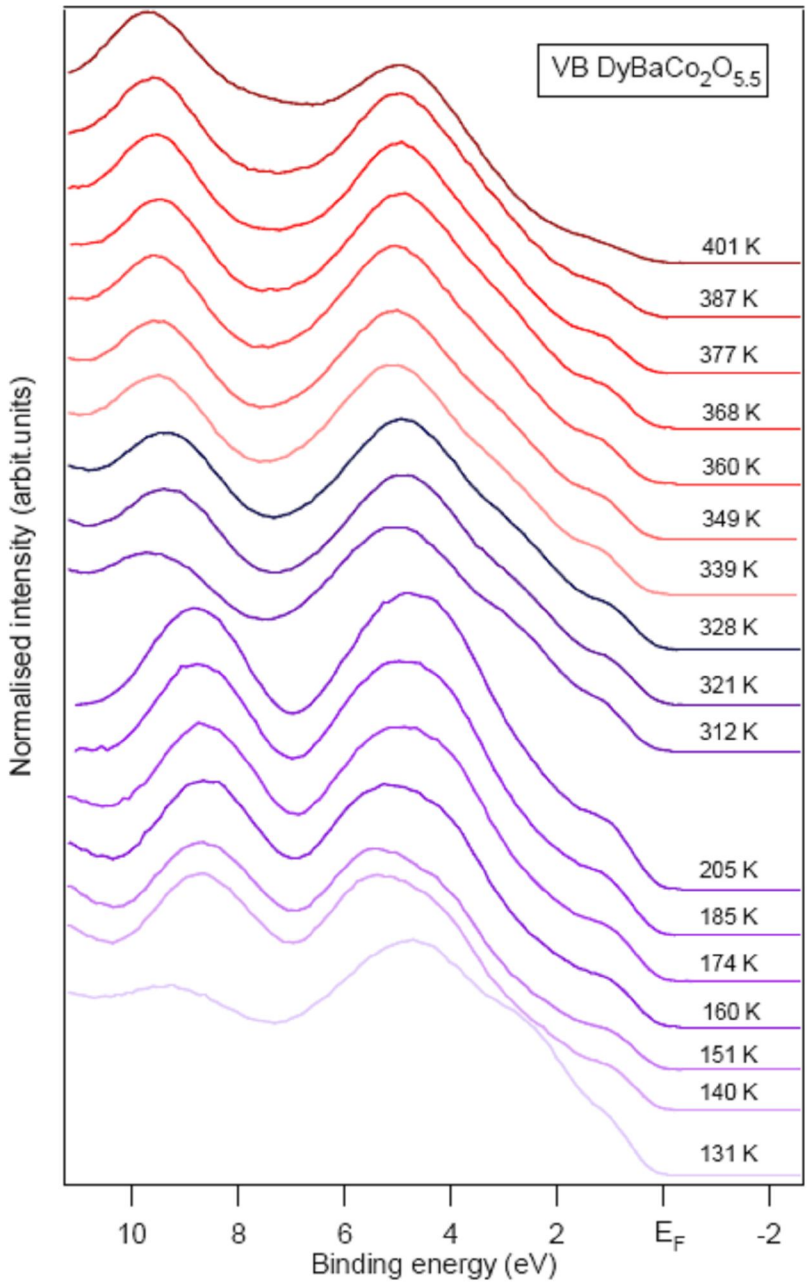

Figure 5.2: *Effect of temperature on the high-resolution valence band EDC spectra of $DyBaCo_2O_{5.5}$. The spectra are normalised to the incident photon flux. . The VB EDCs do not reveal a smooth trend because the data was not recorded in order of increasing temperature and in one experiment.*

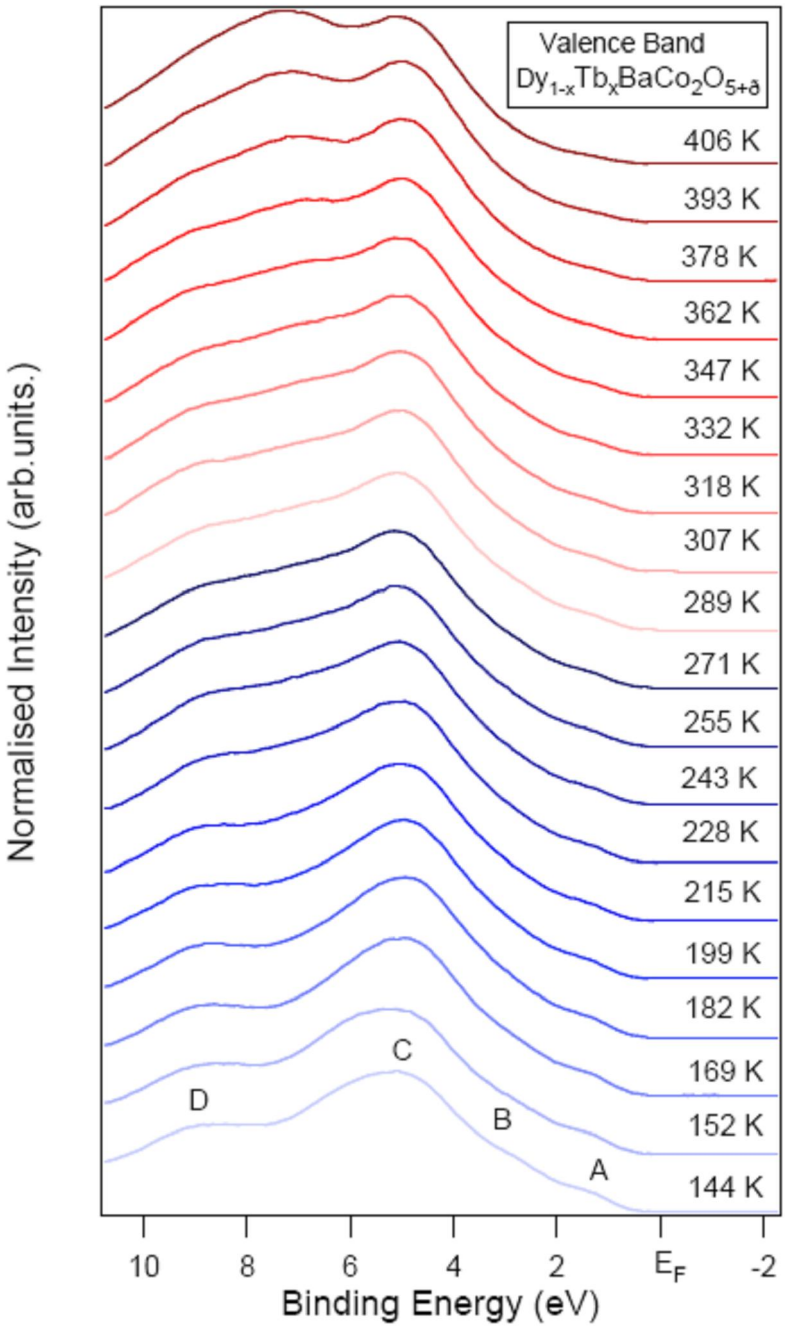

Figure 5.3: *Effect of temperature on the high-resolution valence band EDC spectra of* $Dy_{1-x}Tb_xBaCo_2O_{5+\delta}$ *. The spectra are normalised to the incident photon flux. Points A-C refer to the points later selected for intensity measurement as a function of temperature. Later, points A-D were also selected for O 2s→2p resonance photoemission at room temperature. Sample was scraped at 144 K.*

5.2.1 Temperature-dependent Co Spin States in $Dy_{1-x}Tb_xBaCo_2O_{5+\delta}$

To identify the depopulation of the Co^{3+} LS states as a function of temperature (over the 144-406 K temperature range) in the valence band of $Dy_{1-x}Tb_xBaCo_2O_{5+\delta}$, the photo-emission intensity of the density of states of the features located at binding energies of 1.25 eV, 3.25 eV and 4.95 eV marked by the letters A, B and C respectively was measured using the data in Figure 5.3. The data points of the normalised intensity thus obtained were plotted against the corresponding temperature values. This set of data produced a scatter plot of intensity vs temperature as shown in Figure 5.4. Keeping in view the randomness of the data points, a linear best fit was applied to approximate the data by a straight line in order to draw conclusions about the depopulation of the Co^{3+} LS states as a function of temperature. The linear best fit is a guide to the eye to show the decrease in intensity as a function of temperature. However there is no a physical reason for a linear decrease.

Part (a) of Figure 5.4 shows that the data points are close to the best fit line I_A with relatively little scatter whereas in part (b) of Figure 5.4, the data points are a bit more scattered around the best fit line I_B. The first two data points in the low temperature range may be excluded due to an artefact of the instrument caused by an abrupt change in the temperature during the experiment. Both the best fit lines I_A and I_B have negative gradients. In part (c) of Figure 5.4 , the data points are widely scattered around the best fit line I_C (with positive gradient) and suggest a poor fit to the linear function. One can conclude that the LS states of Co^{3+} ions, within around 3.5 eV binding energy range of the Fermi energy depopulate very gradually with temperature. As the absolute value of the gradient of line I_B is nearly double than that of I_A, so another conclusion can also be made that the rate of depopulation of the states as a function of temperature related to feature B is double that of those related to feature A. The large scatter of data points in part (c) suggests that there is almost no effect of temperature on the density of states associated with feature C in the valence band of $Dy_{1-x}Tb_xBaCo_2O_{5+\delta}$. Hence the transition from LS states to intermediate spin states (IS) and high spin (HS) states of Co^{3+} within 3.5 eV binding energy from the Fermi energy takes place slowly and gradually which is contrary to the sudden switch from

LS to HS proposed by Frontera *et al.* [10]. The data also suggest that the density of states associated with the Co low spin states is centred on feature B, consistent with earlier measurements from simple Co (III) perovskites [7, 11-13].

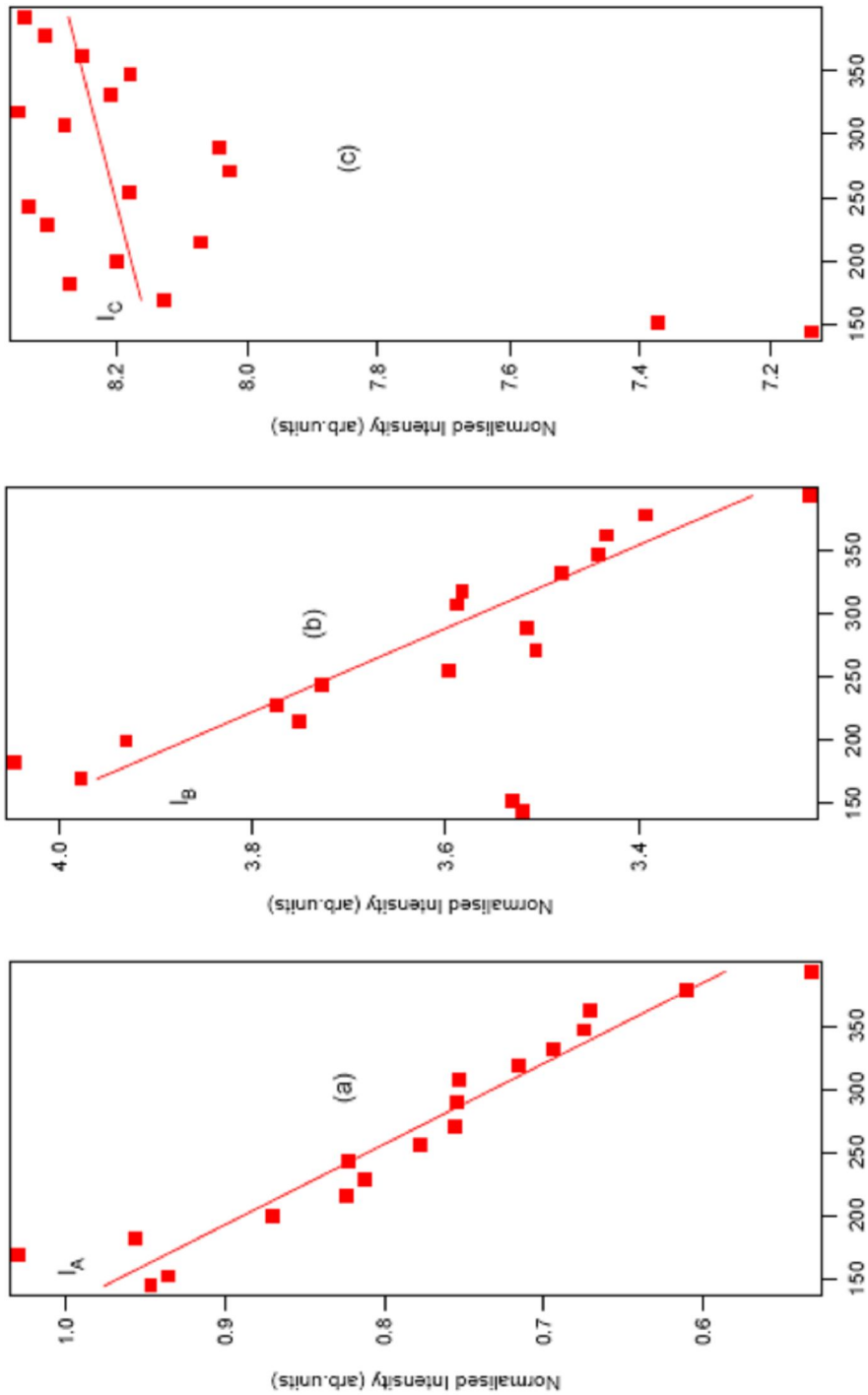

Figure 5.4 : *Effect of temperature on the density of states related to the features located around 1.25 eV(A), 3.25 eV(B) and 4.95 eV(C) binding energies in the valence band of* $Dy_{1-x}Tb_xBaCo_2O_{5+\delta}$ *. Lines (a)* I_A*,(b)* I_B *and(c)* I_C *are the best fit lines to the Co LS states data points related to features A, B and C respectively in the VB.*

5.3 The Metal-Insulator Transition in $LnBaCo_2O_{5+\delta}$ (Ln = Gd, Dy, $Dy_{1-x}Tb_x$)

One of the main aims of the current work is to study the non-metal-to-metal transition in $LnBaCo_2O_{5+\delta}$ (Ln = Gd, Dy, $Dy_{1-x}Tb_x$), so the variation in the density of states near the Fermi energy with temperature was probed through high-resolution photoemission. The metal-insulator transition in such compounds has been observed to occur in the 280-400 K temperature range [14] and several mechanisms for the MI transition have been suggested elsewhere [15-17].

Figures 5.5, 5.6 and 5.7 show high-resolution photoemission spectra of the temperature dependence of the low energy states of $GdBaCo_2O_{5.5}$, $Dy_{1-x}Tb_xBaCo_2O_{5+\delta}$ and $DyBaCo_2O_{5.5}$ respectively. Figures 5.6 and 5.7 reveal an obvious decrease in intensity with increasing temperature at around 1-1.5 eV binding energy. However in Figure 5.5, it is difficult to observe an apparent reduction in intensity for the features linked with the Co^{3+} LS states with the increase of temperature. This difficulty may be due to the fact that the spectra were not recorded in order of increasing temperature and a smooth trend in the data could not be obtained. To identify the metal-insulator transition, all these spectra were expanded in the immediate vicinity of the Fermi energy as shown in the corresponding Figures 5.8, 5.9 and 5.11.

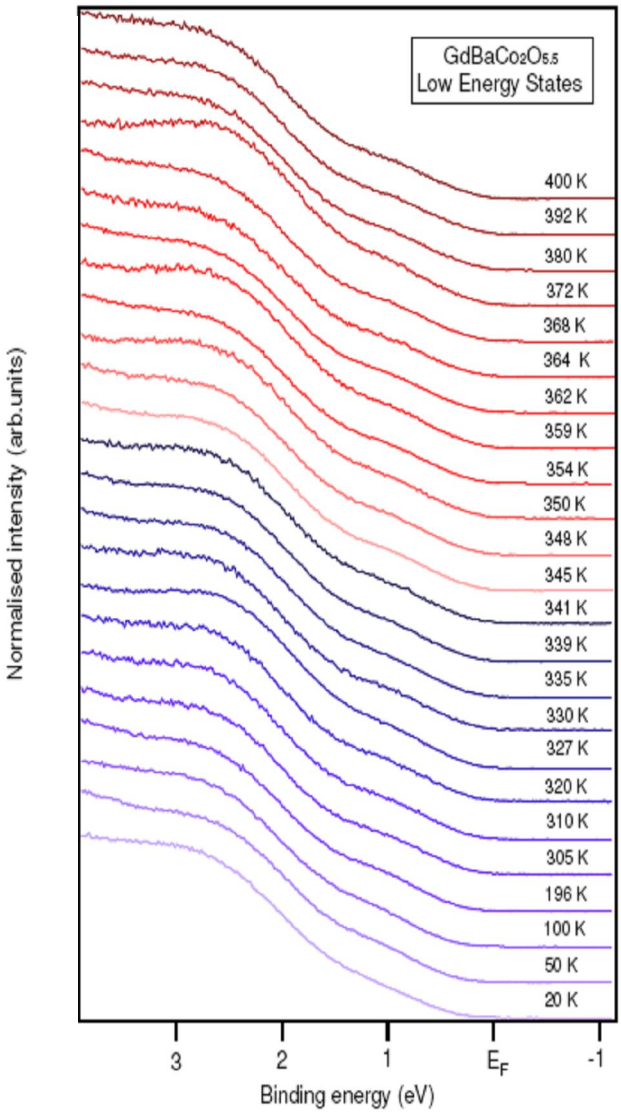

Figure 5.5: *Effect of temperature on the high-resolution photoemission of low energy (LE) states of $GdBaCo_2O_{5.5}$. The spectra are normalised to the incident photon flux. The spectra do not reveal a smooth trend because the data was not recorded in order of increasing temperature and in one experiment.*

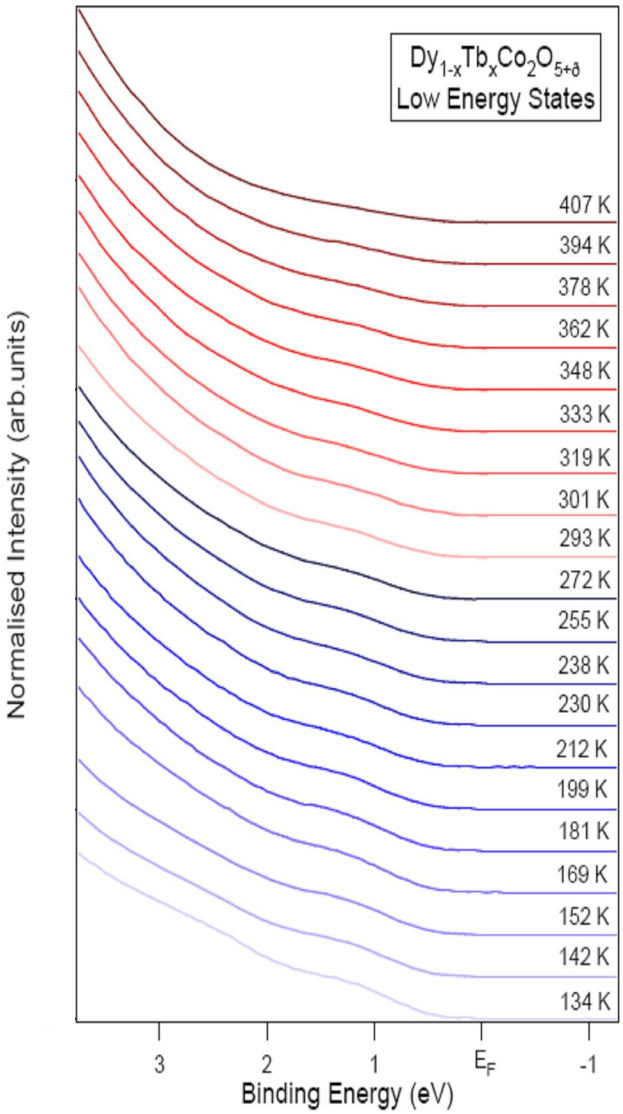

Figure 5.6: *Effect of temperature on the high-resolution photoemission of low energy (LE) states of $Dy_{1-x}Tb_xBaCo_2O_{5+\delta}$. The spectra are normalised to the incident photon flux. Sample was scraped at 134 K.*

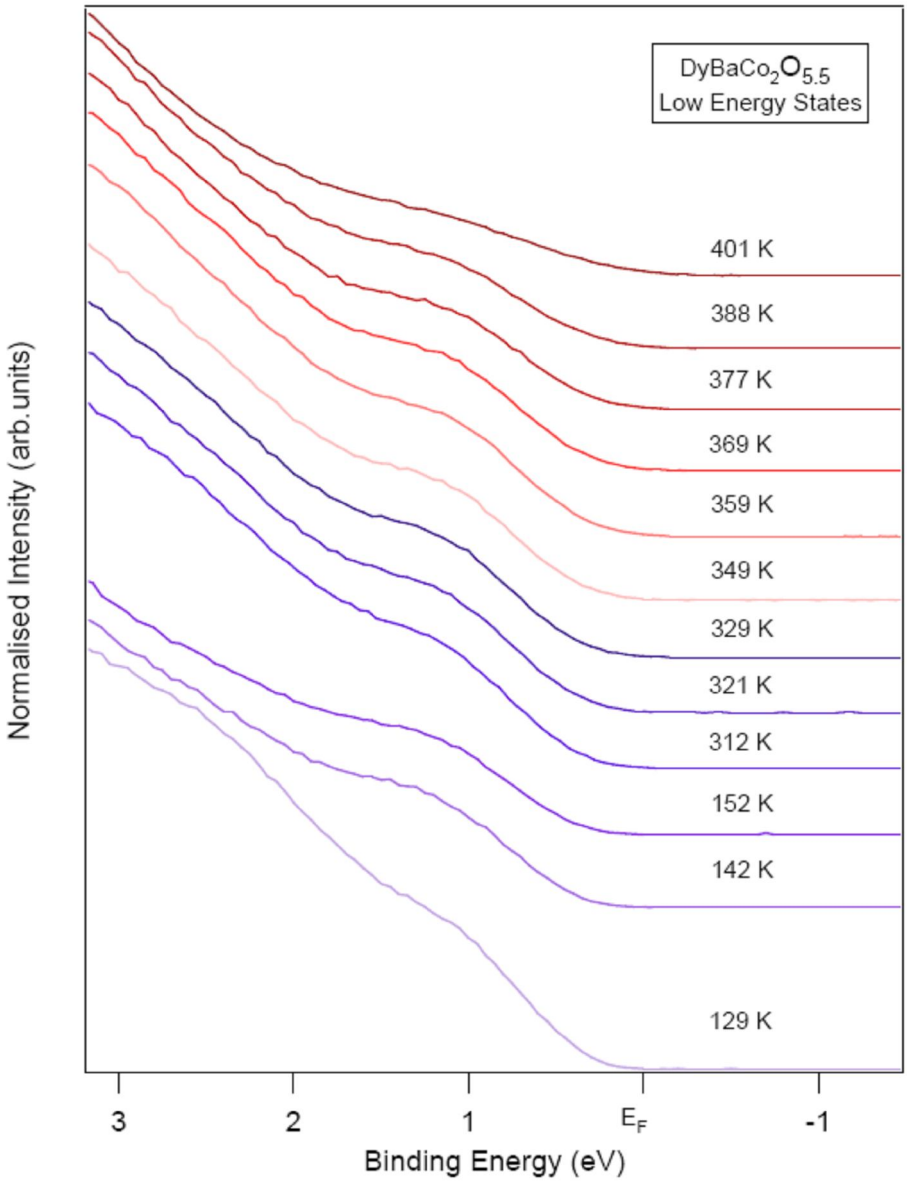

Figure 5.7: *Effect of temperature on the high-resolution photoemission of the low energy (LE) states of $DyTbBaCo_2O_{5.5}$. The spectra are normalised to the incident photon flux. Sample was scraped at 129 K.*

In $GdBaCo_2O_{5.5}$, the MI transition occurs in the region of 350 K for oxygen stoichiometry close to $O_{5.5}$ [18]. In the vicinity of the Fermi energy (around 200 meV from E_F), a very small but gradual increase in the density of states (DOS) as a function of temperature can

be observed in the 300-400 K temperature range which may be indicative of the MI transition in $GdBaCo_2O_{5.5}$.

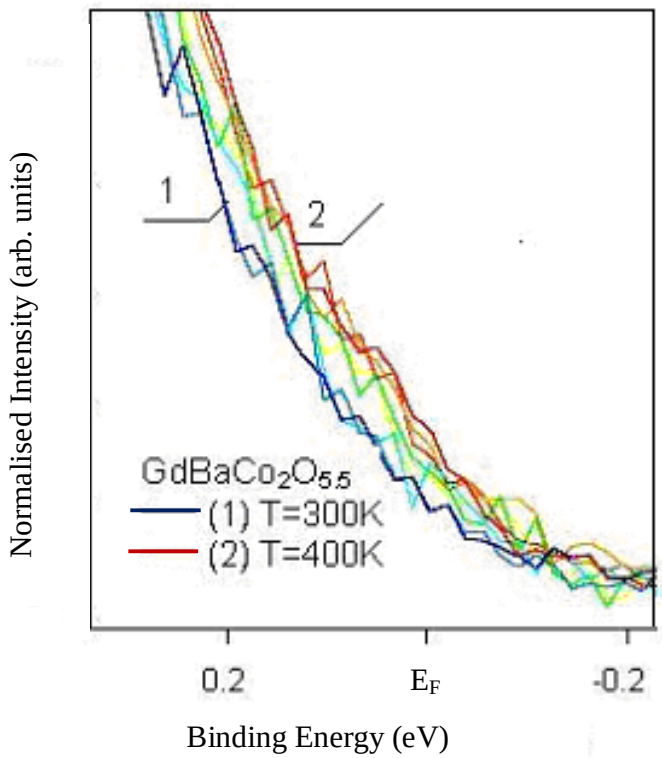

Figure 5.8: *An expansion of the valence band EDCs of $GdBaCo_2O_{5.5}$ in a 400 meV range in the vicinity of E_F exhibiting a gradual and small increase in DOS at E_F between 300 and 400 K. Visible spectrum colours between blue and red have been used to show the increase in temperature from 300 to 400 K* (*Taken from* [18]).

Figure 5.9 shows an expanded view of the valence band EDCs within 400 meV binding energy of the Fermi energy (E_F) in the single crystal sample of $Dy_{1-x}Tb_xBaCo_2O_{5+\delta}$. Although an increase in the DOS to the higher binding energy side of E_F can be observed as the temperature increases, there is no obvious change at the Fermi energy. The difficulty is either due to the low resolution of the instrument or one can conclude that the metal-insulator transition is absent in this sample of $Dy_{1-x}Tb_xBaCo_2O_{5+\delta}$. This is surprising because it is weakly observed in another sample of $Dy_{1-x}Tb_xBaCo_2O_{5+\delta}$ studied during the same project as shown in Figure 5.10. As oxygen stoichiometry controls the structural, the

magnetic and the electronic properties of these compounds (such as the MI transition) [18], variation in the oxygen content of the sample may affect these properties. Consequently the metal-insulator transition of the compound may be suppressed and can be restored on achieving an optimal stoichiometry of oxygen close to δ = 0.50 in the compound through proper oxygen annealing of the sample.

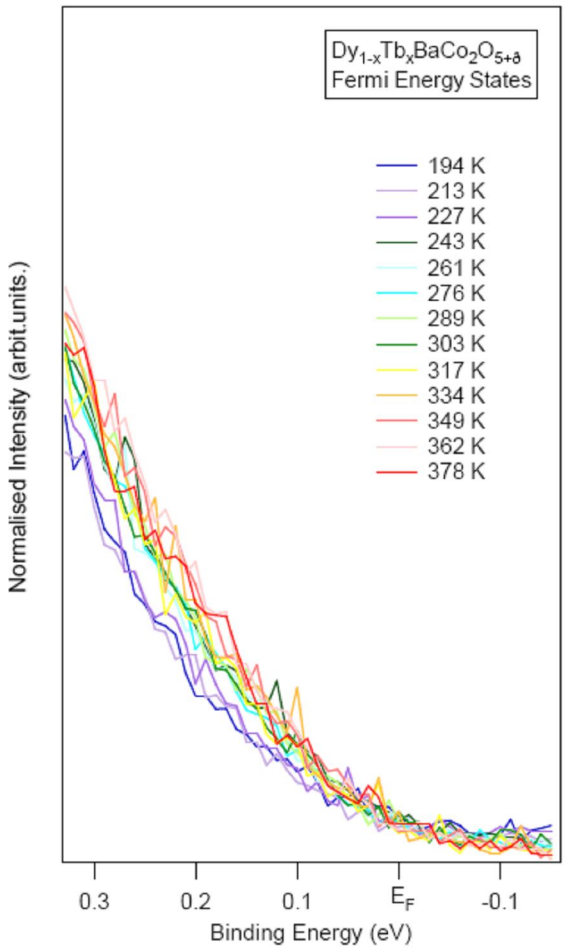

Figure 5.9: *An expansion of the valence band EDCs of $Dy_{1-x}Tb_xBaCo_2O_{5+\delta}$ in a 400 meV range in the vicinity of E_F exhibiting the DOS as a function of temperature.*

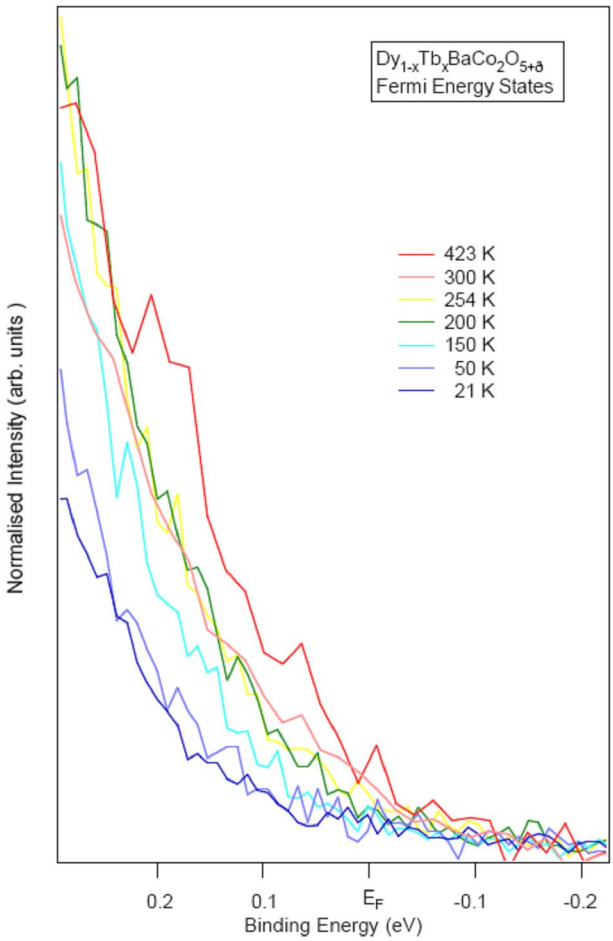

Figure 5.10: *An expansion of the valence band EDCs for a 2nd sample of $Dy_{1-x}Tb_xBaCo_2O_{5+\delta}$ in a 400 meV range in the vicinity of E_F exhibiting a gradual and small increase in DOS at E_F with temperature.*

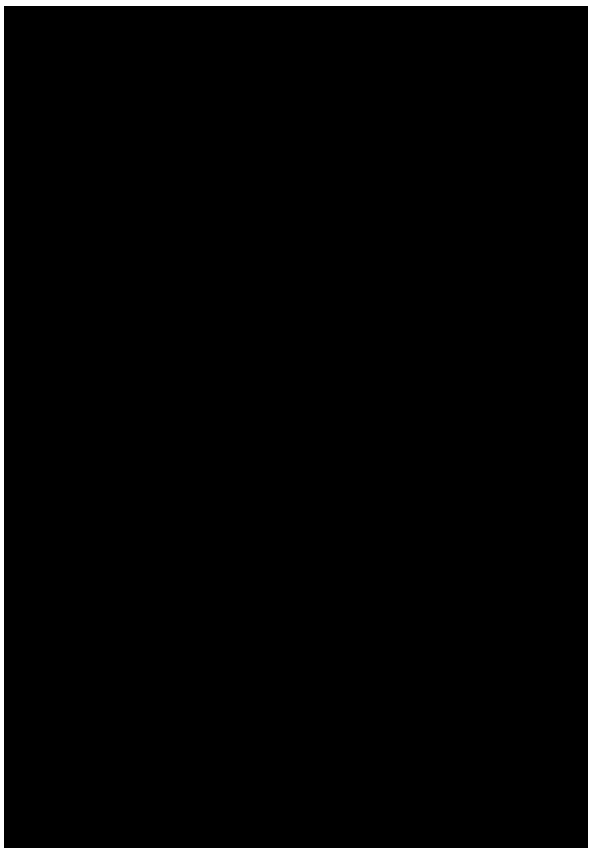

Figure 5.11: *An expansion of the valence band EDC of $DyBaCo_2O_{5.5}$ in a 700 meV range in the vicinity of E_F exhibiting increase in DOS at E_F between 311 and 401 K.*

The oxygen annealing process of the single crystal samples was discussed earlier in Section 2.5.3. To observe a marked MI transition in $DyBaCo_2O_{5+\delta}$, an as-grown sample was well-oxygenated according to the annealing plan shown in Figure 2.13. After oxygen annealing of the sample, the optimal oxygen stoichiometry for the MI transition was obtained. Figure 5.11 shows an expanded view of the data for this $DyBaCo_2O_{5.5}$ sample within 700 meV binding energy of the E_F. A significant increase in DOS at E_F between 311 K and 401 K confirms the MI transition of $DyBaCo_2O_{5.5}$. Visible spectrum colours between blue and red have been used to show increase in temperature from 311 to 401 K.

The temperature-dependent subtle changes in intensity around the MI transition in Ln-112 (Ln = Gd, Dy) contradict the suggestion made by Frontera *et al.* [10]. These authors

suggest that the transition occurs via a sudden switch from LS to the high spin state (HS, *S* = 2). M. Hidaka *et al.* [15] in a recent study based on the measured X-ray absorption spectra in Tb-112 have reported that the spin state transition is absent in the vicinity of the MI transition. Furthermore, our recent study of the temperature-dependent Co spin states in $Dy_{1-x}Tb_xBaCo_2O_{5+\delta}$ (Section 5.2.1) is also in disagreement with the conclusions of Frontera *et al.* [10]. From the above discussed results, we can conclude that our observations support the '3-spin state' model of Asai *et al.* [22] adopted for doped $LaCoO_3$ [13].

From the above results and discussions on the MI transition of Ln-112, it can be confirmed that thorough oxygenation of the samples has a marked effect on the MI transition. The quantification of this effect can be figured out from a comparison of the DOS at the Fermi level for an as-grown and a well-oxygenated sample at a particular temperature which lies within the MI transition temperature range. We cannot compare intensities from different experiments on different crystals. It can only be done if one can normalise the intensity at the E_F level to a feature that is common to both samples and whose intensity does not change with temperature. An attempt was made to find out such a common feature for as-grown sample of $Dy_{1-x}Tb_xBaCo_2O_{5+\delta}$ and a well-oxygenated sample of $DyBaCo_2O_{5.5}$ recorded at 423 K (Figures 5.10) and 401 K (Figures 5.11) respectively but no such common feature was identified. Alternatively a feature located at around 5 eV binding energy from the valence band EDCs of $Dy_{1-x}Tb_xBaCo_2O_{5+\delta}$ (feature C at T = 406 K, Figure 5.3) and those of $DyBaCo_2O_{5.5}$ (at T = 401 K, Figure 5.2) was selected and then the intensity of the VB feature C was equalised, with a scale factor ~ 1.9 (calculated from the ratio of their intensities at 5 eV BE), to that of the corresponding VB feature (Figure 5.2) of $DyBaCo_2O_{5.5}$. Then the intensity of the corresponding Fermi energy scan of $Dy_{1-x}Tb_xBaCo_2O_{5+\delta}$ (T = 423 K, Figure 5.10) was reduced by a factor 1.9 to compare its intensity at the Fermi level with the intensity of the Fermi energy spectrum of $DyBaCo_2O_{5.5}$ (T = 401, Figure 5.11). Both the spectra, one with reduced intensity, are shown in Figure 5.12. From Figure 5.12, the magnitude of the intensity at the Fermi level for $Dy_{1-x}Tb_xBaCo_2O_{5+\delta}$ (as-grown) and $DyBaCo_2O_{5.5}$ (oxygenated) samples is calculated to be in 1:17 ratio. From this ratio, it can be concluded that the oxygen annealing (achieving

an optimal stoichiometry of oxygen close to δ = 0.50) of the as-grown single crystal samples of Ln-112 may enhance the MI transition effect by a factor ~ 17.

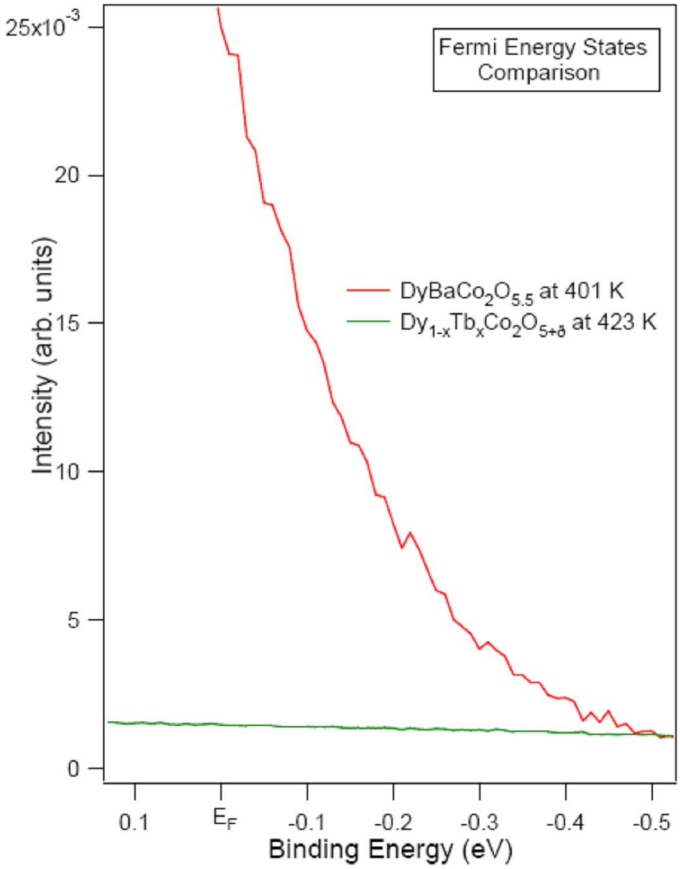

Figure 5.12: *Valence band EDC spectra in the vicinity of E_F from an as-grown sample of $Dy_{1-x}Tb_xBaCo_2O_{5+\delta}$ and a well-oxygenated sample of $DyBaCo_2O_{5.5}$ recorded at 423 K and 401 K respectively. First the spectra were normalised to the incident photon flux and then the intensity of EDC at T = 401 K was reduced by a factor ~ 1.9.*

5.4 Oxygen Resonance Photoemission

As it mentioned earlier (in Chapter 3) resonant photoemission is a powerful technique to understand the features of the valence band. It is quite useful in identifying the contributions of electronic states from particular elements in the features of the valence band. This technique has extensively been employed to study the electronic structure of transition metal oxides and rare-earth compounds.

It has been reported that when there is hybridisation between the O 2p and transition metal 3d levels, then the resonance takes place via an interatomic process [19, 20]. The oxygen resonant photoemission process arises from the interference of a direct photoemission channel and an interatomic process which leads to an enhancement of the photoemission intensity of the O 2p states. The Super-Coster Krönig [SCK] decay process (Chapter 3) does not occur only on the O atom because the O 2p levels are full. Therefore, resonance must happen due to delocalisation of holes onto the O^{2-} ion from the metal (*M*) ion. In the O 2s→2p resonance, the direct and the interatomic processes are given by equations 5.1 and 5.2 respectively:

$$O2s^2 2p^6 + h\nu \rightarrow O2s^2 2p^5 + e^-, \qquad \text{Equation 5.1}$$

$$\begin{cases} M3d^m O2s^2 2p^6 \leftrightarrow M3d^{m+1} O2s^2 2p^5 + h\upsilon \rightarrow \\ \{M3d^{m+1} O2s^1 2p^6\}^* \rightarrow M3d^{m+1} O2s^2 2p^5 + e^-. \end{cases} \qquad \text{Equation 5.2}$$

Here the asterisk (*) represents a transient excited state. More details on resonant photoemission can be found in the review by L. C. Davis [21] and references therein.

5.4.1 Oxygen Resonance Photoemission in $LnBaCo_2O_{5+\delta}$ (Ln = Gd, $Dy_{1-x}Tb_x$)

Figures 5.13 and 5.14 present valence band energy distribution curves (VB EDCs) recorded from clean single crystal samples of $GdBaCo_2O_{5.5}$ and $Dy_{1-x}Tb_xBaCo_2O_{5+\delta}$ respectively over the O 2s→2p threshold in the range of 20-24 eV photon energy. The spectra were recorded at room temperature over the photon energy range $h\upsilon$ = 18 to 30 eV and normalised to the incident photon flux. A third order polynomial background has been subtracted from the spectra of $GdBaCo_2O_{5.5}$. Features labelled by letters A, B, C and D situated around 1 eV, 3 eV, 5 eV and 9 eV respectively in the VB were selected to generate constant initial state (CIS) spectra in the region of the O 2s→2p threshold. The peak at point D is due to Gd 4f states [7] and surface contamination (Chapter 4) while the peaks at the points A-C are assigned to contributions from Co 3d states expected to be mixed with O 2p states [7]. The fluctuation in intensity of these features can be observed at photon

energies of around 22-24 eV and 20-24 eV for $GdBaCo_2O_{5.5}$ and $Dy_{1-x}Tb_xBaCo_2O_{5+\delta}$ respectively. These fluctuations can be seen more clearly in the CIS spectra generated from

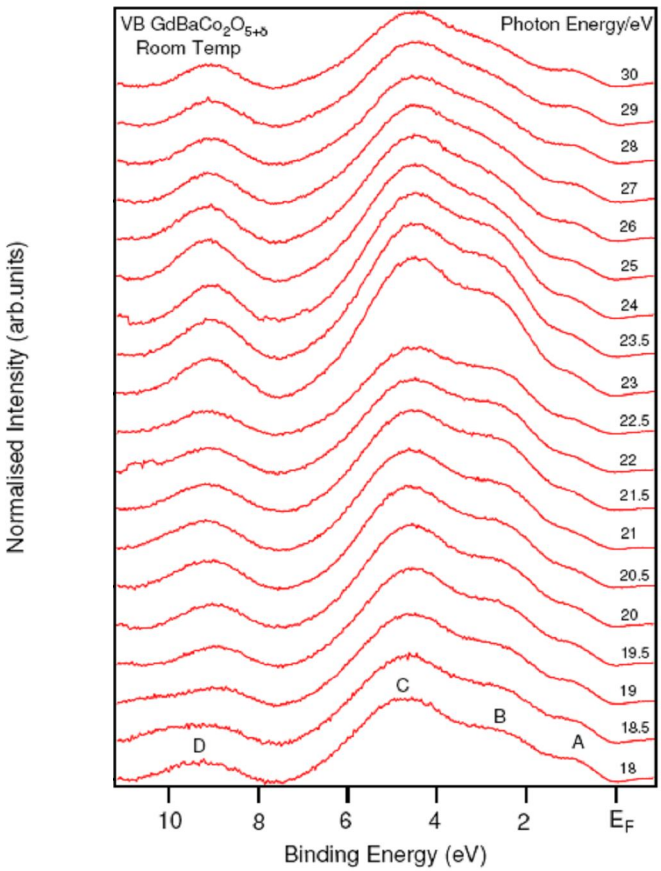

Figure 5.13: *Valence band EDCs recorded from $GdBaCo_2O_{5.5}$, in the vicinity of the O 2s→2p resonance. Spectra are background subtracted using a third order polynomial and normalised to the incident photon flux. The spectra were recorded at room temperature. Points A-D were later selected for CIS measurements.*

the VB EDCs at the points A-D, as shown in Figures 5.15 and 5.16 respectively. The spectra of features B and C show a large resonance effect (which is largest at point C) showing a substantial contribution of O 2p states to the valence band density of states function. It is worth mentioning in Figure 5.15, that the CIS spectra show an abrupt increase in intensity approximately at 23 eV photon energy caused by an experimental artefact. This may be due to a shift in the synchrotron beam that gave rise to a sudden

increase in the incident photon flux and hence an increase in the count rate. This abrupt increase in the incident flux could not be normalised properly.

It has been reported that O 2p-derived states contribute more strongly to the regions where Co 3d states are dominant and have little overlap and hybridisation with the rare earth 4f states in the valence band of double perovskite oxides [7]. Hence, smaller O 2p resonance effects are observed at point D, where the Gd 4f states are located. The resonance observed is likely to be mainly related to the surface contamination (due to surface –OH) which is also observed at similar binding energy [7].

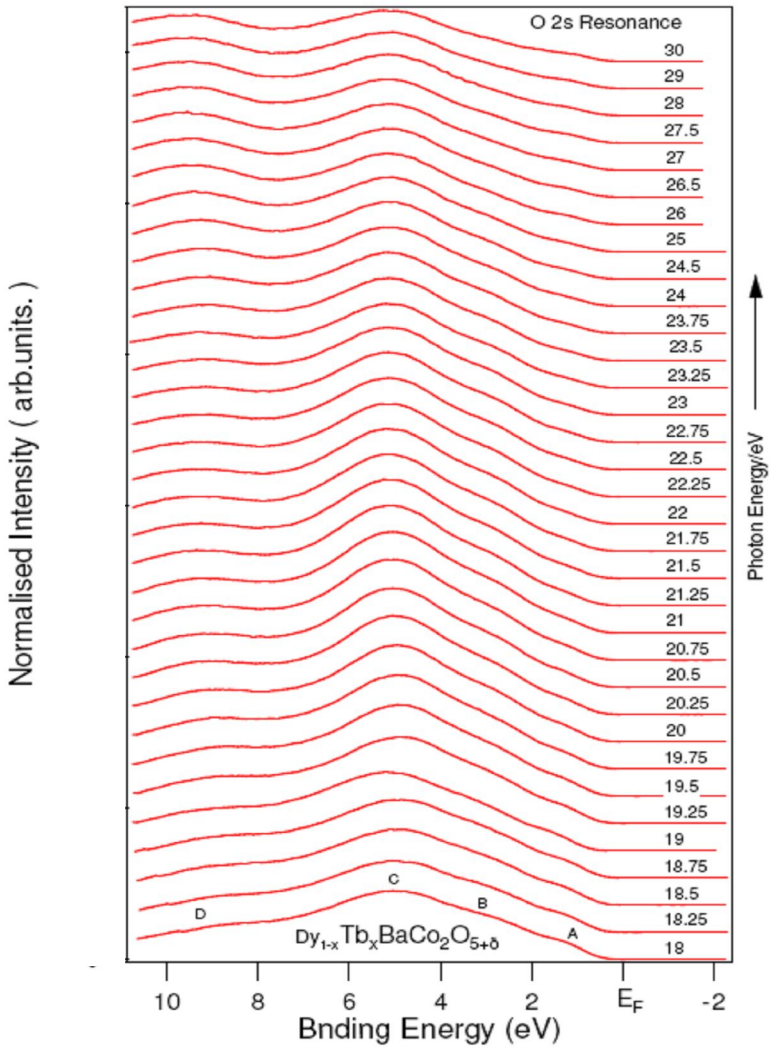

Figure 5.14: *Valence band EDCs recorded from $Dy_{1-x}Tb_xBaCo_2O_{5+\delta}$ in the vicinity of the O 2s→2p resonance. Points A-D were later selected for CIS measurements. Spectra were recorded at room temperature and are normalised to incident photon flux.*

The CIS spectrum for feature D of $Dy_{1-x}Tb_xBaCo_2O_{5+\delta}$ depicted in Figure 5.16 shows another maximum around 26 eV photon energy. This is also an artefact caused by the attenuated signal generated from the emitted photoelectrons that are coming from the sample surface measured in the low kinetic energy regime.

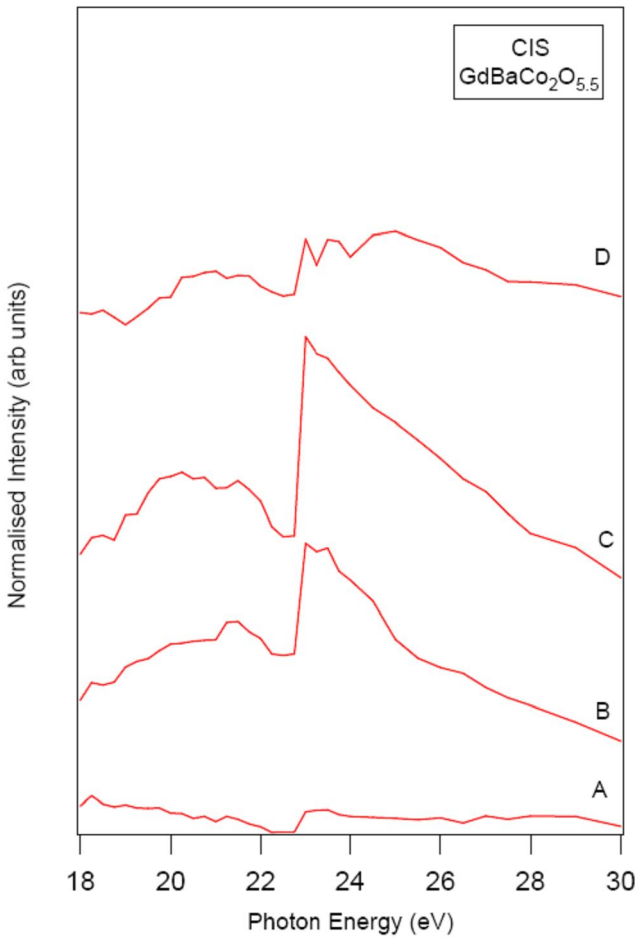

Figure 5.15: *CIS spectra generated from valence band EDCs of $GdBaCo_2O_{5.5}$ in the region of the O 2s→2p resonance at the selected points A, B, C and D in the valence band.*

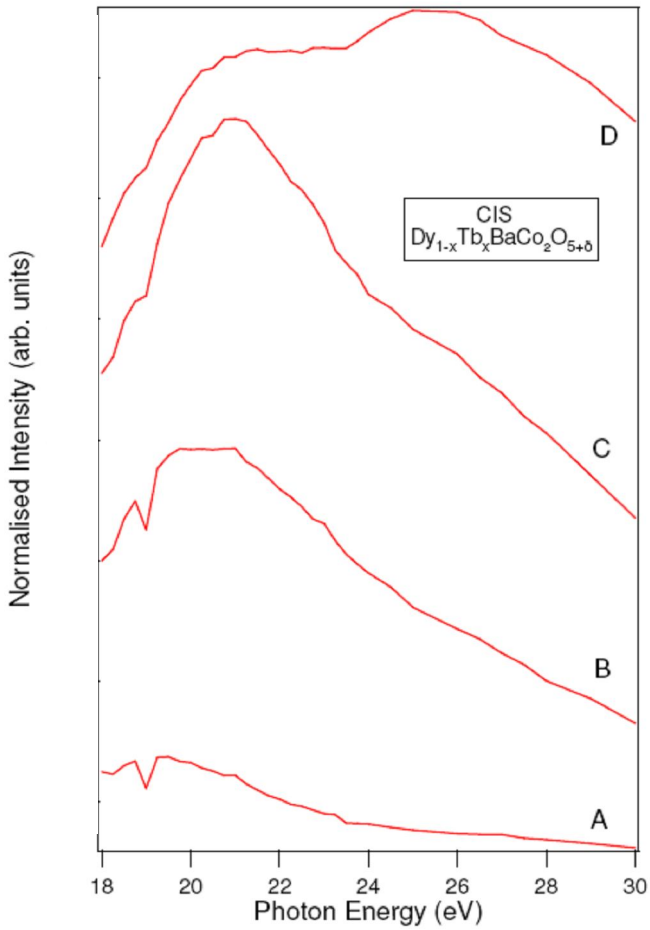

Figure 5.16: *CIS spectra generated from valence band EDCs of $Dy_{1-x}Tb_xBaCo_2O_{5+\delta}$ in the region of the O 2s→2p resonance at the selected points A, B, C and D in the valence band.*

The above discussion on oxygen resonance can be paired with the cation resonance results for Gd-112 [10], to give a complete picture of the assignment of the VB states in Gd-112. Resonant photoemission results undertaken by Flavell *et al.* [7] indicate that the VB of $GdBaCo_2O_{5+\delta}$ (Gd-112) is made up of strongly hybridised O 2p and Co 3d states. The Gd 4f contribution to the VB is centred at around 8 eV binding energy. No 4f states close to the Fermi level were found [7].

5.5 Conclusions

From the above high resolution photoemission results on the single crystal samples of $GdBaCo_2O_{5.5}$, $Dy_{1-x}Tb_xBaCo_2O_{5+\delta}$ and $DyBaCo_2O_{5.5}$, it can be concluded that the temperature based MI transitions in these compounds occurs in the 300-400 K temperature range. A post-growth oxygen annealing treatment for the as-grown single crystals of Ln-112 is necessary, achieving oxygen contents close to 5.50, to observe a marked non-metal-to-metal transition. This transition takes place from LS states to intermediate spin (IS) and high spin (HS) states of Co^{3+} slowly and gradually [22] which is contrary to sudden switch from LS to HS proposed by Frontera *et al.* [10]. Moreover, the MI transition effect in the as-grown single crystal samples of Ln-112 may be enhanced by a factor ~ 17 through a post-growth annealing treatment achieving oxygen contents close to $\delta = 0.50$

The oxygen resonance photoemission study of $LnBaCo_2O_{5+\delta}$ (Ln = Gd, $Dy_{1-x}Tb_x$) reveals that the features labelled by letters B,C and D situated at around 3 eV, 5 eV and 9 eV binding energy respectively in the VB of $GdBaCo_2O_{5.5}$ and $Dy_{1-x}Tb_xBaCo_2O_{5+\delta}$ contribute O 2p states to the valence band density of states function. The features B and C show a large resonance effect which is largest at point C. Thus we conclude that the O 2p states contribute most strongly to the valence band at 5 eV binding energy.

References

[1] S. Sugano, Y. Tanabe and H. Kamimura, *Multiplets of Transition-Metal Ions in Crystals*, Academic New York (1970).

[2] M. A. Korotin, S. Yu. Ezhov, I. V. Solovyev, V. I. Anisimov, D. I. Khomskii, and G. A. Sawatzky, *Phys. Rev. B*, **54**, 5309 (1996).

[3] M. Imada, A. Fujimori, and Y. Tokura, *Rev. Mod. Phys.*,**70**, 1039 (1998).

[4] A. Maignan, C. Martin, D. Pelloquin, N. Nguyen and B. Raveau *J. Solid State Chem.*, **142**, 247(1999).

[5] A. A. Taskin, A. N. Lavrov and Y. Ando, *Phys. Rev. B*, **71**, 134414 (2005)

[6] S. Streule, A. Podlesnyak, J. Mesot, M. Medarde, K. Conder, E. Pomjakushina, E. Mitberg and V. J. Kozhevnikov, *J. Phys. Condens. Matter*, **17**, 3317 (2005).

[7] W. R. Flavell, A. G. Thomas, D. Tsoutsou, A. K. Mallick, E. A. Seddon, C. Cacho, A. E. R. Malins, R. L. Stockbauer, R. L. Kurtz, P. T. Sprunger, S. N. Barilo, S. V. Shiryaev and G. L. Bychkov, *Phys. Rev. B*, **70**, 224427 (2004).

[8] K. Takubo, J. Y. Son, T. Mizokawa, M. Soda, and M. Sato, *Phys. Rev. B*, **73**, 075102 (2006).

[9] H. Kusuya, A. Machida, Y. Moritomo, K. Kato, E. Nishibori, M. Takata, M. Sakata, and A. Nakamura, *J. Phys. Soc. Jpn.*,**70**, 3577 (2001).

[10] C. Frontera, J. L. Garcia-Munoz, A. Llobet, M. A. G. Aranda, *Phys. Rev. B*, **65**,180405 (2002).

[11] M. Abbate, J. C. Fuggle, A. Fujimori, L. H. Tjeng, C. T. Chen, R. Potze, G. A. Sawatzky, H. Eisaki and S. Uchida, *Phys. Rev. B*, **47**, 16124 (1993).

[12] T. Saitoh, T. Mizokawa, A. Fujimori, M. Abbate, Y. Takeda, and M. Takano, *Phys. Rev. B*, **55**, 4257 (1997).

[13] A. G. Thomas, W. R. Flavell, P. M. Dunwoody, C. E. J. Mitchell, S. Warren, S. C. Grice, P. G. D. Marr, D. E. Jewitt, N. Khan, S.W. Downes, D. Teehan, E. A. Seddon, K. Asai, Y. Koboyashi, and N. Yamada, *J. Phys. Condens. Matter*, **12**, 9259 (2000).

[14] A. Maignan, C. Martin, D. Pelloquin, N. Nguyen and B. Raveau, *J. Solid State Chem.*,**142**, 247 (1999).

[15] M. Hidaka, M. Soejima, R. P. Wijesundera, M. Soda , M. Sato , S. H. Choi , N. E. Sung, M. G. Kim and J. M. Lee, *Phys. Stat. Sol. B*, **243**, 1813 (2006).
[16] W. S. Kim, E. O. Chi, H. S. Choi, N. H. Hur, S. J. Oh and H.C. Ri, *Solid State Commun*., **116**, 609 (2000).
[17] Y. P. Chernenkov, V. P. Plakhty, A. G. Gukasov, S. N. Barilo, S.V. Shiryaev, G.L. Bychkov, V. Hinkov, V. I. Fedorov and V. A. Chekanov, *Phys. Lett. A*, **365**,166 (2007).
[18] S. N. Barilo, S. V. Shiryaev, G. L. Bychkov, A. S. Shestak, W. R. Flavell, A. G. Thomas, H. M. Rafique, Y. P. Chernenkov, V. P. Plakhty, E. Pomjakushina, K. Conder and P. Allenspach, *J. Crystal Growth* , **310**, 1867 (2008).
[19] E. Bertel, R. Stockbauer and T. E. Madey, *Phy. Rev. B*., **27**, 1939 (1986).
[20] E. Bertel, R. Stockbauer and T. E. Madey, *Surf. Sci*., **141**, 355 (1984).
[21] L. C. Davis, *J. Appl. Phys*, **59**, 25 (1986).
[22] K. Asai, A. Yoneda, O. Yokokura, J. M. Tranquada, G. Shirane and K. Kohn, *J. Phys. Soc. Jpn.*, **67**, 290 (1998).

Chapter 6

Photoelectron Spectroscopy of $LnBaCo_4O_{7+\delta}$ (δ=0) - Ln-114

6.1 Introduction

An introduction to $LnBaCo_4O_7$ (Ln-114) has already been given in Section 2.8. $YbBaCo_4O_7$ (Yb-114) is a mixed valence compound whose crystal structure is made up of Kagomé sheets of CoO_4 tetrahedra connected by triangular layers of CoO_4 tetrahedra. It belongs to a geometrically frustrated system at room temperature, presents a long-range antiferromagnetic state below 80 K and undergoes a trigonal to orthorhombic phase transition at 175 K [1]. However, no photoemission studies on $YbBaCo_4O_7$ have been reported so far and are undertaken for the first time in this PhD project. The current chapter presents and discusses photoemission studies of $YbBaCo_4O_7$ which mainly comprise resonant photoemission of the cations (Yb^{3+}, Ba^{2+}) and the anion (O^{2-}). In addition to the resonant photoemission of Yb, the corresponding CIS spectra were also recorded at room temperature on beamline MPW 6.1 of the Daresbury Laboratory Synchrotron Radiation Source (SRS). For Co, only a few useful CIS spectra could be recorded because the deadline for the shutdown of the SRS was approaching. In the last part of the chapter, a comparison of the general features in the valence band of $LnBaCo_2O_{5+\delta}$ (Ln = Gd, δ = 0.5) and those of $LnBaCo_4O_{7+\delta}$ (Ln = Yb, δ = 0) is given. The photoelectron spectroscopy of $LnBaCo_2O_{5+\delta}$ (Ln-112) has already been discussed in Chapter 5.

6.2 Valence Band Photoemission of $YbBaCo_4O_7$

Figure 6.1 shows the valence band EDCs for $YbBaCo_4O_7$ as a function of temperature. The spectra were recorded within the temperature range 120-300 K and are normalised to the incident photon flux.

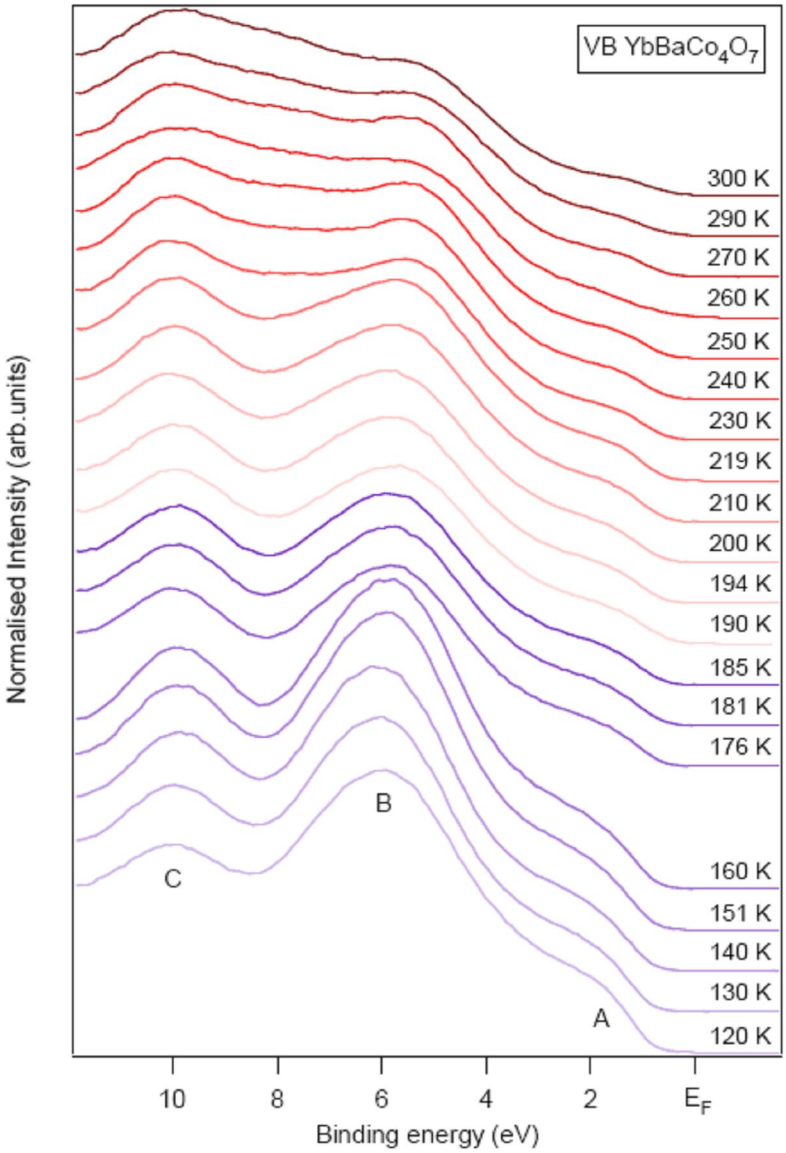

Figure 6.1: *Effect of temperature on the high-resolution valence band EDC spectra of $YbBaCo_4O_7$ recorded at 30 eV photon energy. Points A-C were later selected for O 2s→2p resonance at room temperature. The spectra are normalised to the incident photon flux.*

The EDCs in the 120 K to 160 K temperature range were recorded in one experiment and in order of increasing temperature. On the other hand, the data set in the 176 K to 300 K temperature range was taken on a different day but in order of increasing temperature. Features labelled by the letters A, B and C in the valence band appear approximately

around 1.4 eV , 5.6 eV and 9.6 eV binding energies respectively. The peaks B and C are broadened compared to the peak C. The feature located around 1.4 eV binding energy in the valence band (A) seems to be attenuated in intensity with the increase of temperature and the reason for this is unclear. All these features appear to become less well-resolved as the temperature is raised probably due to contamination of the sample. The contamination of the $YbBaCo_4O_7$ sample has been discussed in Section 4.5.2. The apparent attenuation of the low binding energy features with increase in temperature may be due to their attenuation by adsorption of species from the residual vacuum. The features A-C in the valence band were later selected for O 2s→2p resonance photoemission at room temperature and this is discussed in Section 6.3.3.

6.3 Resonant Photoemission in $YbBaCo_4O_7$

6.3.1 Rare-earth Resonant Photoemission

The rare-earth contribution to the DOS in the valence band of $YbBaCo_4O_7$ was probed by experiments at the Yb 4d→4f resonance. A general introduction to the rare-earth resonant photoemission process is given below.

The direct photoemission process for a rare-earth configuration $4f^n$ can be written as:

$$4d^{10}\,4f^{n} + h\nu \rightarrow 4d^{10}\,4f^{n-1} + e^{-}. \qquad \text{Equation 6.1}$$

During the resonant photoemission experiment, a specific energy hν of the incoming photons is selected which starts a second photoexcitation channel. The second photoemission channel so obtained interferes constructively with the direct photoemission channel. The total final-state configuration $4d^{10}4f^{n-1}$, as in the direct photoemission process, is achieved through an intermediate 4d-hole state. This state is immediately relaxed via a rapid Super-Coster Krönig process. Symbolically, both the steps described above can be written as:

$$4d^{10}\,4f^{n} + h\nu \rightarrow \{4d^{9}\,4f^{n+1}\}^{*} \rightarrow 4d^{10}\,4f^{n-1} + e^{-}; \qquad \text{Equation 6.2}$$

where asterisk (*) denotes an excited state.

6.3.1.1 Rare-earth Resonant Photoemission in $YbBaCo_4O_7$

Figure 6.2 shows a stack of valence band EDC photoemission spectra of $YbBaCo_4O_7$ recorded at room temperature and over the photon energy range hν =170 to 215 eV, passing through the Yb 4d→4f threshold at 180.5 eV photon energy [2, 3]. The spectra are normalised to the incident photon flux. Points A-I refer to the features later selected for CIS measurements. An obvious enhancement in intensity for the features C and D can be seen in the valence band of $YbBaCo_4O_7$. The increase in intensity of the features C and D suggests a strong contribution of the Yb 4f states to the density of states at these points. Features G, H and I, located outside the valence band, within the 24 to 32 eV binding energy range, also undergo resonance photoemission between photon energies 170 eV and 215 eV because a slight increase in intensity for these features can also be seen.

These smaller resonances are more obvious in the CIS spectra of $YbBaCo_4O_7$ shown in Figure 6.3. These CIS spectra were recorded at room temperature while scanning the photon energy through the resonance. The binding energy positions of the features A-I for the CIS spectra are labelled in Figure 6.2. Features A and B show no resonance effect whereas a prompt resonance effect for the features C and D is seen. It is also worthy of note that feature D reveals a comparatively larger resonance effect. However, the features E and F exhibit only a weak resonance effect. The DOS function outside the valence band of $YbBaCo_4O_7$ has contributions of Yb 5p states from the features G-I, where an enhanced resonance is seen [4].

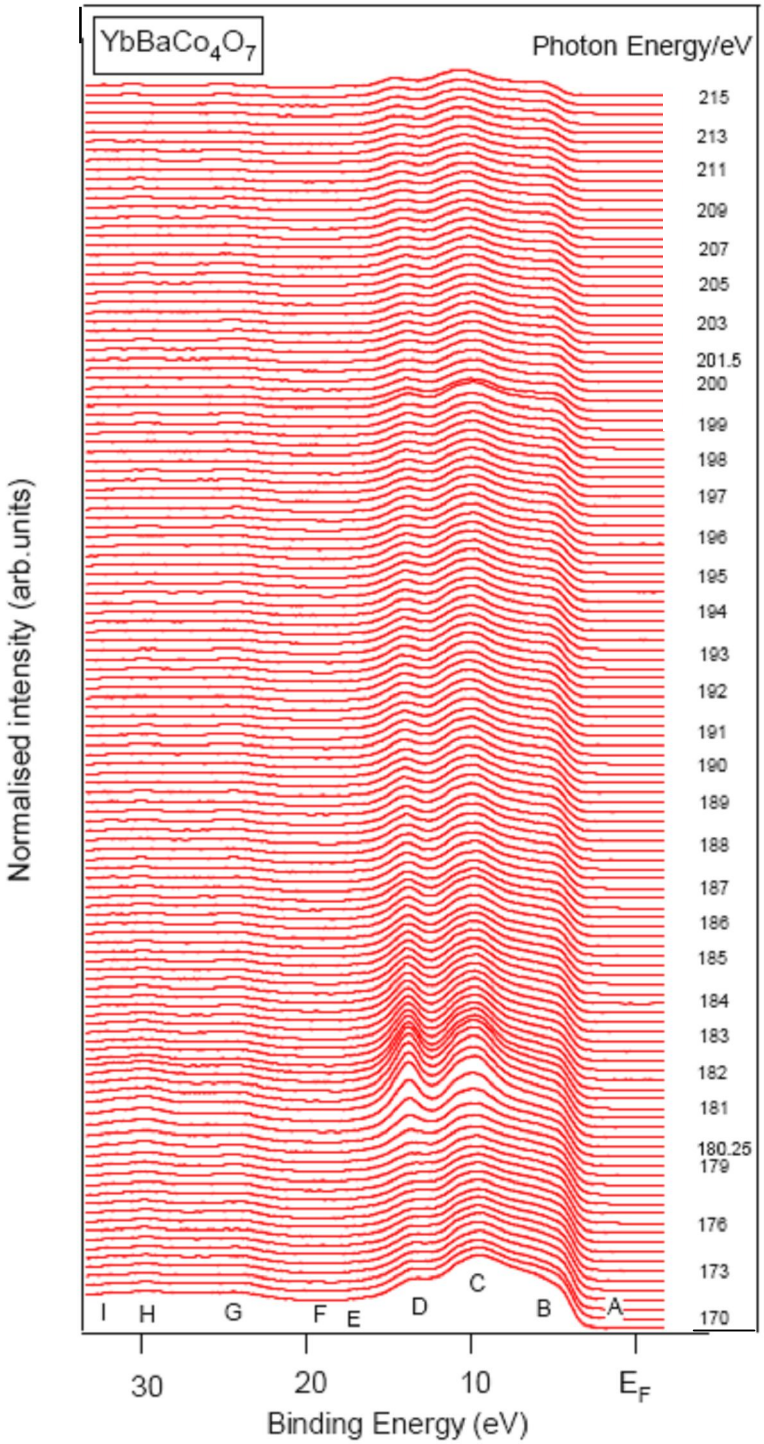

Figure 6.2: *Valence band EDC spectra from $YbBaCo_4O_7$ recorded over the photon energy range hυ = 170 to 215 eV passing through the Yb 4d→4f threshold at around 180.5 eV* [2, 3]. *Points A-I refer to the features later selected for CIS measurements. The spectra are normalised to the incident photon flux. The EDCs were recorded at room temperature.*

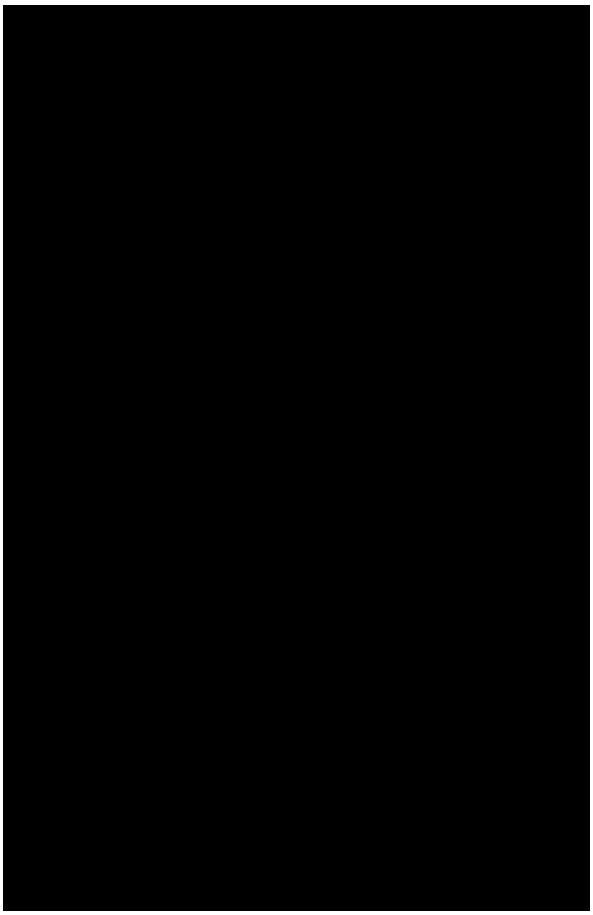

Figure 6.3: *CIS spectra from $YbBaCo_4O_7$ recorded over the photon energy range hυ = 170 to 215 eV passing through the Yb 4d→4f threshold at the selected points A-I in the valence band. The spectra are normalised to the incident photon flux. The spectra were recorded at 300 K.The binding energy positions of the features A-I for the CIS spectra are labelled in Figure 6.2.*

The ground state configuration for Yb metal is [Xe] $4f^{14}6s^2$, indicating that there is a filled shell ($4f^{14}$) in the system. F. Gerken [5] calculated photoemission intensities for different atomic 4f final states for rare earth metals. Results of his calculations suggest that the rare earth 4f shell can be treated as a strongly localised atomic-like level. As Yb metal contains a fully occupied 4f shell, the final state is split only by spin-orbit interaction [5]. For a fully occupied f orbital such as in Yb^{2+} ($4f^{14}$), 4d→4f resonance photoemission does not occur. On the contrary, when Yb is involved in bonding in crystals as Yb^{3+} ($4f^{13}$), the 4f orbital is incompletely filled and 4d→4f resonance photoemission can occur. Hence a distinction can

be made between EDC peaks corresponding to the Yb^{2+} ($4f^{14}$) ions and those of the Yb^{3+} ($4f^{13}$) ions [5].

The Yb^{3+} ($4f^{13}$) emission from oxidised Yb metal (Yb_2O_3) has already been studied both theoretically and experimentally with photon energies around the 4d→4f threshold [2, 3]. The interaction of Yb with oxygen is of particular interest because oxidation causes a change of valence state from the divalent Yb (f^{14}) with a closed 4f shell. The oxidation of the Yb^{2+} (f^{14}) ion opens the closed 4f shell making it trivalent with the ground- state configuration $4f^{13}$. Since the initial occupation number of the 4f shell strongly affects the resonance behaviour of the 4f states, it is possible to identify the valence states of the rare-earth atoms involved [6]. To identify the oxidation state of Yb in $YbBaCo_4O_7$ from the shape and binding energy positions of the features C and D, two previously performed resonance photoemission studies on Yb containing materials (with different oxidation states) are described here.

Okane *et al.*[7] studied valence band electronic structure of a polycrystalline sample of $YbFe_4Sb_{12}$ at T = 15 K using high-resolution synchrotron photoemission spectroscopy and observed the energy positions of the bulk and surface components of the Yb^{2+} signal. Valence band EDC spectra for $YbFe_4Sb_{12}$ (shown in Figure 6.4) were recorded at 500 eV and 700 eV photon energies.

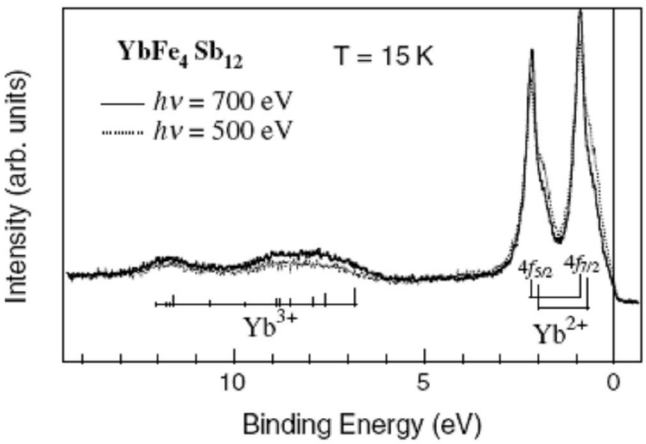

Figure 6.4: *Valence band EDC spectra from $YbFe_4Sb_{12}$ recorded at 700 eV and 500 eV photon energies and temperature 15 K* (*Taken from* [7]).

Features within 3 eV binding energy consist of sharp main doublet peaks and shoulder-like doublet structures on the lower binding energy side of the main peaks which are

contributions from the Yb^{2+} ($4f^{14}$) surface and bulk states. Photoemission signals from mixed-valence Yb compounds are generally comprised of two doublets with surface and bulk contributions [8]. The Yb^{2+} contribution can be interpreted as a spin-orbit doublet of the $4f_{7/2}$ and $4f_{5/2}$ components. On the other hand, features in the 6-13 eV binding range are attributed to the Yb^{3+} ($4f^{13}$) signal. The photoemission intensity for the Yb^{3+} signal recorded at $h\nu$ = 700 eV is higher than to that recorded at $h\nu$ = 500 eV which indicates that the Yb^{3+} signal is predominantly from the bulk. The overall line shape for the Yb^{3+} signal, interpreted in terms of the calculated atomic multiplet lines [5], is shown by a bar diagram in Figure 6.4. Okane *et al*. suggested, as a result of their study, that the main Yb 4f signal in $YbFe_4Sb_{12}$ appears to be divalent-like and the existence of irregular trivalent-like Yb sites is also shown.

Orlowski *et al.* [9] doped a clean semiconductor crystal sample surface of CdTe with controlled Yb metal ions to a thickness of about 0.5 ML and then performed annealing of the sample. They then carried out Yb 4d→4f resonant photoemission to distinguish changes between features corresponding to fully and partially occupied 4f states in the valence band of YbCdTe. Figure 6.5 shows two photoemission spectra from Yb-doped CdTe (lower EDC) and Yb-doped and annealed CdTe (upper EDC) sample surfaces. Both the spectra reveal two sharp features corresponding to the Yb^{2+} ($4f^{14}$) states near the Fermi level. Features situated in the 10-12 eV binding energy range are attributed to Cd 4d states in the valence band of YbCdTe and peaks within 6-9 eV binding energy range correspond to the Yb^{3+} ($4f^{13}$) states.

Orlowski *et al*. infer that deposition of Yb on the CdTe sample surface creates metallic islands on the top of the surface which contain Yb^{2+} ($4f^{14}$) and Yb^{3+} ($4f^{13}$) ions. The subsequent annealing of the sample leads to diffusion of the Yb ions into the sample surface. The quantity of Yb^{2+} ($4f^{14}$) ions decreases and that of Yb^{3+} ($4f^{13}$) ions increases after annealing the doped surface. This is evident from the enhancement of photoemission intensity for the Yb^{3+} ($4f^{13}$) feature (Figure 6.5). Fano-type 4d→4f resonance was only observed for the Yb^{3+} ($4f^{13}$) peaks [10] and did not take place for the Yb^{2+} ($4f^{14}$) features due to fully its occupied 4f orbital [10].

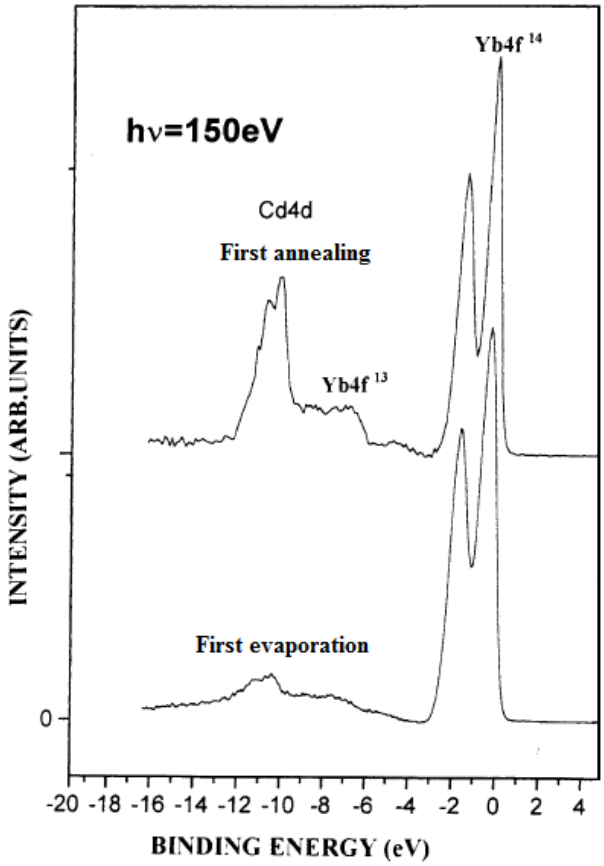

Figure 6.5: *Valence band EDC spectra obtained from clean Yb-doped (lower EDC) and Yb- doped and annealed (upper EDC) CdTe crystal sample surfaces recorded at 150 eV photon energy* (*Taken from* [9]).

Comparing the shapes and binding energy positions (9-13 eV) of the features C and D in the valence band of $YbBaCo_4O_7$ with the previous photoemission results, it can be deduced that the oxidation state of Yb in $YbBaCo_4O_7$ is 3+ because no large Yb^{2+} doublet appears in the vicinity of the Fermi level. We note, however, that in this case, because Yb^{2+} cannot undergo resonance photoemission, the absence of a resonance for features A and B does not in itself rule out the presence of Yb character close to the Fermi energy. However, we see no evidence of the characteristic spin-orbit splitting of Yb^{2+} close to the Fermi energy (as, for example in Figure 6.5). Therefore, it can also be deduced that the DOS close to E_F in the valence band of $YbBaCo_4O_7$ is likely to be made up of Co 3d and O 2p states. Moreover, it is these states that are responsible for the magnetic and electronic behaviour of

$YbBaCo_4O_7$ as in case of other perovskite cobaltites such as $LaCoO_3$ [11-13], $HoCoO_3$ [14] and $GdBaCo_2O_{5+\delta}$ [15].

6.3.2 Barium Resonant Photoemission in $YbBaCo_4O_7$

The contribution of the Ba 5p states to the density of states (DOS) function of $YbBaCo_4O_7$ can also be identified by means of the resonant photoemission technique. Resonant photoemission spectra for $YbBaCo_4O_7$ recorded at room temperature and over the photon energy range $h\nu$ = 96 to 110 eV, passing through the Ba 4d→4f threshold [15], are shown in Figure 6.6.

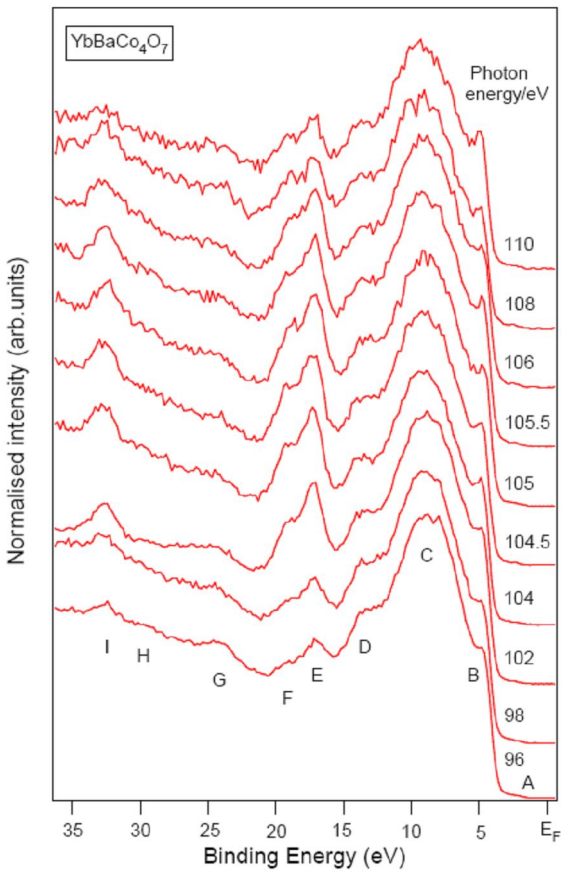

Figure 6.6: *Valence band EDCs from $YbBaCo_4O_7$ recorded at room temperature in the vicinity of the Ba 4d→4f resonance ca.104 eV photon energy* [15]. *The spectra are normalised to the incident photon flux.*

The spectra are normalised to the incident photon flux. For each EDC, the respective photon energy is indicated on the right hand side. Features E and F, within the 16-19 eV

binding energy range, clearly show an increase in intensity and identify the contribution of the Ba 5p states to the DOS function of $YbBaCo_4O_7$. It is worth mentioning that Ba 5p states do not contribute to the valence band of $YbBaCo_4O_7$ as is the case in similar materials such as $LnBaCo_2O_{5+\delta}$ (Ln = Gd, Dy, Eu, $Dy_{0.9}Tb_{0.1}$) [14, 15].

6.3.3 Oxygen Resonant Photoemission in $YbBaCo_4O_7$

Figure 6.7 shows stacked valence band EDC spectra of $YbBaCo_4O_7$ recorded at 300 K over the photon energy range hυ = 20.5 to 30 eV passing through the O 2s→2p threshold. Oxygen resonance photoemission process has already been described in Section 5.4. The photon energy was increased initially with a step size of 0.25 eV from 20.5 to 24.5 eV and finally from 26 to 30 eV with a step size of 1 eV for the last five scans. All the VB EDC spectra are normalised to the photon flux.

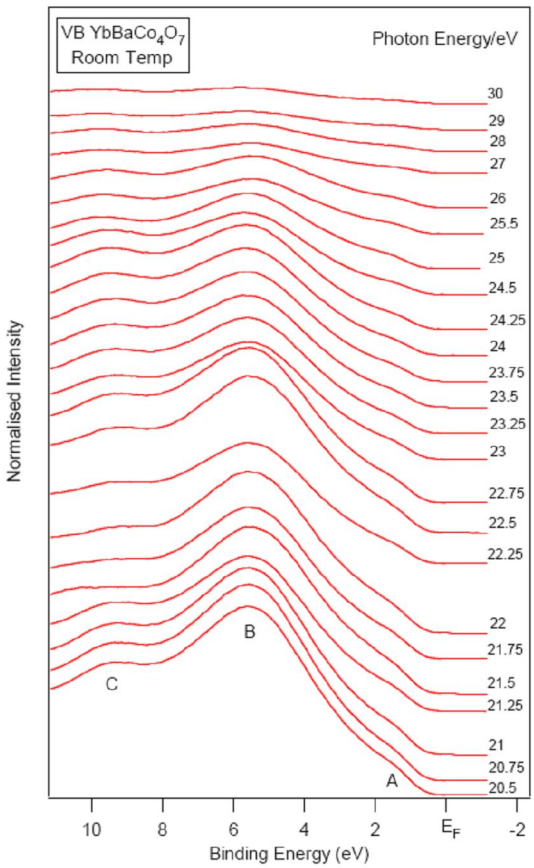

Figure 6.7: *Valence band EDC spectra from $YbBaCo_4O_7$ recorded over the photon energy range hυ = 20.5 to 30 eV passing through the O 2s→2p threshold. Points A-C refer to the features later selected for CIS measurements. The spectra are normalised to the incident photon flux.*

Features marked with letters A, B, C situated at binding energies 1.4 eV, 5.6 eV, 9.6 eV respectively in the valence band were selected to generate constant initial state (CIS) spectra for more detailed examination of the resonance behaviour. The CIS spectra for the peaks labelled in the valence band EDC spectra of $YbBaCo_4O_7$ are shown in Figure 6.8. These show a signal that decreases with increasing photon energy (consistent with the decreasing cross section for O 2p photoemission). Superimposed on this is an enhancement in the range 21.75-23 eV, a typical energy for the O 2s→2p resonance [16].

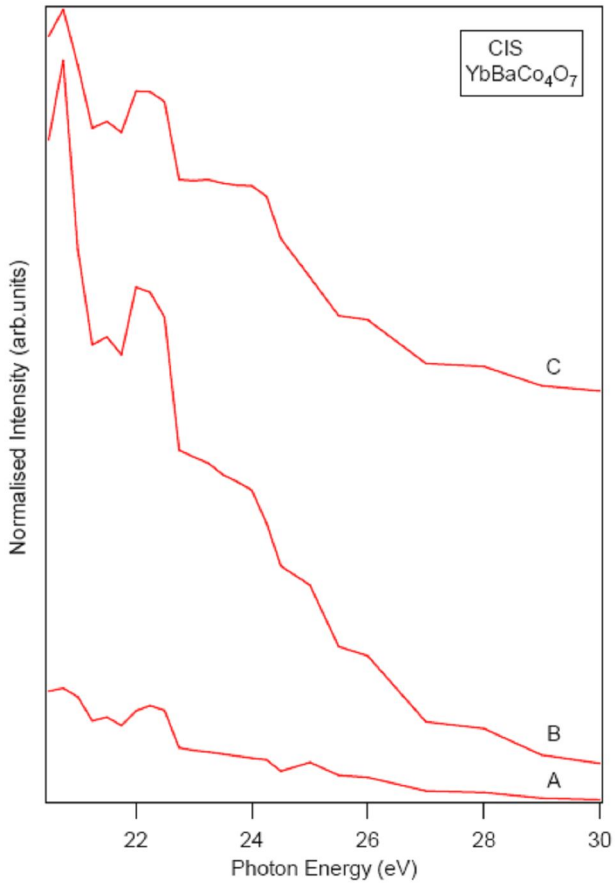

Figure 6.8: *CIS spectra generated from the valence band EDC spectra of $YbBaCo_4O_7$ recorded over the photon energy range hυ = 20.5 to 30 eV passing through the O 2s→2p threshold. Points A, B and C correspond to CIS measurements of the selected features in the valence band.*

The resonance maxima of the three peaks are located around hυ = 22.5 eV photon energy. The middle CIS peak related to feature B shows a strong resonance effect as compared to the top peak which is related to feature C. However, the lower resonance (A) is weak,

probably because feature A is intrinsically quite small. Hence the DOS function of $YbBaCo_4O_7$ has contributions from O 2p-derived states throughout the valence band with the contribution from feature B larger than features A and C.

6.3.4 Cobalt Resonant Photoemission

To identify the Co 3d character of the states in the valence band region, Co 3p→3d resonance experiments can be performed. Resonance effects at transition metal 3p→3d thresholds have smaller cross sections as compared to those of the rare-earth (RE) 4d→4f resonances [16]. The direct photoemission process for Co^{3+} (d^6) can be represented by equation 6.3 as:

$$3p^6 3d^6 + h\nu \rightarrow 3p^6 3d^5 + e^-. \qquad \text{Equation 6.3}$$

A resonance is observed at the 3p→3d optical absorption edge due to the interference of the direct photoemission process and the excitation process of the electrons from the 3p to 3d orbitals followed by Super-Coster Krönig decay. The following equation summarises both the processes:

$$3p^6 3d^6 + h\nu \rightarrow \{3p^5 3d^7\}^* \rightarrow 3p^6 3d^5 + e^-. \qquad \text{Equation 6.4}$$

The asterisk (*) represents an excited state. Synchrotron-excited 3p→3d resonant photoemission may be used as a chemical searchlight to obtain information about the contributions of Co states to the DOS function.

6.3.4.1 Cobalt Resonant Photoemission in $YbBaCo_4O_7$

Figure 6.9 shows CIS spectra from $YbBaCo_4O_7$ recorded over the photon energy range 55 to 70 eV passing through the Co 3p→3d threshold at the selected points A-E. The binding energy positions of the points A-E in the valence band of $YbBaCo_4O_7$ are shown in Figure 6.6. The spectra were recorded at room temperature and are normalised to the incident photon flux.

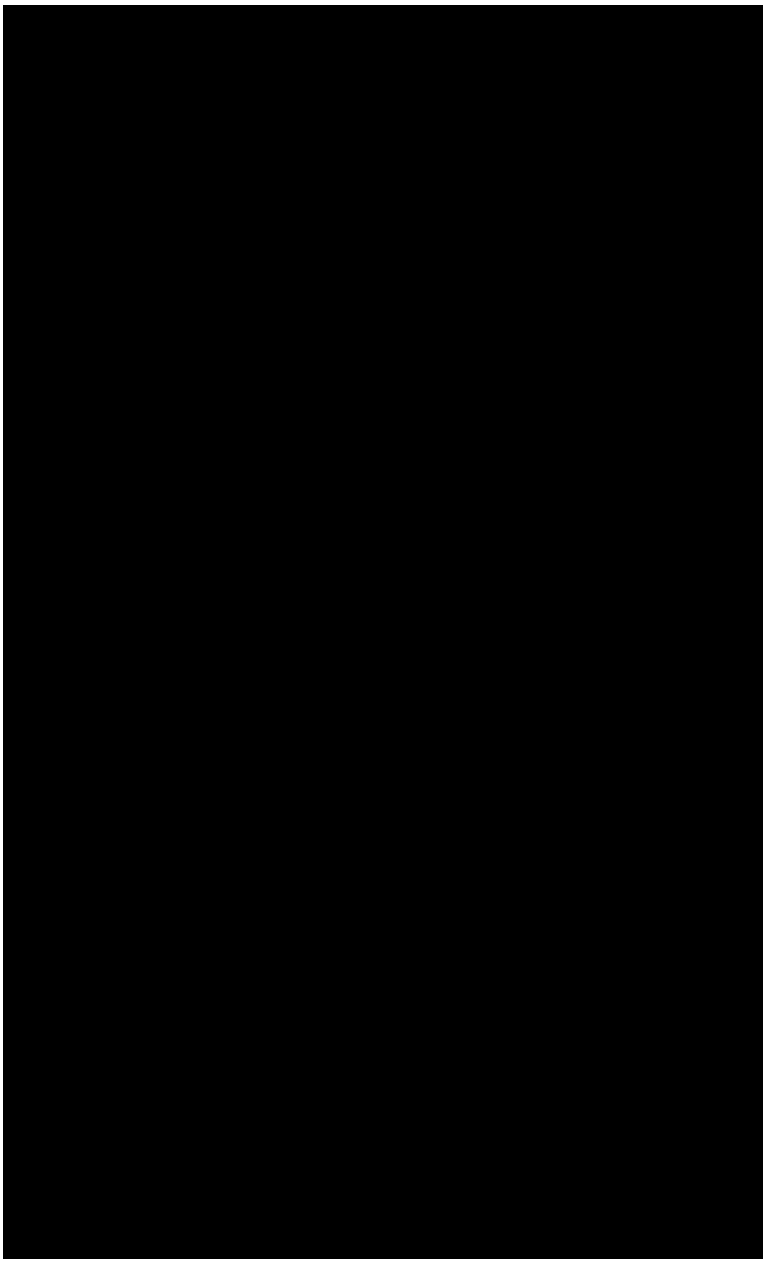

Figure 6.9: *CIS spectra from $YbBaCo_4O_7$ recorded over the photon energy range 55 to 70 eV passing through the Co 3p→3d threshold at the selected points A-E. The binding energy positions of features A-E are shown in Figure 6.6. The CIS spectra were recorded at room temperature and are normalised to the incident photon flux.*

Features A and B reveal no clear resonance effect showing a continuous decrease in intensity. As the spectrum intensity at feature A is very small, we cannot conclude whether or not a resonance is absent in this case. Although there is noise in these spectra, a marked

Co 3p→3d resonance for feature D can be seen in the 57 to 62 eV photon energy range. A dip in the CIS spectrum, related to feature C, at approximately 59.5 eV photon energy corresponds to an anti-resonance for feature C. Resonance photoemission occurs as a result of constructive interference of the direct photoemission channel and Super-Coster Krönig decay. However, anti-resonance photoemission is a kind of destructive interference which takes place when one of the photoemission channels is suppressed. Resonance and anti-resonance photoemission has already been observed in cuprates such as $Nd_2Ni_{0.75}Cu_{0.25}O_4$ [18] and Cu_2O [19] and in nickelates such as $La_2NiO_{4+\delta}$ [18]. The resonance maximum for the feature D is located around hυ = 59.5 eV photon energy. However for feature E, it is difficult to identify the Co 3p→3d resonance due to the noise in the spectrum. Thus we may conclude that the valence band contains contributions from Co 3d states at points C and D, but there are no clear resonances at points A, B and E.

6.4 Summary of Resonance Photoemission Results

The resonance photoemission results allow the atomic character of the valence band states of $YbBaCo_4O_7$ to be determined as summarised here. Figure 6.10 depicts an EDC spectrum recorded at room temperature and photon energy 170 eV from $YbBaCo_4O_7$ showing atomic character labelled. Points A-I refer to the features selected for resonance photoemission. Features labelled by the letters A, B and C in the valence band have been found to appear approximately around 1.4 eV , 5.6 eV and 9.6 eV binding energies respectively. The peaks B and C are broadened compared to peak A. The Yb 4d→4f resonance reveals a prompt resonance effect for the features C and D (with comparatively a larger resonance effect at the feature D) contributing 4f states to the DOS function of $YbBaCo_4O_7$. However, the features E and F (within the 16-19 eV binding energy range) exhibit only a weak resonance effect. The DOS function outside the valence band of $YbBaCo_4O_7$ has contributions of Yb 5p states from the features G-I (within the 24-32 eV binding energy range) [4], where an enhanced resonance is seen. From the shapes and binding energy positions of the features C and D (9-13 eV) in the valence band of $YbBaCo_4O_7$, it can be deduced that the oxidation state of Yb in $YbBaCo_4O_7$ is 3+ because Yb^{2+} signal appears only in the vicinity of the Fermi level. This conclusion is consistent with the photoemission studies carried out by Okane *et al.* [7] and Orlowski *et al.* [9].

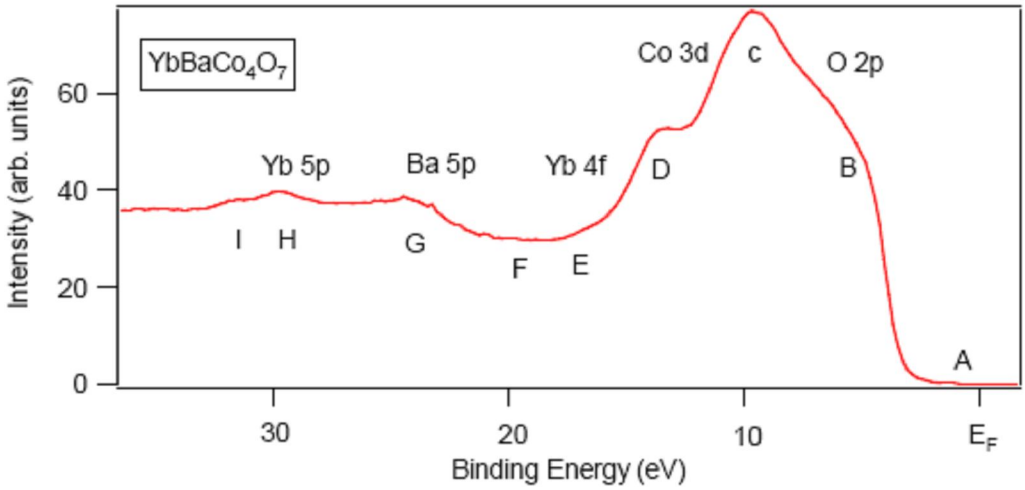

Figure 6.10: *An EDC spectrum from $YbBaCo_4O_7$ (recorded at room temperature and photon energy 170 eV) showing atomic character labelled. Points A-I refer to the features that have been selected for resonance photoemission.*

The O 2s→2p resonance photoemission results show that the DOS function of $YbBaCo_4O_7$ has contributions from O 2p-derived states throughout the valence band with the contribution from feature B larger than features A and C. However, the Ba 4d→4f resonance photoemission reveals that the features E and F, within the 16-19 eV binding energy range, contains the contribution of the Ba 5p states to the DOS function of $YbBaCo_4O_7$. It is worthy of note that Ba 5p states do not contribute to the valence band of $YbBaCo_4O_7$ as is the case of similar materials such as $LnBaCo_2O_{5+\delta}$ (Ln = Gd, Dy, Eu, $Dy_{0.9}Tb_{0.1}$) [14, 15].

The CIS spectra from $YbBaCo_4O_7$ recorded over the photon energy range 55 to 70 eV passing through the Co 3p→3d threshold at the selected points A-E (within the 1.4-16 eV binding energy range) show that the valence band contains contributions from Co 3d states at points C and D, but there are no clear resonances at points A, B and E. Therefore, it can be concluded that the DOS close to E_F in the valence band of $YbBaCo_4O_7$ is likely to be made up of Co 3d and O 2p states and it is these states that are responsible for the magnetic and electronic behaviour of $YbBaCo_4O_7$ as in case of other perovskite cobaltites such as $LaCoO_3$ [11-13], $HoCoO_3$ [14] and $GdBaCo_2O_{5+\delta}$ [15].

6.5 Comparison of $LnBaCo_2O_{5+\delta}$ and $LnBaCo_4O_{7+\delta}$

Figure 6.11 shows valence band EDC spectra of Ln-112 (Ln = Gd) and Ln-114 (Ln =Yb) respectively recorded at room temperature and a photon energy of 21 eV. The spectra are normalised to the incident photon flux. Features labelled by the letters A_1, B_1, C_1 and D_1 in the valence band have been found to appear in the double perovskites cobaltites Ln-112 (Ln = Gd) at around 1 eV , 3 eV, 5 eV and 9 eV binding energies respectively. It must be noted that previously in Chapter 4 (Section 4.3.1) and Chapter 5 (Section 5.2), the features A_1, B_1, C_1 and D_1 were labelled by letters A, B, C and D respectively. The peaks A_1, B_1 and C_1 have contributions from O 2p and Co 3d states whereas D_1 shows mainly rare-earth 4f character [15, 20]. The features labelled by letters A, B and C in the Ln-114 (Ln = Yb) system appear around 1.4 eV, 5.6 eV, and 9.6 eV binding energies respectively. Loosely speaking it can be said that features A, B and C of Ln-114 (Ln = Yb) lie at similar binding energy positions to A_1, C_1 and D_1 of Ln-112 (Ln = Gd) respectively in the valence band. Feature B_1 of Ln-112 (Ln = Gd) is missing in the valence band of Ln-114 (Ln = Yb) and instead, a long tail can be observed at that position between features A and B. The missing feature corresponds to the Co^{3+} LS state in an octahedral environment [21, 22].

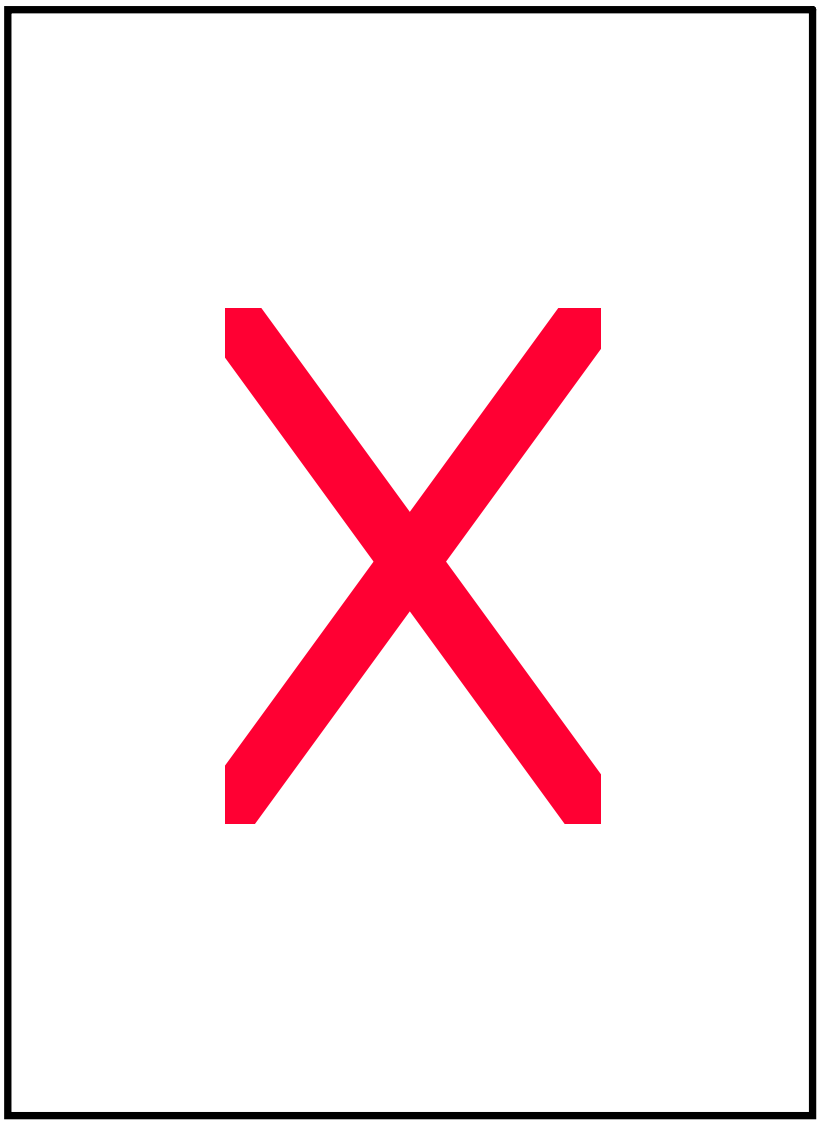

Figure 6.11: *Valence band EDC spectra showing general features A_1, B_1, C_1, D_1 in Gd-112 and A, B, C in Yb-114 cobaltite systems. The spectra are recorded at room temperature and a photon energy of 21 eV. The spectra are normalised to the incident photon flux.*

The Co^{3+} ions in the Ln-114 system are in high spin states because they are surrounded by tetrahedral environments comprising oxygen ligands [5]. There are no Co^{3+} ions in octahedral environments in the 114 system and hence the shoulder at B_1 is absent. In other respects, Figure 6.10 shows that the Co 3d/O 2p hybridisation in the valence band of these two compounds is strikingly similar.

6.6 Conclusions

A high quality single crystal sample of $YbBaCo_4O_7$ was grown by Prof. S. N. Barilo and his group at the ISSSP using the overstoichiometric flux melt technique. Photoemission studies of the sample which mainly comprise resonant photoemission of cations (Yb^{3+}, Ba^{2+}) and the anion (O^{2-}) were performed at the SRS for the first time. In addition to the resonant photoemission of Yb, the corresponding CIS spectra were also recorded at room temperature on beamline MPW 6.1. For Co, only a few useful CIS spectra could be recorded because the deadline for the shutdown of the SRS was approaching. However, the O 2s→2p resonance photoemission of the sample was carried out at beamline 3.2 of the SRS.

The resonance photoemission data allow the atomic character of the valence band states of $YbBaCo_4O_7$ to be determined, as summarised in Section 6.4 (and Figure 6.10). Comparison of the valence band data for Gd-112 and Yb-114 systems shows that the hybridisation of the Co 3d/O 2p states in the valence bands of both systems is strikingly similar. However, the feature ascribed to low spin Co^{3+} in Gd-112 is absent in the spectra of Yb-114. This is because there are no Co^{3+} ions in octahedral environments in this system. This observation is a useful confirmation of the assignment of feature B_1 (Figure 6.11) to low spin Co^{3+} in Gd-112 [17].

References

[1] C. Rabbow and H. Muller-Buschbaum, *Z. Naturforsch B*, **51**, 343 (1996).

[2] L. I. Johansson, J. W. Allen, I. Lindau, M. H. Hecht and **S.** B. M. Hagström, *Phys. Rev. B*, **21**, 1408 (1980).

[3] J. Schmidt-May, F. Gerken, R. Nyholm and L. C. Davis, *Phys. Rev. B*, **30**, 5560 (1984).

[4] G. Rossi and A. Barski, *Solid State Communications*, **57**, 277 (1986).

[5] F. Gerken, *J. Phys. F: Met. Phys.*, **13**, 703 (1983).

[6] J. Barth, F. Gerken, J. Schmidt-May, A. Flodströ and L. I. Johansson, *Chem. Phys. Lett.*, **96**, 532 (1983).

[7] T. Okane, S. Fujimori, K. Mamiya, J. Okamoto, Y. Muramatsu, A. Fujimori, Y. Nagamoto and T. Koyanagi, *J. Phys. Condens. Matter*, **15**, 2197 (2003).

[8] J. J. Joyce, A. B. Andrews, A. J. Arko, R. J. Bartlett, R. I. R. Blyth, C. G. Olson, P. J. Benning and P. C. Canfield, *Phys. Rev. B*, **54**, 17515 (1996).

[9] B. A. Orlowski, B. J. Kowalski, E. Guziewicz, K. S. Sadowska, N. Barrett, C. Guillot, R. L. Johnson and J. Ghijsen, *Prog. Surf. Sci*., **67**, 323 (2001).

[10] K. S. Sadowska, B. J. Kowalski, J. Sadowski, B. A. Orlowski and E. Dynowska, *Electron Technol*., **29**, 294 (1996).

[11] T. Saitoh, T. Mizokawa, A. Fujimori, M. Abbate, Y. Takeda and M. Takano, *Phys. Rev. B*, **56**,1290 (1997).

[12] M. Abbate, J. C. Fuggle, A. Fujimori, L. H. Tjeng, C. T. Chen, R. Potze, G. A. Sawatzky, H. Eisaki, S. Uchida, *Phys. Rev. B*, **47**, 16124 (1993).

[13] A. G. Thomas, W. R. Flavell, P. M. Dunwoody, C. E. J. Mitchell, S. Warren, S. C. Grice, P. G. D. Marr, D. E. Jewitt, N. Khan, V. R. Dhanak, D. Teehan, E. A. Seddon, K. Asai, Y. Koboyashi and N. Yamada, *J. Phys. Condens. Matter*, **12**, 9259 (2000).

[14] D. Tsoutsou, PhD Thesis, The University of Manchester (2005).

[15] W. R. Flavell, A. G. Thomas, D. Tsoutsou, A. K. Mallick, E. A. Seddon, C. Cacho, A. E. R. Malins, R. L. Stockbauer, R. L. Kurtz, P. T. Sprunger, S. N. Barilo, S. V. Shiryaev, and G. L. Bychkov, *Phys. Rev. B*, **70**, 224427 (2004).

[16] S. N. Barilo, S. V. Shiryaev, G. L. Bychkov, A. S. Shestak, W. R. Flavell, A. G. Thomas, H. M. Rafique, Y. P. Chernenkov, V. P. Plakhty, E. Pomjakushina, K.Conder and P. Allenspach, *J. Crystal Growth* , **310**, 1867 (2008).

[17] W. R. Flavell, A. G. Thomas, D. Tsoutsou, A. K. Mallick , J. Hollingworth, S. Patel, E. A. Seddon, R. L. Stockbauer, R. L. Kurtz , P. T. Sprunger , S. N. Barilo, S. V. Shiryaev , G. L. Bychkov, *J. Electron Spectrosc. Rel. Phenom.*, **144**, 777 (2005).

[18] W. R. Flavell, J. Hollingworth, J. F. Howlett, A. G. Thomas, Md. M. Sarker, S. Squire, Z. Hashim, M. Mian, P. L. Wincott, D. Teehan, S. Downes and F. E. Hancock, *J. Synchrotron Rad.*, **2**, 264 (1995).

[19] J. Ghijsen, L. H. Tjeng, H. Eskes, R. L. Johnson and G. A. Sawatzky, *Phys. Rev. B*, **42**, 2268 (1990).

[20] C. Frontera, J. L. Garcia-Munoz, A. Llobet, M. A. G. Aranda, *Phys. Rev. B,* **65**, 180405 (2002).

[21] F. Fauth, E. Suard, V. Caignaert and I. Mirebeau, *Phys. Rev. B* ,**65**, 180405 (2002).

[22] A. A. Taskin, A. N. Lavrov and Y. Ando, *Phys. Rev. B*, **71**, 134414 (2005)

[23] R. James and E. Moore, *Metal-Ligand Bonding*, Bath Press, Glasgow (2004).

Chapter 7

Overall Conclusions

7.1 Introduction

In this work, high quality single crystal samples of $LnBaCo_2O_{5+\delta}$ (Ln = Gd, Dy, $Dy_{1-x}Tb_x$ – Ln-112) and $YbBaCo_4O_7$ (Ln-114), grown by the overstoichiometric flux melt technique were studied using synchrotron photoemission spectroscopy. Magnetic characterisations for $LnBaCo_2O_{5+\delta}$ (Ln = Dy) and $LnBaCo_4O_{7+\delta}$ (Ln = Yb, Tb, Lu) single crystals were also performed in collaboration with Prof. S. N. Barilo and his group from the Institute of Solid State and Semiconductor Physics (ISSSP), Minsk, Belarus. This chapter presents a summary of the main conclusions drawn from the studies performed during this project.

7.2 $LnBaCo_2O_{5+\delta}$ - Ln-112

$LnBaCo_2O_{5+\delta}$ (Ln-112) and $LnBaCo_4O_7$ (Ln-114) are highly correlated Co oxides that show potentially useful magnetic and electronic properties. The 'double perovskites' of general formula $LnBaCo_2O_{5+\delta}$ (Ln = lanthanide element, $0 \leq \delta \leq 1$) show giant magnetoresistive behaviour in narrow composition ranges around $\delta = 0.5$ (Co (III)), a range of poorly understood spin state transitions, and a temperature-dependent metal-insulator (MI) transition. Co (III) is present in two environments, octahedral and pyramidal (with CoO_5 coordination).

High-resolution photoemission results on single crystal samples of $GdBaCo_2O_{5.5}$, $DyBaCo_2O_{5.5}$ and $Dy_{1-x}Tb_xBaCo_2O_{5+\delta}$ revealed that the temperature-based MI transitions in these compounds occurs in the 300-400 K temperature range. To observe a marked non-metal-to-metal transition, a post-growth oxygen annealing treatment for the as-grown single crystals of Ln-112 is necessary, achieving oxygen contents close to 5.50. This transition takes place from LS states to intermediate spin (IS) and high spin (HS) states of Co^{3+}

slowly and gradually which is contrary to sudden switch from LS to HS proposed by Frontera *et al.* [1]. The measurements support the '3-spin state' model of Asai *et al.* [2] adopted for doped $LaCoO_3$ [3].

The oxygen resonance photoemission study of $LnBaCo_2O_{5+\delta}$ (Ln = Gd, $Dy_{1-x}Tb_x$) shows that the features situated at around 3 eV, 5 eV and 9 eV binding energy respectively in the valence band of $GdBaCo_2O_{5.5}$ and $Dy_{1-x}Tb_xBaCo_2O_{5+\delta}$ contribute O 2p states to the valence band density of states function. The feature located at 5 eV shows a large resonance effect. Thus we conclude that the O 2p states contribute most strongly to the valence band at 5 eV binding energy.

Our surface degradation studies for $LnBaCo_2O_{5+\delta}$ (Ln-112) show some physisorption of water and dissociation to OH^- on the surfaces of $GdBaCo_2O_{5.5}$ and $DyBaCo_2O_{5.5}$. Though the sample of $Dy_{1-x}Tb_xBaCo_2O_{5+\delta}$ showed contamination, the nature of the contaminants could not be identified from its difference spectrum. In surface degradation of $YbBaCo_4O_7$, the formation of OH^- is likely. These general observations are consistent with the water adsorption studies previous carried out on transition metal oxides [4-6]. One can conclude that the surfaces of single crystals of transition metal oxides are highly reactive and undergo degradation in UHV due to adsorption of residual gases. Signatures of surface degradation are typically observed in the valence band spectra at 9.1 eV and 5.1 eV. It is important that these signals are monitored during experiments, and the samples rescraped at intervals in order to maintain surface cleanliness.

Neutron diffraction data obtained by our collaborators on a single crystal sample of $DyBaCo_2O_{5.5}$ resulted in four proposed models for the magnetic structure of the high-temperature magnetically ordered phase of $DyBaCo_2O_{5.5}$. Two of them describe a G-type magnetic structure showing a combination of the low spin (LS) and high (HS) states, and the other two are approximately G-type. Additional experiments on spin-density mapping and full polarization analysis of the data are required to choose between these four models [7].

7.3 $LnBaCo_4O_{7+\delta}$ ($\delta = 0$) - Ln-114

$YbBaCo_4O_7$ (Yb-114) is a mixed valence compound whose crystal structure is made up of Kagomé sheets of CoO_4 tetrahedra connected by triangular layers of CoO_4 tetrahedra. No photoemission studies on $YbBaCo_4O_7$ have been reported so far and are carried out for the first time in this PhD project. These photoemission studies consist of resonant photoemission of the cations (Yb^{3+}, Ba^{2+}), the anion (O^{2-}) and a limited number of spectra at the Co 3p→3d threshold.

The resonance photoemission results allow the atomic character of the valence band states of $YbBaCo_4O_7$ to be determined. General features, in the valence band of $YbBaCo_4O_7$, have been found to appear approximately around 1.4 eV, 5.6 eV and 9.6 eV binding energies. The Yb 4d→4f resonance reveals a prompt resonance effect for the features located at 9.6 eV and 13.2 eV binding energies revealing the contribution of 4f states to the DOS function of $YbBaCo_4O_7$. The DOS function outside the valence band of $YbBaCo_4O_7$ has contributions of Yb 5p states within the 24-32 eV binding energy range, where an enhanced resonance is seen. The shapes and binding energy positions of the features located in the 9-13 eV binding energy, in the valence band of $YbBaCo_4O_7$, indicate that the oxidation state of Yb in $YbBaCo_4O_7$ is 3+ because Yb^{2+} signal appears only in the vicinity of the Fermi level [8, 9]. This conclusion is in agreement with the photoemission studies undertaken by Okane *et al.* [8] and Orlowski *et al.* [9].

The O 2s→2p resonance photoemission results show that the DOS function of $YbBaCo_4O_7$ has contributions from O 2p-derived states throughout the valence band. Ba 4d→4f resonance photoemission reveals that the features within the 16-19 eV binding energy range contains the contribution of the Ba 5p states to the DOS function of $YbBaCo_4O_7$. It is worthy of note that the Ba 5p states do not contribute to the valence band of $YbBaCo_4O_7$. This is also the case in similar materials such as Ln-112, $LnBaCo_2O_{5+\delta}$ (Ln = Gd, Dy, Eu, $Dy_{0.9}Tb_{0.1}$) [10, 11].

The CIS spectra from $YbBaCo_4O_7$ recorded over the photon energy range 55 to 70 eV passing through the Co 3p→3d threshold at the features within the 1.4-16 eV binding energy range show that the valence band contains contributions from Co 3d states at peaks

situated at 9.6 eV (anti-resonance) and 13.2 eV binding energies (resonance). Clear resonances are not observed elsewhere in the valence band, but are inherently very noisy. It is likely that the DOS close to E_F in the valence band of $YbBaCo_4O_7$ is made up of Co 3d and O 2p states and it is these states as is the case for other perovskite cobaltites such as $LaCoO_3$ [3, 12, 13], $HoCoO_3$ [10] and $GdBaCo_2O_{5+\delta}$ [11], and these states determine the magnetic and electronic behaviour.

Magnetic characterisation for $LnBaCo_4O_{7+\delta}$ (Ln = Yb, Tb, Lu) single crystals was performed at the University of Manchester. Magnetic characterisation results confirm long-range magnetic ordering of cobalt spins at lower temperatures in nitrogen-annealed, oxygen-annealed and even in off- stoichiometric $YbBaCo_4O_{7+\delta}$ single crystal samples. We did not observe a spin-flip transition at 25 K. These magnetisation results are significantly different from those reported by Huq *et al.* [14] on powder samples of $YbBaCo_4O_7$ and show much more marked AF transition. Our magnetic hysteresis data recorded at T = 20 K reveal the presence of stable AF ordering in $TbBaCo_4O_{7+\delta}$ under applied fields $H < H_c$ and a weak ferromagnetic component at fields higher than H_c. The magnetic hysteresis data on $LuBaCo_4O_{7.2}$ indicate the possible chiral-glass like behaviour of the material at low temperatures. There is still a poor understanding of these findings. Polarised neutron diffraction and AC magnetic susceptibility experiments, at different frequencies, are scheduled by our collaborators in future. These experiments are designed to confirm the chiral-glass-like state, determine the correlation lengths and chirality parameters of short range magnetic ordering at different temperatures, and study the possible AF ordering at 5 K in the $LnBaCo_4O_{7+\delta}$ geometrically frustrated magnetic system.

7.4 Comparison of $LnBaCo_2O_{5+\delta}$ and $LnBaCo_4O_{7+\delta}$

A comparison of the electronic structure of $LnBaCo_2O_{5+\delta}$ (Ln = Gd, Dy, $Dy_{1-x}Tb_x$ – Ln-112; $0 \leq \delta \leq 1$) and $LnBaCo_4O_7$ (Ln = Yb – Ln-114) single-crystal surfaces, as a result of photoemission studies, reveals that the structure of the valence band of two oxides is strikingly similar. The only significant difference is the absence of a feature at around 2 eV BE in Ln-114 that in Ln-112 has been attributed to low spin Co^{3+} in octahedral sites [3, 11]. As there are no Co^{3+} ions in octahedral sites in Ln-114, this provides some confirmation of

the previous assignments [3, 11]. In other respects, we conclude that the Co 3d/ O 2p hybridisation in the valence bands of these two compounds is very similar.

References

[1] C. Frontera, J. L. Garcia-Munoz, A. Llobet, M. A. G. Aranda, *Phys. Rev. B*, **65**,180405 (2002).

[2] K. Asai, A. Yoneda, O. Yokokura, J. M. Tranquada, G. Shirane and K. Kohn, *J. Phys. Soc. Jpn.*, **67**, 290 (1998).

[3] A. G. Thomas, W. R. Flavell, P. M. Dunwoody, C. E. J. Mitchell, S. Warren, S. C. Grice, P. G. D. Marr, D. E. Jewitt, N. Khan, V. R. Dhanak, D. Teehan, E. A. Seddon, K. Asai, Y. Koboyashi and N. Yamada, *J. Phys. Condens. Matter*, **12**, 9259 (2000).

[4] R. L. Kurtz, R. Stockbauer, T.E. Madey, D. Mueller, A. Shih and L. Toth, *Phys. Rev. B*, **37**,7936 (1988).

[5] J. Hollingworth, PhD Thesis, UMIST (1999).

[6] W. R. Flavell, J. H. Laverty, D. S. L. Law, R. Lindsay, C. A. Muryn, C. F. J. Flipse, G. N. Raiker, P. L. Wincott and G. Thornton, *Phys. Rev. B*,**41**,11623(1990).

[7] S. N. Barilo, S. V. Shiryaev, G. L. Bychkov, A. S. Shestak, W. R. Flavell, A. G. Thomas, H. M. Rafique, Y. P. Chernenkov, V. P. Plakhty, E. Pomjakushina, K. Conder and P. Allenspach, *J.Crystal Growth* ,**310**,1867 (2008).

[8] T. Okane, S. Fujimori, K. Mamiya, J. Okamoto, Y. Muramatsu, A. Fujimori, Y. Nagamoto and T. Koyanagi, *J. Phys. Condens. Matter*, **15**, 2197 (2003).

[9] B. A. Orlowski, B. J. Kowalski, E. Guziewicz, K. S. Sadowska, N. Barrett, C. Guillot, R. L. Johnson and J. Ghijsen, *Prog. Surf. Sci*., **67**, 323 (2001).

[10] D. Tsoutsou, PhD Thesis, The University of Manchester (2005).

[11] W. R. Flavell, A. G. Thomas, D. Tsoutsou, A. K. Mallick, E. A. Seddon, C. Cacho, A. E. R. Malins, R. L. Stockbauer, R. L. Kurtz, P. T. Sprunger, S. N. Barilo, S. V. Shiryaev, and G. L. Bychkov, *Phys. Rev. B*, **70**, 224427 (2004).

[12] T. Saitoh, T. Mizokawa, A. Fujimori, M. Abbate, Y. Takeda and M. Takano, *Phys. Rev. B*, **56**,1290 (1997).

[13] M. Abbate, J. C. Fuggle, A. Fujimori, L. H. Tjeng, C. T. Chen, R. Potze, G. A. Sawatzky, H. Eisaki, S. Uchida, *Phys. Rev. B*, **47**, 16124 (1993).

[14] A. Huq, J. F. Mitchell, H. Zheng, L. C. Chapon, P. G. Radaelli, K. S. Knight and P. W. Stephens, *J. Solid State Chem.*, **179**, 1136 (2006).